School of Mathematics, Statistics, and Physics
Newcastle University
Newcastle upon Tyne
United Kingdom

Numerical Simulations of Inhomogeneous Quantum Turbulence

Em Rickinson

Thesis submitted for the degree of Doctor of Philosophy

April 2020

Abstract

The modelling of turbulent fluids has been an active area of research for over a century, with applications in diverse areas such as aeronautics and meteorology. The discovery and realisation of quantum fluids, such as low temperature helium and Bose-Einstein condensates (BECs), offers an experimental and theoretical route toward insights into the dynamics of classical fluids in an ostensibly simpler, due their inviscid properties, context. However, to utilise this we need to appreciate where they are comparable and where they differ significantly, in terms of their material properties, their flows, and any phenomena arising from the underlying quantum mechanics. The work in this thesis aims to further this understanding by considering the problem of vorticity transport, and extending previous work concerning dissipation in quantum fluids.

Turbulence in classical fluids consists of vortices of many length scales, from the size of the system down to the Kolmogorov length scale at which viscosity acts to dissipate energy; the direct numerical simulation of classical flows with even moderate Reynolds numbers is extremely computationally intensive due to the need to resolve at many scales. In contrast, vortices in quantum fluids have quantised circulation, and only those quantum vortices with the lowest circulation are stable. Two distinct regimes of turbulence have been identified in quantum fluids, the quasiclassical regime in which organised bundles of vortex filaments are believed to emulate the range of scales and energy distribution observed in classical turbulence, and the ultraquantum regime, composed of an essentially random tangle of vortices with no large-scale structure.

Despite these fundamental differences many parallels have been observed between classical turbulence and quantum turbulence, including various hydrodynamic instabilities, the development of Kármán vortex streets in the wake of barriers in a flow, and the Kolmogorov velocity statistics and energy spectrum.

The numerical investigations in this thesis can be split into those pertaining to homogeneous turbulence, and those pertaining to inhomogeneous turbulence. Many experiments probe the properties of quantum turbulence in superfluid helium through channel flow experiments, with versatile theory due to Vinen (Proc. Royal Soc. Lond. A **240**, 1220:114-127 (1957)) describing the evolution of the statistical vortex line density in terms of opposing vortex generation and dissipation. We simulate homogeneous turbulence generated by thermal counterflow using the vortex filament method (VFM) in order to quantify the balance of the generation and dissipation of vorticity with an established technique. We then use a new numerical technique to probe the dissipation of homogeneous ultraquantum turbulence, by artifically injecting random vortices to reach statistically steady states.

Other experiments generate quantum turbulence locally, producing systems that are initially inhomogeneous. The behaviour of inhomogeneous quantum turbulence is less well understood than in the homogeneous case, and we address how vorticity spreads in such systems. We first consider the problem in systems of reduced dimensionality, relevant to BECs in which strong confinement in one direction results in quasi-2-D condensates. In these systems vortices are essentially topological point defects, since excitations along vortex lines are suppressed in the tightly confined direction. We model the evolution of an initially confined region of point vortices in such a geometry using the point vortex model and the Gross-Pitaevskii equation, and identify a value for the effective viscosity as an

emergent property of the spreading of the vortices.

A related investigation is performed for turbulence in superfluid ^{4}He at zero temperature in a fully three-dimensional geometry. The dynamics of quantum vortices are modelled with the VFM, and a value for the effective viscosity is found. We compare our method to a previous study, and review the values found for the effective viscosity at zero temperature and finite temperatures below the lamdba-point.

Acknowledgements

I owe a huge debt of gratitude to many people for their parts in my journey to this point. Firstly, I would like to thank my PhD supervisors, Andrew Baggaley and Carlo Barenghi, for the opportunity to work with a wonderful community, and for their invaluable patience, guidance, enthusiasm, and encouragement. I also thank Nick Parker, Yuri Sergeev, and George Stagg for many instructive discussions.

For their guidance and support, and taking a chance on me, I thank Jonathan Ferstenberg, Phil Ansell, and Anvar Shukurov.

To dear friends old and new, without whom I would not be here: James Martin and family, Eline Engels, Tom Wright, Jenny Hay, Ruthie Oldham, Iven Boldon and family, Katie Ashworth, Sam Warren and Sarah Jowett (International Babes! - thank you for proofreading!), and David Cushing; thank you for everything.

I would like to acknowledge EPSRC for funding this project, and pay tribute to the wider spirit of international scientific collaboration, particularly at this difficult time in UK poagenumberingarabiclitics.

I thank Michael Beaty, John Nicholson, and Chris Graham, for almost superhuman levels of patience whenever I poked my head around the door with yet another computer issue. I'd also like to thank the office team, and the wider university support staff.

Thank you to the many people who have contributed to my time at Newcastle University being the best experience of my life: Sultan Alyobi, Jordan Barnes, Clarissa Barratt, Thomas Billam, Thomas Bland, Marios Bounakis, Dimitrios Chiotis, Laura Cole, Paolo Comaron, Robert Cooper, Ged Cowburn, Ryan Doran, Andrew Duncan, Barry Dunne, Michael Ellis, Can Evirgen, Andrew Fletcher, Luca Gallantuci, Naomi Hannaford, Daniel Henderson, Alex Hindle, James Hollins, Emma Jones, Evgenios Kakariadis, Jinzhao Liu, Katie Marshall, Jackie Martin, Joe Matthews, Ashleigh McLean, Mae Mesgarnezhad, Hayley Moore, Keith Newman, Nick Proukakis, Rathish Ratnasingam, David Robertson, Tamara Rogers, Graeme Sarson, Amit Seta, Paula Sinclair, David Stewart, Chris Taylor, William Thomé, Matina Trachana, Laura Wadkin, David Walshaw, Jack Walton, and Toby Wood.

I also thank everybody at Climb Newcastle, and everyone in the local climbing community, of whom there are far too many to list here, for the best stress management possible.

To my Mum and Dad, as well as my brother Jonathan, my Grandparents, Aunt Jess, and the wider family, who have given me unrelenting support and encouragement, I am eternally grateful.

My whole love to Becca Anderson, my constant co-conspirator and companion in being a bit strange, staying curious, and double-dinner. Thank you for all of your patience and humour. Thanks also to Harry Anderson and Sharon Vincent for welcoming me to the family.

Finally, lest they ever learn how to read and feel left out, I thank my cats, Wispa, Slippery Wilf, and Mister Baby, who were instrumental in ensuring that I never slept in.

Contents

Chapter 1

Introduction

1.1 Helium & Superfluidity

It may, in hindsight, appear serendipitous that in the early years of the twentieth century, when the theory of quantum mechanics was first emerging as a dominant and wide-ranging explanation for the behaviour of matter and energy, a series of experiments on the liquefaction of the "permanent gases" (hydrogen, oxygen, nitrogen, carbon monoxide) and helium led to some of the most striking examples of the frequently counterintuitive consequences of quantum physics. In 1908 decades of progress in cryogenic cooling culminated in the liquefaction of helium below 4.2 K by Onnes [1], using the Hampson-Linde cycle [2], which utilises the Joules-Thompson effect: adiabatic expansion of a gas, i.e. a drop in pressure, results in a drop in temperature. In 1911 Onnes made the first observation of superconductivity, the sudden decrease of the electrical resistance of a material and simultaneous ejection of magnetic flux lines, in mercury cooled to 4.2 K, noting that "The temperature measurement was successful. [The resistivity of] Mercury practically zero." [3]. This is a macroscopically observable property that is a direct consequence of quantum mechanics.

The superfluidity of helium below the lambda transition point $T_\lambda \simeq 2.1768$ K (so-called because of the shape of the phase diagram of ^{4}He - see Fig. 1.1), referred to as He II, was first noted by Kapitza in 1938 [5], and independently by Allen and Misener [6], based on the observation of the flow rate of helium through extremely thin capillaries. The fluid exhibited negligible internal frictional forces, or viscosity, giving rise to a number of impressive phenomena. These include persistent current in which a flow induced, e.g., by stirring, in a smooth-walled cylindrical vessel will, theoretically, continue indefinitely [7], superfluid creep, in which helium will climb the sides of a container, due to the lack of internal friction to counteract surface tension [8], the aforementioned flow through fine capillaries that are inaccessible to ordinary fluids (superleak), and the fountain effect, in which the application of thermal energy results in a mechanical flow [9]. The almost instantaneous cessation of boiling below T_λ, due to the extremely efficient heat conduction of He II, is also of interest. The superfluidity of He II was proposed by London as a possible example of Bose-Einstein condensation [10], discussed in the next section, although this was not widely accepted at the time [11].

The behaviour of He II can be understood through the two-fluid model, due to Tisza [12] and refined by Landau [13]: the onset of Bose-Einstein condensation occurs at the λ-point,

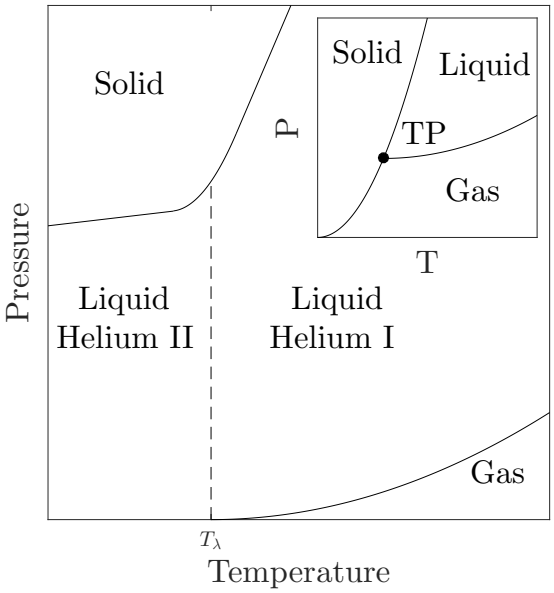

Figure 1.1: Schematic phase diagram of helium adapted from [4], with a typical phase diagram for conventional substances inset, showing the triple point where solid, liquid, and gaseous phases coexist, absent in helium.

and a proportion of the ^{4}He atoms accumulate in the lowest-energy single-particle state. Helium II is then comprised of two interpenetrating fluids, a superfluid component and a normal fluid component. It should be noted that this interpretation of He II as two fluids is made for conceptual ease; strictly speaking what is thought of as the normal fluid consists of thermal excitations, with the superfluid being the remainder. It is tempting to view this superfluid as a condensate, and indeed if the helium atoms are considered as an ideal gas the onset of condensation is expected to occur at ~ 3 K, consistent with T_λ - however, helium does not behave as an ideal gas, and due to the strong interparticle interactions only around 10% of the particles are in a condensed state even at zero temperature [14]. Excitations take the form of two types of quasiparticles, first proposed by Landau [13]: at low momenta excitations take the form of phonons, quantised packets of sound, while at higher momenta excitations known as rotons occur, the exact properties of which are still not fully understood - see, e.g., [15–17]. A sketch of a typical dispersion curve of the excitations is shown in Fig. 1.2. Landau also explained the superfluidity as a consequence of a linear dispersion relation at low momenta, corresponding to the phonons, with a quadratic dispersion relation at higher momenta, corresponding to the rotons, with neutron-scattering experiments confirming this [18].

The superfluid component is effectively at absolutely zero, and has zero viscosity and no entropy, while the normal fluid component has finite viscosity and carries all of the entropy. Both components are described by their density and local velocities, ρ_n and $\mathbf{v}_\mathrm{n}$, and ρ_s and $\mathbf{v}_\mathrm{s}$ respectively for the normal fluid and superfluid components, with $\rho_\mathrm{n} + \rho_\mathrm{s} = \rho$, the total density. Note that as $T \to T_\lambda$, $\rho_\mathrm{s} \to 0$ and $\rho_\mathrm{n} \to \rho$, while as $T \to 0$ K, $\rho_\mathrm{n} \to 0$ and $\rho_\mathrm{s} \to \rho$, although from a modelling point of view the normal fluid component is negligible

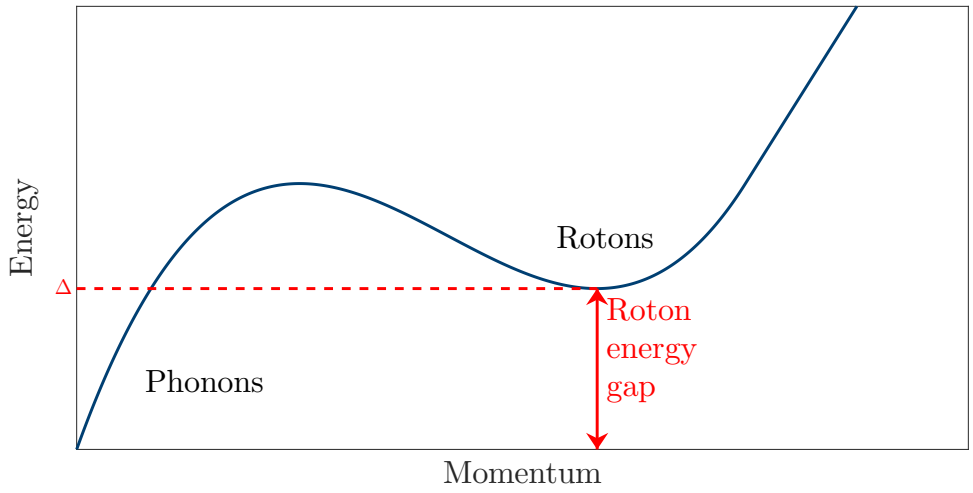

Figure 1.2: Sketch of the dispersion curve for excitations in helium II, showing the low momentum phonons with $E \propto k$, and the high momentum rotons with $E \propto k^2$.

below around 1 K. The precise relation of ρ_n and ρ_s to T is shown in Appx. B, alongside some other relevant physical properties of helium II.

The two fluids are coupled by a mutual friction force, the strength of which is temperature dependent [19, 20]. Since the normal fluid carries all of the entropy and has finite viscosity, while the superfluid has zero viscosity and carries zero entropy, the application of a heat source will induce a flow of normal fluid away from the source, and a corresponding flow of superfluid towards the heat source due to mass conservation, highlighting the separation of the flows in the two components.

An immediate consequence of the two-fluid model is the emergence of two wave equations, the first pertaining to density fluctuations and our everyday conception of sound, and the second pertaining to entropy fluctuations, referred to as second sound. Experimental measurements of the second sound velocity as a function of temperature helped to confirm the two-fluid model [21]. Measurement of the attenuation of second sound also helped to confirm the presence of quantised vorticity (discussed below) in helium II [22], and has been used to measure vortex line density over many orders of magnitude [23]

We also note that recent visualisation techniques [24] have enabled the direct observation of the two fluids' differing flows at the same location, in particular in the case of thermal counterflow (discussed in Sec. 5.3) where the fluid velocities are in opposite directions [25].

Although the lack of viscosity results in intriguing behaviour, and simplifies hydrodynamic descriptions of superfluids, perhaps the most drastic difference from conventional fluids, particularly from the perspective of turbulence, is the quantisation of circulation, predicted by the wavefunction description of He II of Onsager and Feynmann [26, 27]. The evolution of the wavefunction describing the fluid is governed by a nonlinear Schrödinger equation, which can be recast in a hydrodynamic form by splitting the complex-valued wavefunction into a real amplitude and phase: $\psi = f \exp(i\phi)$, with the velocity given by $\mathbf{v} = \hbar/m\nabla\phi$, where $\hbar = h/(2\pi) \simeq 1.055 \times 10^{-34}$ kg·m^2·s^{-1} is the reduced Planck constant.

If the fluid is on a multiply connected region the wavefunction must remain single valued, and thus integrating $\nabla\phi$ around any closed contour is restricted to integer multiples of 2π:

$$\oint_C \nabla\phi \cdot d\mathbf{l} = 2n\pi, \qquad (n \in \mathbb{Z}),$$

and so the circulation is restricted to:

$$\Gamma = \oint_C \mathbf{v} \cdot d\mathbf{l} = n\frac{h}{m}, \qquad (n \in \mathbb{Z});$$

i.e., the circulation is quantised [28]. For nonzero values of the circulation this then implies the existence of singularities in the wavefunction. These are the vortices, which present as topological defects.

Such vortices in He II are typically nucleated by mechanical means, including oscillating wires [29], grids [30], tuning-forks [31], and spheres [32], or by spin-down of containers [33], although they can also be introduced by thermal counterflow [19, 34, 35]. The visualisation of the motion of He II is achieved by the use of micron sized hydrogen tracer particles [36], or by the injection of fluorescent He_2^* molecules [24, 37, 38], with sufficient detail to track a single reconnection event [25].

1.2 Bose-Einstein Condensation

The prediction of Bose-Einstein condensation originated in the work of Bose, in a novel derivation of Planck's law of black-body radiation. Whilst lecturing on the failure of the classical theory of light, Bose inadvertently managed to derive Planck's law from first principles based on two assumptions: the indistinguishability of particles, and the discretisation of their phase space into cells of volume h^3, where h is Planck's constant. Realising the importance of this result, and struggling to get it published, Bose reached out to Einstein, leading to the 1924 publication of "Planck's law and the light quantum hypothesis" [39]. Einstein then extended the idea to massive particles in his 1925 paper "Quantum theory of the monoatomic ideal gas" [40], which predicted the phenomena of Bose-Einstein condensation: the macroscopic occupation of the lowest energy quantum state by bosonic particles (particles with integer spin, named for Bose) under certain conditions. In this section we shall review the basic theory of Bose-Einstein condensation, its experimental realisation, and some properties of the condensates.

First consider the Boltzmann distribution for the probable occupation of states for an ideal gas:

$$N_i = f_{\mathrm{B}}(E_i) = \frac{1}{e^{(E_i-\mu)/k_{\mathrm{B}}T}},$$

where N_i is the occupancy of state i, E_i is the energy corresponding to state i, μ is the chemical potential, $k_{\mathrm{B}} \simeq 1.381 \times 10^{-23}$ $\mathrm{m^2{\cdot}kg{\cdot}s^{-2}{\cdot}K^{-1}}$ is the Boltzmann constant, and T is the temperature in Kelvin, predicted by maximising the number of microstates (exact distribution of distinguishable particles across states) with respect to the possible macrostates

(occupation number of all states) [41]. By including the degeneracy of states, i.e. the number of states in particular energy levels, this can be recast to describe the occupation of the j^{th} energy level:

$$N_j = g_j f_{\text{B}}(E_j),$$

where g_j is the degeneracy of the j^{th} energy level.

For bosons the discretisation of phase space is no longer a mathematical 'trick', but reality. However, the indistinguishability of particles leads to a different distribution of particles across states in an ideal gas, given by the Bose-Einstein distribution:

$$N_i = f_{\text{BE}}(E_i) = \frac{1}{e^{(E_i-\mu)/k_{\text{B}}T} - 1}.$$

At this point it is convenient to treat the discrete energy levels as a continuum, which is valid when there are many accessible energy levels. The number of particles at a given energy E is then:

$$N(E) = g(E) f_{\text{BE}}(E) = \frac{g(E)}{e^{(E_i-\mu)/k_{\text{B}}T} - 1}, \tag{1.1}$$

where $g(E)$ is the density of states, which for an ideal gas in a box of volume $\mathcal{V}$ has the form:

$$g(E) = \frac{2\pi(2m)^{3/2}\mathcal{V}}{h^3} E^{1/2}, \tag{1.2}$$

where m is the mass of the boson under consideration. Integrating eq. (1.1) over energy, and using eq. (1.2) for the density of states, yields an expression for the total number of particles:

$$N = \frac{(2\pi m k_{\text{B}}T)^{3/2}\mathcal{V}}{h^3} g_{3/2}(z), \tag{1.3}$$

where $g_{3/2}(z) = \sum_{p=1}^{\infty} z^p/p^{3/2}$, with $z = e^{\mu/k_{\text{B}}T}$, which reduces to the Riemann zeta function for $z = 1$ [4]. Note also that $z > 0$, and $z \leq 1$ to prevent unphysical negative populations.

Now consider increasing the number of particles in the box. This is accommodated by an increase in $g_{3/2}(z)$, mediated by an increase in μ. However, $g_{3/2}(z)$ has a maximum, for physical values of z, of $g_{3/2}(1) \simeq 2.612$, implying a saturation of the number of particles. It transpires that in the change from discrete to continuous energy levels the ground state is neglected, and the maximum value of eq. (1.3) actually describes the maximum occupation of the excited states, with critical number:

$$N_{\text{c}} = \frac{(2\pi m k_{\text{B}}T)^{3/2}\mathcal{V}}{h^3} g_{3/2}(1), \tag{1.4}$$

beyond which additional particles enter the ground state. Equivalently, for a fixed system size and particle number, there exists a critical temperature T_{c} given by setting $z = 1$ in eq. (1.3) and solving for T:

$$T_{\mathrm{c}} = \frac{h^2}{2\pi m k_{\mathrm{B}}} \left(\frac{N}{g_{3/2}(1)\mathcal{V}} \right)^{2/3}.$$

Below T_{c} the excited states are no longer able to contain all of the particles, with the excess again accumulating in the ground state. This is Bose-Einstein condensation: the macroscopic occupation of the lowest energy state, or condensation of particles in the lowest momentum state. Note that at $T = 0$ all particles must be in the ground state.

We can also view this transition through the lens of wave-particle duality. Dividing eq. (1.4) by $\mathcal{V}$ to get the particle density, then taking the inverse cube root, we find the typical interparticle spacing d to be:

$$d < \frac{1}{\sqrt[3]{g_{3/2}(1)}} \frac{h}{\sqrt{2\pi m k_{\mathrm{B}} T}}. \tag{1.5}$$

For a thermally-excited gas the de Broglie wavelength, pertaining to the wave-like behaviour of the particles, is given by [42]:

$$\lambda_{\mathrm{dB}} = \frac{h}{\sqrt{2\pi m k_{\mathrm{B}} T}}.$$

Combined with eq. (1.5), it is clear that:

$$\frac{1}{\sqrt[3]{g_{3/2}(1)}} \lambda_{\mathrm{dB}} > d, \qquad \text{or}$$

$$\lambda_{\mathrm{dB}} \gtrsim d,$$

after noting that $(g_{3/2}(1))^{-1/3} = (2.612...)^{-1/3} \simeq 1$; the onset of Bose-Einstein condensation occurs as the particle waves begin to overlap each other, eventually forming one giant matter-wave when the critical condition is well exceeded. This is illustrated in Fig. 1.3.

So far we have only considered bosonic particles. Fermionic particles, which obey the Pauli exclusion principle forbidding the simultaneous occupation of the same state within a system, follow the Fermi-Dirac distribution and do not condense in the same manner as bosons. Nevertheless, as spin is additive, at sufficiently low temperatures fermions undergo the Bardeen-Cooper-Schrieffer transition, combining to produce bosons in a process known as Cooper pairing [43]. These can then undergo Bose-Einstein condensation, typically at far lower temperatures than for ordinary bosonic condensates [44, 45]; it is due to this process that the fermionic ^{3}He has superfluid phases below $\sim$ 3 mK [46, 47], three orders of magnitude lower than ^{4}He.

Some seventy years passed between the prediction of Bose-Einstein condensation and the experimental realisation of such systems. In 1995 the Wieman and Cornell group succeeded in condensing a dilute (number density $\sim 2.5 \times 10^{12}$ cm^{-3}; cf. air at Standard Temperature and Pressure with number density $\sim 2.5 \times 10^{19}$ cm^{-3}) vapour of rubidium atoms at $\sim$ 170 nK [48], with evidence including the emergence of a narrow peak in the thermal velocity distribution, centred at zero velocity, shown in Fig. 1.4. The process of cooling a sample

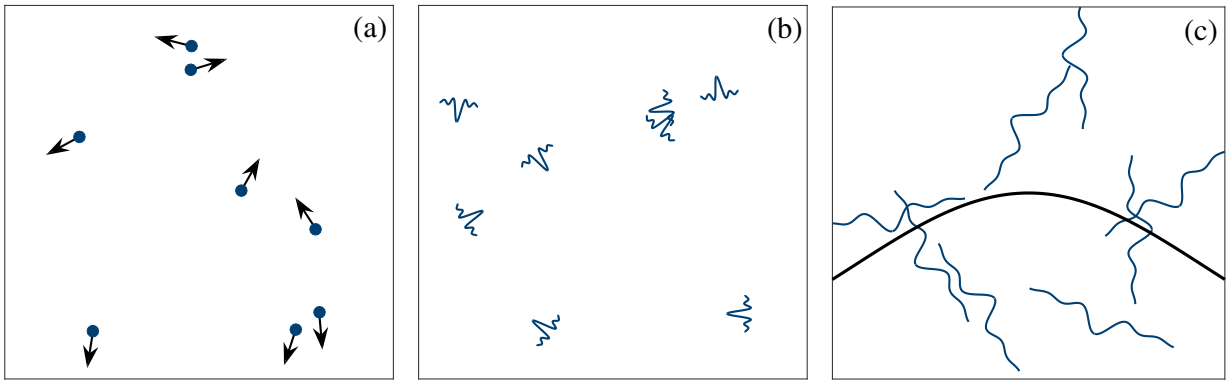

Figure 1.3: Schematic adapted from [4] showing the transition from classical point-like particle behaviour for $T \gg T_c$ (a), as the de Broglie wavelength becomes more prominent while still in the $T > T_c$ regime (b), to the onset of Bose-Einstein condensation as the particle-waves start to overlap at $T \sim T_c$ (c).

to this ultracold regime involved initial laser cooling (see [49] for details of the concept), loading the cooled atoms in a magnetic trap [50], then a final cooling stage by selective evaporation of the most energetic atoms [51].

Since then atomic Bose-Einstein condensates (BECs) have been produced in many independent laboratories from an extensive and expanding array of other particles, including other alkali metals [52–55], spin-polarised hydrogen [56], metastable hydrogen [57], calcium [58], chromium [59], strontium [60, 61], dysprosium [62], erbium [63], ytterbium [64], as well as more exotic magnon [65] and exciton-polariton [66] quasiparticle condensates, spinor condensates [67], and two species condensates [68–70].

Bogoliubov demonstrated that a weakly interacting Bose gas has a linear dispersion curve [71], accounting for the observed superfluidity of BECs [72]. Atomic BECs have some highly desirable properties for experimentalists: the strength, and even the sign, of their interactions can be tuned through Feshbach resonance [73, 74], allowing either repulsive or attractive interactions between particles. Although the physical size of condensates is limited, the control over them is constantly improving, with tight confinement in one or two directions allowing the production of quasi-lower-dimensional systems [75, 76], and other trapping potentials producing systems with homogeneous density [77–80], which can be readily modified by the use of a masked laser to produce traps of arbitrary shape, such as rings [81], double wells [82], and square boxes [80]. The imaging of BECs has also developed, from destructive expansion imaging [83, 84], to imaging that only removes a small fraction of the condensed atoms, allowing multiple images to be taken over the lifetime of an experiment [85], both with sufficient resolution to resolve single vortex cores. Furthermore, Bragg scattering can be used to infer the polarity of vortices, which is not clear from the condensate density alone [86, 87].

BECs are known to support various nonlinear excitations. As highly compressible fluids BECs exhibit density, or sound, waves, and can support wave turbulence [88, 89]. In systems of reduced dimensionality bright or dark, depending on whether interactions are attractive or repulsive, solitons exist: localised non-dispersive waves associated with a jump

in the phase of the condensate wavefunction [90, 91]. In higher dimensions they are unstable, typically decaying into various configurations of vortices [92]. Vortices in quantum fluids, the main focus of this thesis, are characterised by a localised depletion of the condensate density, which acts to mask a singularity in the phase of the condensate wavefunction, with the circulation around the vortex core quantised as a direct consequence of the single-valuedness of the phase. The vorticity of the fluid resides entirely within the vortex lines. Vortices can be nucleated by a variety of methods, with different controllability. By quenching through the BEC transition vortices are created by the Kibble-Zurek mechanism, as disparate coherent regions of the phase grow and merge, leading to defects in the phase at their boundaries which manifest as vortices [93, 94]. The density of vortices generated is predicted by the quench rate; the slower the quench, the more the phase is able to heal, resulting in fewer topological defects and hence fewer vortices [95]. Then, above a critical angular speed, rotation of a condensate will introduce vortices as they become energetically favourable [96], with vortices self-organising into regular lattices [97], with the same phenomenon also observed in superfluid helium [98]. Vortices can also be nucleated, with some degree of control over their number and location, by phase imprinting with lasers [99, 100], bubble collapse [101], and stirring with a laser [83, 102], or equivalently flow past an object [103, 104].

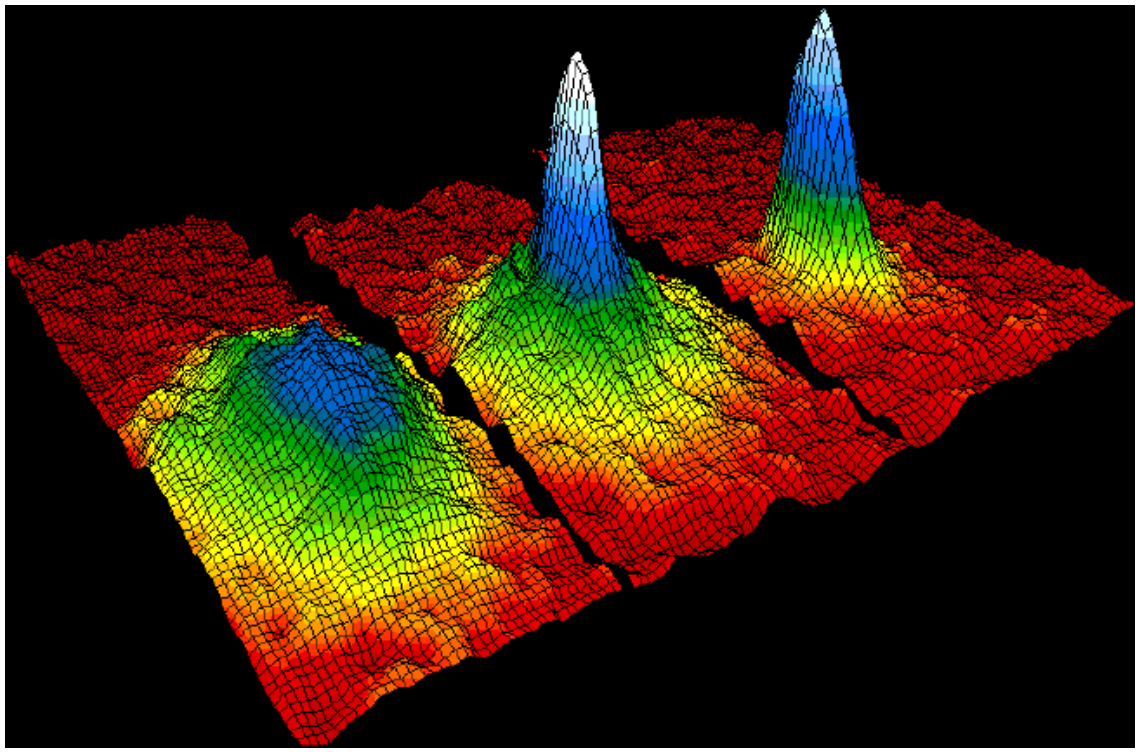

Figure 1.4: Thermal velocity distribution of rubidium atoms at three successive times (left to right) showing the formation of a narrow peak corresponding to the macroscopic occupation of the lowest energy state, i.e., Bose-Einstein condensation [reproduced from NIST/JILA].

1.3 Classical & Quantum Turbulence

Turbulence in classical, viscous fluids is a flow behaviour far from equilibrium, exhibiting chaotic, irregular, and unsteady velocity fields, with many vortices present on a wide range of length scales. Ubiquitous in fluids at all scales, from cardiovascular flows [105], to flows around cars, planes, wind turbines, and other everyday objects [106–109], to oceanic and atmospheric currents [110, 111] (illustrated in Fig. 1.5), to flows on astrophysical scales [112, 113], covering length scales on the order of 10^{-2}–10^{9} m and beyond. Modern computing enables large-scale direct numerical simulations solving the Navier-Stokes equations, as well as numerous sophisticated approximations to the full Navier-Stokes dynamics [114]. However, such studies are still unable to resolve flows on the range of scales required to model the most turbulent flows, with state of the art simulations accessing Reynolds numbers (characterising how developed the turbulence is, defined subsequently) of around 10^{4} [115–117], while real flows can attain Reynolds numbers in excess of 10^{7} [118].

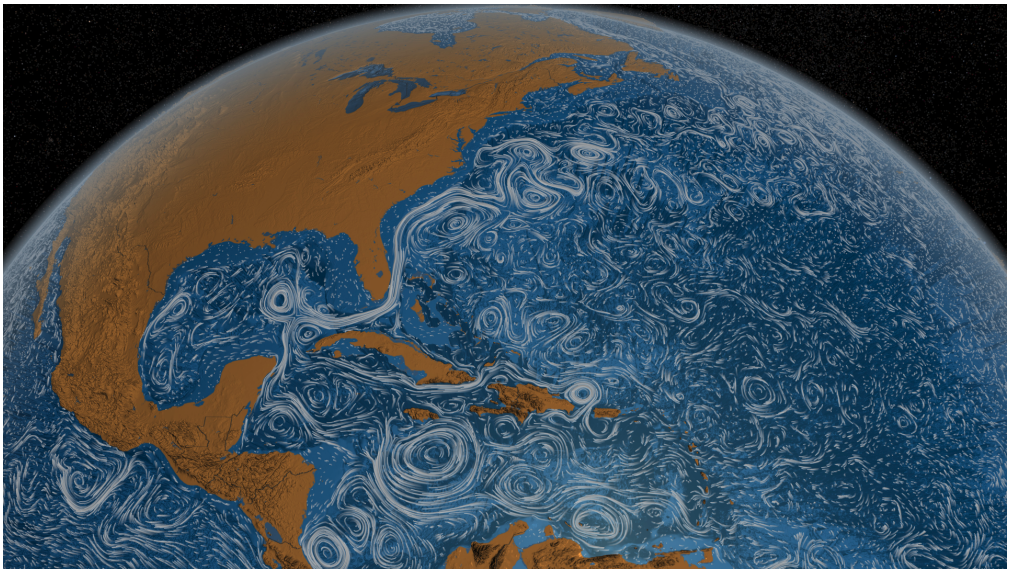

Figure 1.5: Visualisation of turbulent surface currents in the Gulf of Mexico based on a combination of numerical and observational data. Vortices on length scales from approximately 10^{4}–10^{6} m are evident. Reproduced from [119].

Early theorists such as Kelvin and Helmholtz realised the significance of vortices in the description of turbulence [120], with the picture of Richardson, and Kolmogorov's dimensional analysis, forming the basis of our current understanding. Energy is injected, typically by bulk motion, at the largest scale of the system referred to as the integral length scale $\mathcal{L}$, producing vortices at this scale. An oversimplified picture is that these vortices are unsteady and break down, producing smaller vortices, which in turn break down into successively smaller vortices, producing a cascade of energy down length scales, known as the Richardson cascade [121]. This cascade terminates when the vortices reach a length scale at which energy can be efficiently dissipated by the conversion of kinetic energy to thermal energy by viscosity, with this scale referred to as the Kolmogorov microscale, denoted η, and scales $\gg \eta$ and $\ll \mathcal{L}$ referred to as the inertial range.

The mean kinetic energy density of the flow, as a function of the wavenumber k, is given by [122]:

$$\int_0^\infty E(k)dk = \frac{1}{2}\langle \bar{\mathbf{u}} \cdot \bar{\mathbf{u}} \rangle,$$

where $\mathbf{u}$ is the flow velocity, giving the dimensions of E(k) as $[E(k)] = L^3/T^2$, with L length and T time. Considering the relevant quantities for describing the flow in the inertial range, we can neglect $\mathcal{L}$, as well as the characteristic velocity at this scale, and the kinematic viscosity ν as we are far from the scales at which they affect the flow. Kolmogorov proposed that the flow is self-similar at all scales within the inertial range, with the flow statistics depending entirely on the rate of energy dissipation [123]. The rate of energy dissipation per unit mass, ε, has dimensions $[\varepsilon] = L^2T^{-3}$. If $E(k)$ can only depend on the wavenumber k and the energy dissipation rate ε, then the only possible combination of ε and k which is dimensionally consistent is:

$$E(k) = C\varepsilon^{2/3}k^{-5/3},$$

where C is a dimensionless constant of order unity. This is the famous Kolmogorov $-5/3$ scaling law, illustrated in Fig. 1.6. This universal scaling has been confirmed by a huge body of experimental and observational evidence [124–127].

The structure of turbulence can be described by the structure functions:

$$S_p(\mathbf{r}) = \langle (u(\mathbf{x}+\mathbf{r}) - u(\mathbf{x}))^p \rangle,$$

where $\mathbf{x}$ and $\mathbf{r}$ are points in a turbulent flow field, u is the component of the velocity field in the direction of $\mathbf{r}$, p is the order of the structure function, and the angle brackets denote an ensemble average. Kolmogorov found the second- and third-order structure functions obeyed the power laws $S_2(\mathbf{r}) \sim (\varepsilon r)^{2/3}$, $S_3(\mathbf{r}) \sim (\varepsilon r)$ [128, 129], which was subsequently generalised to $S_p(\mathbf{r}) \sim (\varepsilon r)^{p/3}$ [130]. However, this was challenged by Landau and Lifshitz [131] as the derivation is based on treating ε as a constant, when it is in fact spatially inhomogeneous, and indeed experiments and simulations show that the exponent falls increasingly short of this prediction for higher-order structure functions [132, 133]. This feature of turbulence is termed intermittency, which manifests as 'clumpiness' in the turbulence, or more abrupt changes in the velocity than would be expected without intermittency [134]. Intermittency corrections to models of turbulence have been described which agree well with the data [135].

Classical fluid motion is well described by the Navier-Stokes equation:

$$\frac{\partial \mathbf{u}}{\partial t} + (\mathbf{u} \cdot \nabla)\mathbf{u} = \frac{-\nabla P}{\rho} + \nu \nabla^2 \mathbf{u}, \tag{1.6}$$

where $\mathbf{u}$ is the fluid velocity, P is the pressure, ρ is the fluid density, and ν is the kinematic viscosity. By considering the ratio of inertial forces $(\mathbf{u}\cdot\nabla)\mathbf{u}$ to dissipative forces $\nu\nabla^2\mathbf{u}$, with characteristic scales of U^2/L and $\nu U/L^2$ respectively, where U is the characteristic velocity scale and L is the characteristic lengthscale, we can construct the dimensionless Reynolds number:

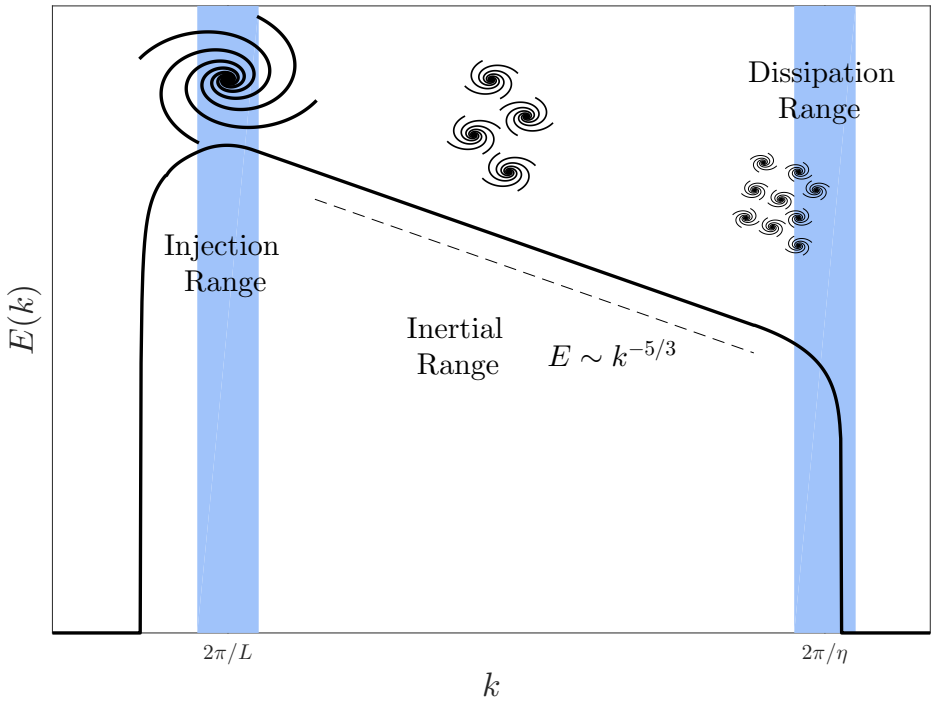

Figure 1.6: Sketch showing the distribution of energy over wavenumbers for a turbulent flow, on a logarithmic scale to highlight the Kolmogorov scaling. Energy cascades from the largest vortices, at the left of the figure, to the smallest vortices at the Kolmogorov microscale, at the right of the figure.

$$Re = \frac{UL}{\nu}, \tag{1.7}$$

which characterises the resulting flow. At low Reynolds numbers flows tend to be laminar, while at high Reynolds numbers flows will tend to be turbulent, with the particular transition point depending on the geometry of the system. The Kolmogorov microscale can be estimated by $\eta \approx L\mathrm{Re}^{-3/4}$ [136], which decreases as Re increases, leading to a larger inertial range; the Reynolds number can be interpreted as a measure of how developed turbulence is in a system.

The discussion so far relates to turbulence in three dimensions, yet turbulent flows also exist in two-dimensional systems. Systems which are apparently 3-D may in effect be 2-D; the surface currents shown in Fig. 1.5 are effectively 2-D as vertical density stratification suppresses 3-D effects [137, 138], as does strong rotation [139], or simple confinement in one direction. Turbulence in two dimensions is also dominated by vortices, but the reduced dimensionality has important implications for its character. The most surprising difference from 3-D is the inversion of the energy cascade: rather than energy flowing, on average, from large scales to small scales, it cascades from small scales to large scales. This phenomenon can be understood by considering the enstrophy, defined as ω^2, which measures the strength of the local rotation. The enstrophy can change by dissipation or by vortex

stretching, in which vorticity, and thus enstrophy, increases as a vortex is elongated [140]. The rate of kinetic energy dissipation in classical fluids is $\varepsilon = \nu\langle\omega^2\rangle$, which experiments show is independent of the viscosity for flows with very high Reynolds numbers, or as the viscosity goes to zero; the decrease in viscosity is balanced by an increase in vortex stretching [141]. However, in 2-D vortices are unable to stretch as they are confined to the plane, and so $\varepsilon \to 0$ as $\nu \to 0$, or in high Re flows. Hence, energy is not efficiently dissipated by viscosity in strong 2-D turbulence, but energy at small scales must still be dissipated by viscous heating. The resolution is that energy cascades to larger scales than the injection scale; the Fjørtoft argument gives a detailed reasoning for the direction of the cascade [142]. Similar dimensional arguments as for the energy cascade in 3-D find a cascade of enstrophy in 2-D, with a k^{-3} energy spectrum. Experiments and simulations confirm this dual-cascade, obtaining an $E(k) \sim k^{-5/3}$ power law at scales above the injection scale, driven by the inverse energy cascade, and an $E(k) \sim k^{-3}$ power law at scales below the injection scale due to the enstrophy cascade [143–145]. As with 3-D turbulence the flow can be described by velocity structure functions, with a predicted linear relation between the order of the structure function and the exponent that emerges; it has been suggested that these should not suffer from intermittency as 3-D turbulence does [146], although experiments on soap films do find evidence of intermittency [147, 148].

In contrast to classical fluids, in quantum fluids vorticity is quantised, with only the vortices with a single quantum of circulation stable, and there in no viscosity. Turbulence in this setting is primarily an irregular set of quantised vortex lines, accompanied by noisy density waves. This form of turbulence was first investigated by Feynman [27], and soon after realised in experiments by Vinen [19, 20, 149, 150]. On one hand, this simplified analogue to classical turbulence is an ideal setting to study vortex behaviour, often described as the skeleton of turbulence, with a great deal of experimental and theoretical work comparing them [151–159]. On the other, the description of classical turbulence, based on viscous fluids and a continuum of vortex scales, is clearly no longer valid.

Two distinct regimes of turbulence have been observed in quantum fluids: quasiclassical turbulence, and ultraquantum turbulence, often referred to as Kolmogorov turbulence and Vinen turbulence respectively [160].

As the name suggests, quasiclassical turbulence shares many of the features of classical turbulence, particularly the cascade of energy through length scales, energy again being distributed over scales as $E(k) \sim k^{-5/3}$. Simulations suggest that bundles of aligned vortices play the role of large vortices [161, 162], with the circulation around such a bundle being the sum of the vortices is contains. As there is no viscosity to act as a source of dissipation, some other process must take this role. Various mechanisms have been proposed for the decay of vortex tangles. Feynmann suggested a cascade-like breakdown of vortex loops, in which reconnections of vortex lines produce smaller and smaller vortex loops until they reach the scale of intervortex distances, at which point the vortex motion is dissipated into thermal excitations [27]. Energy can also be removed from the vortices by the emission of sound, either during reconnection events, or by the motion and oscillation of vortices [157]. This latter source of phonon emission is only efficient at large velocities [163], critically at higher harmonics of Kelvin waves [164], following a cascade from lower frequency Kelvin waves, typically initiated by reconnection events [165, 166]. These are all mechanisms which act at the smallest scales, whereas at larger scales energy can be dissi-

pated by the emission of vortex rings which subsequently annihilate at boundaries [157]. It is generally believed that the Kelvin wave cascade is the dominant dissipation mechanism in the quasiclassical regime, while the emission of vortex rings may also have an important role in the ultraquantum regime [167–172].

Ultraquantum turbulence is distinguished from quasiclassical turbulence by the lack of an energy cascade, with no large-scale structure present in what is essentially a random tangle of vortices [173]. No scaling law is evident for the distribution of energy, and the rate of decay in the absence of forcing further separates this regime from the quasiclassical regime, with the vortex line density decaying like $t^{-3/2}$ for Kolmogorov turbulence, and like t^{-1} for Vinen turbulence [174].

A wide variety of studies of quantum turbulence in statistically steady, homogeneous and isotropic systems have identified similarities and differences with classical turbulence, in their velocity statistics [175–177], energy spectra [156, 173, 178], decay [160, 174], and intermittency [179–181]. Specific flow patterns and instabilities, familiar in the context of classical fluids, have also been predicted in quantum fluids [104, 182–184].

In order to facilitate comparisons with classical turbulence it is convenient to introduce an effective kinematic viscosity, and in turn a superfluid Reynolds number; one would naïvely assume the Reynolds number to be infinite for an inviscid fluid, but this is not borne out by observations of superfluid helium at the lowest temperatures, and gives no insight into the nature of the fluid [185]. One typical approach is to introduce, on dimensional grounds, a quantum analogue to the classical kinetic energy dissipation rate $\epsilon = \nu\langle\omega^2\rangle$, where ω is vorticity, of the form: $\epsilon = \nu_{\text{eff}}(\kappa L)^2$, where κ is the quantum of circulation and L is the vortex line density, estimating ν_{eff} by measuring the decay of a turbulent tangle, with a range of measurements for different systems and alternative methodology [19, 20, 33, 149, 150, 160, 186–192].

While quantum turbulence is often referred to as the 'skeleton' of classical turbulence, alluding to the quantised nature of vorticity in quantum fluids, for analogies between quantum and classical turbulence to be meaningful the distinctions between them must be put on more rigorous ground. The main contribution of this thesis in this regard is the investigation of vorticity transport in turbulent regions. The dynamics of the vortices themselves are well understood, and there has been much focus on the generation and dissipation of quantum turbulence, e.g. [19, 20, 33, 193]. However, the bulk transport of vorticity is less well studied; in classical turbulence vorticity undergoes a nonlinear diffusion process, with the viscosity playing the role of the diffusion coefficient. As we shall see, in spite of the inviscid nature of quantum fluids, we also observe a diffusion process, with the diffusion coefficient proportional to the quantum of circulation, supporting the use of this as an effective viscosity as is done by considering the dissipation rate in other work such as [186–188, 191].

Pioneering work by Tsubota *et al.* [194] examined vortices diffusing in one geometry; we go further and show that a diffusion process exists based on particle statistics, as well as exploring the effects of vortex density (analogous to turbulence intensity) and boundaries. Additionally, a mechanism at the level of the individual vortices for the observed diffusion is proposed, with supporting evidence. We note that the problem of vorticity transport is also significant for the Grenoble-Lancaster experiment [195] which uses analogies between symmetry-breaking at the superfluid phase transition of ^{3}He to symmetry-breaking in the early universe to try and gain insight into galaxy formation processes.

We also revisit dissipation at zero temperature, and find evidence that the dissipation rate depends on the vortex line density in such a way that the effective viscosity also depends on the vortex line density; this is in contrast to the effective viscosity identified from vorticity transport, for which we observe no such dependence.

Although both atomic BECs and He II are quantum fluids supporting quantum turbulence, there are important distinctions between them. The length scales involved are very different, with vortices typically having a core radius on the order of a micron in atomic condensates, while vortices in He II have a core radius on the order of an ångström [196]. Helium experiments can be performed in systems on the order of a meter [197] (although they are typically much smaller, yet still many orders of magnitude away from the vortex core size), while the size of condensates is limited by the number of atoms that can experimentalists are able to condense - typically on the order of 10^5-10^6 atoms [52, 55, 59, 60], producing condensates on the order of 100 vortex core sizes. Despite the relatively poor separation of scales in atomic condensates, there is still compelling evidence for the existence of Kolmogorov turbulence in them [151, 171, 198, 199].

We note also that atomic condensates and He II are highly compressible fluids, and as such density waves are readily excited in these systems; this can be seen in Fig. 4.5 later in this thesis, which shows the evolution of a region of vorticity in a 2-D BEC modelled using the GPE, with a great deal of acoustic waves generated by the motion of the vortices. We restrict our attention to the turbulent motion of vortices, without including turbulent wave motion in our analysis. We stress also that, of the models used, only the GPE includes density waves, while the other models which we use include only the dynamics of the vortices themselves, and not the motion of the fluid.

1.4 Measurement & Current Experiments

There are a number of active experimental groups investigating quantum turbulence and vortices in the context of low temperature helium. In this section we review some experiments relevant to the work in this thesis, and discuss some of the instruments and techniques used to probe these systems.

In the Manchester group experiments on the dissipation and spectra of quantum turbulence are performed in ^{4}He at temperatures ranging from 0.08 K (effectively zero temperature from a modelling perspective) up to 1.6 K [33]. Turbulence is induced both globally and locally, using ion injection [159], towed grids, and spin-down of rotating systems [200](with Lancaster). The dissipation mechanisms of quantum turbulence are probed with experiments in rotating systems below 0.2 K [201], and on the reconnection of vortex rings generated with charged particles [202].

In the Lancaster group instruments for generating turbulence and probing systems are developed. Turbulence is generated and measured in ^{4}He using piezoelectric tuning forks at temperatures down to 1.2 K [203–205], dissipation mechanisms are probed using nanomechanical resonators from the transition temperature down to the millikelvin range [193], and in the related context of ^{3}He-B turbulence is generated by vibrating grids and vibrating wires, and measurement of the critical velocity for vortex shedding made [206, 207]. Less recently, an experiment was done in collaboration with the CNRS group in which a

localised region of vorticity was generated by neutron capture and the subsequent heating and quench in ^{3}He, with possible analogies to the creation of topological defects in the very early universe [195].

In the Aalto group experiments are conducted on rotating systems of ^{3}He-B, examining vortex generation mechanisms [208], mutual friction [209], and wave turbulence on vortex lines [210].

In the Florida group fluid motion in both components of ^{4}He above 1 K is visualised with the use of fluorescent He_2^* molecules, allowing direct velocimetry to be performed [24, 25, 211–213]. Experiments probing the intermittency [181, 214] and dissipation [215] of quantum turbulence, and the effective viscosity [192] are performed using this technique, with quantum turbulence generated by thermal counterflow [25, 192, 211–215] and towed grids [181].

In the Prague group, in ^{4}He at temperatures from 1.17 K to the transition temperature, turbulence is generated in channels, by thermal counterflow [216–218], bellows driven superflow [219] and co-flow [190], as well as by localised structures including vibrating grids [220] and vibrating forks [31, 221], with studies examining the decay of quantum turbulence [216], the effective viscosity [190], and the transition to turbulence [218].

In the CNRS group instruments for velocimetry are developed, including hot-wire anemometers [222, 223] and microscale cantilevers [224, 225]. These are deployed in studies of the energy spectra and intermittency of quantum turbulence in steady wake flows in ^{4}He from 1.28 K up to the transition temperature [180], and the effective viscosity of ^{4}He from 1.17 K up to the transition temperature in bellows driven co-flows [190].

We now discuss the probing of these systems, particularly the vortex line density and local velocity. The vortex line density in ^{4}He is measured by the attenuation of second sound: density waves in the normal and superfluid components in anti-phase, that manifest as temperature or entropy waves (as opposed to the density/pressure waves of first sound), which are damped by the presence of vortex filaments; the particular intensity of the damping can be used to infer the vortex line density [226, 227]. A recent study [217] suggests that this technique may also be extended to reconstruct the spatial profile of a vortex tangle by the use of higher harmonics. In ^{3}He-B the vortex line density can be inferred using Andreev-reflection. Thermal excitations (in the form of quasiparticles and quasiholes) have a mean free path for collisions far in excess of experimental dimensions, and thus move ballistically, only scattering on boundaries. However, excitations can also be Andreev-reflected by vortices; the proportion of excitations Andreev-reflected then gives an estimate of the vortex line density. As excitations can also be Andreev-reflected by the background superfluid flow, knowledge of the complete velocity field is necessary for a more accurate estimate [228, 229].

Velocimetry in superfluid helium is typically performed using micro-scale cantilevers, which measure the strain due to the flow, from which the velocity can be inferred [224]. Other approaches include pitot tubes, which infer the velocity from the difference between the pressure in the flow and the stagnant pressure [156], and hot-wire anemometers [222], where the measured excess cooling of a wire held at a constant temperature due to the flow past is used to infer the local fluid velocity. The oscillation of vibrating structures, with most focus on tuning forks, are damped by acoustic emission, scattering of excitations, and hydrodynamic losses [193], and make versatile probes which have be used to measure tem-

perature, pressure, density, and viscosity [230–232].

In many of these experiments turbulence is generated locally, typically by a vibrating structure [31, 206, 207, 220, 221], but also by ion injection [159] and a localised quench [195]. However, most numerical studies focus on homogeneous turbulence, particularly in periodic or hard wall systems. We seek to answer the question, first in 2-D systems then in 3-D systems, 'How does quantum turbulence spread into turbulence-free regions?'. In classical (incompressible) fluids described by the Navier-Stokes equation:

$$\frac{D\mathbf{u}}{Dt} = -\frac{\nabla P}{\rho} + \nu\nabla^2\mathbf{u}, \tag{1.8}$$

where $D\mathbf{u}/Dt = \partial\mathbf{u}/\partial t + (\mathbf{u}\cdot\nabla)\mathbf{u}$ is the material derivative, P is the pressure, ρ the density, and ν the kinematic viscosity, a vorticity transport equation can be found by taking the curl of eq. (1.8), yielding:

$$\frac{D\boldsymbol{\omega}}{Dt} = (\boldsymbol{\omega}\cdot\nabla)\mathbf{u} + \nu\nabla^2\boldsymbol{\omega}.$$

This is a (nonlinear) diffusion equation for the vorticity, with the kinematic viscosity acting as the diffusion coefficient. It is not clear from this how vorticity will be transported in a superfluid, as the viscosity vanishes.

We will also explore this as a means to estimate the effective viscosity of quantum fluids based on the spreading of vorticity, in contrast to approaches which are typically based on the dissipation of energy [160, 187, 188, 190–192].

1.5 Thesis Overview

The structure of this thesis is briefly reviewed in this section. After this introduction, we discuss theory and numerical methods pertaining to 2-D systems in Chapters 2 & 3, and numerical studies in 2-D in Chapter 4. We then discuss theory and numerical methods pertaining to 3-D systems in Chapters 5 & 6, and 3-D numerical studies in Chapter 7. We also include a set of appendices.

The results presented in Chapters 4 & 7 are given in part in the following publications, with collaborations indicated:

- Diffusion of Quantum Vortices [233]
  E. Rickinson, N. G. Parker, A. W. Baggaley, & C. F. Barenghi, *Phys. Rev. A.* **98** 023608 (2018)

- Inviscid Diffusion of Vorticity in Low-Temperature Superfluid Helium [234]
  E. Rickinson, N. G. Parker, A. W. Baggaley, & C. F. Barenghi, *Phys. Rev. B.* **99** 224501 (2019)

- Superfluid Turbulence Driven by Cylindrically Symmetric Counterflow
  E. Rickinson, C. F. Barenghi, Y. A. Sergeev, & A. W. Baggaley, *Phys. Rev. B.* (Accepted April 2020)

- Dissipation of Quantum Turbulence in ^{4}He at 0K
  E. Rickinson, N. G. Parker, A. W. Baggaley, & C. F. Barenghi, (**In preparation**)

Simulations of the 2-D Gross-Pitaevskii equation used George Stagg's implementation [235, 236] as a basis.

Simulations of the vortex filament method used Andrew Baggaley's QVORT [237] as a basis.

Chapter 1 - Introduction

We introduce concepts and theory of superfluidity in helium, Bose-Einstein condensation, turbulence in classical and quantum fluids, and discuss some relevant experiments.

Chapter 2 - 2D Models

We describe the point vortex model (PVM), a simple Lagrangian model for 2-D vortex dynamics, and some relevant boundaries and solutions. We then describe the Gross-Pitaevskii equation (GPE), a nonlinear Schrödinger equation derived from mean-field methodology, which accurately describes the physics of a dilute, weakly interacting Bose gas at temperatures far below the critical temperature. We introduce a non-dimensional version of the GPE, some relevant physical quantities and solutions, and discuss the quantisation of circulation.

Chapter 3 - Numerical Methods I

We describe methods for approximating derivatives and the numerical integration of differential equations. We test the accuracy of our implementation of the PVM. The initialisation of the GPE, with methods for finding the ground state and imprinting vortices, is discussed, and we describe post-processing techniques for identifying and tracking vortices. We test the accuracy of our GPE simulations in terms of the conservation of energy.

Chapter 4 - 2D Numerical Experiments & Results

A numerical study of the spread of quantum vortices in 2-D is carried out using the PVM and the GPE. We quantify the diffusion process that emerges, and identify the diffusion coefficient as an estimate of the effective viscosity. We explore the effects of boundaries and vortex number density on the observed diffusion process. We also present some preliminary work in which we examine the potential use of the velocity statistics and other quantities of tracer particles to infer the vortex number density in experiments.

Chapter 5 - 3D Models

We describe the vortex filament method (VFM), relevant to quantum vortex filaments in helium, and the effect of finite temperature effects on the vortex dynamics.

Chapter 6 - Numerical Methods II

The implementation of the VFM is discussed, including the reconnection procedure and some relevant boundaries. A criterion to set the numerical time-step is given, and we test the accuracy of the implementation by comparing simulations with theoretical vortex evolution in several scenarios. An algorithm for reconstructing the trajectories of vortex filaments is described.

Chapter 7 - 3D Numerical Experiments & Results

The results of three numerical studies are presented. In the first we reproduce results concerning the vortex line density generated by thermal counterflow. In the second we report a new technique for inferring the dissipation rate of ultraquantum turbulence in He II, and relate this to the effective viscosity. Finally, we examine the spread of a region of quantum turbulence into free space, quantifying the diffusion process that emerges, and relating this to the effective viscosity.

Chapter 8 - 2D Conclusions

We summarise the results of our numerical investigations, and consider the potential direction of future work and experimental feasibility.

Appendices

We give detailed derivations of the PVM, GPE, and VFM. The numerical methods used are derived, including finite difference methods, Runge-Kutta time-stepping schemes, and Adams-Bashforth time-stepping schemes. Finally, some relevant physical properties of ^{4}He are summarised.

Chapter 2

2-D Models

We describe the models used in investigations in 2-D and some relevant features and solutions of them. We use the point vortex model, an idealised Lagrangian model that captures the essential features of vortex dynamics, and the Gross-Pitaevskii equation, which includes the key physics of Bose-Einstein condensates that are absent in the point vortex model. We note that the Gross-Pitaevskii equation is a 3-D model, but valid in 2-D for tightly confined condensates, with minor modifications to some of the physical parameters that enter into the equation.

2.1 The Point Vortex Model

We use the point vortex model (PVM) introduced by Helmholtz in 1858 [238]. The model describes the motion of irrotational point (having infinitessimal core size) vortices embedded in a two-dimensional, inviscid, incompressible fluid plane as a system of coupled ordinary differential equations.

For an unbounded system of N point vortices the equations of motion for the i^{th} vortex are:

$$\frac{dx_i}{dt} = -\frac{1}{2\pi}\sum_{j\neq i}\frac{\Gamma_j(y_i - y_j)}{r_{ij}^2} \qquad\qquad \frac{dy_i}{dt} = \frac{1}{2\pi}\sum_{j\neq i}\frac{\Gamma_j(x_i - x_j)}{r_{ij}^2} \tag{2.1}$$

where (x_i, y_i) is the position of the i^{th} vortex, r_{ij} is the separation between the i^{th} and j^{th} vortices, and Γ_j is the circulation around the j^{th} vortex [239]. Note the omission of the singular term $i = j$; point vortices have zero self-induced velocity. The velocity field may be evaluated at an arbitrary point (x, y) by susbtituting for (x_i, y_i) in eq. (2.1), with the summation then over all vortices. A derivation is given in Appx. A.1.

If we transform from our cartesian coordinate system to a polar coordinate system, we can express the equations of motion for the fluid around a single vortex at the origin as:

$$\begin{aligned}\frac{dr}{dt} &= \frac{\partial r}{\partial x}\frac{dx}{dt} + \frac{\partial r}{\partial y}\frac{dy}{dt} \\ &= \frac{2x}{r}\frac{dx}{dt} + \frac{2y}{r}\frac{dy}{dt}\end{aligned}$$

$$
\begin{aligned}
&= \frac{2x}{r}\left(\frac{-\Gamma y}{2\pi r^2}\right) + \frac{2y}{r}\left(\frac{\Gamma x}{2\pi r^2}\right) \\
&= 0, \\
\frac{d\theta}{dt} &= \frac{\partial\theta}{\partial x}\frac{dx}{dt} + \frac{\partial\theta}{\partial y}\frac{dy}{dt} \\
&= \frac{-y}{r^2}\frac{dx}{dt} + \frac{x}{r^2}\frac{dy}{dt} \\
&= \frac{-y}{r^2}\left(\frac{-\Gamma y}{2\pi r^2}\right) + \frac{x}{r^2}\left(\frac{\Gamma x}{2\pi r^2}\right) \\
&= \frac{\Gamma}{2\pi r^2},
\end{aligned}
$$

so the motion around a point vortex is entirely azimuthal. Recalling $|\mathbf{v}| = \sqrt{v_r^2 + (rv_\theta)^2}$, it is clear that the speed of the flow around the vortex is proportional to $1/r$. This is illustrated in Fig. 2.1

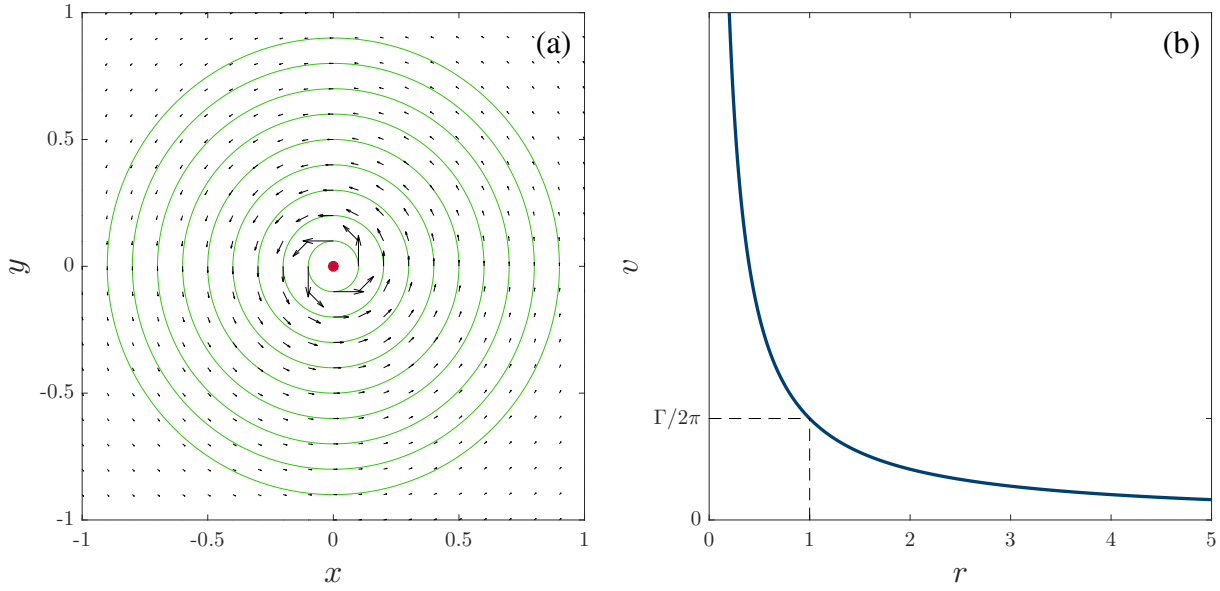

Figure 2.1: [Dimensionless units] Flow around a single point vortex. Panel (a) shows the velocity field (black arrows) and streamlines (green lines) around a positive vortex at the origin (red), (b) shows the magnitude of the flow velocity as a function of the distance r from the vortex.

The dynamics of a system of point vortices can be equivalently described by the Hamiltonian equations:

$$\Gamma_i \frac{dx_i}{dt} = \frac{\partial H}{\partial y_i}, \qquad \Gamma_i \frac{dy_i}{dt} = -\frac{\partial H}{\partial x_i}, \tag{2.2}$$

where

$$H = -\frac{1}{4\pi} \sum_{i \neq j} \Gamma_i \Gamma_j \ln (r_{ij}) \tag{2.3}$$

is the vortex Hamiltonian. The Hamiltonian H is conserved during the evolution of the vortices, and corresponds to the kinetic energy of the flow around them [239]. Although we do not offer a rigorous statement here, the dependence of the autonomous Hamiltonian on the separation of vortices offers a tantalising glimpse of some of the emergent vortex dynamics discussed in Sec. 4.1. If the system spread homogeneously the energy of the system would change; one way in which the system can then conserve energy is by bringing individual pairs of vortices of opposite sign circulation closer together, or pairs of the same sign circulation further apart. The value of H for pairs of vortices with $|\Gamma| = 1$ is shown in Fig. 2.2. We note that a pair of opposite circulation closer than $r = 1$ lowers the total energy of the system, while the total energy of the system is lowered by a pair of the same circulation further apart than $r = 1$, although the actual effect on the total energy also depends on their position in relation to the rest of the configuration.

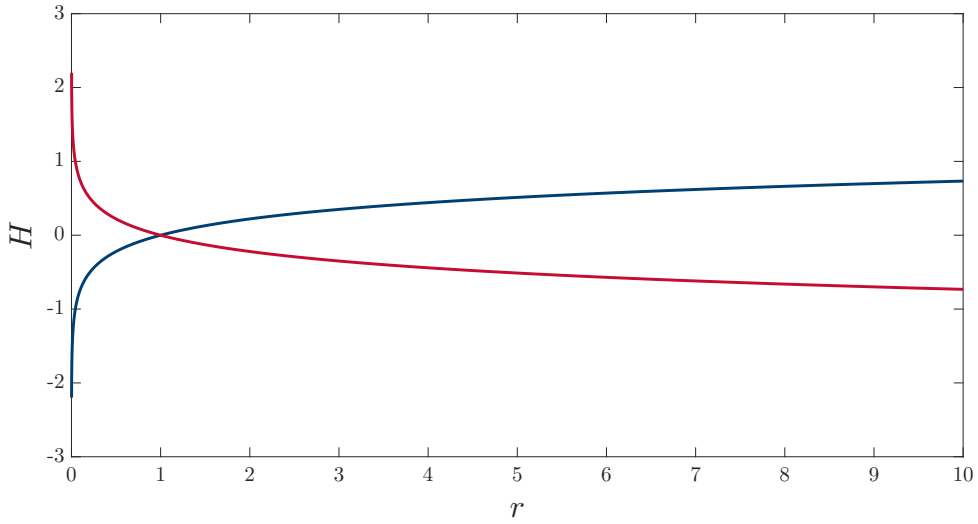

Figure 2.2: [Dimensionless units] Values of the autonomous hamiltonian H for an isolated pair of vortices with opposite circulation $\Gamma = \pm 1$ (blue) and identical circulation Γ=1 (red) as a function of the separation r between the two vortices.

Furthermore, H is invariant under rotation and translation; it follows from Noether's Theorem [240] that there are three first integrals of motion:

$$L_z = \sum_{i=1}^{N} \Gamma_i (x_i^2 + y_i^2), \qquad P_x = \sum_{i=1}^{N} \Gamma_i x_i, \qquad P_y = \sum_{i=1}^{N} \Gamma_i y_i, \tag{2.4}$$

corresponding to conservation of angular momentum and linear momenta.

2.1.1 Boundaries

As well as the unbounded PVM we consider two standard boundary conditions: periodic boundaries and hard wall boundaries. As the PVM is a Lagrangian model, as opposed to an Eulerian model, the methods used to impose these boundary conditions may be unfamiliar to some.

Consider the velocity contribution felt by a vortex in a singly periodic domain, say in x, with $x \in [0, L)$. As well as the usual summation eq. (2.1), it will feel contributions from the other vortices and itself at $(\mathbf{x} + L, \mathbf{y})$ and $(\mathbf{x} - L, \mathbf{y})$, where $(\mathbf{x}, \mathbf{y})$ is the position of the vortices. In full it will feel contributions from $(\mathbf{x} + nL, \mathbf{y})$, for $\forall n \in \mathbb{Z} \neq 0$. These additional vortices, used as a numerical 'trick' to impose periodicity, are referred to as ghost vortices. The equations of motion then become:

$$\begin{aligned}
\frac{dx_i}{dt} &= -\frac{1}{2\pi}\left[\sum_{j\neq i} \frac{\Gamma_j (y_i - y_j)}{r_{ij}^2} + \sum_{n\in\mathbb{Z}\neq 0}\sum_{j=1}^{N} \frac{\Gamma_J (y_i - y_j)}{(x_i - (x_j + nL))^2 + (y_i - y_j)^2}\right] \\
\frac{dy_i}{dt} &= \frac{1}{2\pi}\left[\sum_{j\neq i} \frac{\Gamma_j (x_i - x_j)}{r_{ij}^2} + \sum_{n\in\mathbb{Z}\neq 0}\sum_{j=1}^{N} \frac{\Gamma_J (x_i - (x_j + nL))}{(x_i - (x_j + nL))^2 + (y_i - y_j)^2}\right]
\end{aligned} \tag{2.5}$$

Similarly, for a doubly periodic domain with $x \in [0, L_x)$, $y \in [0, L_y)$, we have velocity contributions from ghost vortices at $(\mathbf{x} + nL_x, \mathbf{y} + mL_y)$, for $\forall (n, m) \in \mathbb{Z}^2 \neq \mathbf{0}$, to give equations of motion:

$$\begin{aligned}
\frac{dx_i}{dt} &= -\frac{1}{2\pi}\left[\sum_{j\neq i} \frac{\Gamma_j (y_i - y_j)}{r_{ij}^2} + \sum_{(n,m)\in\mathbb{Z}^2\neq\mathbf{0}}\sum_{j=1}^{N} \frac{\Gamma_J (y_i - (y_j + mL_y))}{(x_i - (x_j + nL_x))^2 + (y_i - (y_j + mL_y))^2}\right] \\
\frac{dy_i}{dt} &= \frac{1}{2\pi}\left[\sum_{j\neq i} \frac{\Gamma_j (x_i - x_j)}{r_{ij}^2} + \sum_{(n,m)\in\mathbb{Z}^2\neq\mathbf{0}}\sum_{j=1}^{N} \frac{\Gamma_J (x_i - (x_j + nL_x))}{(x_i - (x_j + nL_x))^2 + (y_i - (y_j + mL_y))^2}\right]
\end{aligned} \tag{2.6}$$

We illustrate the use of ghost vortices in this manner in Fig. 2.3.

The infinite and double infinite summations make the direct use of these equations of motion awkward; in practice we either truncate the series, or use an Ewald summation [241], discussed in more detail in Sec. 3.2.2.

Hard wall boundaries are imposed using the method of images [242], which constructs boundaries by using image vortices to enforce streamlines coinciding with the desired boundary. Since streamlines cannot intersect (as the velocity field is single-valued) no other streamline can cross that of the boundary, preventing any flow through the boundary.

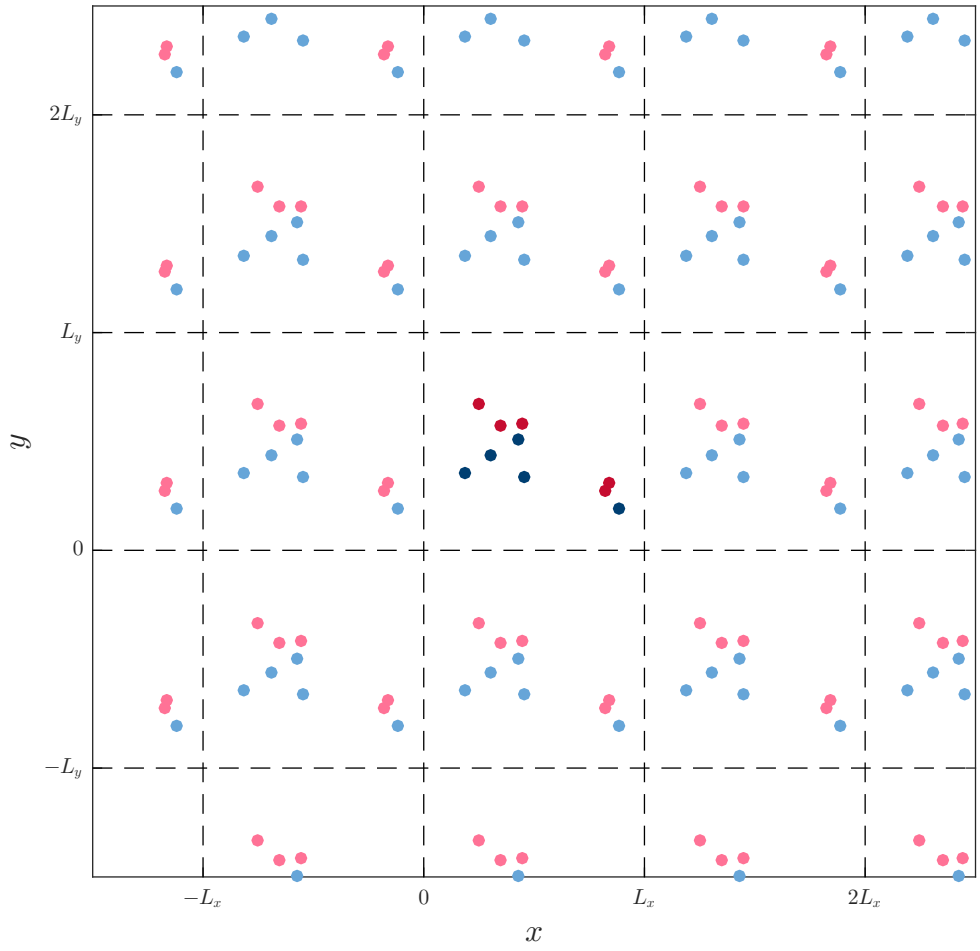

Figure 2.3: Schematic showing the use of ghost vortices to enforce periodic boundaries. The real vortices are shown in dark red and blue, and the ghost vortices in light red and blue.

We principally use hard wall boundaries in a disc geometry. For each point vortex of circulation Γ at position (x, y) inside a disc of radius a centred at the origin, we create an image vortex of circulation $-\Gamma$ at $(a^2x/(x^2+y^2), a^2y/(x^2+y^2))$, to give equations of motion:

$$\frac{dx_i}{dt} = -\frac{1}{2\pi}\left[\sum_{j\neq i}\frac{\Gamma_j(y_i-y_j)}{r_{ij}^2} + \sum_{j=1}^{N}\frac{-\Gamma_j(y_i-\frac{a^2y_j}{x_j^2+y_j^2})}{(x_i-\frac{a^2x_j}{x_j^2+y_j^2})^2+(y_i-\frac{a^2y_j}{x_j^2+y_j^2})^2}\right]$$

$$\frac{dy_i}{dt} = \frac{1}{2\pi}\left[\sum_{j\neq i}\frac{\Gamma_j(x_i-x_j)}{r_{ij}^2} + \sum_{j=1}^{N}\frac{-\Gamma_j(x_i-\frac{a^2x_j}{x_j^2+y_j^2})}{(x_i-\frac{a^2x_j}{x_j^2+y_j^2})^2+(y_i-\frac{a^2y_j}{x_j^2+y_j^2})^2}\right] \tag{2.7}$$

Consider the radial velocity component at an arbitrary position:

$$\frac{dr}{dt} = \frac{\partial r}{\partial x}\frac{dx}{dt} + \frac{\partial r}{\partial y}\frac{dy}{dt}$$

$$= \frac{2x}{r}\frac{dx}{dt} + \frac{2y}{r}\frac{dy}{dt}$$

$$= -\frac{1}{\pi}\sum_{i=1}^{N}\left[\frac{\Gamma_i(y-y_i)x}{((x-x_i)^2+(y-y_i)^2)r} + \frac{-\Gamma_i\left(y-\frac{a^2y_i}{x_i^2+y_i^2}\right)x}{\left(\left(x-\frac{a^2x_i}{x_i^2+y_i^2}\right)^2+\left(y-\frac{a^2y_i}{x_i^2+y_i^2}\right)^2\right)r}\right]$$

$$+\frac{1}{\pi}\sum_{i=1}^{N}\left[\frac{\Gamma_i(x-x_i)y}{((x-x_i)^2+(y-y_i)^2)r} + \frac{-\Gamma_i\left(x-\frac{a^2x_i}{x_i^2+y_i^2}\right)y}{\left(\left(x-\frac{a^2x_i}{x_i^2+y_i^2}\right)^2+\left(y-\frac{a^2y_i}{x_i^2+y_i^2}\right)^2\right)r}\right]$$

$$= \frac{1}{\pi}\sum_{i=1}^{N}\Gamma_i\left[\frac{xy_i-yx_i}{((x-x_i)^2+(y-y_i)^2)r} + \frac{y\frac{a^2x_i}{x_i^2+y_i^2}-x\frac{a^2}{x_i^2+y_i^2}}{\left(\left(x-\frac{a^2x_i}{x_i^2+y_i^2}\right)^2+\left(y-\frac{a^2y_i}{x_i^2+y_i^2}\right)^2\right)r}\right]$$

Putting over a common denominator:

$$= \frac{1}{2\pi}\sum_{i=1}^{N}\Big[\Big(xy_i(x-\frac{a^2x_i}{x_i^2+y_i^2})^2 + xy_i(y-\frac{a^2y_i}{x_i^2+y_i^2})^2 - yx_i(x-\frac{a^2x_i}{x_i^2+y_i^2})^2 - yx_i(y-\frac{a^2y_i}{x_i^2+y_i^2})^2$$
$$+y\frac{a^2x_i}{x_i^2+y_i^2}(x-x_i)^2 + y\frac{a^2x_i}{x_i^2+y_i^2}(y-y_i)^2 - x\frac{a^2y_i}{x_i^2+y_i^2}(x-x_i)^2 - x\frac{a^2y_i}{x_i^2+y_i^2}(y-y_i)^2\Big)$$
$$/\left(((x-x_i)^2+(y-y_i)^2)((x-\tfrac{a^2x_i}{x_i^2+y_i^2})^2+(y-\tfrac{a^2y_i}{x_i^2+y_i^2})^2)r\right)\Big]$$

Focusing on the numerator and expanding terms we have:

$$x^3y_i - 2x^2y_i\frac{a^2x_i}{x_i^2+y_i^2} + xy_i\left(\frac{a^2x_i}{x_i^2+y_i^2}\right)^2 + xy^2y_i - 2xyy_i\frac{a^2y_i}{x_i^2+y_i^2} + xy_i\left(\frac{a^2y_i}{x_i^2+y_i^2}\right)^2 - x^2yx_i +$$
$$2xyx_i\frac{a^2x_i}{x_i^2+y_i^2} - yx_i\left(\frac{a^2x_i}{x_i^2+y_i^2}\right)^2 - y^3x_i + 2y^2x_i\frac{a^2y_i}{x_i^2+y_i^2} - yx_i\left(\frac{a^2y_i}{x_i^2+y_i^2}\right)^2 + x^2y\frac{a^2x_i}{x_i^2+y_i^2} -$$
$$2xyx_i\frac{a^2x_i}{x_i^2+y_i^2} + yx_i^2\frac{a^2x_i}{x_i^2+y_i^2} + y^3\frac{a^2x_i}{x_i^2+y_i^2} - 2y^2y_i\frac{a^2x_i}{x_i^2+y_i^2} + yy_i^2\frac{a^2x_i}{x_i^2+y_i^2} - x^3\frac{a^2y_i}{x_i^2+y_i^2} +$$
$$2x^2x_i\frac{a^2y_i}{x_i^2+y_i^2} - xx_i^2\frac{a^2y_i}{x_i^2+y_i^2} - xy^2\frac{a^2y_i}{x_i^2+y_i^2} + 2xyy_i\frac{a^2y_i}{x_i^2+y_i^2} - xy_i^2\frac{a^2y_i}{x_i^2+y_i^2}$$

Gathering terms and substituting $x^2+y^2=a^2$ the numerator reduces to:

$$a^2xy_i - \frac{2a^4x_iy_i}{x_i^2+y_i^2} + \frac{a^4xy_i}{x_i^2+y_i^2} - a^2yx_i - \frac{a^4yx_i}{x_i^2+y_i^2} + \frac{a^4yx_i}{x_i^2+y_i^2} + a^2yx_i - \frac{a^4xy_i}{x_i^2+y_i^2} + \frac{2a^4x_iy_i}{x_i^2+y_i^2} - a^2xy_i,$$

which all cancel, giving us:

$$\left.\frac{dr}{dt}\right|_{x^2+y^2=a^2} = 0,$$

provided there are no singularities coming from vortices lying exactly on the boundary. Thus for any configuration of vortices, with no vortices lying on the boundary, the method of images ensures that the velocity is entirely azimuthal on the circle $x^2 + y^2 = a^2$. As the velocity is tangential to the streamlines, the boundary is a streamline as desired.

Figure 2.4 shows four vortex configurations of increasing complexity confined within a disc, with the resulting instantaneous streamlines superimposed.

2.1.2 Solutions

We now consider some analytic solutions to our equations of motion for the unbounded PVM, before discussing the transition to chaos. As we are considering quantum vortices which are only stable for $\Gamma = \pm h/m$, we limit this discussion to configurations of vortices where Γ can take only two possible values. of $\pm A$ for some constant A.

First, we examine the behaviour of pairs of point vortices. Consider a pair of vortices at (x, y), $(-x, -y)$ with identical circulation Γ. Note that any pair of vortices at (x_1, y_1), (x_2, y_2) can be mapped to this by selecting a coordinate system with the origin at $((x_1 + x_2)/2, (y_1 + y_2)/2)$, and recalling that a translation of an entire system of point vortices does not modify the dynamics.

The velocities of the vortices are then:

$$\mathbf{v}_1 = \left(\frac{-\Gamma y}{4\pi(x^2+y^2)}, \frac{\Gamma x}{4\pi(x^2+y^2)}\right), \mathbf{v}_2 = \left(\frac{\Gamma y}{4\pi(x^2+y^2)}, \frac{-\Gamma x}{4\pi(x^2+y^2)}\right).$$

Transforming to polar coordinates we have:

$$\begin{aligned}
\mathbf{v}_1 &= \left(\frac{2x}{r}\left(\frac{-\Gamma y}{4\pi(x^2+y^2)}\right) + \frac{2y}{r}\left(\frac{\Gamma x}{4\pi(x^2+y^2)}\right), \frac{-y}{r^2}\left(\frac{-\Gamma y}{4\pi(x^2+y^2)}\right) + \frac{x}{r^2}\left(\frac{\Gamma x}{4\pi(x^2+y^2)}\right)\right) \\
&= \left(0, \frac{\Gamma}{4\pi r^2}\right), \\
\mathbf{v}_2 &= \left(\frac{-2x}{r}\left(\frac{\Gamma y}{4\pi(x^2+y^2)}\right) + \frac{-2y}{r}\left(\frac{-\Gamma x}{4\pi(x^2+y^2)}\right), \frac{y}{r^2}\left(\frac{\Gamma y}{4\pi(x^2+y^2)}\right) + \frac{-x}{r^2}\left(\frac{-\Gamma x}{4\pi(x^2+y^2)}\right)\right) \\
&= \left(0, \frac{\Gamma}{4\pi r^2}\right),
\end{aligned}$$

so both rotate at the same constant speed $\Gamma/4\pi r$ about their joint centre, or $\Gamma/2\pi\delta$ where δ is the separation between them. The positions of a pair of vortices of equal circulation at time t are thus:

$$\mathbf{x}_1(t) = \left(\frac{x_1+x_2}{2} + r\cos\left(\theta_1 + \frac{\Gamma}{8\pi^2 r^2}t\right), \frac{y_1+y_2}{2} + r\sin\left(\theta_1 + \frac{\Gamma}{8\pi^2 r^2}t\right)\right),$$

$$\mathbf{x}_2(t) = \left(\frac{x_1+x_2}{2} + r\cos\left(\theta_2 + \frac{\Gamma}{8\pi^2 r^2}t\right), \frac{y_1+y_2}{2} + r\sin\left(\theta_2 + \frac{\Gamma}{8\pi^2 r^2}t\right)\right),$$

where $\theta_1 = \arctan(y_1 - y_2)/(x_1 - x_2)$, $\theta_2 = \arctan(y_2 - y_1)/(x_2 - x_1)$, and $(x_1, y_1), (x_2, y_2)$ are the initial positions of the vortices.

Next, consider a pair of vortices at (x_1, y_1), (x_2, y_2) with opposite circulation: $\Gamma_2 = -\Gamma_1$. We then have:

$$\mathbf{v}_1 = \left(\frac{-\Gamma_2(y_1 - y_2)}{2\pi r_{12}^2}, \frac{\Gamma_2(x_1 - x_2)}{2\pi r_{12}^2} \right),$$

$$\mathbf{v}_2 = \left(\frac{-\Gamma_1(y_2 - y_1)}{2\pi r_{12}^2}, \frac{\Gamma_1(x_2 - x_1)}{2\pi r_{12}^2} \right) = \left(\frac{-\Gamma_2(y_1 - y_2)}{2\pi r_{12}^2}, \frac{\Gamma_2(x_1 - x_2)}{2\pi r_{12}^2} \right) = \mathbf{v}_1.$$

The vortices have identical velocity, so move parallel to each other at a constant speed $v = |\Gamma_1|/2\pi r_{12}$. Furthermore, if we consider the vector from the first to the second vortex $(x_2 - x_1, y_2 - y_1)$, then we have $(x_2 - x_1, y_2 - y_1) \cdot \mathbf{v}_1 = 0$; the vortices move perpendicular to the line between them.

The positions of a pair of vortices with opposite circulation are then:

$$\mathbf{x}_1(t) = \left(x_1 - \frac{\Gamma_2(y_1 - y_2)}{2\pi r_{12}^2} t, y_1 + \frac{\Gamma_2(x_1 - x_2)}{2\pi r_{12}^2} \right),$$

$$\mathbf{x}_2(t) = \left(x_2 - \frac{\Gamma_2(y_1 - y_2)}{2\pi r_{12}^2} t, y_2 + \frac{\Gamma_2(x_1 - x_2)}{2\pi r_{12}^2} \right).$$

We illustrate the trajectories of both of these combinations in Fig. 2.5.

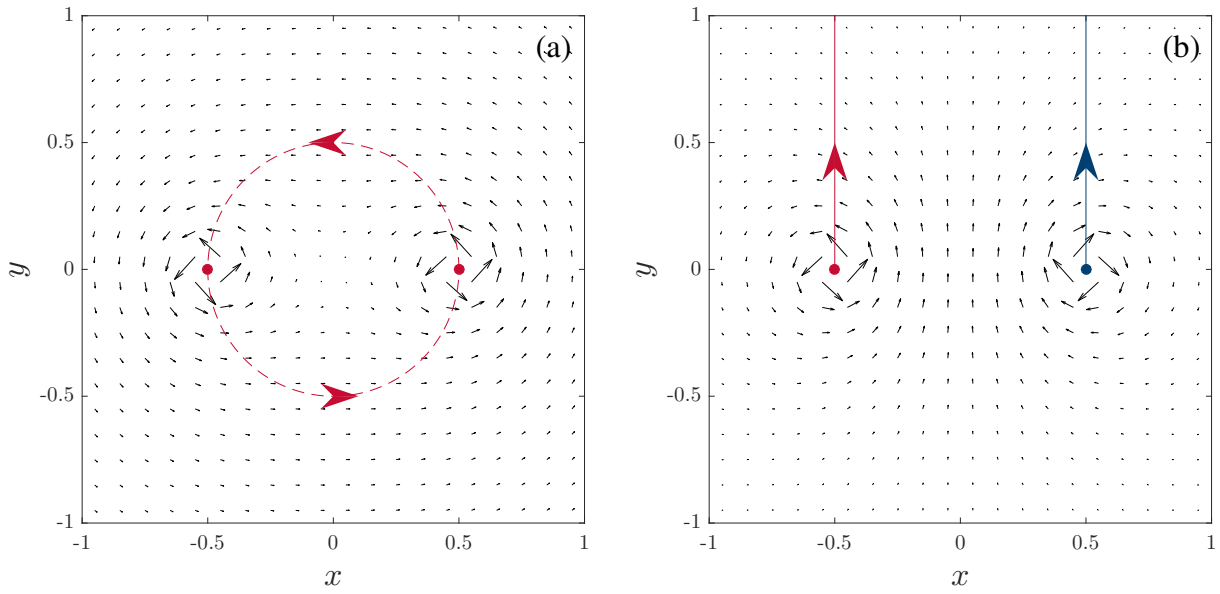

Figure 2.5: [Dimensionless units] Velocity fields and trajectories of pairs for vortices under the point vortex model. Two positive vortices with circulation $\Gamma = 1$ are shown in (a). Two vortices with opposite circulation are shown in (b), with $|\Gamma| = 1$ for both.

Although slightly more complicated analytic solutions exist, these two behaviours, the co-rotation of a like-signed pair, and the co-translation of an opposite-signed pair, form the kernel of the dynamics seen for the larger systems of vortices discussed in this work.

A detailed discussion of solutions, with the looser restriction that $\Gamma_i \in \mathbb{R}$, to the N-vortex problem can be found in [242]. Perhaps the most salient point with respect to this work is the emergence of chaos: systems of 3 or fewer vortices are integrable [243], while systems of 4 vortices are non-integrable except for cases where the total vorticity is zero [244, 245], with all systems of 5 or more vortices non-integrable and thus exhibiting chaotic dynamics [246].

We note that families of (unstable) stationary and translating solutions exist [247], a selection of which are illustrated in Fig. 2.6 for interest.

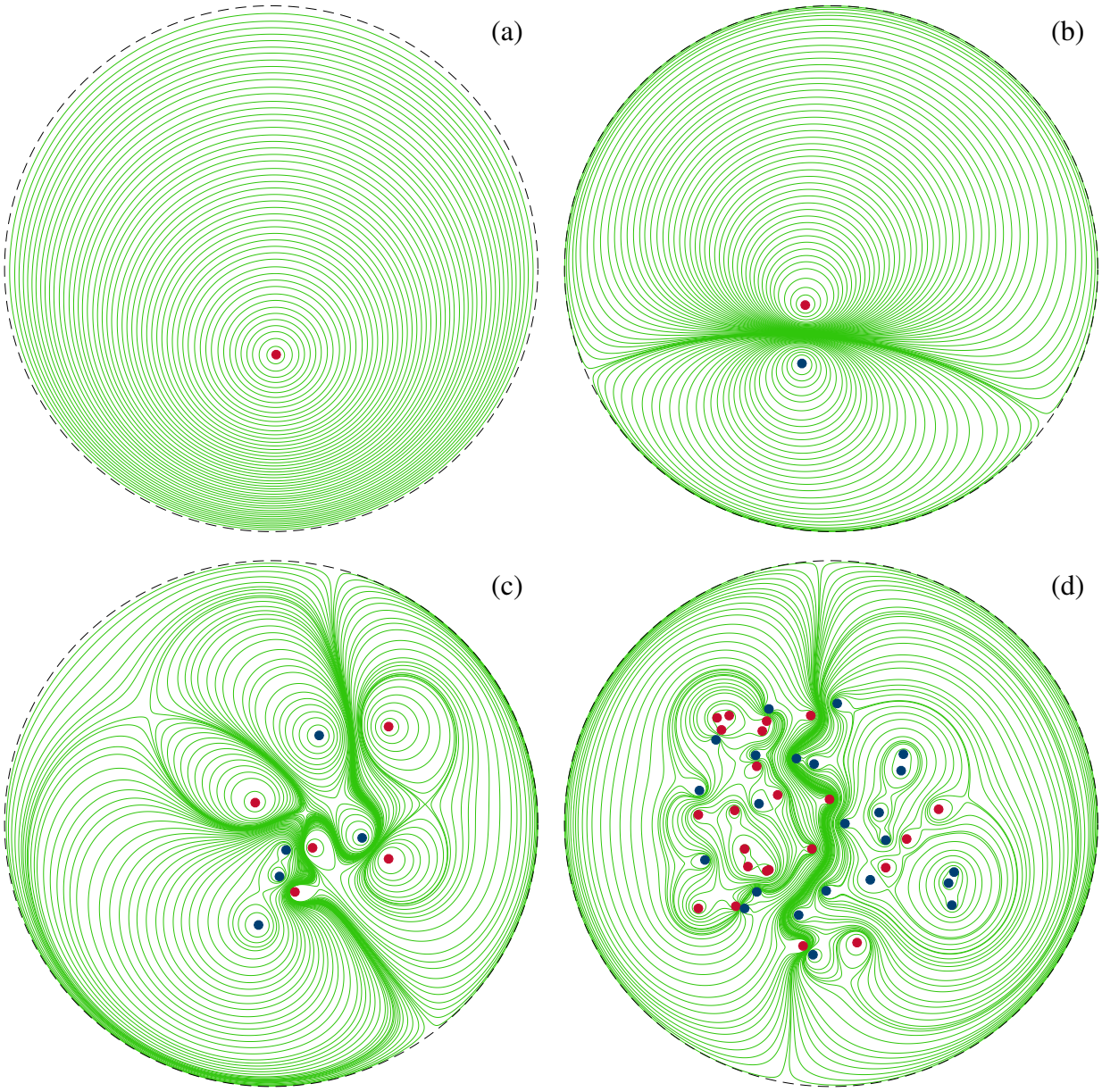

Figure 2.4: Four realisations of the point vortex model in a disc. Positive vortices are marked with red discs, negative vortices with blue discs. The hard wall boundary imposed is shown as a dashed black line, with the streamlines of the flow calculated numerically shown in green.

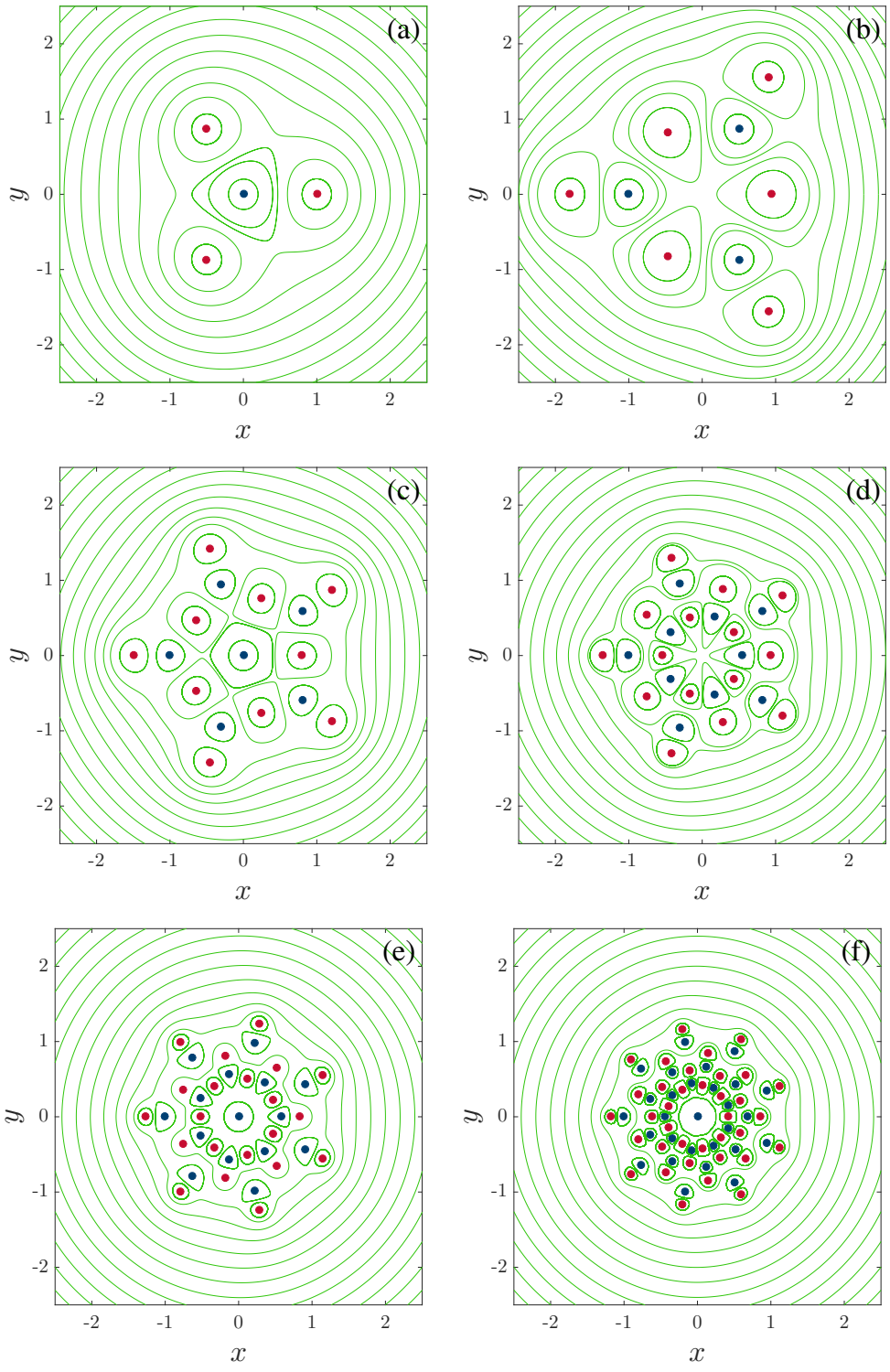

Figure 2.6: [Dimensionless units] Selected stationary solutions of the point vortex model. Vortices with circulation $\Gamma = 1$ are marked with red discs, those with circulation $\Gamma = -1$ with blue discs, with streamlines shown in green.

2.2 The Gross-Pitaevskii Equation

We wish to model the dynamics of a weakly interacting, dilute Bose gas, at very low or zero temperature. In principle one could do this by constructing an n-body wavefunction, which would obey the Schrödinger equation; in practice this is unwieldy for BECs typically containing upwards of 10^3, or as many as 10^9, particles [48, 248]. Mean-field theory allows for a more manageable approach. The assumption is made that particle interactions are binary, which can be justified by the dilute nature of the system, and that every particle is described by a single macroscopic wavefunction $\psi(\mathbf{r}, t)$, with $\mathbf{r}$ position and t time.

The dynamics of such a wavefunction $\psi(\mathbf{r}, t)$ associated with a Bose-Einstein condensate can be described by the Gross-Pitaevskii equation (GPE) [42]:

$$i\hbar\frac{\partial}{\partial t}\psi(\mathbf{r},t) = \left(-\frac{\hbar}{2m}\nabla^2 + g|\psi(\mathbf{r},t)|^2 + V(\mathbf{r},t) - \mu\right)\psi(\mathbf{r},t), \tag{2.8}$$

where $\hbar$ is the reduced planck constant, m is the mass of the boson comprising the system, g governs the strength of particle-particle interactions, V is an external potential field, and μ is the chemical potential. The number density of atoms is $n(\mathbf{r}, t) = |\psi(\mathbf{r}, t)|^2$, with the wavefunction then normalised such that the integrated number density gives the total number of atoms N:

$$\int |\psi(\mathbf{r},t)|^2 d^3\mathbf{r} = N.$$

Also known as the nonlinear Schrödinger equation (NLSE), it is an enduringly popular model for describing the dynamics of BECs at zero temperature, as it captures many physical aspects of such systems, and exists as part of a larger theoretical framework capable of a more comprehensive description, including finite temperature effects and multispecies systems. Perhaps surprisingly, it has been successful in modelling the dynamics of Bose-Einstein condensates for a range of scenarios with temperatures as high as roughly half the critical temperature [249]. The GPE is also used as a phenomenological model for superfluid helium, although it should be stressed that it does not capture the features of the excitation spectrum of helium.

The first and third terms on the RHS describe the energy of a particle in a potential field V, while the second term describes interactions between particles in the condensed state, with the strength of interactions generally taken to be $4\pi\hbar^2 a_s/m$, where a_s is the s-wave scattering length of the boson. A detailed derivation of the GPE is given in Appx. A.2

2.2.1 Time-Independent GPE

We find a time-independent version of the GPE by writing the wavefunction as $\psi(\mathbf{r}, t) = \psi_0(\mathbf{r})$, with $\psi_0(\mathbf{r})$ a stationary solution, and taking the external potential to be constant in time. Inserting this into eq. (2.8) gives:

$$0 = \left(-\frac{\hbar}{2m}\nabla^2 + g|\psi_0(\mathbf{r})|^2 + V(\mathbf{r}) - \mu\right)\psi_0(\mathbf{r}), \tag{2.9}$$

the time-independent GPE. We can use this to find stationary solutions of the GPE, which will be useful as trial solutions to the full time-dependent GPE. We note that, in the absence of interactions, this reduces to the standard time-independent Schrödinger equation, with the chemical potential μ then mapping to the energy per particle.

2.2.2 Hydrodynamic Formulation

The GPE can be reinterpreted as a set of hydrodynamic equations via the Madelung transform. This viewpoint can be helpful when trying to conceptualise the dynamics of condensates. The complex-valued wavefunction is rewritten in terms of magnitude and angle:

$$\psi(\mathbf{r},t) = R(\mathbf{r},t)\exp\left(i\phi(\mathbf{r},t)\right), \tag{2.10}$$

and we relate the magnitude of the wavefunction to the fluid mass density as $\rho_{\mathrm{m}} = mR^2$, and the phase to the fluid velocity as $\mathbf{v} = \hbar\nabla\phi/m$. Inserting eq. (2.10) into the GPE and separating out the real and imaginary terms yields two equations which, after some manipulation [250] can be stated as a continuity equation:

$$\frac{\partial\rho_{\mathrm{m}}}{\partial t} + \nabla\cdot(\rho_{\mathrm{m}}\mathbf{v}) = 0, \tag{2.11}$$

and an equation akin to Euler's equation for an inviscid fluid:

$$\frac{D\mathbf{v}}{Dt} = -\frac{\nabla p}{\rho_{\mathrm{m}}} - \frac{\nabla\mathbf{P}}{\rho_{\mathrm{m}}} - \nabla\left(\frac{V}{m}\right), \tag{2.12}$$

where D/Dt is the material derivative, $p = (g/2)\left(\rho_{\mathrm{m}}/m\right)^2$ is the pressure, and $P_{ij} = (-\hbar^2/4m^2)\rho_{\mathrm{m}}(\partial^2/\partial x_i\partial x_j)\ln\rho_{\mathrm{m}}$ is the so-called quantum pressure.

2.2.3 Healing Length

The healing length ξ describes the minimum distance over which a large perturbation can recover to the equilibrium value, and provides a characteristic length scale of condensates. Considering only the kinetic and interaction terms in the time-independent GPE, eq. (2.9), we have:

$$\frac{\hbar^2}{2m}\nabla^2\psi(\mathbf{r},t) = g|\psi(\mathbf{r},t)|^2\psi(\mathbf{r},t). \tag{2.13}$$

We replace $\nabla^2\psi(\mathbf{r},t)$ with the dimensionally consistent $\psi(\mathbf{r},t)/\xi^2$ to give:

$$\frac{\hbar^2}{m\xi^2}\psi(\mathbf{r},t) = g|\psi(\mathbf{r},t)|^2\psi(\mathbf{r},t). \tag{2.14}$$

Cancelling $\psi(\mathbf{r},t)$ and using $|\psi(\mathbf{r},t)|^2 = n(\mathbf{r},t)$ we have:

$$\frac{\hbar^2}{m\xi^2} = gn(\mathbf{r},t)$$

$$\implies \xi = \frac{\hbar}{\sqrt{mgn}}. \tag{2.15}$$

Note that the healing length will generally depend on the local condensate density. However, for the homogeneous GPE, as the condensate density is uniform the healing length is also uniform, allowing us to write:

$$\xi = \frac{\hbar}{\sqrt{mg\rho},} \tag{2.16}$$

where $\rho = n(\mathbf{r}, t)$ is the uniform number density of particles.

2.2.4 Speed of Sound

The dispersion relation of a weakly-interacting Bose gas is:

$$E(p_\mathrm{e}) = \sqrt{\frac{ngp_\mathrm{e}^2}{m} + \frac{p_\mathrm{e}^4}{4m^2}}, \tag{2.17}$$

where p_e is the momentum of elementary excitations, and $E(p_\mathrm{e})$ their corresponding energies [251]. If we consider excitations with small momentum, this relation becomes approximately:

$$E(p_\mathrm{e}) \approx \sqrt{\frac{ng}{m}} p_\mathrm{e}, \tag{2.18}$$

a linear, sound-like dispersion relation with a local speed of sound $c = \sqrt{ng/m}$. As with the healing length, this quantity depends on the local condensate density $n(\mathbf{r}, t)$; for homogeneous condensates we can write:

$$c = \sqrt{\frac{\rho g}{m}}, \tag{2.19}$$

where $\rho = n(\mathbf{r}, t)$ is the uniform number density of particles.

2.2.5 The Homogeneous Dimensionless GPE

Bose-Einstein condensation is understood to occur in a number of different regimes, from ultracold atomic BECs with length scales on the order of 10^{-5}–10^{-4} m [4], to the extremely hot, extremely dense, cores of neutron stars [252], with length scales on the order of 10^3–10^4 m. Additionally, the particular scales of atomic condensates are modified by the species involved, by the strength and geometry of the trapping potential, and by the tuning of particle-particle interaction strength through Feshbach resonance [253].

Rather than adjusting numerical parameters to accommodate this, it is conventional to make the GPE dimensionless. Beyond allowing us to model the dynamics of a wide range of systems in a generic fashion, this has the advantage of rescaling all values involved to the scale of unity, avoiding scales at which floating point errors are liable to rapidly introduce serious numerical inaccuracy into our calculations. We discuss the procedure for making the GPE dimensionless for a homogeneous system; note that for other geometries, in

particular harmonically trapped condensates, a similar procedure can be followed to find dimensionless equations, but different characteristic scales may be needed.

We consider an infinite, homogeneous system, with no trapping potential ($V(\mathbf{r},t) = 0$), and repulsive interactions, described by:

$$i\hbar\frac{\partial}{\partial t}\psi(\mathbf{r},t) = \left(-\frac{\hbar^2}{2m}\nabla^2 + g|\psi(\mathbf{r},t)|^2 - \mu\right)\psi(\mathbf{r},t). \tag{2.20}$$

In the ground state the wavefunction has no dependence on $\mathbf{r}$ or t, so the derivatives vanish, leading to:

$$0 = \left(g|\psi(\mathbf{r},t)|^2 - \mu\right)\psi(\mathbf{r},t), \tag{2.21}$$

which immediately gives the homogeneous density of the system to be $\rho = |\psi(\mathbf{r},t)|^2 = \mu/g$. Using the healing length $\xi = \hbar/\sqrt{mg\rho}$ as the characteristic length scale (See Sec. 2.2.3), and the speed of sound $c = \sqrt{\rho g/m}$ as the characteristic velocity scale (See Sec. 2.2.4), we can find a characteristic time scale through dimensional arguments of $\tau = \xi/c = \hbar/\rho g$, with this set of units generally referred to as the natural units. Taking m, the mass of the boson under consideration, as the obvious choice of mass scale, we can find a characteristic energy scale, again using dimensional arguments: $\varepsilon = mc^2 = \rho g$.

Using this to rescale our variables yields:

$$t = \tau\bar{t} = \frac{\hbar}{\rho g}\bar{t}, \qquad \mathbf{r} = \xi\bar{\mathbf{r}} = \frac{\hbar}{\sqrt{mg\rho}}\bar{\mathbf{r}}, \qquad \psi = \sqrt{\rho}\bar{\psi}, \qquad \mu = \rho g\bar{\mu}. \tag{2.22}$$

Substituting these into eq. (2.20):

$$i\hbar\sqrt{\rho}\frac{\rho g}{\hbar}\frac{\partial}{\partial\bar{t}}\bar{\psi}(\bar{\mathbf{r}},\bar{t}) = \left(-\frac{\hbar^2}{2m}\frac{mg\rho}{\hbar^2}\bar{\nabla}^2 + g\rho|\bar{\psi}(\bar{\mathbf{r}},\bar{t})|^2 - \rho g\bar{\mu}\right)\sqrt{\rho}\bar{\psi}(\bar{\mathbf{r}},\bar{t}), \tag{2.23}$$

which, after cancellation, gives:

$$i\frac{\partial}{\partial\bar{t}}\bar{\psi}(\bar{\mathbf{r}},\bar{t}) = \left(-\frac{\bar{\nabla}^2}{2} + |\bar{\psi}(\bar{\mathbf{r}},\bar{t})|^2 - \bar{\mu}\right)\bar{\psi}(\bar{\mathbf{r}},\bar{t}), \tag{2.24}$$

which, since $\bar{\mu}$ is a constant now rescaled to unity, gives (dropping bars):

$$i\frac{\partial}{\partial t}\psi(\mathbf{r},t) = \left(-\frac{\nabla^2}{2} + |\psi(\mathbf{r},t)|^2 - 1\right)\psi(\mathbf{r},t) \tag{2.25}$$

as our final expression for the homogeneous dimensionless GPE, with the normalisation condition:

$$\int |\psi(\mathbf{r},t)|^2 d^3\mathbf{r} = 1. \tag{2.26}$$

2.2.6 Quantised Circulation

An important feature of the GPE is the emergence of quantisation of circulation. Consider the circulation, defined as:

$$\Gamma = \oint_C \mathbf{v} \cdot d\mathbf{l}, \tag{2.27}$$

where $d\mathbf{l}$ is the line element along the closed path C. We have $\mathbf{v} = \frac{\hbar}{m}\nabla\phi$, which we substitute in:

$$\Gamma = \frac{\hbar}{m} \oint_C \nabla\phi \cdot d\mathbf{l}. \tag{2.28}$$

We require that the wavefunction be single-valued, leading to:

$$\exp(i\phi_0) = \exp(i\phi_0)\exp(i\Delta\phi), \tag{2.29}$$

where ϕ_0 is the phase at the start of the integration path, and $\Delta\phi$ is the change in phase along the integration path. For this to hold, we require that $\Delta\phi = 2\pi n$, for $n \in \mathbb{Z}$. Returning to eq. (2.28), this immediately restricts values of the circulation to:

$$\Gamma = n\frac{h}{m}, \tag{2.30}$$

that is, the circulation can only take values of integer multiples of h/m, referred to as the quantum of circulation. Compare this to classical fluids, where the circulation must be real but is otherwise unconstrained.

For $n \neq 0$, note that a singularity necessarily occurs in the phase and velocity; thus in order to avoid infinite energy density at the centre of such vortices the density of the condensate must vanish at these points. Such vortices can be viewed as topological defects in the phase. We note that so-called multicharged vortices, i.e. vortices where $|n| > 1$, are unstable, unless under rapid rotation, and decay into n singly-charged vortices [254, 255].

2.2.7 Basic Solutions

Because of the nonlinearity of the GPE few analytic solutions are known, and we must rely on numerical methods to understand the more complex behaviour of the equation. Nevertheless, we consider a few simple known solutions which illuminate some features of these systems.

First, consider the time-independent 1-D GPE without an external potential:

$$-\frac{\hbar}{2m}\frac{\partial^2}{\partial x^2}\psi(x) + g_{\text{1-D}}|\psi(x)|^2\psi(x) - \mu_{\text{1-D}}\psi(x) = 0, \tag{2.31}$$

where $g_{\text{1-D}}$ and $\mu_{\text{1-D}}$ are the interaction strength and chemical potential for a 1-D system, with the boundary condition $\psi(0) = 0$, corresponding to a hard wall boundary at $x = 0$, and $\psi(x) = \sqrt{\rho}$ as $x \to \infty$. This has solution:

$$\psi(x) = \sqrt{\rho}\tanh\left(\frac{x}{\xi}\right), \tag{2.32}$$

shown in Fig. 2.7. The form of this solution gives an insight into how the density of a condensate governed by the GPE heals from large perturbations; it is apparent that there is a minimum distance related to the healing length ξ as defined in Sec. 2.2.3 over which the condensate density can recover the bulk value from a depletion to zero.

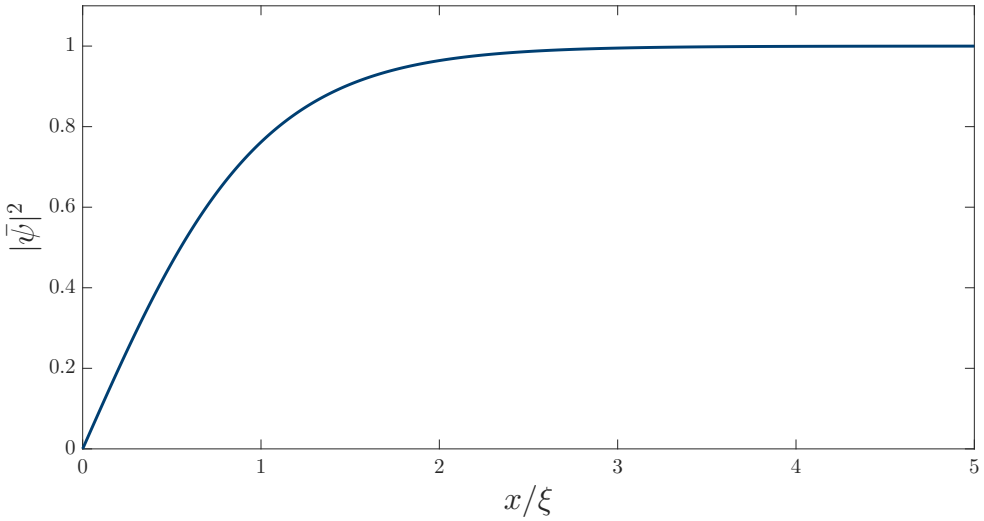

Figure 2.7: Density profile of a condensate described by the GPE in the presence of a hard wall boundary at the origin.

The GPE can support solitary wave solutions, in particular solitons: localised non-dispersive wave packets sustained by the nonlinearity of the system. The GPE can support bright and dark solitons, named for their appearance in nonlinear optics [256], depending on the sign of the interaction parameter g. As we only consider repulsive interactions in this work we shall only discuss dark solitons, which consist of a dip in the density, coinciding with a phase slip of up to π. The 1-D dark soliton solutions [257, 258] are given by:

$$\psi(x,t) = \sqrt{\rho}\exp\left(-\frac{i\mu_{\text{1-D}}}{\hbar}t\right)\left[\sqrt{1-\frac{v^2}{c^2}}\tanh\left(\sqrt{1-\frac{v^2}{c^2}}\frac{x-vt}{\xi}\right)+\frac{iv}{c}\right] \tag{2.33}$$

where c is the speed of sound and v is the speed of the soliton, with several examples shown in Fig. 2.8. The deepest possible soliton, with the density dropping to zero at its center, has $v = 0$, and a sharp phase slip of π; shallower solitons have correspondingly greater speeds and smaller, softer phase slips.

Solitary wave solutions also exist in higher dimensions, but are not true solitons as they are unstable and decay via the snake instability into other topological defects [92]. However, recent work has had some success in finding stable solitons in higher dimensions through time-modulated traps, see e.g. [259].

In Sec. 2.2.6 we discussed the quantisation of circulation in quantum fluids, and that the condensate density must vanish at the corresponding singularity in the phase. Such topological defects are supported in the 2-D and 3-D GPE, respectively as point-like vortices (with a finite core) and as vortex lines.

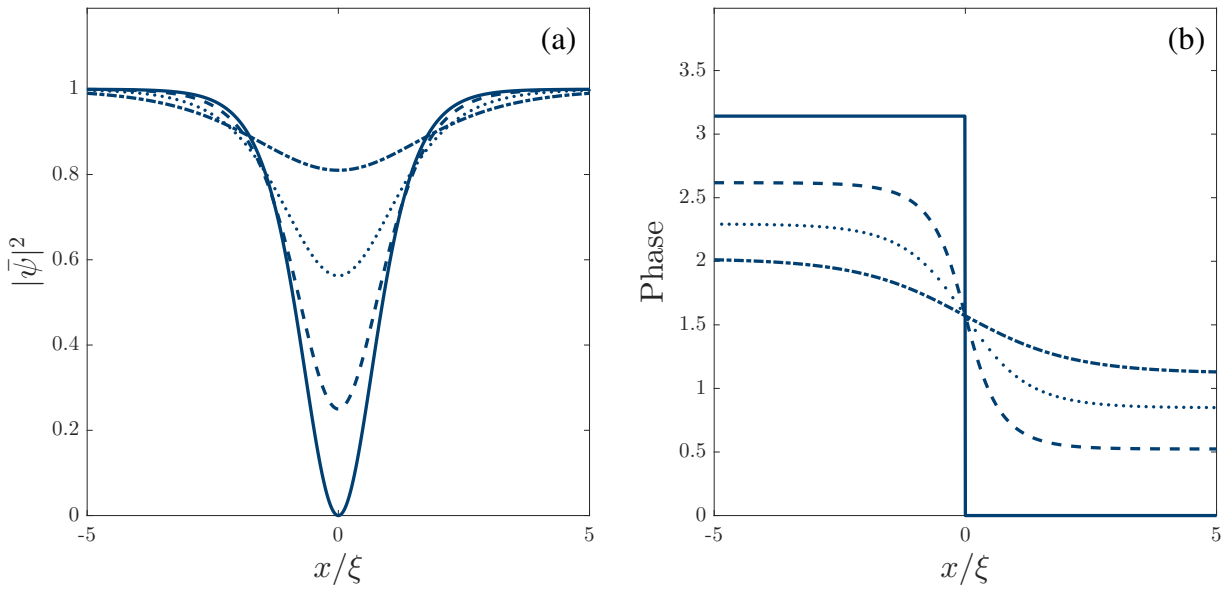

Figure 2.8: Density (a) and phase (b) profiles of 1-D dark soliton solutions to the GPE with a range of speeds: $v = 0$ (solid line), $v = 0.5$ (dashed line), $v = 0.75$ (dotted line), and $v = 0.9$ (dot-dashed line).

Vortices in 2-D are azimuthally symmetric, and in 3-D are symmetric about the axis of the vortex line (disregarding distortions due to sound waves, interactions with other vortices, and interactions with boundaries), and the solution for a single vortex can be written as:

$$\psi(r, \theta) = f(r)\sqrt{\rho}\exp(ni\theta), \tag{2.34}$$

where $n \in \mathbb{Z}$ is the winding number or charge of the vortex, and $f(r)$ describes the density profile of the vortex. No analytical form exists for $f(r)$; we will discuss approximations to $f(r)$ and finding the true vortex solution numerically in Sec. 3.3.4. We show the density profile and phase near a singly-charged vortex in Fig. 2.9, noting the coincidence of the singularity in the phase with the condensate density vanishing. In the related context of ^{4}He, many-body simulations show that the density in the vortex cores, while still depleted, does not vanish [260].

Recall that the gradient of the phase can be related to the local fluid velocity by $\mathbf{v} = \frac{\hbar}{m}\nabla\phi$ (Sec. 2.2.2). Combining this with eq. (2.34) gives an expression for the velocity around a vortex:

$$\mathbf{v}(r, \theta) = \frac{n\hbar}{mr}\hat{\theta}, \tag{2.35}$$

where $\hat{\theta}$ is the azimuthal unit vector. Note that the velocity is entirely azimuthal, and the speed is proportional to $1/r$, as for the point vortices previously discussed in Sec. 2.1.

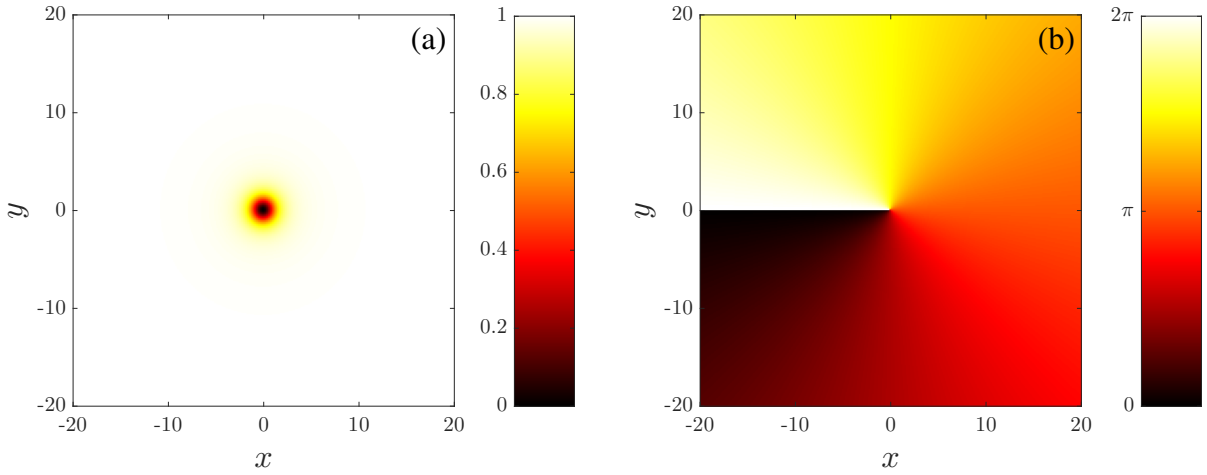

Figure 2.9: [Dimensionless units] Density (a) and phase (b) of a 2-D condensate with a singly-charged vortex at the origin.

2.2.8 Vortex-Antivortex Annihilation

The reconnection of vortex filaments [261] in superfluids has long been known to play a critical role in the dynamics of quantum turbulence [262]. In 2-D condensates such reconnection events take the form of vortex-antivortex annihilations. When vortices of opposite signs approach within a distance comparable to the healing length they are mutually destroyed, releasing a burst of sound. One such annihilation event is shown in Fig. 2.10.

It has been noted that, in the absence of finite temperature effects, the annihilation process is a four-body process [263, 264]: an interaction with a third body, typically another vortex, is necessary to push the vortices within the dipole together and start the annihilation. The vortices within the dipole then form a Jones-Roberts soliton [265], a crescent shaped dip in the density which propagates at close to the speed of sound. These solitons are liable to reform as a vortex dipole, unless disrupted by some obstacle, typically a fourth vortex. This process is neatly summarised by the Feynmann diagram shown in Fig. 2.11, adapted from [264]: a vortex and an antivortex are forced together by a vortex of either arbitrary sign, emitting sound and producing a Jones-Roberts soliton, while the catalytic vortex remains. The Jones-Roberts soliton propagates through the condensate, until it collides with another vortex, again of arbitrary sign, destroying the soliton and emitting a second burst of sound, again with the incident vortex unaffected. The initial annihilation event and the subsequent dissipation of the Jones-Robert soliton are driven by interaction with other, catalytic, vortices in this illustration, but can also be triggered by interactions with boundaries, other physical objects such as lasers, and sound.

It should be stressed that the route to annihilation described here and illustrated by Fig. 2.11 is far from the only way in which annihilation can occur, nor necessarily the most frequent, but rather the prototypical interaction. The driving together of two vortices with opposite circulation can also be due to interactions with obstacles or boundaries in the condensate, the action of sound waves or bulk flows, two vortex-antivortex dipoles colliding, or more generally the flow induced by all other vortices present. The Jones-Robert

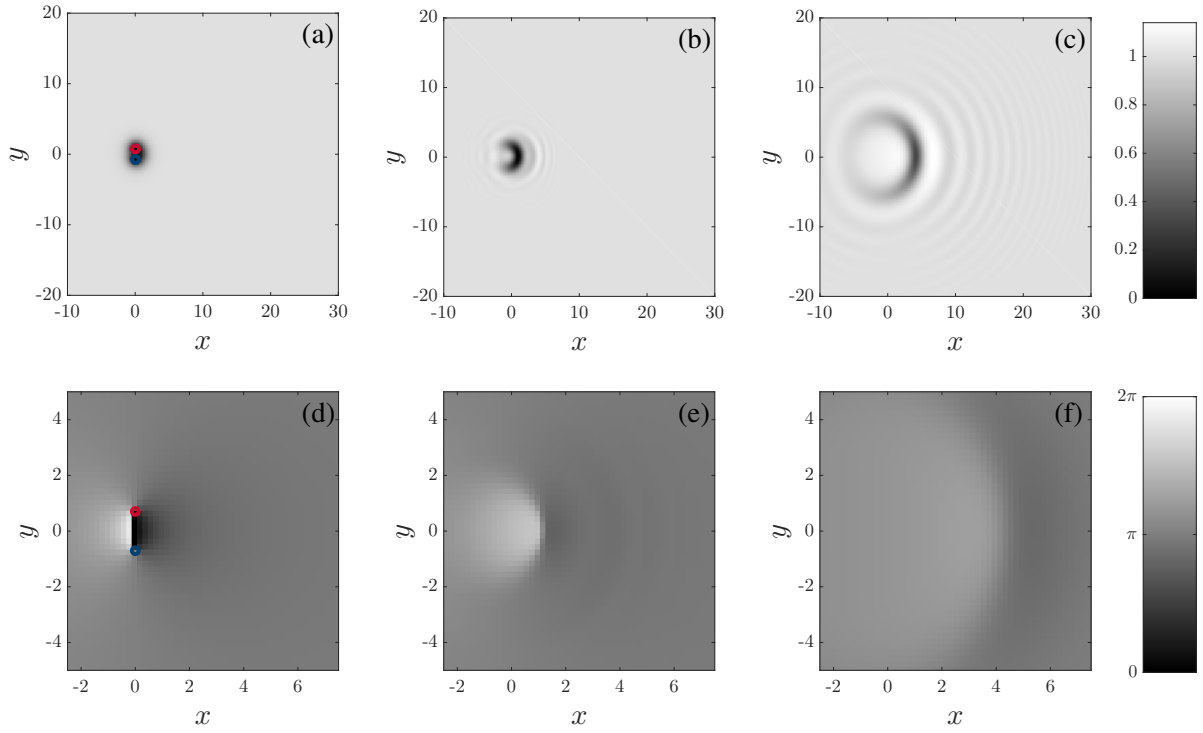

Figure 2.10: [Dimensionless units] GPE simulation of an isolated annihilation event. We show the condensate density in the top row (a-c), and the condensate phase in the bottom row (d-f). In panels (a,d) we show the initial wavefunction of two vortices of opposite circulation, marked with hollow red and blue discs, with a separation of 1.4ξ, which annihilate, healing the 2π phase slip and emitting sound, to form a Jones-Roberts soliton visible in panels (b,e), spreading into the condensate in (c,f). Note the different scale for the top and bottom rows, and that these snapshots are cropped from a larger condensate, with the specific event shown here occuring far from boundaries.

soliton is likewise not necessarily disrupted by another vortex, but could instead involve interactions with obstacles, boundaries, or intense sound waves. Furthermore, the presence of thermalised atoms at finite temperatures acts to damp the motion of vortices [266, 267], driving dipoles towards annihilation and disrupting the resulting Jones-Robert soliton without the presence of any of the mechanisms discussed above.

2.2.9 Trapping Potentials and Reduced Dimensionality

There are a number of justifications for studying the dynamics of condensates in 2-D and 1-D systems. Quantum fluids inform our understanding of classical fluids through strong analogies between them, and many regimes occur where classical fluids are effectively 2-D, for example atmospheric systems, where the scale of one dimension can be orders of magnitude smaller than the others, and strongly rotating systems, where the flow is uniform in the direction parallel to the axis of rotation, following the Taylor-Proudman

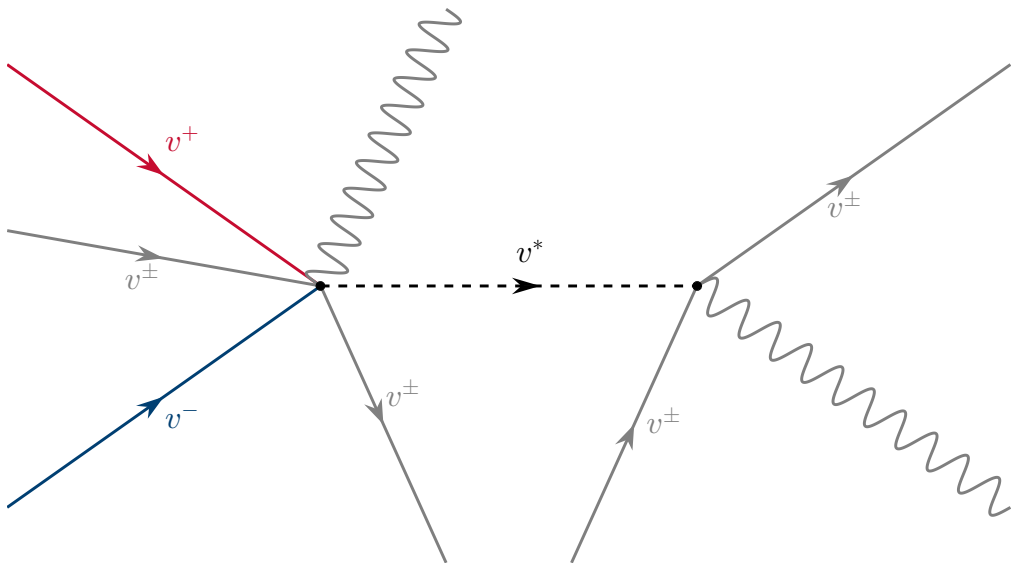

Figure 2.11: Feynmann diagram for the four-body annihilation process described, with time advancing from left to right. The straight solid lines represent vortices, with v^+, v^-, $v^\pm$ corresponding to vortices, antivortices, and incident vortices of arbitrary sign, respectively. The dashed black line represents a Jones-Roberts soliton, and the wavy lines indicate sound emitted at each vertex.

Theorem (see, e.g. [139]). From a more philosophical point of view, one could argue that the existence of such quantum systems is alone enough to merit investigation of the novel physics that emerge. Moreover, there are many practical reasons for considering systems of reduced dimensionality.

Firstly, the dynamics of vortices are inherently simpler in 2 dimensions, and depending on the focus of a numerical experiment could be modelled using the extremely fast and simple PVM as we do. Solitonic solutions, although possible in higher dimensions, are best understood and most stable in 1-D [268]; there is considerable crossover here with the field of nonlinear optics, see, e.g. [269], where 1-D systems are particularly relevant for the geometry of optical fibres. From an experimental viewpoint, quasi-2-D and quasi-1-D condensates can be realised through appropriate trapping potentials [270]. Additionally, the imaging of lower dimensional systems [85], see Fig. 2.12, is considerably less involved than the imaging of 3-D systems, as imaging techniques yield column integrated densities, requiring several simultaneous orthogonal projections to reconstruct a 3-D field.

From a numerical viewpoint it is typically far less computationally intensive to simulate a 2-D system than it is to simulate a 3-D system; the 2-D GPE simulations in this thesis were performed on either a desktop computer or on a single node of a High-Performance Computing (HPC) cluster, while 3-D simulations of any useful resolution can require vast amounts of CPU-hours over multiple nodes.

Due to long-wave fluctuations in the phase [41], a true condensate can only exist in 2-D in the zero temperature limit [272]. However, below a critical temperature $T_{\mathrm{BKT}} = (\pi\hbar^2/2m)\rho_{\mathrm{s}}$, where ρ_{s} is the superfluid density just below T_{BKT}, a superfluid phase transition occurs. This transition, the Berezinksii-Kosterlitz-Thouless (BKT) transition

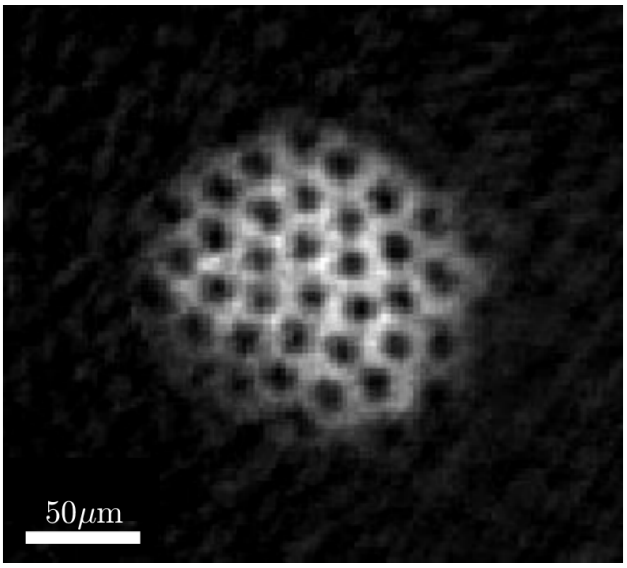

Figure 2.12: Absorption image of an irregular vortex lattice in a rotating quasi-2-D condensate, reproduced from [271]. The intensity corresponds to the column density of the condensate post expansion, with vortices appearing as dark holes.

[273], is associated with the generation of bound vortex-antivortex dipoles, and characterised by the existence of a condensate with fluctuating phase [274], known as a quasi-condensate. In trapped systems the momentum of excitations is bounded, and the phase fluctuations reduced, by the finite size of the condensate; in particular, in the geometries we consider the phase fluctuations well below the critical temperature are small, and the system is a true condensate in the equilibrium state [272].

We will now discuss specific trapping potentials and the resulting condensate geometries. Due to the relative ease with which such traps can be generated experimentally [50], BECs are typically confined using a harmonic potential of the form:

$$V(x,y,z) = m\omega_x^2\frac{x^2}{2} + m\omega_y^2\frac{y^2}{2} + m\omega_z^2\frac{z^2}{2}, \tag{2.36}$$

where ω_x, ω_y, ω_z are the trapping frequencies controlling the strength of trapping in a particular direction. When $\omega_x = \omega_y = \omega_z$ a spherical condensate results, shown in Fig. 2.13 (a). By varying the trapping frequencies it is possible to produce quasi-lower-dimensional condensates. Consider the trapping potential:

$$V(x,y,z) = m\omega_\perp^2\frac{(x^2+y^2)}{2} + m\omega_z^2\frac{z^2}{2}, \tag{2.37}$$

where $\omega_\perp$ controls the strength of trapping perpendicular to the z-axis. In the situation where $\omega_z \gg \omega_\perp$, provided $\hbar\omega_z \gg \mu$, the condensate is very tightly confined in the z direction in comparison with the x and y directions, resulting in a highly oblate condensate, often referred to as a 'pancake-shaped' condensate, shown in Fig. 2.13 (b).

This tight confinement causes the wavefunction along z to become frozen in the time-independent ground state of the harmonic oscillator, allowing us to write:

$$\psi(\mathbf{r}, t) = \psi_\perp(x, y, t)\psi_z(z), \tag{2.38}$$

with $\int |\psi_\perp|^2 d^2\mathbf{r} = N$ conventionally. With significant trapping in the z-direction, atom-atom interactions are dominated by kinetic and potential energy, such that the solution along z approaches the solution in the absence of interactions, giving the Gaussian ground state:

$$\psi_z(z) = \pi^{-1/4} l_z^{-1/2} \exp\left(-z^2/2l_z^2\right), \tag{2.39}$$

with $l_z = \sqrt{\hbar/m\omega_z}$ the harmonic oscillator length, and ψ_z normalised by $\int |\psi_z|^2 dz = 1$. Substituting this into the GPE, eq. (2.8), leads to a 2-D GPE suitable for modelling such systems, with the main difference being the modified interaction term $g_{\text{2-D}} = g/(l_z\sqrt{2\pi})$, and the modified chemical potential $\mu_{\text{2-D}} = \mu - \hbar\omega_z/2$.

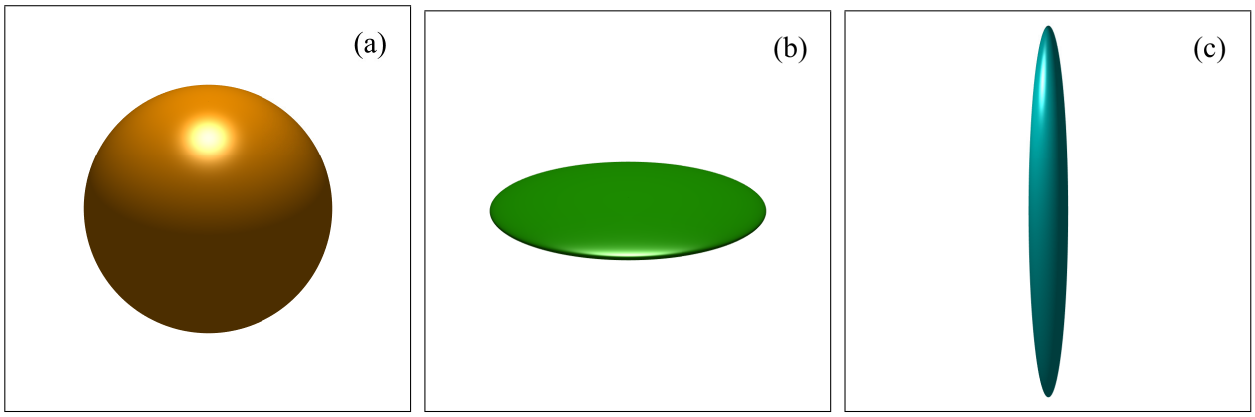

Figure 2.13: Illustrative isosurfaces of condensates confined by harmonic trapping potentials with (a) $\omega_x = \omega_y = \omega_z$, (b) $\omega_z \gg \omega_\perp$; a 'pancake-shaped' condensate, and (c) $\omega_z \ll \omega_\perp$; a 'cigar-shaped' condensate.

Similarly, in the situation where $\omega_z \ll \omega_\perp$, the condensate is very tightly confined perpendicular to the z-axis, in comparison with the z-direction, resulting in a highly prolate condensate, frequently called a 'cigar-shaped' condensate, shown in Fig. 2.13 (c). In a similar way to quasi-2-D condensates, such condensates can be modelled by a 1-D GPE, with modified interaction term and chemical potential. Our focus is on quasi-2-D condensates; more details on quasi-1-D condensates can be found in, e.g., [275].

As discussed in Sec. 2.2.3 and Sec. 2.2.4, the healing length and speed of sound depend on the local density of the condensate. As the density is non-uniform in many trapped systems, including harmonic traps, this becomes a complicating factor which can limit experimental studies, for example when considering correlation lengths [79], as well as making it more difficult to make comparisons with homogeneous classical systems.

Experimentalists have realised systems with a homogeneous region using a variety of schemes [77, 79, 276], with the most successful to date able to produce a system uniform to the edges of the trap, with an area of up to 900 μm^2 , in a variety of shapes [80]. This is achieved by confinement with two orthogonal lasers, one propagating in the x-direction and prepared in a Hermite-Gauss mode [277] with a node in the $z = 0$ plane providing

strong confinement in the z-direction, and the other a hollow beam propagating in the z-direction providing confinement in the xy-plane. An intensity mask on the latter modifies the shape of the confinement to produce disc, box, double-rectangle, or arbitrarily shaped condensates as required.

We model disc traps using a potential of the form:

$$V(r) = \frac{1}{2} V_0 r^2 \left(\frac{r}{r_0} \right)^{\alpha}, \tag{2.40}$$

where V_0 controls the strength of the trap, r_0 controls the extent of the trap and α controls the steepness of the trap wall - we typically use $V_0 = 1$, $r_0 = 180$ (in dimensionless units) and $\alpha = 100$, resulting in the condensate shown in Fig. 2.14 (a).

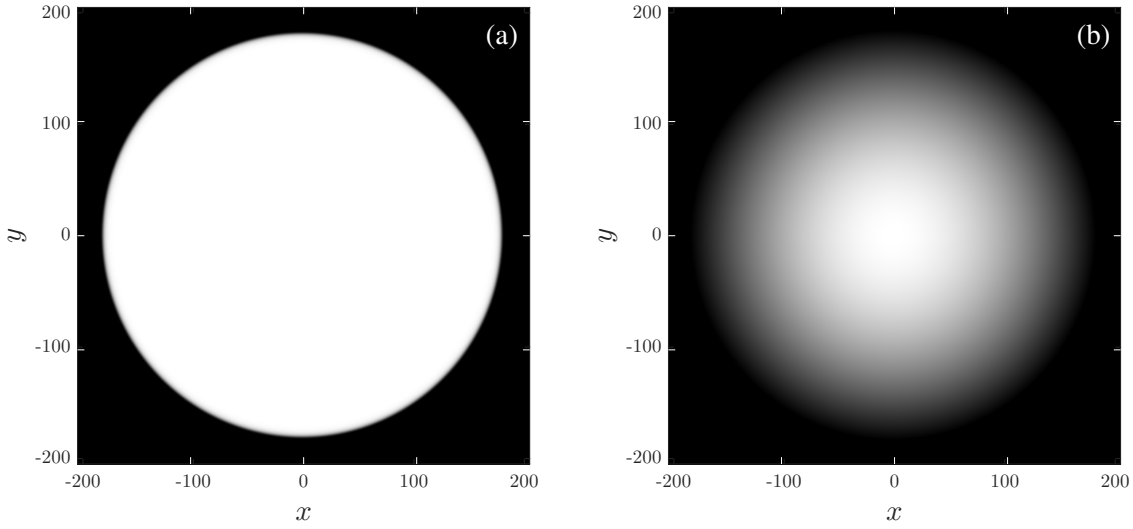

Figure 2.14: [Dimensionless units] Density $|\psi|^2$ for typical condensate ground states in (a) box-like traps with a potential of the form given in eq. (2.40) with $r_0 = 180$ (in dimensionless units) and $\alpha = 100$, (b) harmonic traps with a comparible Thomas-Fermi radius (Sec. 2.2.11) (with colour scales scaled to the maximum density of each condensate). Note the uniform density for almost the full extent of the condensate in (a), in comparison with the strongly radially dependent density in (b).

2.2.10 Physical Quantities

In order to characterise our condensates we will make use of their energy and momenta. Firstly, the energy functional of the GPE is:

$$\varepsilon(\psi) = \frac{\hbar^2}{2m} |\nabla \psi|^2 + \frac{g}{2} |\psi|^4 + V |\psi|^2, \tag{2.41}$$

with the first term corresponding to kinetic energy E_{kin}, the second to atom-atom interactions E_{int}, and the third to potential energy E_{pot} associated with the external potential V.

The total energy of the condensate is then:

$$E = \int \varepsilon(\mathbf{r}) d\mathbf{r}. \tag{2.42}$$

This can be straightforwardly decomposed into the contributions from the different types of energy as:

$$E = E_{\text{kin}} + E_{\text{int}} + E_{\text{pot}}, \tag{2.43}$$

with

$$E_{\text{kin}} = \int \frac{\hbar^2}{2m} |\nabla\psi|^2 d\mathbf{r}, \qquad E_{\text{int}} = \int \frac{g}{2} |\psi|^4 d\mathbf{r}, \qquad E_{\text{pot}} = \int V|\psi|^2 d\mathbf{r}. \tag{2.44}$$

The linear momentum operator for a quantum mechanical system is:

$$\hat{p}_i = -i\hbar \frac{\partial}{\partial x_i}, \tag{2.45}$$

giving the total linear momenta as:

$$P_{x_i} = -i\hbar \int \psi^* \frac{\partial}{\partial x_i} \psi d\mathbf{r}. \tag{2.46}$$

Then, the angular momentum operator about the z-axis is

$$\hat{l}_z = -i\hbar \left(x\frac{\partial}{\partial y} - y\frac{\partial}{\partial x} \right), \tag{2.47}$$

with the total angular momentum:

$$L_z = -i\hbar \int \psi^* \left(x\frac{\partial}{\partial y} - y\frac{\partial}{\partial x} \right) \psi d\mathbf{r}. \tag{2.48}$$

Rewriting in terms of the homogeneous dimensionless units given in Sec. 2.2.5 yields:

$$E_{\text{kin}} = \sqrt{\frac{\mu}{m}} \frac{\hbar}{4\pi a_s} \bar{E}_{\text{kin}}, \qquad E_{\text{int}} = \sqrt{\frac{\mu}{m}} \frac{\hbar}{4\pi a_s} \bar{E}_{\text{int}}, \qquad E_{\text{pot}} = \sqrt{\frac{\mu}{m}} \frac{\hbar}{4\pi a_s} \bar{E}_{\text{pot}} \tag{2.49}$$

where

$$\bar{E}_{\text{kin}} = \int \frac{|\bar{\nabla}\bar{\psi}|^2}{2} d\bar{\mathbf{r}}, \qquad \bar{E}_{\text{int}} = \int \frac{|\bar{\psi}|^4}{2} d\bar{\mathbf{r}}, \qquad \bar{E}_{\text{pot}} = \int \bar{V}|\bar{\psi}|^2 d\bar{\mathbf{r}}, \tag{2.50}$$

are the dimensionless kinetic energy, interaction energy, and potential energy respectively.

Likewise, we have:

$$P_{x_i} = \frac{\hbar}{4\pi a_s} \bar{P}_{x_i}, \qquad L_z = \frac{\hbar\xi}{4\pi a_s} \bar{L}_z, \tag{2.51}$$

where

$$\bar{P}_{x_i} = -i \int \bar{\psi}^* \frac{\partial}{\partial \bar{x}_i} \bar{\psi} d\bar{\mathbf{r}}, \qquad \bar{L}_z = -i \int \bar{\psi}^* \left(\bar{x}\frac{\partial}{\partial \bar{y}} - \bar{y}\frac{\partial}{\partial \bar{x}} \right) \bar{\psi} d\bar{\mathbf{r}} \tag{2.52}$$

are the dimensionless linear and angular momenta of our system. The kinetic energy can be further split into compressible and incompressible components,

$$E_{\text{kin}} = E^{\text{c}}_{\text{kin}} + E^{\text{i}}_{\text{kin}}, \tag{2.53}$$

using $\sqrt{\rho}v_j = (\sqrt{\rho}v_j)^c + (\sqrt{\rho}v_j)^i$, with $\nabla \cdot (\sqrt{\rho}\mathbf{v}^i) = 0$, and $\mathbf{v} = (\hbar/m)\nabla\phi$ the fluid velocity [198].

2.2.11 Thomas-Fermi Profile

Consider a stationary solution to the dimensionless, homogeneous GPE with repulsive interactions. Such a solution must satisfy the time-independent GPE:

$$\left(-\frac{\nabla^2}{2} + |\psi(\mathbf{r})|^2 + V(\mathbf{r}) - 1\right)\psi(\mathbf{r}) = 0. \tag{2.54}$$

Furthermore, suppose the external potential $V(\mathbf{r})$ is nonzero, leading to spatial variation in the wavefunction. We assume that $V(\mathbf{r})$ varies slowly with r, and thus ψ varies slowly and $\nabla^2\psi$ is small compared to the atom-atom interactions, allowing us to neglect the kinetic term in eq. (2.54) to give:

$$\left(|\psi(\mathbf{r})|^2 + V(\mathbf{r}) - 1\right)\psi(\mathbf{r}) = 0, \tag{2.55}$$

which leads to $|\psi(\mathbf{r})|^2 = 1 - V(\mathbf{r})$, from which we can construct the approximate solution:

$$\psi(\mathbf{r}) = \begin{cases} \sqrt{1 - V(\mathbf{r})}, & V \leq 1 \\ 0, & \text{otherwise.} \end{cases} \tag{2.56}$$

This is the Thomas-Fermi profile. It is an extremely useful starting point for finding true ground state solutions to the time-dependent GPE by methods discussed in Sec. 3.3.2 and 3.3.3. In Fig. 2.15 we compare the Thomas-Fermi profile with the actual ground state for two geometries.

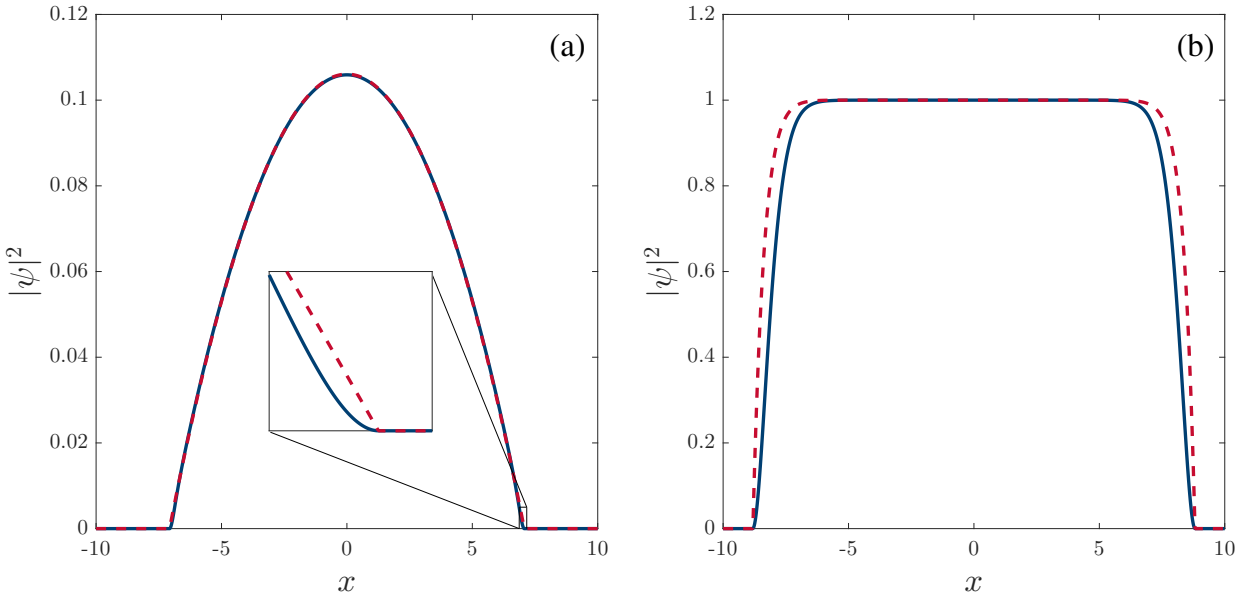

Figure 2.15: [Dimensionless units] Comparison of Thomas-Fermi profile (red dashed line) with ground state solution (solid blue line) in two trapped geometries: a harmonic trap potential (a) and a box trap type potential (b).

This approximate solution gives a useful estimate of the size of a condensate. The condensate density drops to zero when $V(\mathbf{r}) = 1$, so for our disc traps (Sec. 2.2.9) we have:

$$r_{\mathrm{TF}} = \sqrt[\alpha+2]{\frac{2}{V_0} r_0^{\alpha}} \tag{2.57}$$

$$\implies r_{\mathrm{TF}} \to r_0 \text{ as } \alpha \to \infty.$$

For harmonic trapping potentials, a similar approach finds the approximate Thomas-Fermi radius to be:

$$r_{\mathrm{TF}} = \sqrt{\frac{2\mu}{m\omega_r^2}}. \tag{2.58}$$

In this chapter we have discussed the models we will use to simulate two-dimensional quantum turbulence. In the next chapter we shall detail the numerical methods use to realise these simulations.

Chapter 3

Numerical Methods I

We introduce methods of numerical integration, which are applied in both the 2-D and 3-D numerical experiments, and describe the implementation of our 2-D models. We also describe some numerical procedures that are particular to our analysis.

3.1 Numerical Differentiation & Integration

3.1.1 Finite Difference Schemes

We numerically approximate spatial derivatives using finite difference methods [278]. For a quantity $F(x)$ with known values $F_0, F_1, F_2, ..., F_{n-2}, F_{n-1}, F_n$ at corresponding regularly spaced points $x_0, x_1, x_2, ..., x_{n-2}, x_{n-1}, x_n$, with a constant separation of Δx between neighbouring points, we make use of the following central difference approximations:

$$\left.\frac{dF}{dx}\right|_{x=x_i} = \frac{-F_{i-1} + F_{i+1}}{2\Delta x} + \mathcal{O}((\Delta x)^2), \tag{3.1}$$

$$\left.\frac{dF}{dx}\right|_{x=x_i} = \frac{\frac{1}{12}F_{i-2} - \frac{2}{3}F_{i-1} + \frac{2}{3}F_{i+1} - \frac{1}{12}F_{i+2}}{\Delta x} + \mathcal{O}((\Delta x)^4), \tag{3.2}$$

$$\left.\frac{d^2F}{dx^2}\right|_{x=x_i} = \frac{F_{i-1} - 2F_i + F_{i+1}}{(\Delta x)^2} + \mathcal{O}((\Delta x)^2), \tag{3.3}$$

$$\left.\frac{d^2F}{dx^2}\right|_{x=x_i} = \frac{-\frac{1}{12}F_{i-2} + \frac{4}{3}F_{i-1} - \frac{5}{2}F_i + \frac{4}{3}F_{i+1} - \frac{1}{12}F_{i+2}}{(\Delta x)^2} + \mathcal{O}((\Delta x)^4). \tag{3.4}$$

Detailed derivations of these schemes are given in Appx. A.5.1.

Note that these methods require a number of points either side of the point F_i in order to evaluate the approximation at F_i. We use 'ghost' points as a numerical 'trick' to allow

the evaluation of derivatives close to the boundary, and additionally to enforce particular boundary conditions.

In some situations we require that the quantity F be 0 at the boundaries (Dirichlet boundary conditions). This is enforced by setting $F_0 = F_n = 0$ at each numerical step. Further points beyond the region we are simulating are created and held to be 0; $F_{-1} = F_{n+1} = 0$ for 2^{nd}-order methods, and also $F_{-2} = F_{n+2} = 0$ for 4^{th}-order methods; higher-order methods will require yet further ghost points.

In other situations we require that the first derivative of F be 0 at the boundaries (Neumann boundary conditions). This is achieved by setting $F_{-1} = F_1, F_{n+1} = F_{n-1}$ for the 2^{nd}-order method, and additionally $F_{-2} = F_2, F_{n+2} = F_{n-2}$ for the 4^{th}-order method. Substituting these values into eq. (3.1) or (3.2) appropriately at $x = x_0$ or $x = x_n$ immediately gives the approximation to the derivative at the boundary as zero by our choice of F at the ghost points.

In some contexts the spacing of the discretisation points will be irregular, and we will need to approximate derivatives using a more general form of these finite difference methods.

Suppose we have a function F, with known values $F_0, F_1, F_2, ..., F_{n-2}, F_{n-1}, F_n$ at positions $x_0, x_1, x_2, ..., x_{n-2}, x_{n-1}, x_n$, where $x_i - x_{i-1}$ is not necessarily constant, and introduce the notation $\Delta_{+i} = x_{i+1} - x_i$, $\Delta_{-i} = x_i - x_{i-1}$. We then use the following 2^{nd}-order approximations to the first and second derivatives:

$$\left.\frac{dF}{dx}\right|_{x=x_i} = \frac{-\Delta_{+i}F_{i-1} + (\Delta_{-i} - \Delta_{+i})F_i + \Delta_{-i}F_{i+1}}{2\Delta_{+i}\Delta_{-i}} + \mathcal{O}(\Delta_i^2) \tag{3.5}$$

$$\left.\frac{d^2F}{dx^2}\right|_{x=x_i} = 2\left[\frac{\Delta_{+i}F_{i-1} - (\Delta_{+i} + \Delta_{-i})F_i + \Delta_{-i}F_{i+1}}{\Delta_{+i}\Delta_{-i}(\Delta_{+i} + \Delta_{-i})}\right] + \mathcal{O}(\Delta_i^2) \tag{3.6}$$

where Δ_i is the larger of Δ_{+i} and Δ_{-i}; note that when we use these schemes the numerical grid is set up in such a way that there is at most a factor of two difference between any intervals. We discuss the derivation of these methods in Appx. A.5.2.

3.1.2 Runge-Kutta Methods

We evolve our numerical solutions to the point vortex model (PVM) and the Gross-Pitaevskii equation (GPE) in time using explicit Runge-Kutta time-stepping methods [279]. Higher-order methods can be viewed as extensions of the 1^{st}-order Euler method, with trial steps forward in time made, and the system evolved forward in time by a linear combination of these trial steps with coefficients selected to match the Taylor expansion of the system's velocity up to the specified order. A detailed derivation in given in Appx. A.6.

We make use of a 4^{th}-order method, frequently referred to as 'the Classical Runge-Kutta method' or 'RK4', which, following the description of [280], consists of an initial value problem:

$$\frac{dy}{dt} = f(t, y), \qquad y(t_0) = y_0$$

A time-step, $\Delta t > 0$, is selected as a parameter governing the temporal resolution of the solution. The solution $y_{n+1} = y(t_{n+1})$ at $t_{n+1} = (n+1)\Delta t$ is then approximated by the scheme:

$$k_1 = f(t_{n-1}, y_{n-1}),$$

$$k_2 = f\left(t_{n-1} + \frac{\Delta t}{2}, y_{n-1} + \frac{\Delta t}{2} k_1\right),$$

$$k_3 = f\left(t_{n-1} + \frac{\Delta t}{2}, y_{n-1} + \frac{\Delta t}{2} k_2\right),$$

$$k_4 = f\left(t_{n-1} + \Delta t, y_{n-1} + \Delta t k_3\right),$$

$$y_n = y_{n-1} + \Delta t \left(\frac{k_1 + 2k_2 + 2k_3 + k_4}{6}\right) + \mathcal{O}((\Delta t)^4).$$

We also make use of a 6^{th}-order scheme, detailed in Appx. A.6.

In all of our GPE simulations the right hand side of the dimensionless inhomogeneous GPE takes the place of f. In our PVM simulations the right hand side of the equations of motion takes the place of f; note that for a coupled system each step is calculated for each ODE concurrently, that is, we calculate k_1 for the x and y velocity components of all vortices first, then k_2 for the x and y velocity components of all vortices, and so forth.

We note that time-adaptive extensions of Runge-Kutta schemes exist [281], which consist of n^{th}-order methods used to estimate the error in the current time-step, and an embedded $(n-1)^{\text{th}}$-order method used to perform the time-step itself. By selecting upper and lower thresholds for the error, and adjusting the time-step appropriately when these thresholds are breached, the scheme adapts to handle rapid or slow change in the solution accurately and efficiently. We have elected not to use such schemes for a number of reasons:

- Adaptive time-steps create additional work to approximate solutions at regularly spaced intervals.
- Extra function evaluations necessary for adaptive schemes can be less efficient than choosing an appropriate time-step initially.
- Convergence criteria can be found for the GPE (see [236]), allowing us to choose an appropriate time-step.
- The PVM is a system of coupled ODEs; single pairs of vortices interacting tend to force the time-step down for the entire system unnecessarily, and it is not practical to use different time-steps for different individual ODEs in the system.
- The time scale of motion does not typically fluctuate dramatically in our simulations.

3.1.3 Simpson's Rule

Numerical integration in space is performed using Simpson's rule, a Newton-Cotes scheme which approximates integrals by quadratic polynomials [282]. For a function $f(x)$ with known values $f(x_0), f(x_1), ..., f(x_n)$ for some regularly spaced $x_0, x_1, ..., x_n$, with $\Delta x = x_i - x_{i-1}$, the integral of f over this region is approximated by:

$$\int_{x_0}^{x_n} f(x)dx = \frac{\Delta x}{3}(f(x_0)+4f(x_1)+2f(x_2)+4f(x_3)+2f(x_4)+...+4f(x_{n-1})+f(x_n)). \quad (3.7)$$

Note that this requires an odd number of known function values; the integral can be evaluated for functions known at an even number of points by padding with zeros. This rule can be easily extended to higher dimensions by repeating over each dimension as required.

3.2 The Point Vortex Model

Having introduced the numerical schemes used to evolve our PVM simulations, we discuss the accuracy of our implementation, and introduce a further method for the efficient enforcement of periodic boundary conditions.

3.2.1 Accuracy

We test the qualitative and quantitative accuracy of our implementation of the point vortex model, using known exact solutions and conserved quantities.

Pairs of vortices with identical or opposite circulation follow stable linear or circular trajectories, as discussed in Sec. 2.1.2, and the separation between the constituent vortices should remain constant. In Fig. 3.1 we show the change in separation $|\delta - \delta_0|$, where δ is the separation of vortices and δ_0 is the initial separation, for a pair of like-sign vortices, and for a pair of opposite-sign vortices, with an initial separation $\delta = 1$ and circulation $|\Gamma| = 1$. Their motion is simulated using a 6^{th}-order Runge Kutta scheme and a time-step of $\Delta t = 10^{-3}$ as per our full simulations in Sec. 4.1.1.

The separation within opposite-sign pairs is well conserved (to within 10^{-10} after 10^6 time-steps), while the separation within like-sign pairs, while still conserved to within 10^{-2} after 10^6 time-steps, is noticeably less well conserved. We explore this further in Fig. 3.2, which shows the derivative of the separation with respect to time as a function of the separation. It is clear that like-sign vortices approaching extremely close will lead to unexpected behaviour, however we expect these to be vanishingly rare events. Note also that these deviations are particular to the numerical scheme used.

Knowing that numerical inaccuracy can be introduced in this manner, we make use of the autonomous Hamiltonian associated with the point vortex model (see Sec. 2.1) as a measure of the total energy of the system, and the first integrals of the Hamiltonian corresponding to the linear and angular momenta [239] to quantify the accuracy of the full simulations of 500 vortices described in Sec. 4.1.1. As these four quantities are theoretically

conserved, the deviation in them gives a measure of how accurate our numerical methods are in evolving the system.

Figure 3.3 shows the absolute percentage change[1] in the autonomous Hamiltonian over the lifetime of the simulations. The energies of all realisations are conserved within 5%, with the mean absolute percentage change being slightly over 1% and the median slightly below 1%.

In Fig. 3.4 we explore the effect of changing the step-size on the conservation of the autonomous Hamiltonian. We generate 20 initial vortex configurations, again with 500 vortices and with the same distribution as for our full simulations. We then evolve them through 1000 time units using step-sizes between 10^{-3} and 10^{-1}, so that for each step-size we use each of the 20 configurations. We observe that the change in H scales like $\sqrt{\Delta t}$; in order to improve the conservation of H by an order of magnitude we would need to reduce the step-size by two orders of magnitude. Furthermore, Fig. 3.5 shows the values of ν'/κ (the value we are principally interested in estimating from these simulations, discussed in detail in Sec. 4.1) extracted from these simulations as a function of the step-size used. No trend in the value is evident, and so combined with the severe cost of improving the conservation of H we conclude that our chosen step-size and numerical integration scheme are sufficient.

The absolute percentage change in the momenta are shown in Fig. 3.6, 3.7, and 3.8. The angular momentum is conserved within 0.1% for all simulations, with the mean conservation better than 0.01%, while the linear momenta (with the exception of a single realisation) are conserved within 10^{-5}%, and the mean and median conservation again orders of magnitude better.

[1]The Hamiltonian is strictly speaking only defined up to a constant, with the relative change in the Hamiltonian then $(H(t) - H(0))/(H(0) + C)$; by making the conventional choice of $C = 0$ we maximise the relative change, so as to consider the maximum error. We note also that, while the Hamiltonian of these systems is not sign-definite, we have $H \gg 0$ for all of our systems at all times.

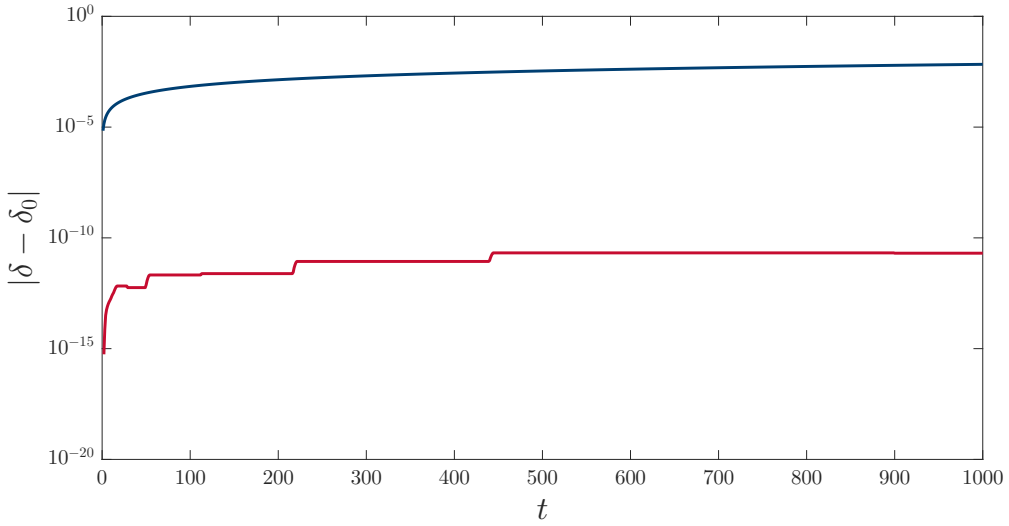

Figure 3.1: [Dimensionless units] Absolute change in separation between a pair of point vortices of opposite circulation (red) and identical circulation (blue), with an initial separation of 1.

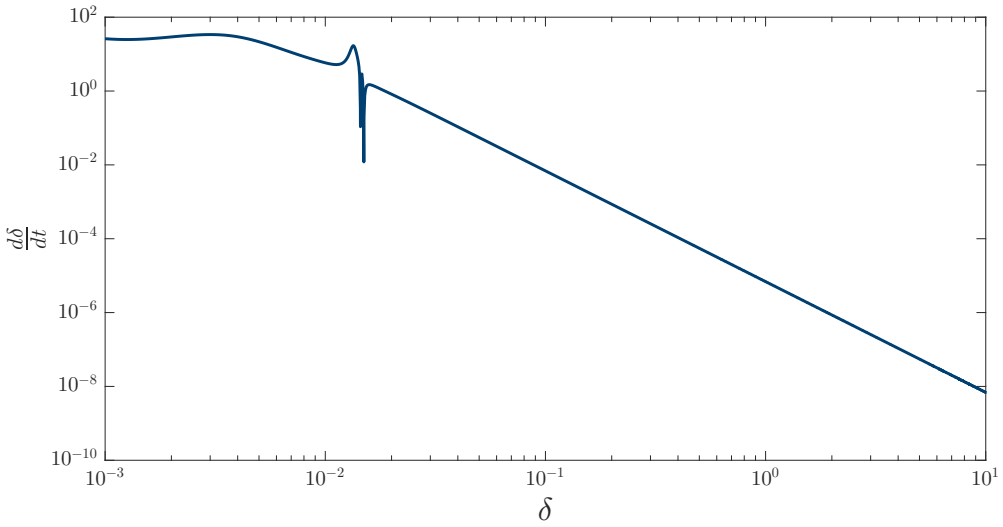

Figure 3.2: [Dimensionless units] Rate of change in separation vs. initial separation for a pair of point vortices with identical circulation.

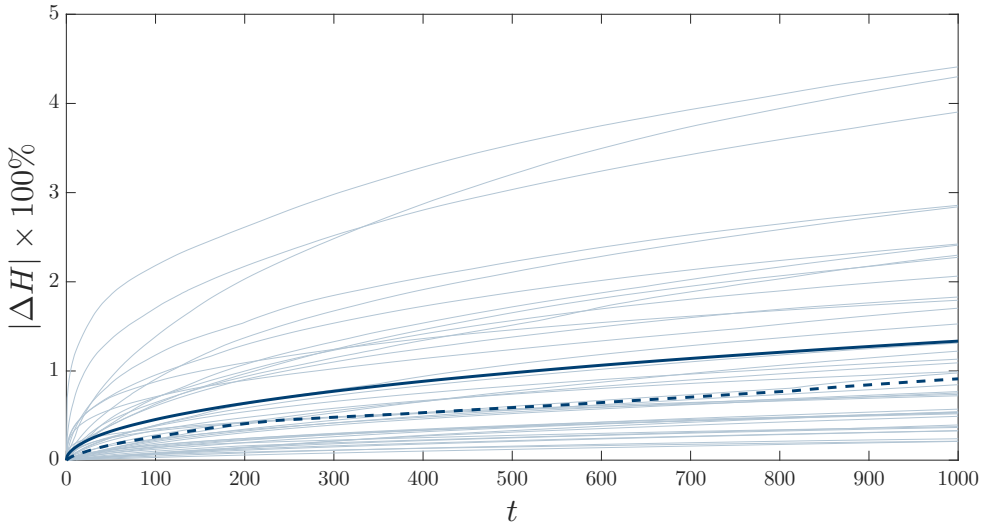

Figure 3.3: [Dimensionless units] Absolute percentage change in the autonomous Hamiltonian associated with the point vortex model in free space for 40 realisations, discussed in detail in Sec. 4.1.1, vs. time t. Individual realisations are shown as pale blue lines, with the mean indicated as a thick solid line, and the median as a thick dashed line.

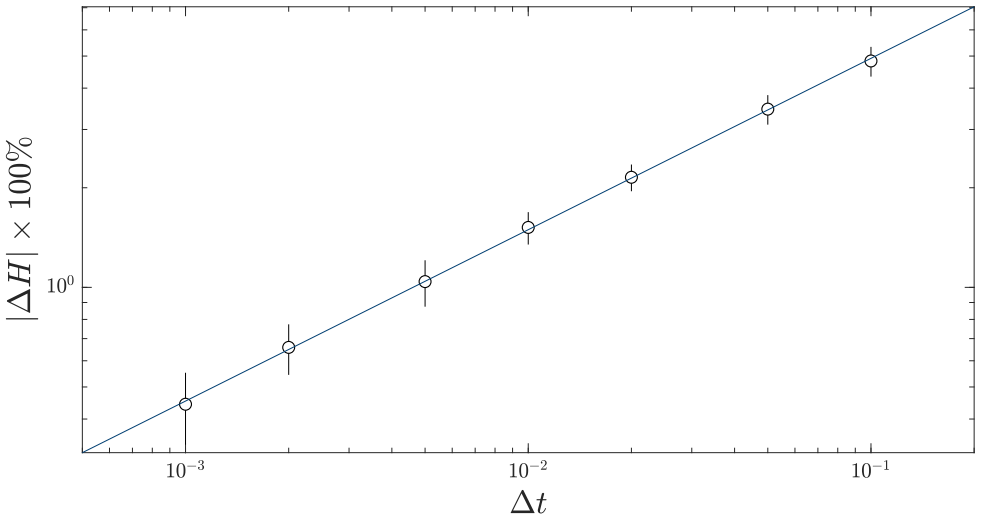

Figure 3.4: [Dimensionless units] Relative percentage change in the autonomous Hamiltonian after evolving through 1000 time units for a range of step-sizes Δt, averaged over 20 realisations for each step-size, with 95% confidence intervals indicated. The blue line indicates scaling $\sim \sqrt{\Delta t}$.

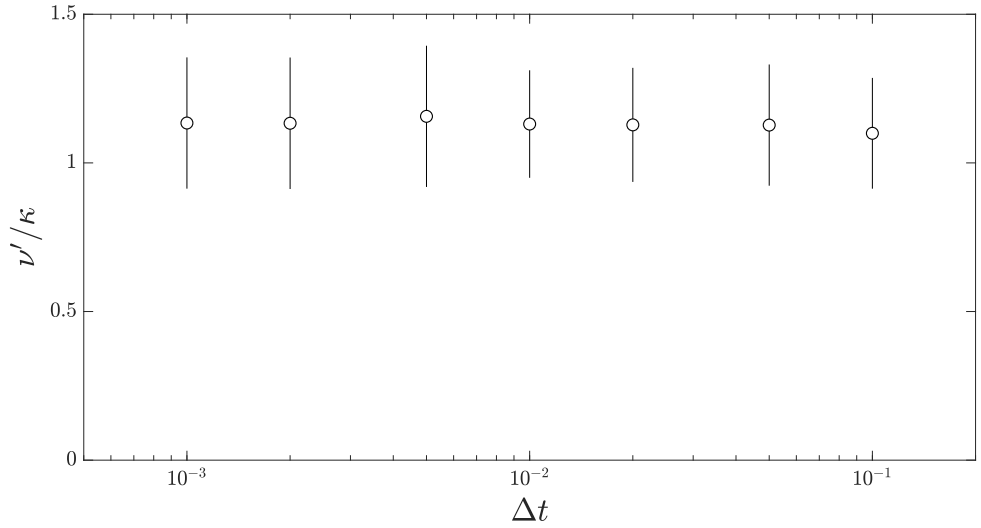

Figure 3.5: [Dimensionless units] Values of ν'/κ (see Sec. 4.1) averaged over 20 simulations, with 95% confidence intervals, for a range of step-sizes.

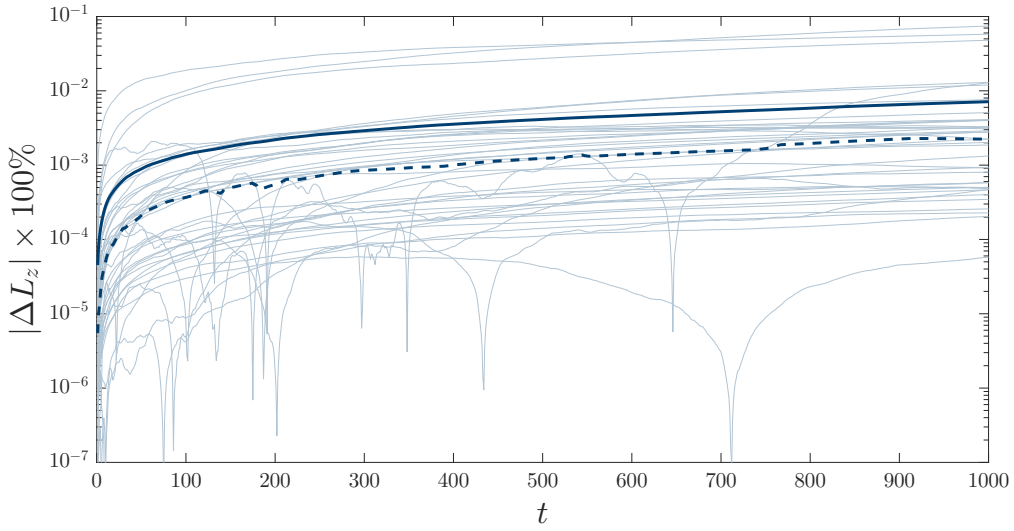

Figure 3.6: [Dimensionless units] Absolute percentage change in the angular momentum L_z for 40 realisations of the point vortex model, discussed in detail in Sec. 4.1.1, vs. time t . Individual realisations are shown as pale blue lines, with the mean indicated as a thick solid line, and the median as a thick dashed line.

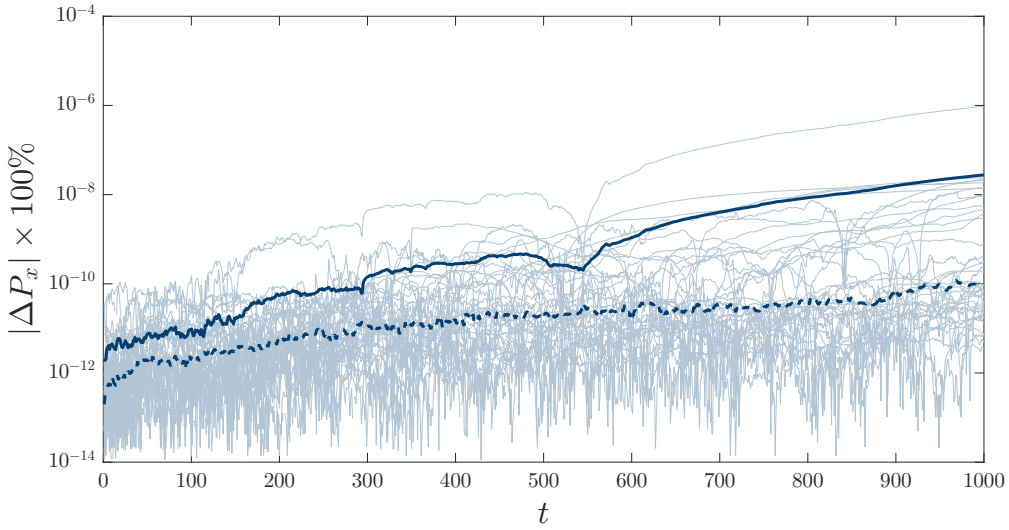

Figure 3.7: [Dimensionless units] Absolute percentage change in P_x, the x-component of the linear momentum, for 40 realisations of the point vortex model, discussed in detail in Sec. 4.1.1, vs. time t. Individual realisations are shown as pale blue lines, with the mean indicated as a thick solid line, and the median as a thick dashed line.

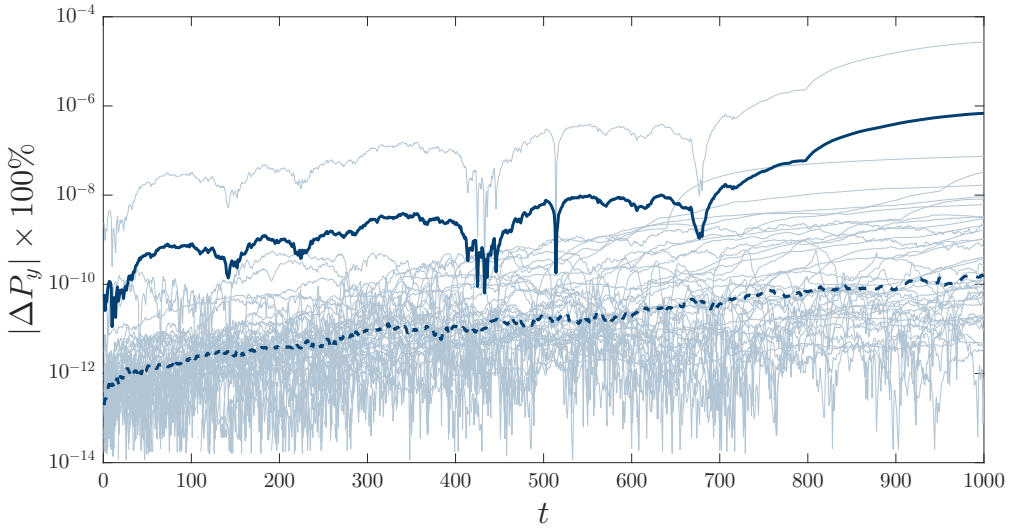

Figure 3.8: [Dimensionless units] Absolute percentage change in P_x, the y-component of the linear momentum, for 40 realisations of the point vortex model, discussed in detail in Sec. 4.1.1, vs. time t. Individual realisations are shown as pale blue lines, with the mean indicated as a thick solid line, and the median as a thick dashed line.

3.2.2 Ewald Summation

In Sec. 2.1.1 we introduced a crude method for imposing double periodic boundaries in the PVM, involving a double infinite summation which in practice must be truncated at some point. We now discuss an Ewald summation, derived by Weiss [283], which reduces this to a single infinite summation by finding an analytical form for one of the summations.

Consider a configuration of N point vortices described by positions $\mathbf{x}$ and circulations $\mathbf{\Gamma}$ within a periodic domain $x, y, \in [0, L)$. By introducing scaled quantities $\mathbf{x}' = (2\pi/L)\mathbf{x}$, $\mathbf{\Gamma}' = (2\pi/L)\mathbf{\Gamma}$, we can calculate the velocities of the original vortices as:

$$\begin{aligned}\frac{dx}{dt} &= \frac{1}{4\pi}\sum_{j\neq i}\Gamma'_j \sum_{n=-\infty}^{\infty} \frac{-\sin(y'_{ij})}{\cosh(x'_{ij}-2\pi n)-\cos(y'_{ij})},\\ \frac{dx}{dt} &= \frac{1}{4\pi}\sum_{j\neq i}\Gamma'_j \sum_{n=-\infty}^{\infty} \frac{\sin(x'_{ij})}{\cosh(y'_{ij}-2\pi n)-\cos(x'_{ij})},\end{aligned} \tag{3.8}$$

which involve only a single summation (besides the summation over the vortices themselves). We still have to choose when to truncate the remaining summation; in order to verify the accuracy of this method and get a feel for a suitable point at which to truncate we compare the velocity at the boundaries as we increase the number of terms retained. For perfectly periodic boundaries the velocities at $(x, 0)$ and (x, L), and likewise at $(0, y)$ and (L, y), should be equal; in practice they differ, which we explore for 100 vortices in a 10×10 periodic domain in Fig. 3.9. The error rapidly decreases, reaching the level of numerical noise by the time we include terms from $n = -6$ to $n = 6$, suggesting that this is a natural point at which to truncate.

This method, and the method using ghost vortices described in Sec. 2.1.1, are suitable for modelling vortices in an ideal fluid with periodic boundaries. However, they do not match the dynamics of the GPE, even leaving aside such effects as sound and vortex-antivortex annihilations, due to the periodicity of the phase, which must also wind around vortices in a precise fashion. For the systems that we consider, consisting of even number of positive and negative vortices, the correction to eq. (3.8) found by Griffin *et al.* [284] amounts to imposing a background velocity given by:

$$\mathbf{u}_b = \sum_{i=1}^{N} \frac{\Gamma_i}{(2\pi)^2}\hat{\mathbf{e}}_z \times \mathbf{x}_i, \tag{3.9}$$

where $\mathbf{x}_i$ is the position of the i^{th} vortex.

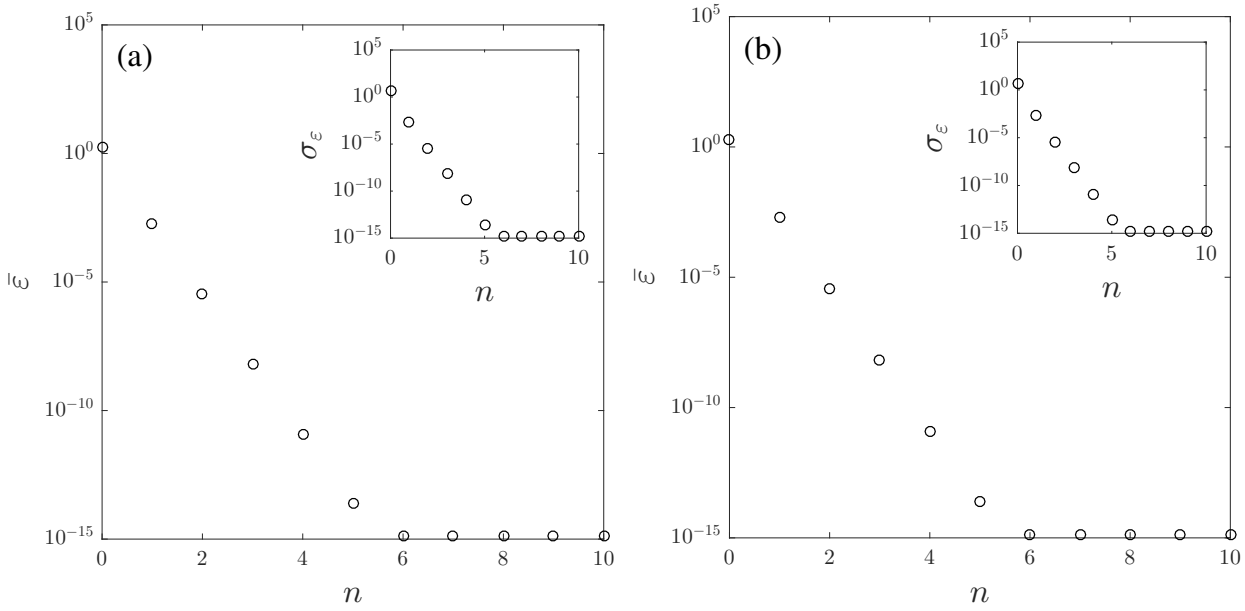

Figure 3.9: Mean proportional error $\bar{\varepsilon}$ in the velocity calculated at boundaries $(x, 0)$ and (x, L) (a), and $(0, y)$ and (L, y) (b) when retaining terms from $-n$ to n in the calculation of velocity using the given Ewald summation, with standard deviations σ_ε inset.

3.3 The Gross-Pitaevskii Equation

In addition to the numerical methods for integrating solutions to the GPE, supplementary routines are needed to initialise simulations. Here we discuss finding ground state solutions and imprinting vortices, as well as post-processing identification of vortices and reconstructing their trajectories. We then quantify the accuracy of our simulations.

3.3.1 Ground State Solutions

The dynamic behaviour of quantum systems can be greatly affected by the initial conditions [285], so it is natural to begin simulations from a ground state. Analytic solutions often exist, but as we need to find the ground state solution for random configurations of vortices it is convenient to use a reliable numerical method. A number of sophisticated methods exist, see e.g. [286–288], but for ease of implementation two simple methods are used: the imaginary time propagation method [285], and the dissipative Gross-Pitaevskii Equation (DGPE) [289].

To reduce the computation time needed to find the ground state solution by these methods, the initial 'guess' wavefunction is taken to be the Thomas-Fermi profile, discussed in Sec. 2.2.11, in both cases.

3.3.2 Imaginary Time Propagation

The core idea of the imaginary time propagation method [285] is to perform a Wick rotation:

$$t \to \tau = -it, \tag{3.10}$$

which leads to a diffusion-like equation with nonlinear forcing:

$$\frac{\partial \psi}{\partial \tau} = \left(\frac{\nabla^2}{2} - V - |\psi|^2 + 1 \right) \psi, \tag{3.11}$$

here corresponding to the dimensionless, homogeneous GPE. Consider a wavefunction:

$$\psi(\mathbf{r}, t) = \sum_n \psi_n(\mathbf{r}) \exp\{-iE_n t/\hbar\}, \tag{3.12}$$

with ψ_n and E_n respectively eigenfunctions and their corresponding eigenvalues. Under eq. (3.11) the wavefunction decays as:

$$\psi(\mathbf{r}, \tau) = \psi_n(\mathbf{r}) \exp\{-E_n \tau/\hbar\}. \tag{3.13}$$

Note that the decay rate is linked to the eigenvalue; in particular the eigenfunctions with the greatest eigenvalues, and hence the greatest energy, will decay fastest. In theory the ground state can be found by evolving the system in imaginary time by the same numerical scheme to be used for real time propagation, until all excited states have decayed. In practice, the wavefunction is renormalised at every time-step to preserve optimal signal to noise ratio, until the ground state energy has converged to within some desired threshold.

3.3.3 Dissipative Gross-Pitaevskii Equation

First introduced by Pitaevskii [290] to describe dissipation near the λ point, and later honed by others [289, 291, 292], the dissipative Gross-Pitaevskii equation (DGPE) seeks to model finite temperature effects on condensate dynamics by introducing dissipation in a phenomenological manner. We will employ this model to approximate localised finite temperature effects in Sec. 4.1.1, but it is also a convenient tool for identifying equilibrium states. We make use of this to find ground states in geometries where the imaginary time propagation method fails.

Following the derivation of Choi [291], we first consider the equation of motion for our wavefunction $\psi(\mathbf{r}, t)$ under the (dimensionless, homogeneous) GPE:

$$i\frac{\partial}{\partial t}\psi(\mathbf{r}, t) = \hat{\mathcal{H}}\psi(\mathbf{r}, t), \tag{3.14}$$

where

$$\hat{\mathcal{H}} = \left(-\frac{\nabla^2}{2} + |\psi(\mathbf{r}, t)|^2 + V(\mathbf{r}, t) - 1 \right), \tag{3.15}$$

which implies

$$\hat{\mathcal{H}}\psi_0 = 0 \tag{3.16}$$

for a non-trivial equilibrium state ψ_0. We seek a modified equation of motion that approaches an equilibrium state in time through a damping process. In order to describe a relaxation process, the Hermitian operator $\hat{\mathcal{H}}$ must be replaced by a non-Hermitian operator, say $\hat{\mathcal{L}}$:

$$i\frac{\partial}{\partial t}\psi(\mathbf{r},t) = \hat{\mathcal{L}},\psi(\mathbf{r},t) \tag{3.17}$$

with the anti-Hermitian part of $\hat{\mathcal{L}}$ associated with the mechanism driving toward equilibrium. We can find a suitable form for $\hat{\mathcal{L}}$ by enforcing two requirements: that the anti-Hermitian part must vanish when equilibrium is reached, and that we must recover the usual $T = 0$ behaviour of the GPE when the anti-Hermitian part vanishes.

One can satisfy the former by taking the anti-Hermitian part to be $-i\gamma\hat{\mathcal{H}}$, giving $-i\gamma\hat{\mathcal{H}}\psi_0 = 0$ from eq. (3.16), with γ a dimensionless, real parameter governing the strength of the damping, and the minus sign by convention. It is apparent that taking $\hat{\mathcal{H}}$ as the Hermitian part of $\hat{\mathcal{L}}$ will yield the desired behaviour for $\gamma = 0$, giving us $\hat{\mathcal{L}} = (1 - i\gamma)\hat{\mathcal{H}}$, and allowing us to state the DGPE as:

$$i\frac{\partial}{\partial t}\psi(\mathbf{r},t) = (1 - i\gamma)\left(-\frac{\nabla^2}{2} + |\psi(\mathbf{r},t)|^2 + V(\mathbf{r},t) - 1\right)\psi(\mathbf{r},t), \tag{3.18}$$

or for numerical convenience as:

$$(i - \gamma)\frac{\partial}{\partial t}\psi(\mathbf{r},t) = \hat{\mathcal{H}}\psi(\mathbf{r},t) \tag{3.19}$$

We use the DGPE to initialise equilibrium states for the simulations detailed in Sec. 4.1.1. The evolution of the total energy of the condensate during this procedure is displayed in Fig. 3.10, showing the convergence to the desired equilibrium state.

3.3.4 Vortex Imprinting

Vortices can be introduced in our systems through a number of techniques, including trap rotation [289, 293], laser stirring [84, 294], bubble collapse [101], and quench dynamics nucleating vortices through the Kibble-Zurek mechanism [95]. However, for precise control over the configuration of vortices it is preferable to directly imprint vortices before the start of the simulation, which can be likened to experimental phase imprinting [295].

Having prepared a ground state solution for the potential used, vortices are imprinted by multiplying the condensate wavefunction by $\exp(i\theta)$ to introduce a 2π phase-winding, and multiplying by a suitable initial density profile. No analytic form is known for the density profile, and it is typical to use an approximation to the solution for a singly charged straight-line vortex $\Psi = R(r)\exp(i\theta)$ satisfying the steady GP equation:

$$R''(r) + \frac{1}{r}R'(r) - \frac{1}{r^2}R(r) + [1 - R^2(r)]R(r) = 0, \tag{3.20}$$

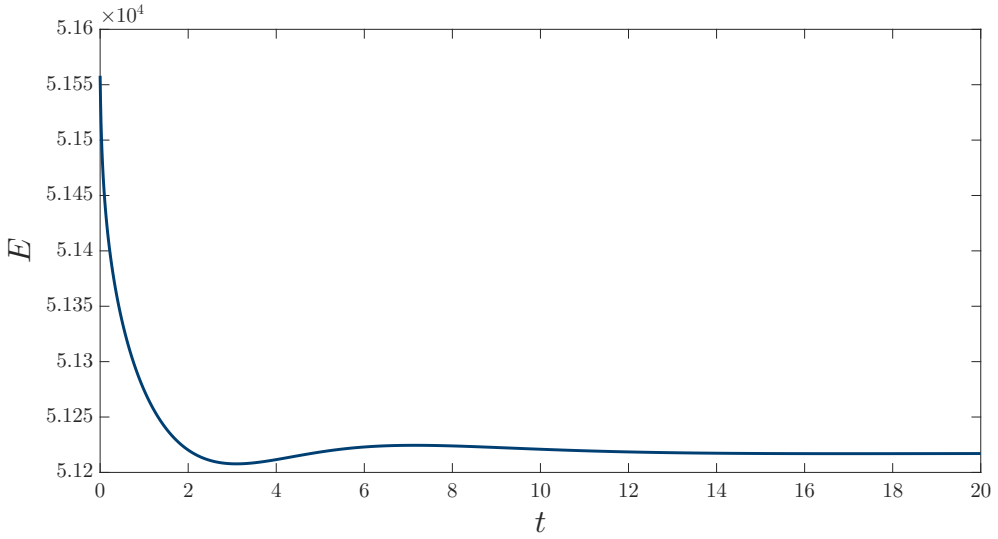

Figure 3.10: [Dimensionless units] Total energy of a condensate converging to an equilibrium solution through the DGPE, from an initial Thomas-Fermi profile.

with boundary conditions $R(0) = 0$, $R(\infty) = 1$. Power series approximations to the solution about zero and about infinity can be found, with forms:

$$R(r) \simeq \sum_{i=1}^{\infty} p_i r^{2i-1} \text{ and } R(r) \simeq \sum_{i=0}^{\infty} q_i r^{-2i}$$

respectively, for some p_i and q_i. However, the former have a very limited radius of convergence, while the latter diverge, and they are thus of limited practical use. This was resolved by Berloff [296] introducing a Padé approximation of the form:

$$R(r) \simeq \sqrt{\frac{r^{2n} \sum_{i=1}^{N} a_i r^{2i}}{\sum_{j=0}^{N+n} b_j r^{2j}}}, \tag{3.21}$$

with $a_N = q_0^2 b_{N+n}$ and $q_0 = R(\infty)$, which recovers the asymptotic behaviour of both power series. The particular approximation they find, which we use as our initial vortex density profile, is:

$$R(r) = \sqrt{\frac{r^2(0.3437 + 0.0286r^2)}{1 + 0.3333r^2 + 0.0286r^4}}. \tag{3.22}$$

We then evolve the wavefunction through 1000 time-steps under the DGPE with heavy damping ($\gamma = 1$) to find the true vortex profile. We compare the true vortex profile found after this process to the initial Padé approximation in Fig. 3.11. We show the energy convergence of this procedure in Fig. 3.12. We note that the approximation deviates considerably from the true vortex density profile. The crucial part of the approximation is that it captures the broad features of the vortex; to initialise simulations it would be sufficient to use a crude linear profile and evolve in imaginary time or under the dGPE until converged, however the use of an appropriate Padé approximation speeds this process up.

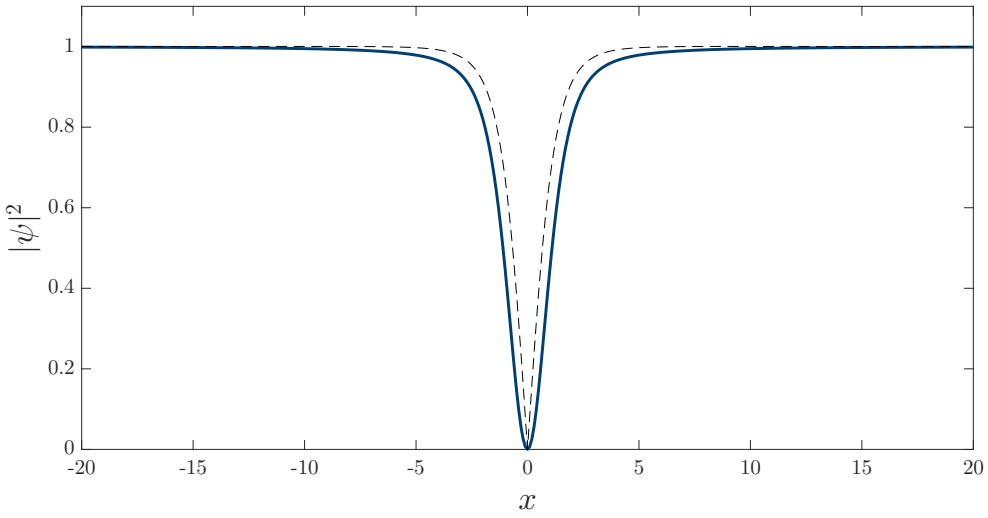

Figure 3.11: [Dimensionless units] Comparison of the true vortex profile (blue) with the initial Padé approximation used (dashed black) in the $y = 0$ plane for a 2-D condensate with a vortex at the origin.

3.3.5 Vortex Identification

In order to analyse the dynamics of vortices we need to access their trajectories, which requires knowledge of their position at discrete points in time, and a method to link vortices from one frame to the next. A number of methods for identifying vortices have been discussed, see e.g. [297–300], and most involve taking integrals of $\nabla\phi$ around closed paths, with nonzero values implying a singularity in the phase and thus a vortex within the area enclosed by the path. We make use of one such algorithm given in [236]. Such algorithms will usually identify so-called 'ghost' vortices in regions where the condensate density is close to zero; spurious topological defects which carry negligible energy and momentum and are thus of no interest. As we are using very steep trapping potentials we have a clear condensate boundary, and simply discard any vortices identified outside this region. An example of vortices identified through this procedure is given in Fig. 3.13.

There are scenarios in which the removal of 'ghost' vortices is less clear-cut, in particular if the boundaries are less sharp or if other regions of near zero density are produced by obstacles. One simple approach in this situation is to create a mask using the Thomas-Fermi profile, just as we do for our sharp boundaries. However, this method can fail if 'breathing' or 'sloshing' bulk modes are excited. A more sophisticated approach that handles such behaviour is to multiply the circulation calculated at each point by the condensate density at that point, relative to the maximum condensate density. Applying a Gaussian filter to eliminate residual noise, then proceeding to identify vortices as before, efficiently removes 'ghost' vortices in these cases.

Having identified the positions of vortices at discrete points in time we need to reconstruct trajectories using particle tracking. Here, vortices are tracked between two adjacent frames using the Hungarian algorithm [301] which links points by minimising the sum of distances within pairs. We impose two additional rules to prevent unphysical trajectories

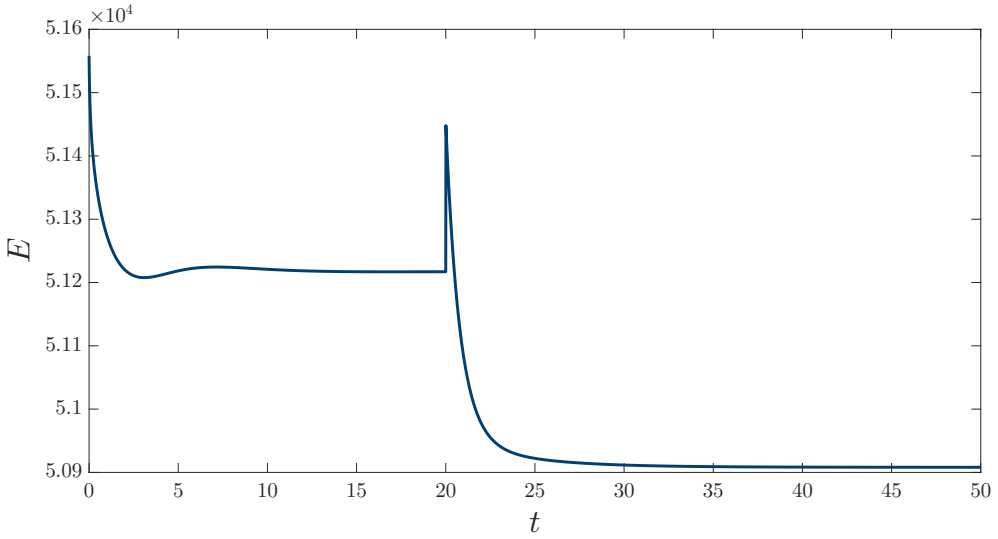

Figure 3.12: Total energy of a condensate converging to an equilibrium solution through the DGPE after the imprinting of 100 vortices. This is an extension of Fig. 3.10, with vortex imprinting occuring at $t = 20$.

being constructed: positive and negative vortices are treated separately, so a vortex cannot flip sign, and a maximum linking distance is imposed, so vortices cannot travel further than is physically possible. Some reconstructed trajectories are shown in Fig. 3.14.

3.3.6 Accuracy

We use a spatial resolution of $\Delta x = 0.2$ and a temporal resolution of $\Delta t = 0.01$, in dimensionless units, recommended by convergence analysis in [236]. We track the total energy and normalisation of a condensate from a GPE simulation with these parameters, and an otherwise identical set-up to the simulations detailed in Sec. 4.1.1, with the exception of the phenomenological damping. We note that these quantities, shown in Fig. 3.15, should be conserved - the damping is omitted precisely because it violates these conservation laws. As evident in Fig. 3.15, these quantities are indeed well conserved, to within 0.05% for the energy and 4×10^{-5}% for the norm, from which we conclude that our choice of numerical parameters is appropriate. For comparison we show the conservation of energy for simulations with localised damping in Fig. 3.16

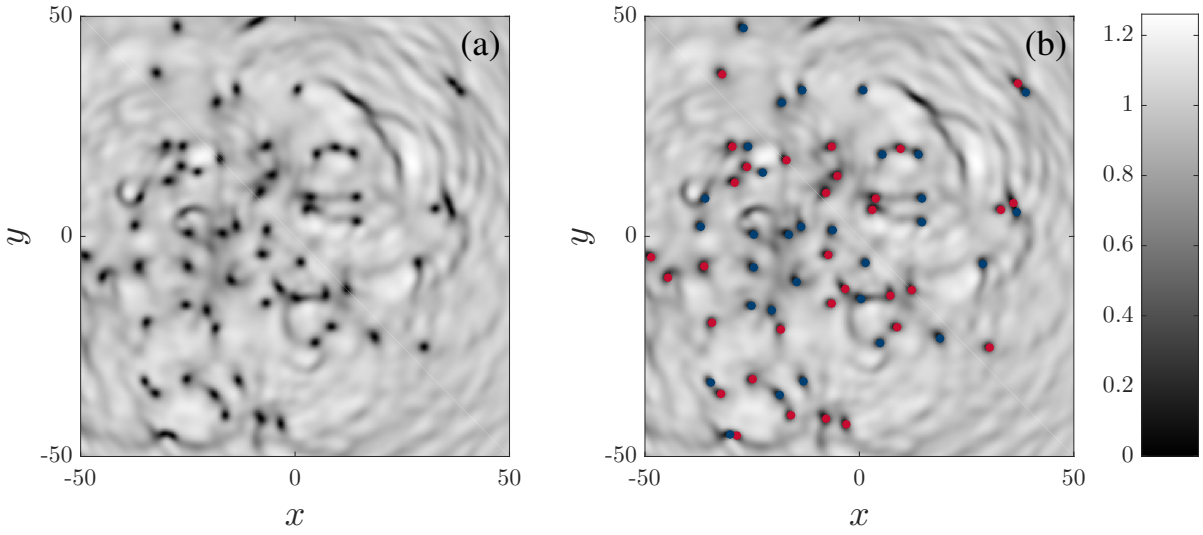

Figure 3.13: [Dimensionless units] Condensate density cropped from a larger condensate in a disc-shaped trapping potential (a), with lots of sound and vortices present, and the same snapshot with the vortices identified superimposed as red and blue discs corresponding to positive and negative circulation respectively (b).

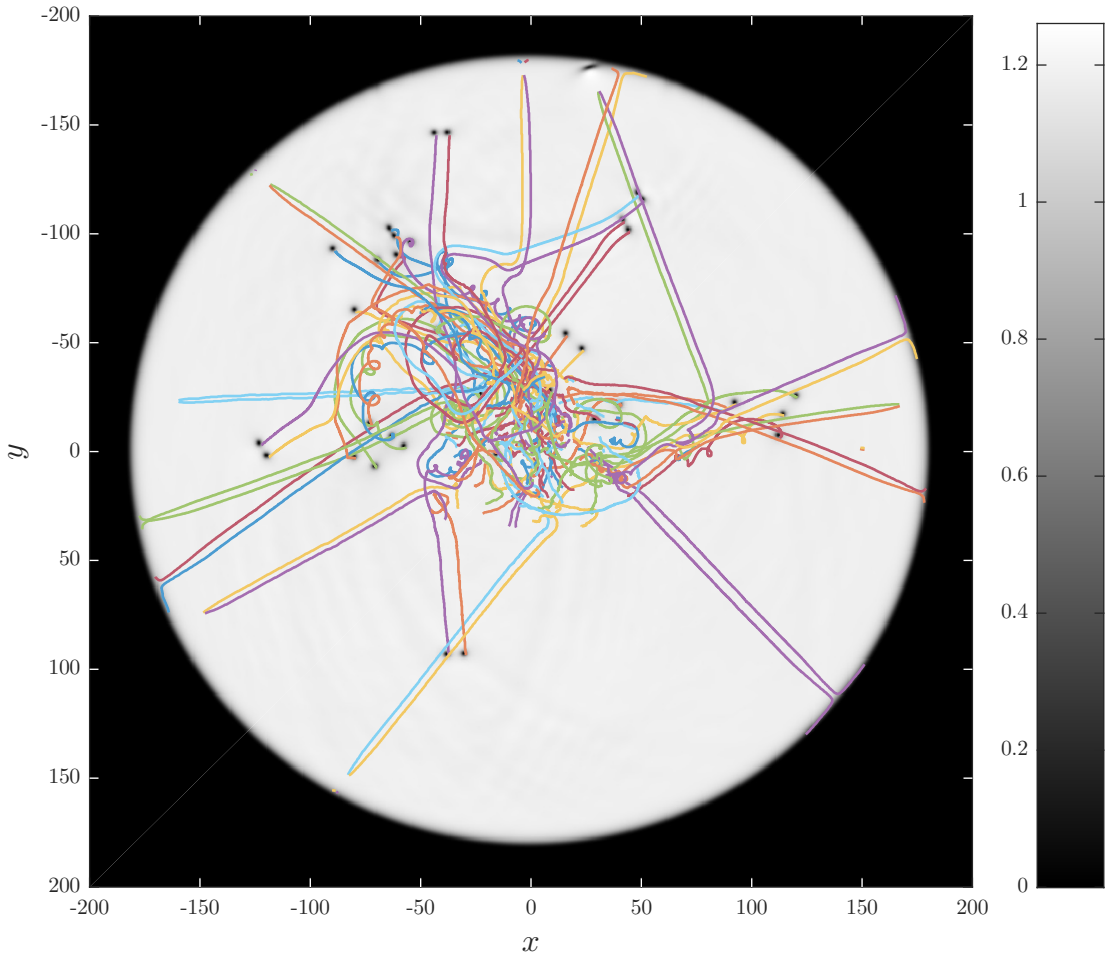

Figure 3.14: [Dimensionless units] Reconstructed vortex trajectories, superimposed over the condensate density at the final time of the simulation.

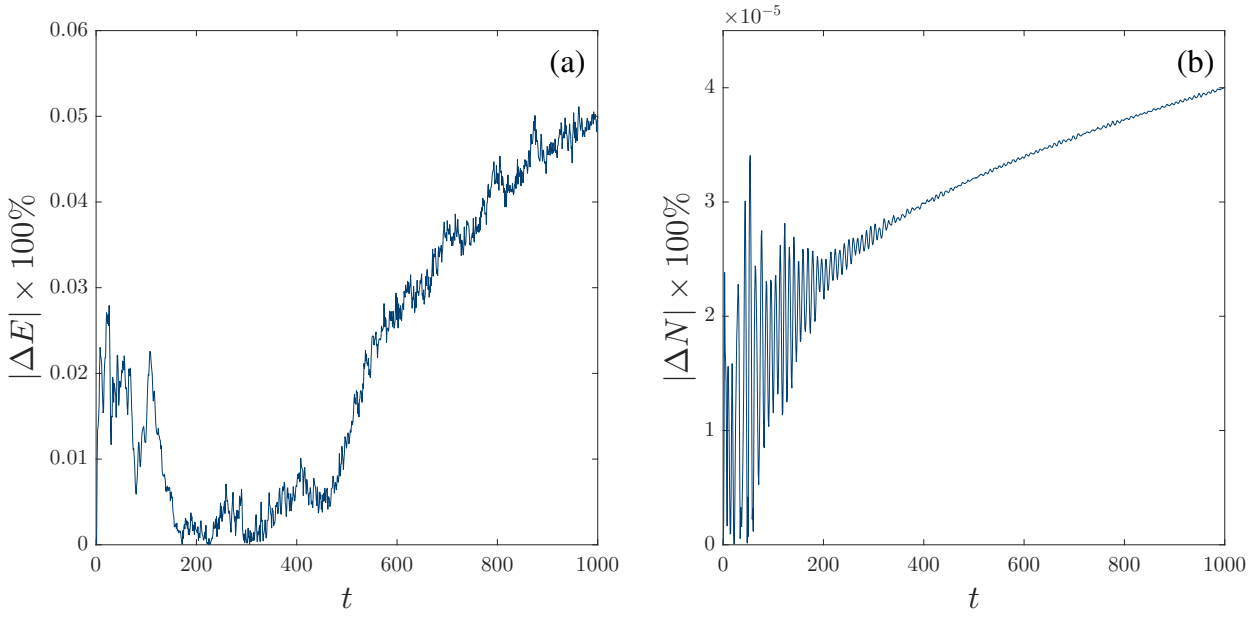

Figure 3.15: [Dimensionless units] Absolute percentage change in total energy (a) and normalisation (b) over one GPE simulation.

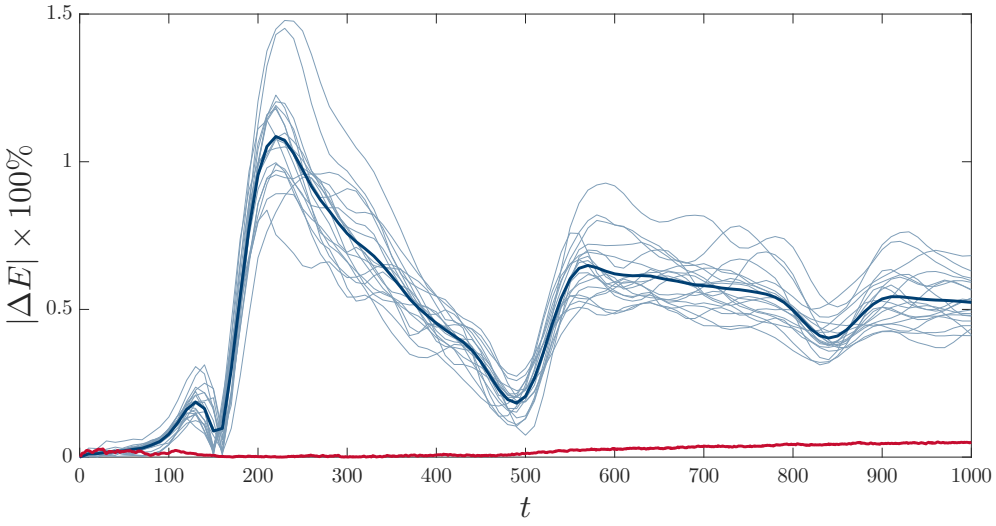

Figure 3.16: [Dimensionless units] GPE simulations. Absolute percentage change in total energy for individual (damped) simulations vs. time, with ensemble average shown as a thicker line (blue), and for a single undamped simulation (red)

3.4 Dipole and Cluster Identification

Numerical simulations of localised regions of vorticity, in three dimensions in the context of superfluid helium, predict the generation of small vortex loops which ballistically 'evaporate' from the initial region [302]. Visualising analogous two-dimensional simulations performed using either the point vortex model of the Gross-Pitaevskii equation, in which an initial region contains numerous vortices of a mixture of positive and negative circulation, are allowed to evolve into free space, shown in Fig. 3.17, it is apparent that a similar process occurs in 2-D. Vortices are observed to form vortex-antivortex dipoles, analogous to the small vortex loops in 3-D (see Fig. 3.18), which also ballistically 'evaporate' from the initial region. The remaining vortices are observed to spread slowly; in order to facilitate analysis of this slower process we algorithmically identify dipoles. We use the first stage of the recursive cluster algorithm (RCA) [303] with an additional condition for this purpose. The recursive clustering algorithm is:

1. Mutually nearest vortices of opposite circulation are identified as dipoles, and removed from the algorithm's consideration.

2. Vortices of the same circulation which are closer to each other than either is to a vortex of the opposite circulation are placed in the same cluster.

Each rule is applied recursively until no further vortices can be identified as belonging to either a dipole or a cluster. The remaining vortices are considered 'free' vortices. Some examples of how vortices are classified by this algorithm are shown in Fig. 3.19.

We only want to separate dipoles which have escaped from the initial cluster. To reduce the number of vortices classified as dipoles within the initial cluster we require, in addition to step one of the RCA, that the separation of the vortices within the dipole be less than half the distance from either vortex to the nearest vortex of the same circulation. We find that relaxing or restricting this additional criteria by a factor of two has negligible effect on the identification of dipoles. The results of applying this algorithm to our PVM and GPE simulations are shown in Fig. 3.20

In this chapter we have discussed the numerical implementation of the PVM and GPE models, and some relevant post-processing techniques. We now move on to the particular numerical investigations we have performed with these models.

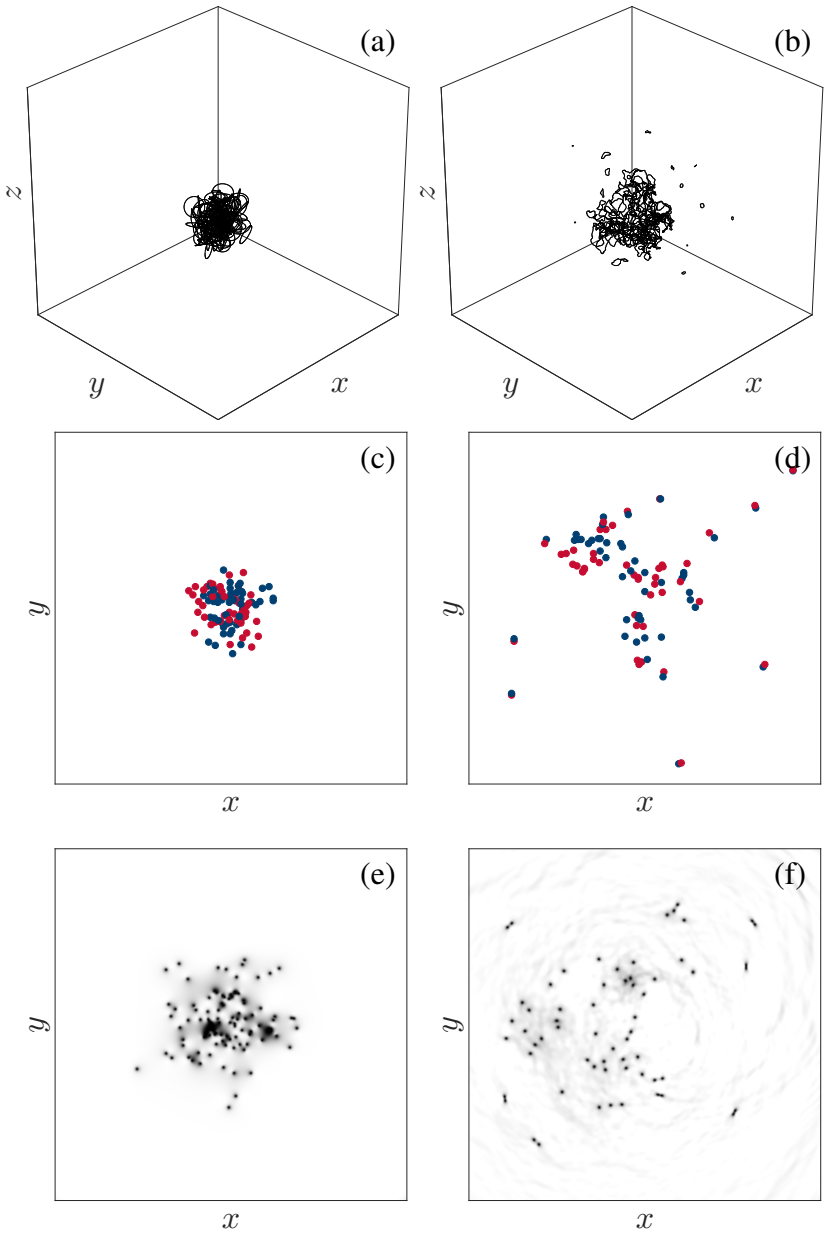

Figure 3.17: Three-dimensional vortex filament method simulation (a) and (b), 2-D point vortex model simulation (c) and (d), and 2-D Gross-Pitaevskii equation simulation (e) and (f). The initial configurations, in all cases a localised region of vorticity, are shown in (a), (c), and (e). The systems are shown at a later time in (b), (d), and (f), with several evaporating vortex loops visible in (b), and several evaporating vortex dipoles visible in (d) and (f). Panels (a,b) show the region -3 cm $\leq\ x, y, z\ \leq\ 3$ cm, panels (c,d) show the region $-100 \leq x, y \leq 100$ (in dimensionless units), and panels (e,f) show the region $-60 \leq x, y \leq 60$ (in dimensionless units).

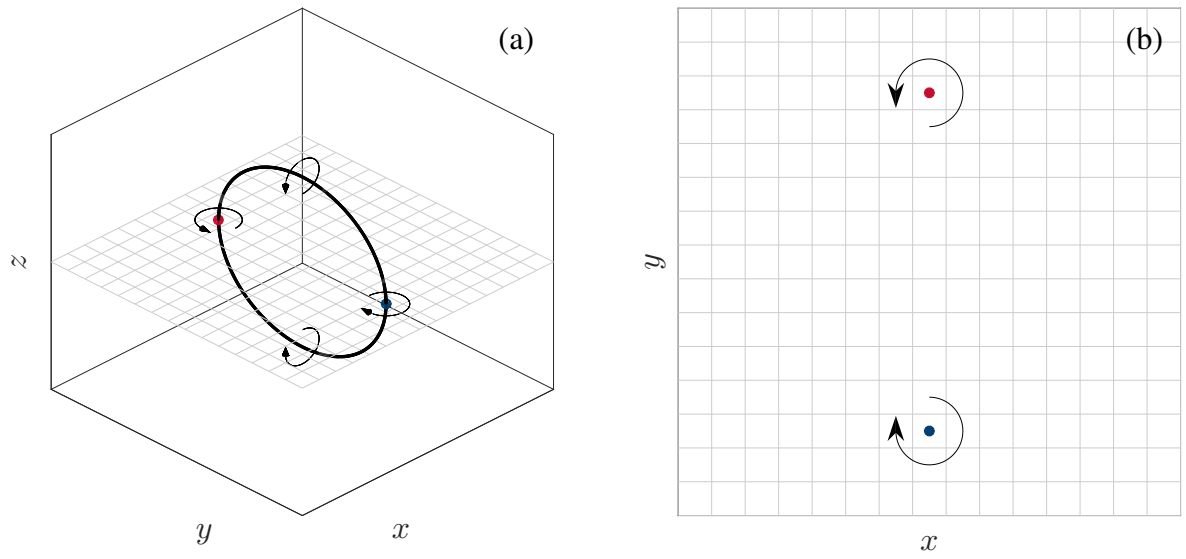

Figure 3.18: Vortex ring in a vortex filament method simulation (a), with direction of flow indicated. Intersection with the xy-plane is shown in (b), cf. Fig. 2.5 (b). The region shown is -0.5 cm $\leq x, y, z \leq 0.5$ cm.

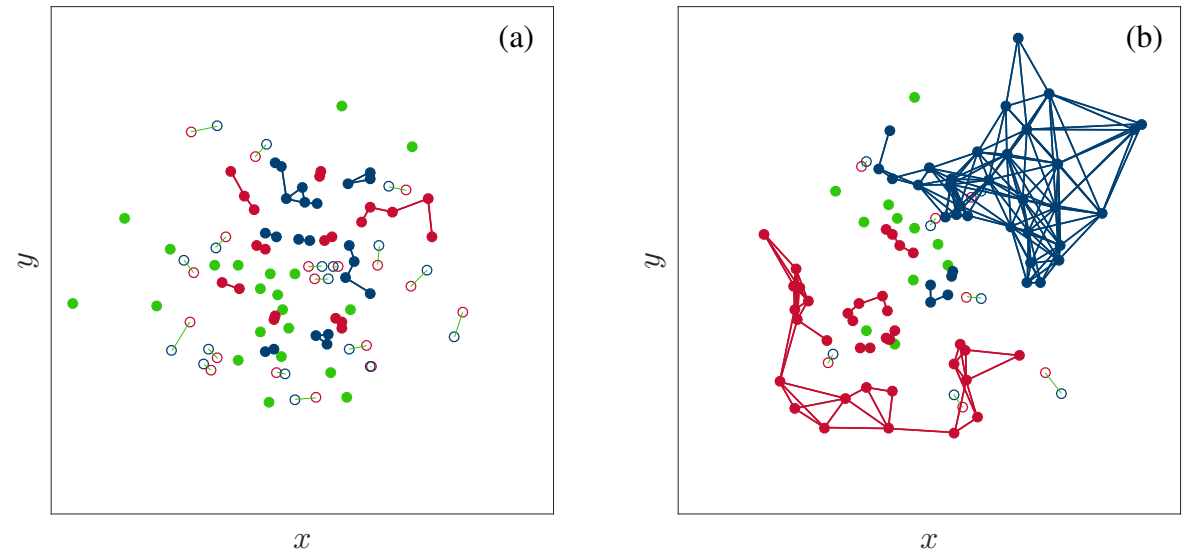

Figure 3.19: Classification of vortices using the recursive clustering algorithm for (a) all vortex positions sampled from the same distribution and (b) positive and negative vortex positions sampled from distributions with different means. Vortices comprising dipoles are shown as hollow discs with a green line indicating their partner. Vortices belonging to clusters are marked with solid discs, with connecting lines indicating direct clustering. Vortices in dipoles or clusters are marked as red for positive circulation and blue for negative circulation. 'Free' vortices are marked with solid green discs.

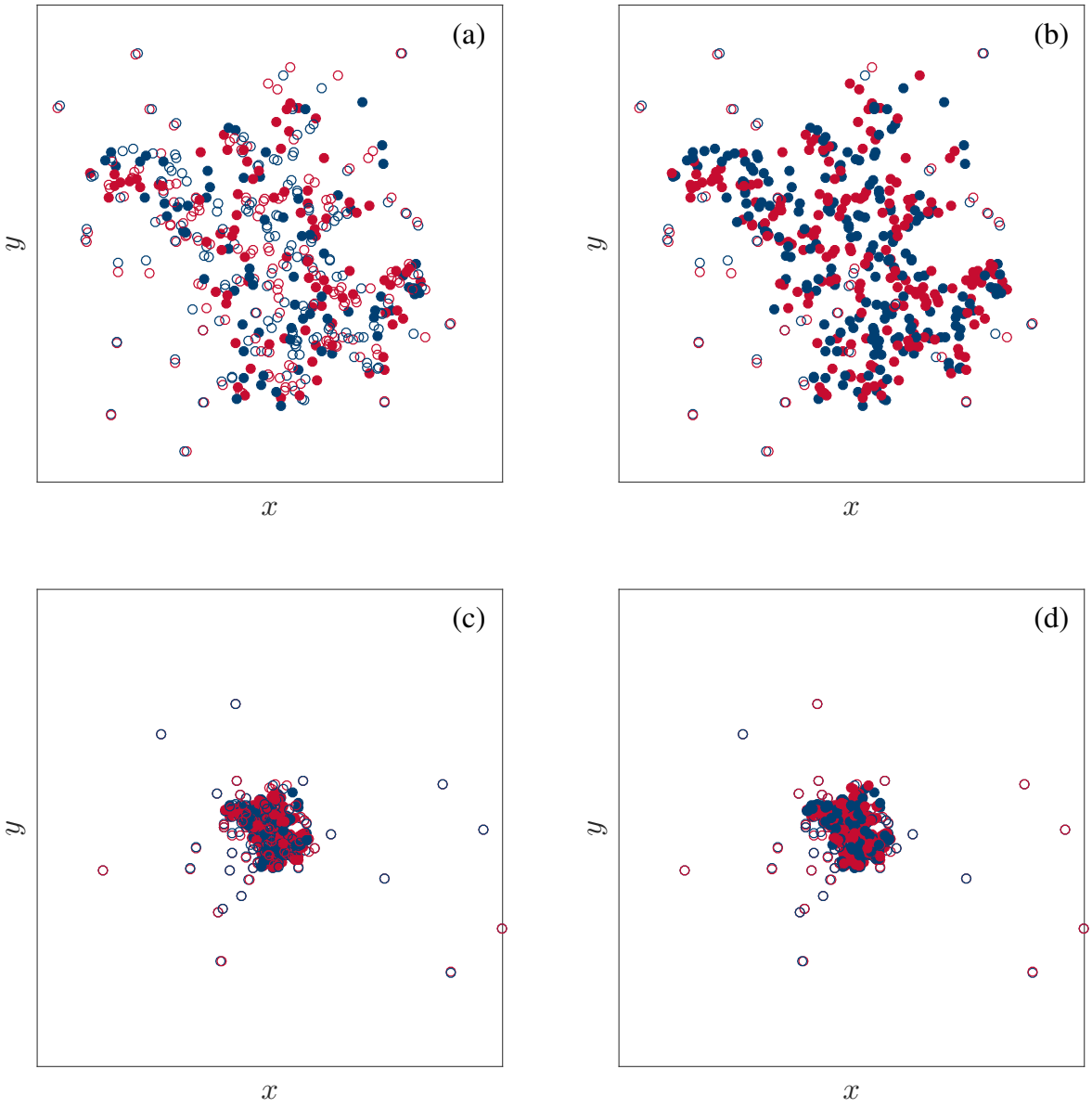

Figure 3.20: Point vortex model simulation showing the identification of dipoles using the first step of the RCA (a), (c), and using the additional requirement of separation from vortices with identical circulation (b), (d). Vortices in dipoles are shown as hollow discs, with all other vortices as solid discs. All panels show the same configuration; panels (a) and (b) highlight the dense central region, while (c) and (d) show the entire configuration. It can be seen in (c) and (d) that both versions correctly identify dipoles far from the central region; however comparing (a) and (b) it is observed that far fewer vortices are classified as dipoles within the central region in the latter.

Chapter 4

2-D Numerical Experiments & Results

We discuss two numerical investigations in this chapter: a study of the spread of quantum vortices in two-dimensional systems, using the point vortex model (PVM) and the Gross-Pitaevskii equation (GPE), and a preliminary investigation into the effect of vortex number density on the statistics of tracer particles, relevant to the use of inert tracer particles suspended in superfluid helium.

4.1 2-D Diffusion

We begin our numerical investigation of the spreading of quantum turbulence into vorticity-free regions by considering systems of reduced dimensionality. The problem is simplified in this context, as 3-D effects including vortex reconnections and Kelvin waves are not present. Moreover, such systems are experimentally relevant to atomic Bose-Einstein condensates, which can be tightly confined in one or more directions to produce quasi-2-D systems (Sec. 2.2.9). The standard model for such systems at zero temperature is the GPE (Sec. 2.2), but we shall also use the PVM (Sec. 2.1) to probe how the presence or absence of boundaries affects the spreading of vortices. As well as enabling infinite domains, this simple model captures the 'skeleton' of quantum vortex dynamics, without much of the associated physics, including vortex-antivortex annihilation and phonon emission, which may help to determine how crucial such physics is to the dynamics we observe.

In 2-D the vorticity transport equation:

$$\frac{D\boldsymbol{\omega}}{Dt} = (\boldsymbol{\omega} \cdot \nabla)\mathbf{u} + \nu\nabla^2\boldsymbol{\omega}$$

reduces to

$$\frac{D\omega_z}{Dt} = \nu\nabla^2\omega_z,$$

analogous to a diffusion equation with diffusion coefficient ν, the kinematic viscosity. It is unclear from this how vorticity is transported in a superfluid with no viscosity. We find that a portion of the vortices spread through a diffusion process, which suggests a possible candidate for the effective viscosity ν' in such systems.

4.1.1 Set-up

We perform two primary sets of simulations, using the PVM in an infinite domain for one, and the GPE in a disc trap for the other. We use an equal number of positive and negative vortices in all simulations, so that the net vorticity is zero.

For the PVM simulations the initial positions of 500 point vortices are sampled from a bivariate normal distribution centred at the origin, with standard deviations $\sigma_0 = \sigma_x = \sigma_y = 20$. This distribution is selected to reflect the Green's function solution of the diffusion equation in 2-D; other initial distributions are observed to tend to normal distributions as the system evolves in time. We impose circulation $\Gamma = 1$ on 250 of the vortices and circulation $\Gamma = -1$ on the remaining 250.

The system is evolved in time by solving the equations of motion for the individual vortices, given in Sec. 2.1, as a system of coupled ODEs, using a 6^{th}-order Runge-Kutta scheme, detailed in Appx. A.6, with a time-step of $\Delta t = 10^{-3}$. We evolve our system through 10^6 time-steps until a final time $t = 10^3$. The energy of a typical simulation, measured through the autonomous Hamiltonian, eq. (2.3), is conserved with relative percent error $100 \times |(H(t) - H(0))/H(0)|\% \approx 3\%$ over the entire simulation, shown in Fig. 3.3. The evolution of an illustrative PVM simulation with a reduced number of vortices is shown in Fig. 4.1.

We use the homogeneous dimensionless formulation of the GPE, eq. (2.25) for the second set of simulations. The condensate wavefunction is discretised on a 2049×2049 grid, with grid spacing $\Delta x = 0.2$. We model a disc-shaped trapping potential as:

$$V = \frac{1}{2} r^2 \left(\frac{r}{180} \right)^{100}, \tag{4.1}$$

giving an effective trap radius of ~ 180. Starting with the Thomas-Fermi profile (Sec. 2.2.11) we find the ground state of the condensate by evolving the wavefunction under the dissipative GPE (DGPE) (Sec. 3.3.3) with strong damping ($\gamma = 0.5$).

We imprint the condensate with 100 vortices, half with circulation 2π and half with circulation -2π, with positions sampled from a bivariate normal distribution, centred about the origin, with $\sigma_0 = \sigma_x = \sigma_y = 20$ - see Sec. 3.3.4 for details of vortex imprinting. We take the resulting wavefunction as our initial condition at $t = 0$. The system is then evolved in time according to eq. (2.25), with spatial derivatives approximated by a 4^{th}-order finite difference scheme detailed in Sec. 3.1.1, marching forward in time by a 4^{th}-order Runge-Kutta scheme detailed in Sec. 3.1.2, with a time-step $\Delta t = 10^{-2}$. We evolve the system through 10^5 time-steps until a final time $t = 10^3$.

In preliminary simulations we observe that vortex dipoles which reach the edge of the condensate split into their constituent vortex and antivortex, which then travel along the edge of the condensate in opposite directions as shown in Fig. 4.2. As the simulation progresses they inevitably encounter a vortex of the opposite circulation travelling in the other direction, and form a new dipole which then travels towards the centre of the condensate. We believe that this reinjection occurs at only the lowest temperatures described

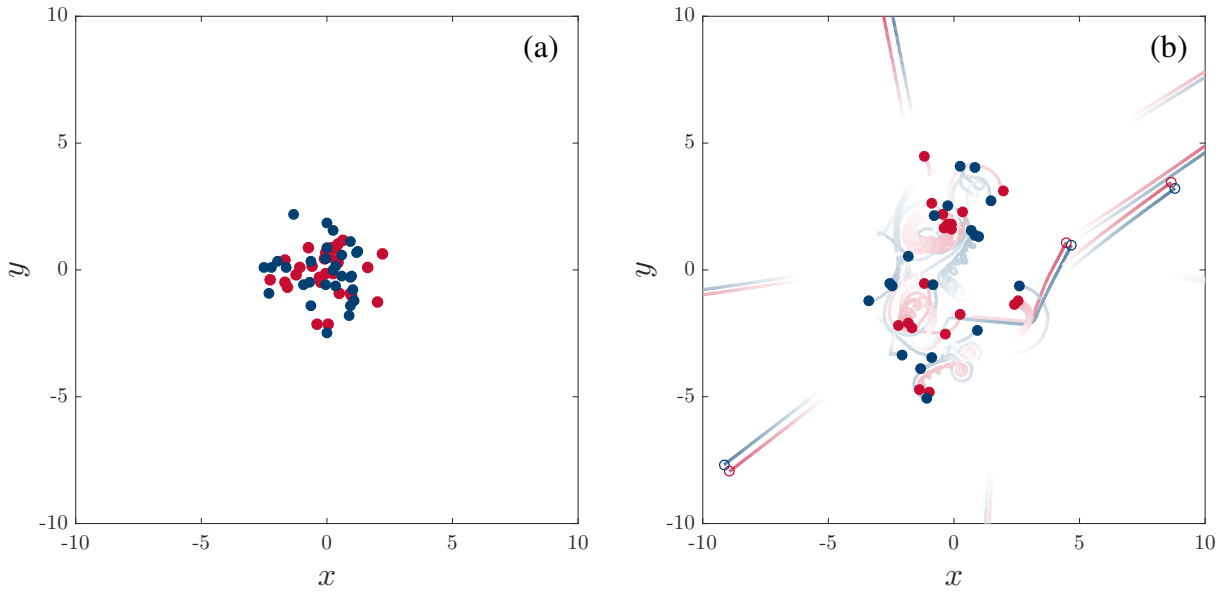

Figure 4.1: [Dimensionless units] Point-vortex simulation (with a low number of vortices for clarity). Snapshots of vortex configurations at $t = 0$ (a) and $t = 20$ (b). The range of the display is for visualisation only; the computational domain is the infinite plane. Vortices and antivortices are marked with solid red discs and solid blue discs respectively. Vortices comprising dipoles are marked with hollow discs. The fading comet tails show vortex trajectories, helping to visually identify vortex dipoles which 'evaporate' from the cluster.

by the GPE, as friction occurs between vortices and the cloud of thermal atoms at finite temperatures. This friction leads to isolated vortices spiralling out of the condensate [266], and vortex dipoles shrinking and mutually annihilating, generating Jones-Roberts solitons in the process [265, 304]. Moreover, it is known that the thermal atoms are concentrated at the boundary of the trap, where the condensate density vanishes [249, 266], and thus we anticipate a region with non-negligible friction close to the boundary.

We model this effect by replacing $i\partial/\partial t$ in eq. (2.25) by $(i-\gamma)\partial/\partial t$, as for the DGPE, but with a radially dependent γ of the form:

$$\gamma(r) = \begin{cases} 0, & \text{if } 0 \leq r < 150. \\ \dfrac{\gamma_c}{2}\left[1 + \tanh\left\{\pi(r'-1)\right\}\right], & \text{if } 150 \leq r < 160, \\ \gamma_c, & \text{otherwise,} \end{cases} \tag{4.2}$$

where $r' = (r - 150)/\beta$, with $\beta = 5$ here, controls the width of the transition from $\gamma = 0$ to $\gamma = \gamma_c$, and $\gamma_c = 0.03$ (as inferred from experiments and typically used in numerical simulations [289, 291]), with the tanh function chosen to provide a smooth transition between regimes, as a discontinuous function may reflect vortices and phonons. We note that this alteration recovers the standard GPE for $r < 150$, so does not inherently modify the dynamics in the main region of the simulations. We illustrate the localised damping profile with the condensate density profile in Fig. 4.3. With this finite temperature modifica-

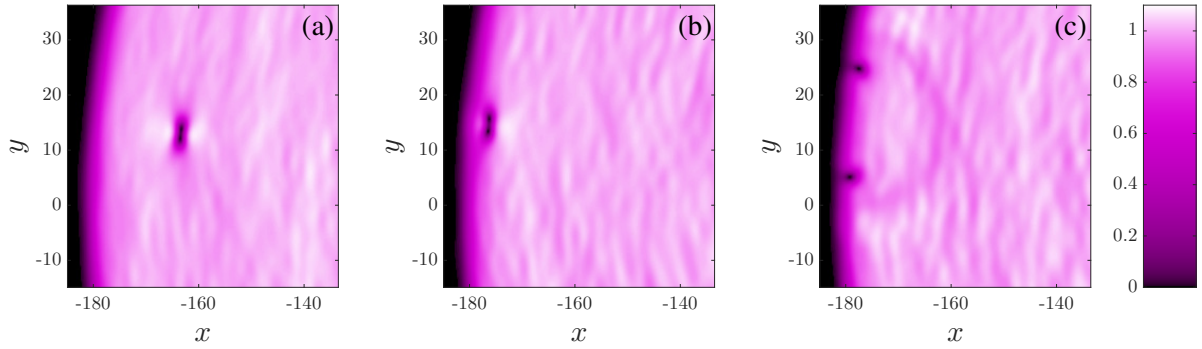

Figure 4.2: [Dimensionless units] GPE simulation in a disc trap without damping. A vortex-antivortex dipole is seen approaching the boundary in (a), meeting the boundary in (b), and the two component vortices travelling in opposite directions along the boundary having separated in (c). Note the nonlinear colour scale used to highlight small density perturbations.

tion we observe that vortex dipoles which reach the edge of the trap annihilate, producing sound waves that propagate back into the condensate bulk, as shown in Fig. 4.4, with minimal effect on the vortex dynamics in the central region.

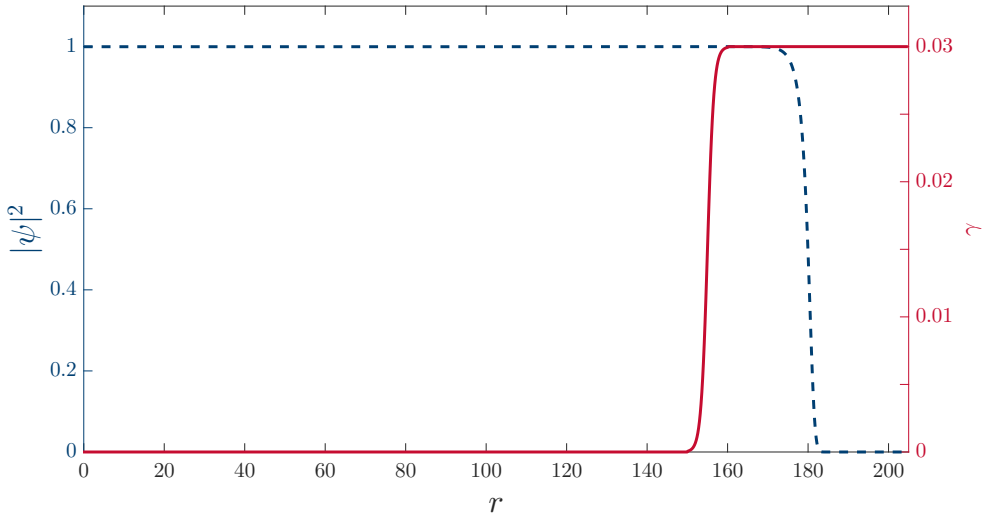

Figure 4.3: [Dimensionless units] GPE simulation in a disc trap with localised damping. Density $|\psi|^2$ (dashed blue line) and phenomenological damping γ (solid red line) are plotted against radius. Note the separate y-axis scales for each line.

The total energy (defined in Sec. 2.2.10) of our systems is typically conserved within 1% over the entire simulation, shown in Fig. 3.16. For comparison we also show the conservation of energy for a single simulation performed with the exact same set-up, but without localised damping. The energy is conserved within 0.05% over this simulation, and we at-

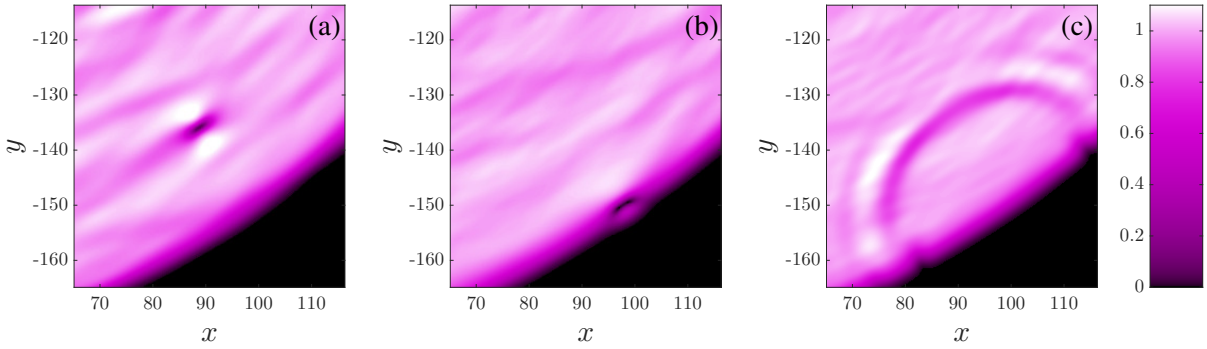

Figure 4.4: [Dimensionless units] GPE simulation in a disc trap with localised phenomenological damping at the edges of the trap as described in the main text. A vortex-antivortex dipole is seen approaching the boundary in (a), meeting the boundary in (b), and having annihilated and emitted a coherent density wave in (c). Note the same nonlinear colour scale as in Fig. 4.2

tribute the majority of the change in energy in our damped simulations to the localised damping, rather than numerical inaccuracy. The evolution of a typical GPE simulation is shown in Fig. 4.5.

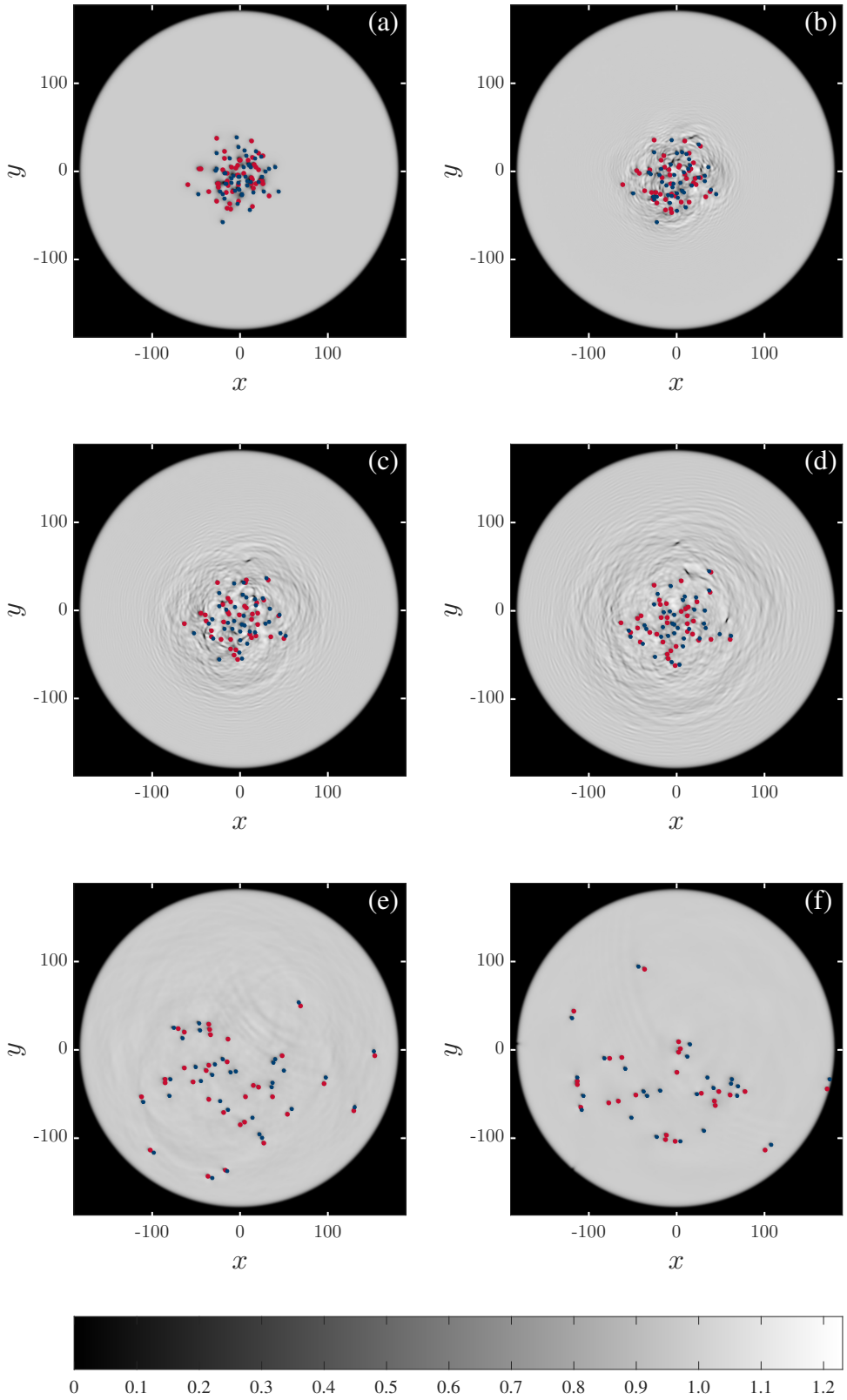

Figure 4.5: [Dimensionless units] GPE simulation (disc trap). Plots of the condensate density $|\psi|^2$ at $t = 0$ (a), $t = 25$ (b), $t = 50$ (c), $t = 75$ (d), $t = 500$ (e) and $t = 1000$ (f). Positive and negative vortices are marked by solid red discs and solid blue discs respectively. Note the sound waves generated by vortices, particularly in panels (b), (c) and (d).

4.1.2 Analysis

We now focus on the dynamics of the vortices in both sets of simulations. Vortices are observed to spread through two processes: the formation and ballistic flight of vortex-antivortex dipoles, and the gradual spread of the remaining vortices. We seek to characterise this second gradual spreading of vortices, so identify dipoles algorithmically (See Sec. 3.4) and remove them from our analysis, having identified the positions and signs of vortices in the GPE simulations using the algorithm discussed in Sec. 3.3.5. The proportion of vortices which form dipoles and which remain unpaired is shown in Fig. 4.6, as well as the proportion of vortices which have annihilated in the GPE simulations. The proportion annihilated is based on losses to the total number of vortices identified, corroborated by visual inspection of the wavefunction's evolution, with some noise due to numerical error in the vortex identification algorithm. We note that a significant proportion remain unpaired until the end of the simulations.

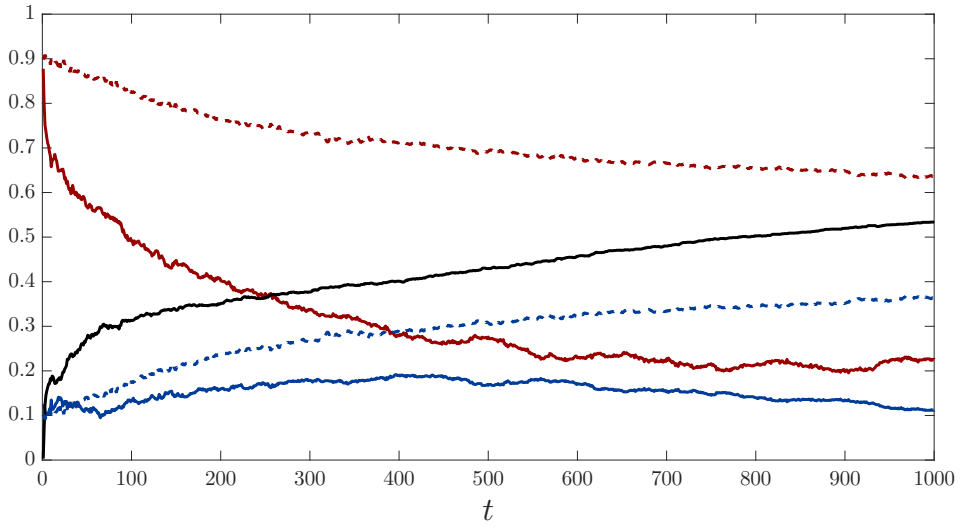

Figure 4.6: [Dimensionless units] PVM (dashed lines) and GPE (solid lines) simulations. Proportion of (initial) vortices which have formed vortex-antivortex dipoles (blue), remained unpaired (red), and annihilated (black) as a function of time, ensemble averaged over 40 PVM simulations and 20 GPE simulations.

We perform 40 PVM simulations and 20 GPE simulations with the set-ups discussed, and analyse the behaviour of the vortices which remain in the main cluster. We calculate the root-mean-square deviation $d_{\mathrm{rms}}(t)$ of vortices from their initial positions:

$$d_{\mathrm{rms}}(t) = \sqrt{\frac{1}{N_0(t)} \sum_{i=1}^{N_0(t)} (x_i(t) - x_i(0))^2 + (y_i(t) - y_i(0))^2}, \tag{4.3}$$

where $N_0(t)$ is the number of vortices in the main cluster at time t. We show the ensemble averaged d_{rms} vs. t in Fig. 4.7. The vortices initially spread with $d_{\mathrm{rms}} \sim t$, followed by $d_{\mathrm{rms}} \sim t^{1/2}$ for large t, typical of diffusion processes [305]. Like with Brownian motion,

where particles follow straight trajectories before colliding with other particles, vortices initially move at approximately constant speed from their starting positions, producing linear (ballistic) spread, until they approach another vortex close enough for its contribution to the velocity field to become dominant, with a large number of such events appearing to mimic a random walk. The observation that the transition from $d_{\mathrm{rms}} \sim t$ to $d_{\mathrm{rms}} \sim t^{1/2}$ occurs when d_{rms} is comparable to the typical intervortex spacing supports this interpretation.

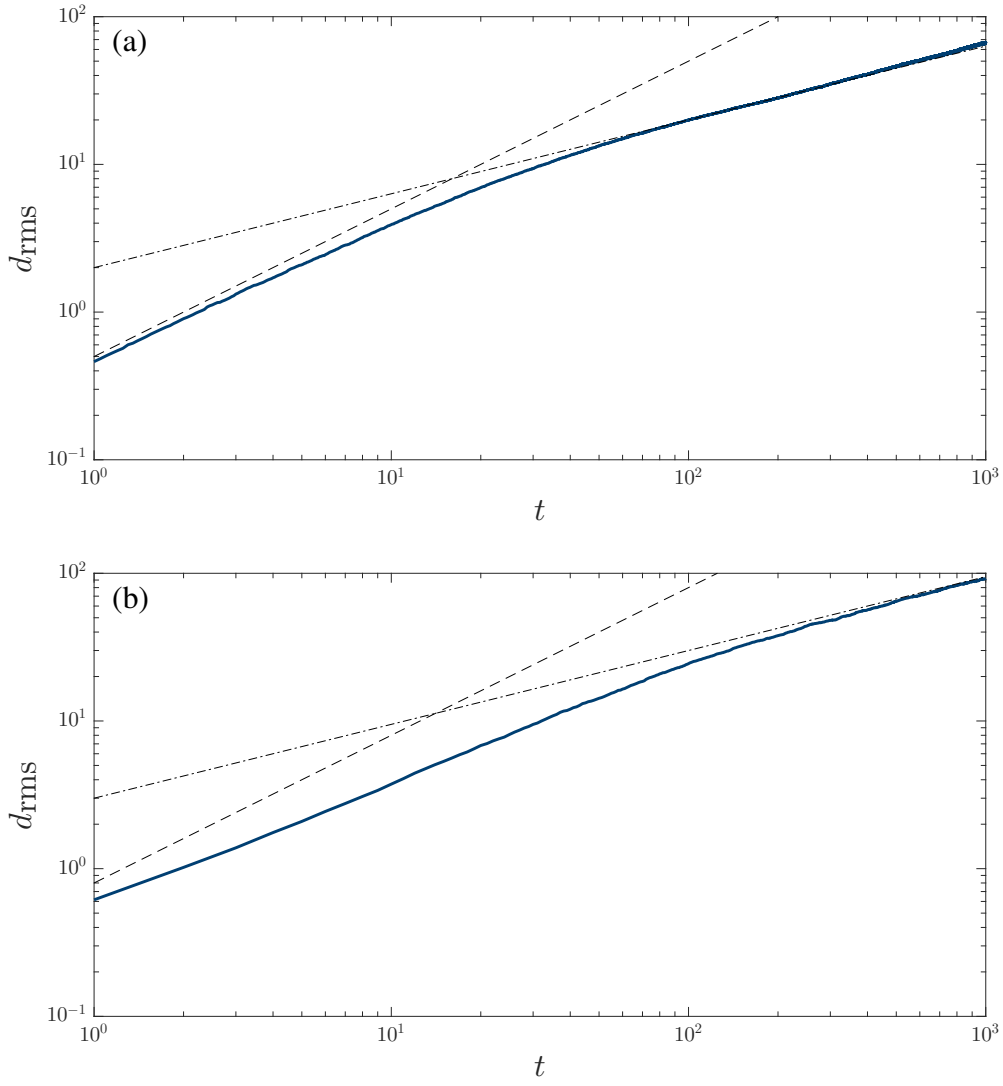

Figure 4.7: [Dimensionless units] PVM simulations (a) and GPE simulations (b). Root mean square deviation of vortices from their initial position, d_{rms}, vs. time, t. Only the vortices which are identified as part of the cluster are used in the calculation of d_{rms}. The dashed and dot-dashed lines correspond to t and $t^{1/2}$ scalings respectively.

For a scalar field $f(x, y, t)$ satisfying the 2-D diffusion equation:

$$\frac{\partial f}{\partial t} = D\nabla^2 f, \tag{4.4}$$

where D is a constant diffusion coefficient, we can relate the root-mean-square deviation d_{rms} of vortices to D by [305]:

$$D = \frac{d_{\text{rms}}^2}{4t}. \tag{4.5}$$

As noted previously, by analogy to the classical vorticity transport equation we can then equate this diffusion coefficient to an effective viscosity ν'. In order to compare results obtained from the PVM simulations with those obtained from GPE simulations, and with results in the literature, it is convenient to express ν' in units of the relevant quantum of circulation: under the PVM $\kappa = |\Gamma| = 1$, while $\kappa = 2\pi$ under the GPE. We show the values of ν' for both sets of simulations in Fig. 4.8.

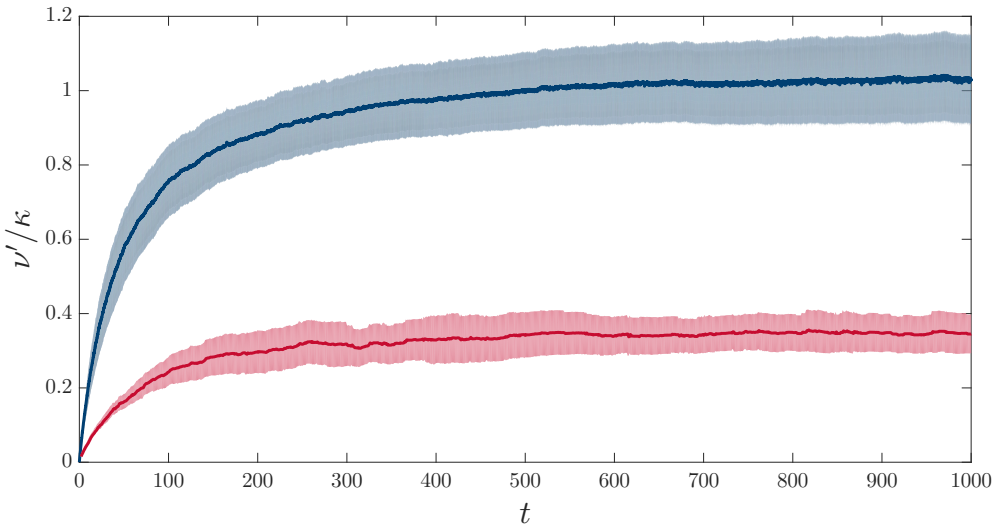

Figure 4.8: [Dimensionless units] Estimated values of ν'/κ from PVM simulations (blue) and GPE simulations (red). Solid lines show the ensemble average, with shaded regions indicating a 95% confidence interval.

We note that, for large t, ν'/κ settles towards a constant value. For the PVM in an infinite domain we find $\nu'/\kappa \approx 1$, a surprising emergent property given that the fluids modelled are inviscid. We find a slightly lower value of $\nu'/\kappa \approx 0.3$ for the GPE simulations in a disc trap, which we shall attempt to reconcile with the PVM result in the next section.

We now examine the initial energy and momenta of our systems, to test whether our initial conditions are representative of similar random configurations.

We generate a large number of initial configurations of vortices drawn from the same bivariate normal distributions as our simulations, 10^4 for the PVM and 10^3 for the GPE (fewer due to the computation time required to prepare the system for the GPE). We then calculate the energy and momenta of our PVM configurations using the associated Hamiltonian and its first integrals (Sec. 2.1), and the energy and momenta of the condensates

as discussed in Sec. 2.2.10. The energy of our GPE systems can be decomposed into interaction energy E_{int} associated with atom-atom interactions, potential energy E_{pot} associated with the external trapping potential, and kinetic energy E_{kin}. The kinetic energy can then be further decomposed into compressible and incompressible components, $E^{\text{c}}_{\text{kin}}$ and $E^{\text{i}}_{\text{kin}}$ respectively. The probability density functions for these quantities are shown in Fig. 4.9 and Fig. 4.10, with histograms of these quantities for the initial conditions of the full simulations for comparison. From visual inspection, the distribution of initial energy and momenta appear to be reasonably representative of the energy and momenta distributions from which they are sampled. The Quantile-Quantile plots in Fig. 4.11 and Fig. 4.12 confirm this: by plotting the quantiles of the two data sets against each other we can determine whether their distributions are comparable. If the samples are identical the data points will fall on the identity line, with systematic deviations from this helping us to identify differences in the samples; for example, in Fig. 4.11(b) the data drops below the identity line at the highest values of L_z, indicating that we undersample initial distributions with the highest angular momentum to an extent. As our data lies close to the identity line, with some noise, and some limited evidence of under/oversampling at the most extreme values for some measured quantities, we are satisfied that the initial configurations used are representative of available configurations.

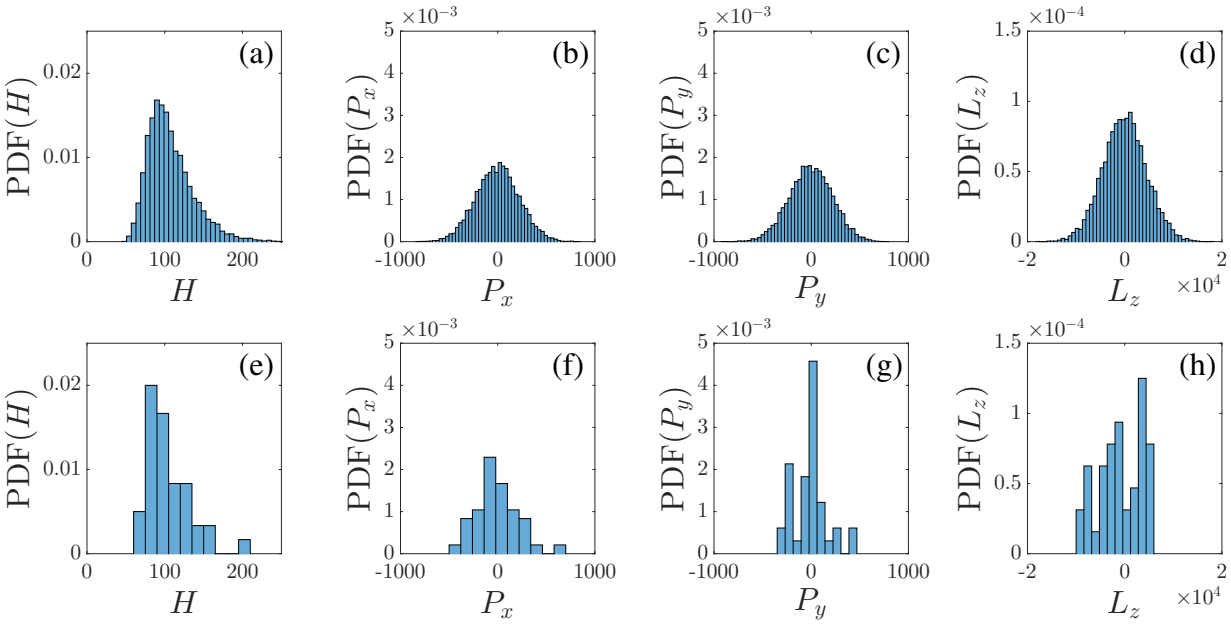

Figure 4.9: [Dimensionless units] PVM simulations. Probability density functions of energy (a,e), linear x-momentum (b,f), linear y-momentum (c,g), and angular momentum (d,h), for a large number of vortex configurations sampled from our chosen bivariate normal distribution (a-d), and for the initial configurations of our full simulations (e-h).)

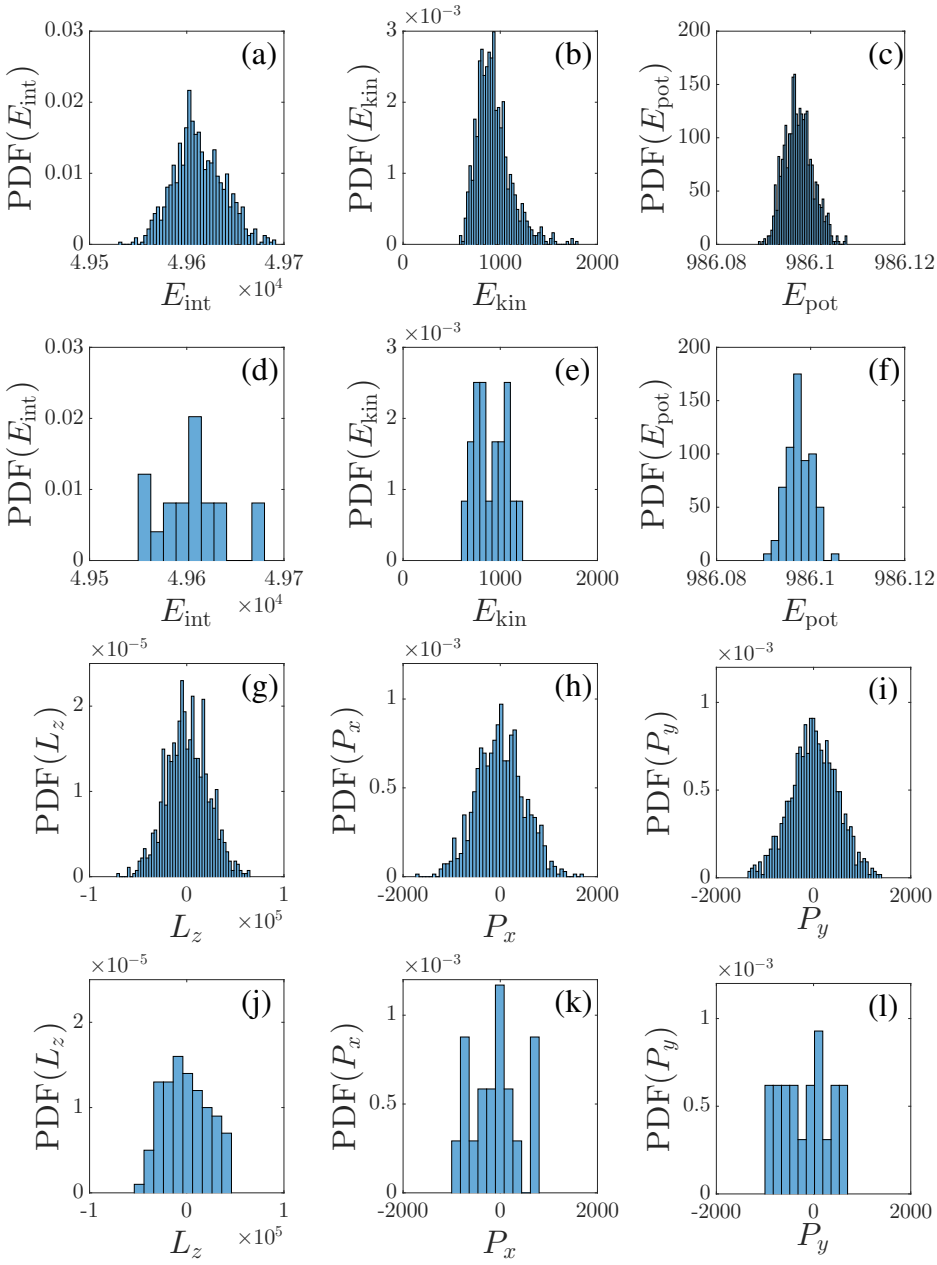

Figure 4.10: [Dimensionless units] GPE simulations. Probability density functions of interaction energy (a,d), kinetic energy (b,e), potential energy (c,f), angular momentum (g,j), linear x-momentum (h,k), and linear y-momentum (i,l), for a large number of condensates with the initial vortex configuration sampled from our chosen bivariate normal distribution (a-c,g-i), and for the initial configurations of our full simulations (d-f,j-l).

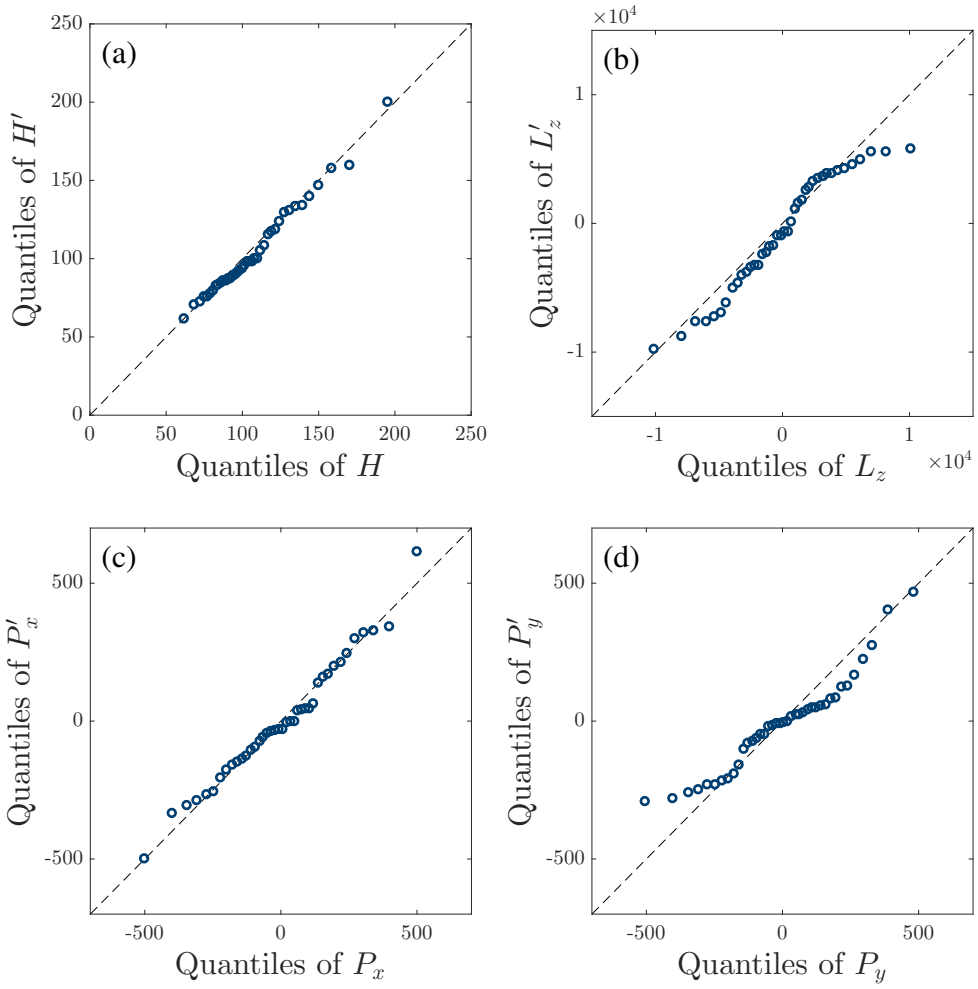

Figure 4.11: [Dimensionless units] PVM simulations. Quantile-Quantile plots comparing the quantiles of energy (a), angular momentum (b), linear x-momentum (c) and linear y-momentum (d) for a large sample of initial distributions (unprimed quantities) with those for the initial configurations of the full simulations (primed quantities).

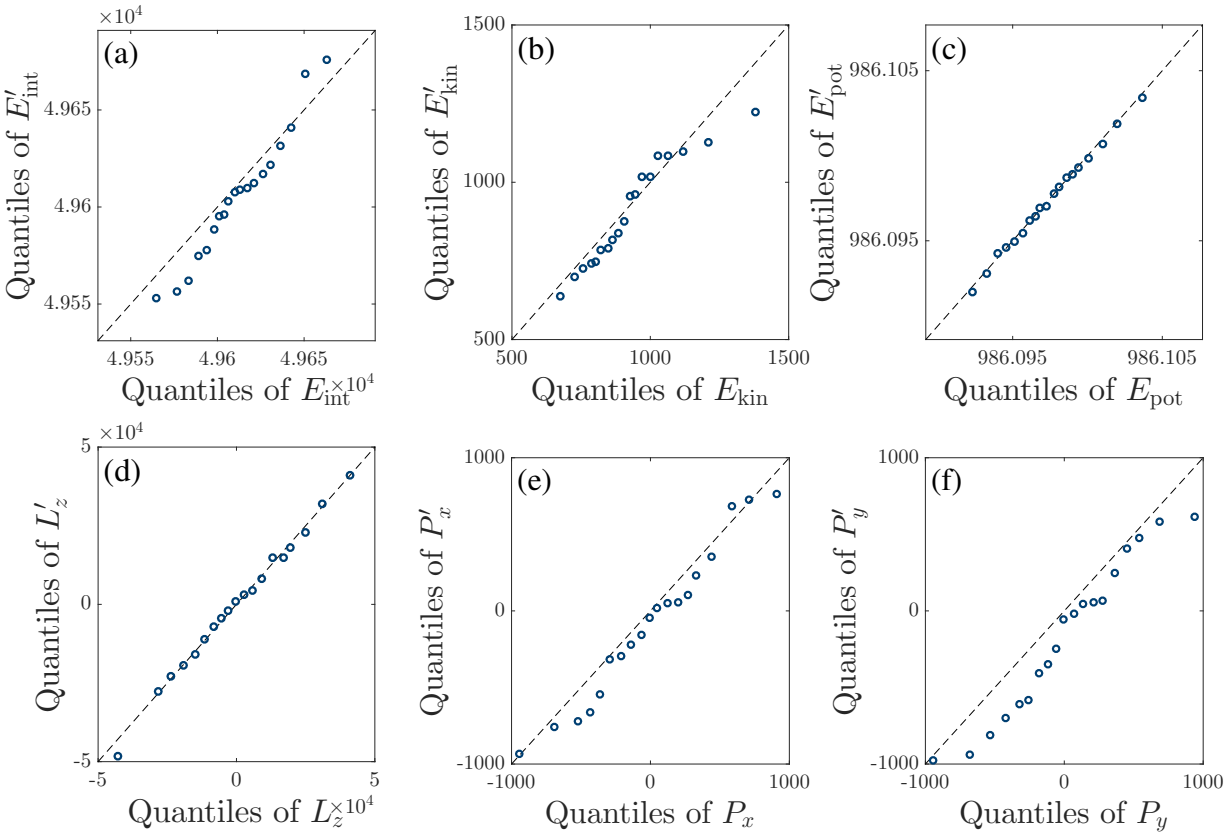

Figure 4.12: [Dimensionless units] GPE simulations. Quantile-Quantile plots comparing the quantiles of interaction energy (a), kinetic energy (b), potential energy (c), angular momentum (d), linear x-momentum (e) and linear y-momentum (f) for a large sample of initial distributions (unprimed quantities) with those for the initial configurations of the full simulations (primed quantities).

We also note that there are extremely improbable (in terms of random sampling), but possible, configurations with extremely low and extremely high energies, where vortices are all in tight dipoles in the low energy case, and separated by sign into two large vortex clusters in the high energy case [26, 306]. Although our simulations are initialised far from these regimes, such clusters, known as Onsager vortices [307] are known to develop in steep trapping potentials [264]. We do not expect this to affect our analysis, as we start with a localised region of vorticity which must explore a large proportion of the system in order to form such clusters; the $d_{\rm rms}$ would saturate in such a scenario as there is a clear maximum posible deviation set by the effective trap radius, and we observe no such saturation by the end of our simulations (Fig. 4.7 (b)). Nevertheless, we track the dipole moment:

$$d = \sum_{i=1}^{N} q_i \mathbf{r}_i, \tag{4.6}$$

where N is the number of vortices, $q_i = s_i\kappa$ the charge of the $i^{\rm th}$ vortex, with $s_i = 1$ for vortices and $s_i = -1$ for antivortices, $\kappa = 2\pi$ is the quantum of circulation, and $\mathbf{r}_i$ the position of the $i^{\rm th}$ vortex. This is then normalised by the radius of the trap, the quantum of

circulation, and the number of vortices. The evolution of d is shown in Fig. 4.13 (a). The value of d is smaller than that observed in simulations of the formation of Onsager vortices [307], where values approaching 1 are found. However, d grows in every realisation, hinting that such a state may eventually be reached if these simulations were continued. We also show, in Fig. 4.13 (b), the final vortex configuration for the simulation which attains the largest value of d, noting that the configuration appears to have drifted in the direction expected from the large-scale clusters, in contrast with the isotropic spread typically seen (cf. Fig. 4.5 (f)).

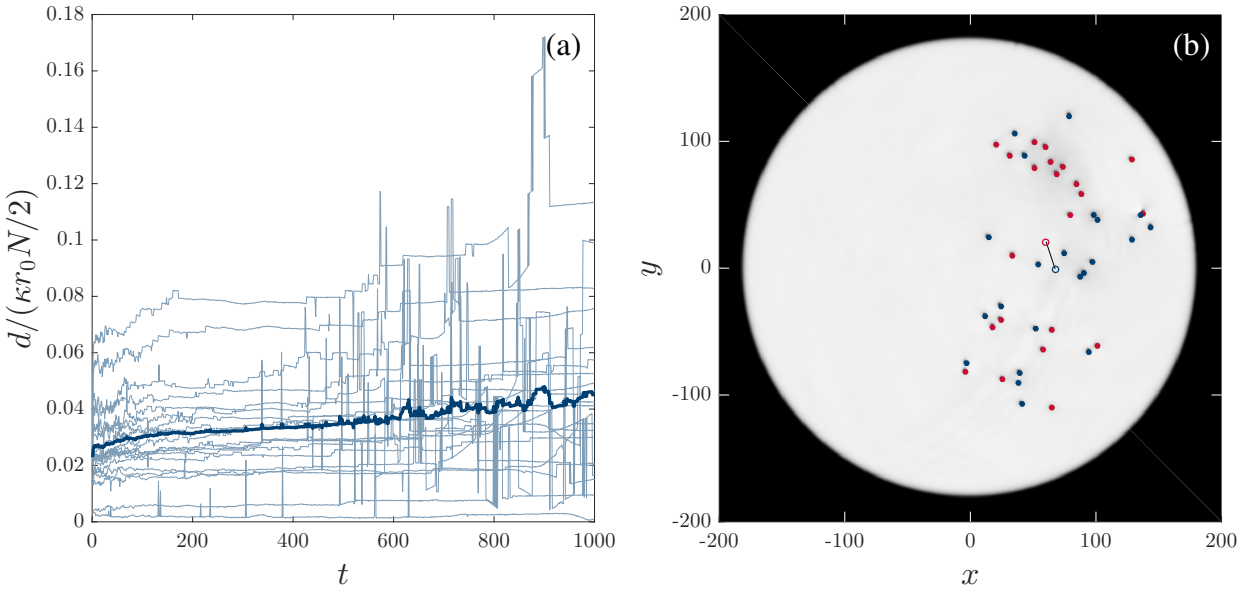

Figure 4.13: [Dimensionless units] GPE simulations. Evolution of the dipole moment, normalised by the number of vortices N, the effective trap radius r_0, and the quantum of circulation κ (a), for individual simulations (light blue lines) and ensemble average (thick blue line). The condensate density for the final time of the simulation with the highest dipole moment is shown in (b), with vortices and antivortices marked in red and blue respectively, and the dipole moment indicated by a black line, with the centroids of vortices and antivortices marked by hollow red and blue discs.

4.1.3 Reconciling Models

In the related 3-D context of diffusing vortex filaments in He II, Tsubota *et al.* give an argument for the scale of the diffusion coefficient on dimensional grounds [194], which is also applicable to these simulations. The only relevant length scale for the vortex motion is the average intervortex distance $L = \ell$, and the only relevant velocity scale is then $V = \kappa/\ell$, with time scales then set by these. The dimensions of the diffusion coefficient are $[D] = L^2T^{-1}$, which can only be constructed from $L \times V = \kappa$, suggesting that ν' should be on the scale of the quantum of circulation κ. Our estimated value of ν' from PVM simulations is in good agreement with this, while our estimated value from GPE simulations

is somewhat lower. There are several differences between the models which may contribute to this difference: the GPE is a confined system, while the PVM is unbounded, the circulation is different between the two models, the initial density of vortices differs, and the GPE contains physics beyond that of the PVM, most prominently vortex-antivortex annihilation and sound.

We first address the effect of the circulation on the dynamics. Scaling $\Gamma \to c\Gamma$ in eq. (2.1), the equations of motion for the PVM, results in $\mathbf{v} \to c\mathbf{v}$, which can be interpreted as scaling time $t \to t/c$, resulting in $\nu' \to c\nu'$; in other words we expect ν'/κ to be independent of the quantum of circulation. We verify this with three sets of PVM simulations for different values of Γ, with the collapse of ν' onto a single curve under this scaling shown in Fig. 4.14.

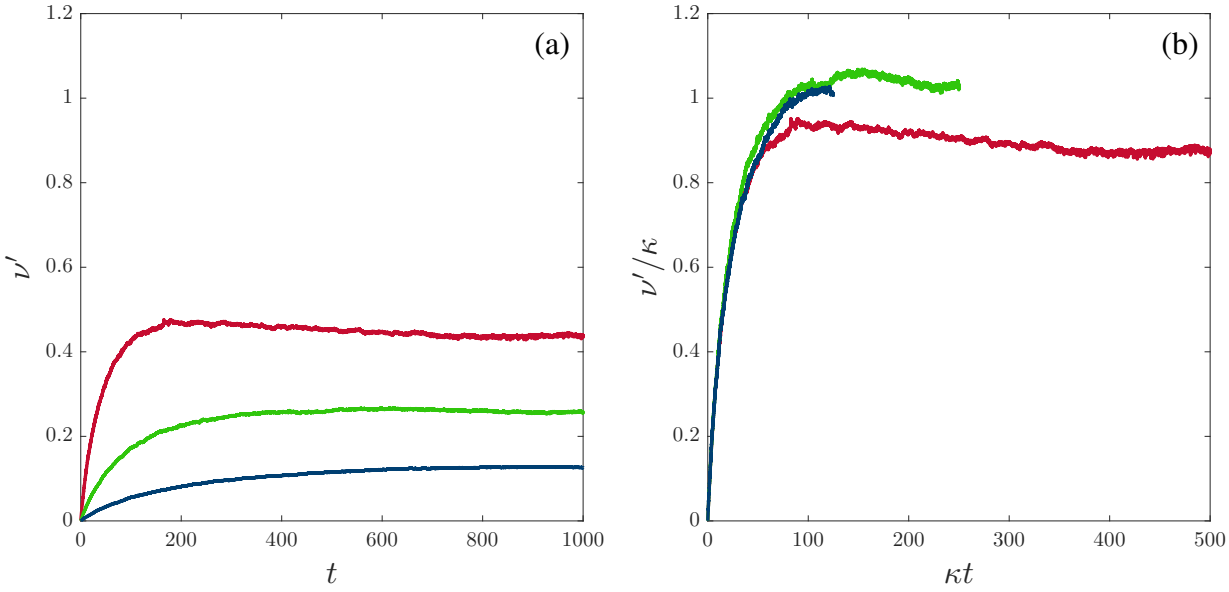

Figure 4.14: [Dimensionless units] Effective viscosity estimates from PVM simulations with $|\Gamma| = 1/2$ (red), $|\Gamma| = 1/4$ (green), and $|\Gamma| = 1/8$ (blue). Panel (a) shows the raw estimates, while panel (b) shows the collapse of curves given by rescaling $\nu' \to \nu'/\kappa$, $t \to \kappa t$.

We now consider boundary effects. We incorporate a circular boundary into the PVM using the method of images (Sec. 2.1.1), and vary the radius of the boundary wall. To facilitate comparison with the GPE, we now use 100 point vortices with circulation $\pm 2\pi$, drawn from the same initial distribution as the GPE simulations. We also remove vortices which approach the boundary to mimic the localised damping in the GPE simulations. In Fig. 4.15 (a) we show the value of ν'/κ found as we vary the trap radius; it is clear that tight confinement suppresses the diffusion of the vortices. We also consider the initial number density of vortices in an infinite domain, calculated as N/A_0, where $A_0 = \pi\sigma_0^2$, with the value of ν'/κ found as we vary N/A_0 shown in Fig. 4.15 (b). We observe that ν'/κ increases with N/A_0, until $N/A_0 \approx 1$, at which point it saturates at $\nu'/\kappa \approx 1$. We interpret this as a low density resulting in too few 'collisions' between vortices for the full diffusive

behaviour to emerge. The confinement and reduced vortex number in the GPE simulations seems to account for the majority of the suppressed value of ν'/κ found.

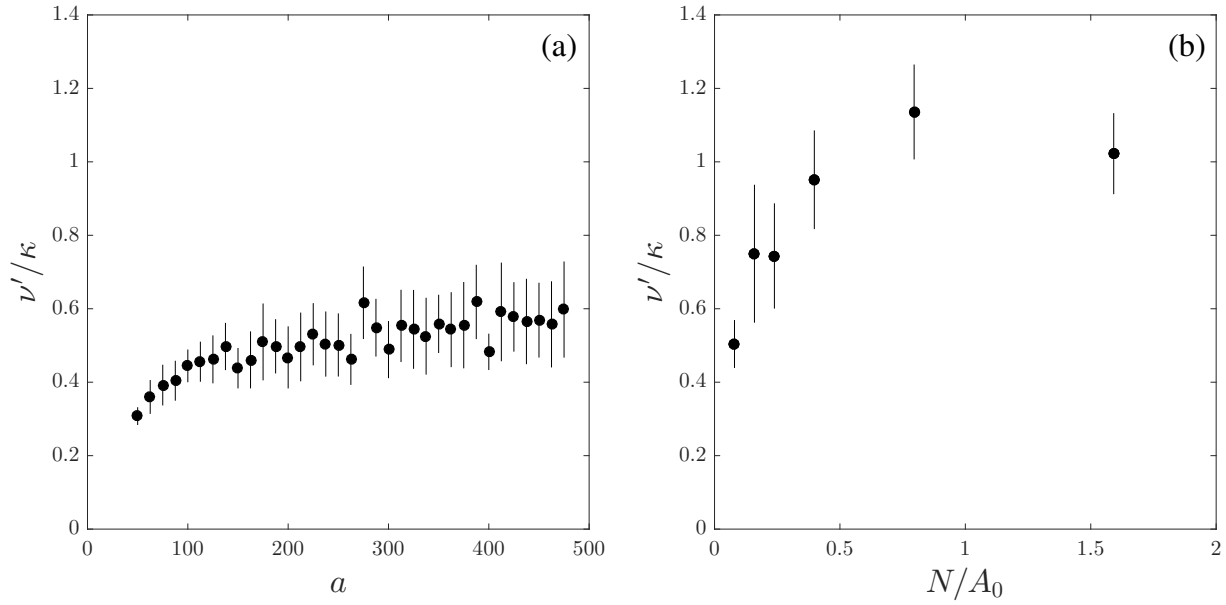

Figure 4.15: [Dimensionless units] PVM simulations. In panel (a) we show the value of ν'/κ found from simulations within a disc of radius a, as a function of a. In panel (b) we show the value of ν'/κ found as a function of the initial vortex density, as defined in the main text, in an infinite plane. The first point in panel (b) corresponds to the initial vortex density in panel (a).

4.1.4 Discussion

We simulate the evolution of a localised region of vortices in a system relevant to 2-D atomic condensates. The vortices are observed to spread through two processes: the formation and ballistic flight of vortex-antivortex dipoles, and the gradual spread of the remaining vortices. Vortices that reach the boundary under the GPE travel along the boundary until they meet a vortex of the opposite sign travelling in the opposite direction, whereupon they re-enter the central region of the disc as a dipole. A small amount of damping, expected from residual thermalised atoms at the edge condensate, mitigates this effects, with vortices instead annihilating at the boundary and producing a density wave. Calculating d_{rms} of the vortices in the remaining central cluster, we find that, after an initial ballistic period interpreted as the time taken for vortices to 'collide', $d_{\mathrm{rms}} \sim t^{1/2}$, consistent with a diffusion process. We calculate the diffusion coefficient of this process, finding $D \approx \kappa$ for the PVM, and a slightly lower value for the GPE. Recalling the vorticity transport equation in classical fluids we interpret this as an effective viscosity, with $\nu'/\kappa \approx 1$.

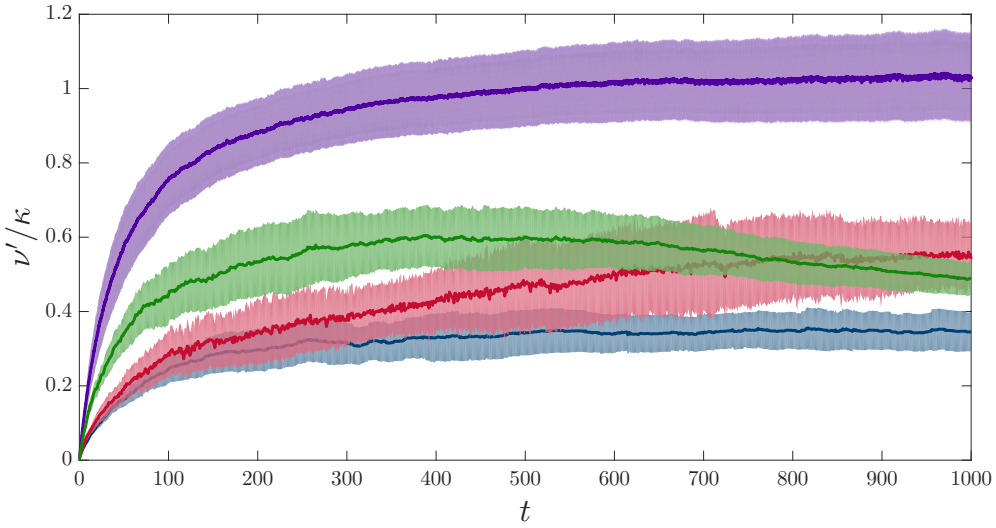

Figure 4.16: [Dimensionless units] Effective viscosity in units of the quantum of circulation ν'/κ for PVM simulations in an infinite domain (purple), PVM in a disc (green), GPE simulations in a disc trap with damping near boundaries (blue), and GPE in a square box trap (red). The 95% confidence intervals are indicated by the shaded regions.

We find that, separately, reducing the initial vortex density, and imposing circular boundaries, both suppress the values of ν'/κ found under the PVM, suggesting that the additional physics included in the GPE is not the origin of the lower values found under it. In Fig. 4.16 we compare values of ν'/κ for various sets of simulations. We note that similar suppression is also observed in square well potentials. The evaporation of dipoles and the spread of the remaining cluster should be observable in experiments at sufficiently low temperatures. The values that we find for ν'/κ are higher than, but not incompatible with, those found in other estimates of the effective viscosity based on the related problem of the decay of quantum turbulence in helium [160]. We extend this investigation into 3-D in this related context of superfluid helium in Sec. 7.3.

4.2 Particle Trajectories & Vortex Configuration

Recent advances in the use of tracer particles in helium [24, 308] have introduced the possibility of directly visualising the motion of the normal fluid and superfluid components [25, 211, 212]. As well as offering an insight into the microscopic vortex dynamics, these techniques could provide new means of accessing the collective properties of flows. In this section we present some preliminary work investigating the potential to infer the vortex line density (VLD), which is usually measured by the attenuation of second sound [309], from the motion of inert tracer particles.

We perform 10 simulations under the PVM in a 20×20 periodic domain, with between 10 and 100 vortices, half with positive and half with negative circulation. We also simulate 500 inert tracer particles, which simply move with the local velocity field generated by the

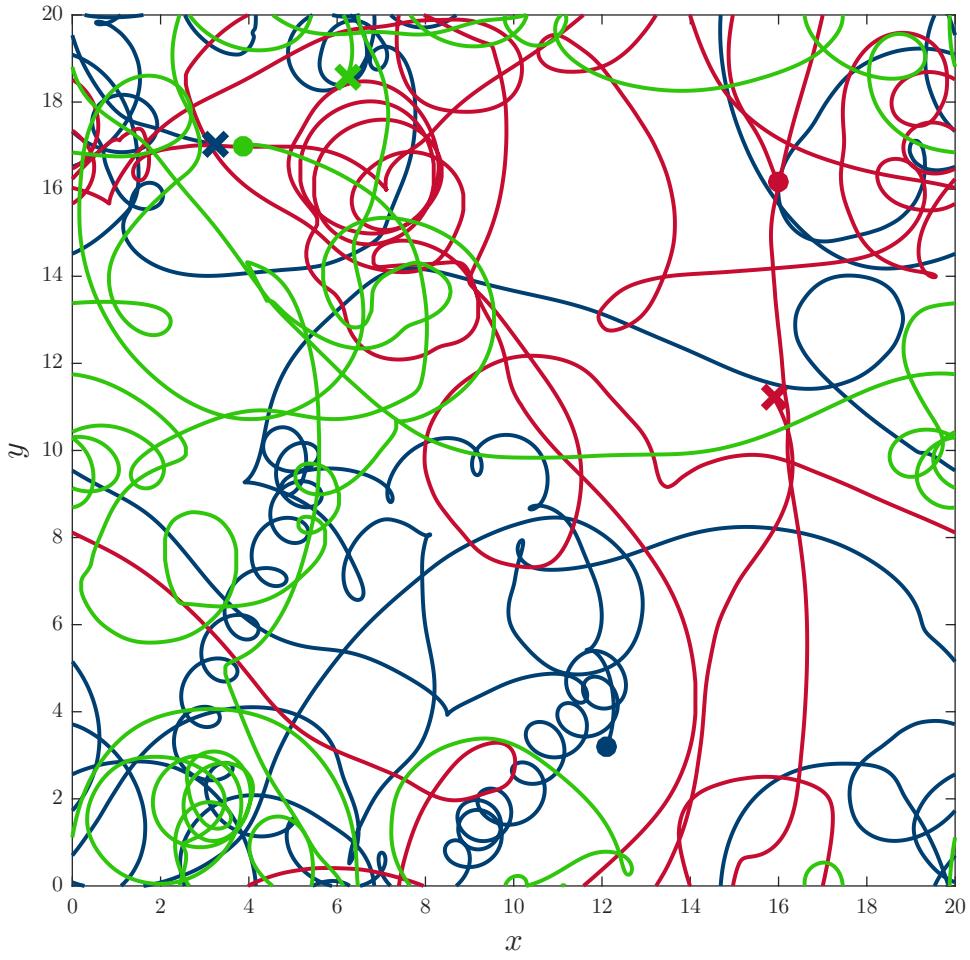

Figure 4.17: [Dimensionless units] Trajectories of three tracer particles from one simulation with 50 point vortices. The initial and final positions of the tracer particles are respectively indicated by crosses and discs.

vortices. The velocity is calculated using the Ewald summation introduced in Sec. 3.2.2, and the system is evolved in time using a 4^{th}-order Runge-Kutta scheme with a time-step $\Delta t = 10^{-3}$. A selection of typical particle trajectories are shown in Fig. 4.17. We then summarise the motion of the tracer particles by their speed c, magnitude of acceleration a, and curvature R, calculated as:

$$R = \sqrt{(\nabla^2 \mathbf{x}) \cdot (\nabla^2 \mathbf{x})}. \tag{4.7}$$

The distribution of these quantities for some vortex densities is shown in Fig. 4.18. We then summarise these distributions by their estimated mode, mean, and maximum probability, which we plot in relation to the number of vortices N in Fig. 4.19. The distribution of c and a appear to be clearly related to the number of vortices, while the relation with the distribution of curvature is somewhat less clear. As the velocity is the simplest of these quantities to calculate, this would seem to be the natural place to commence any experimental investigation.

As preliminary work there are caveats, as well as clear possible future extensions to this work. This investigation was only performed in 2-D, and the extension to 3-D to match realistic systems, which could be achieved with the vortex filament method discussed in Sec. 5.1, is of primary importance. Different forms of turbulence have been observed in superfluids [173], how does the distinction between quasiclassical and ultraquantum regimes modify the relation observed? How sensitive are the predictions to noise?

This concludes the two-dimensional studies in this work, with the study of spreading vorticity to be extended to three dimensions in a later chapter. In order to do this and perform other numerical investigations of three-dimensional quantum turbulence we now introduce the model of vortices in helium that we shall use.

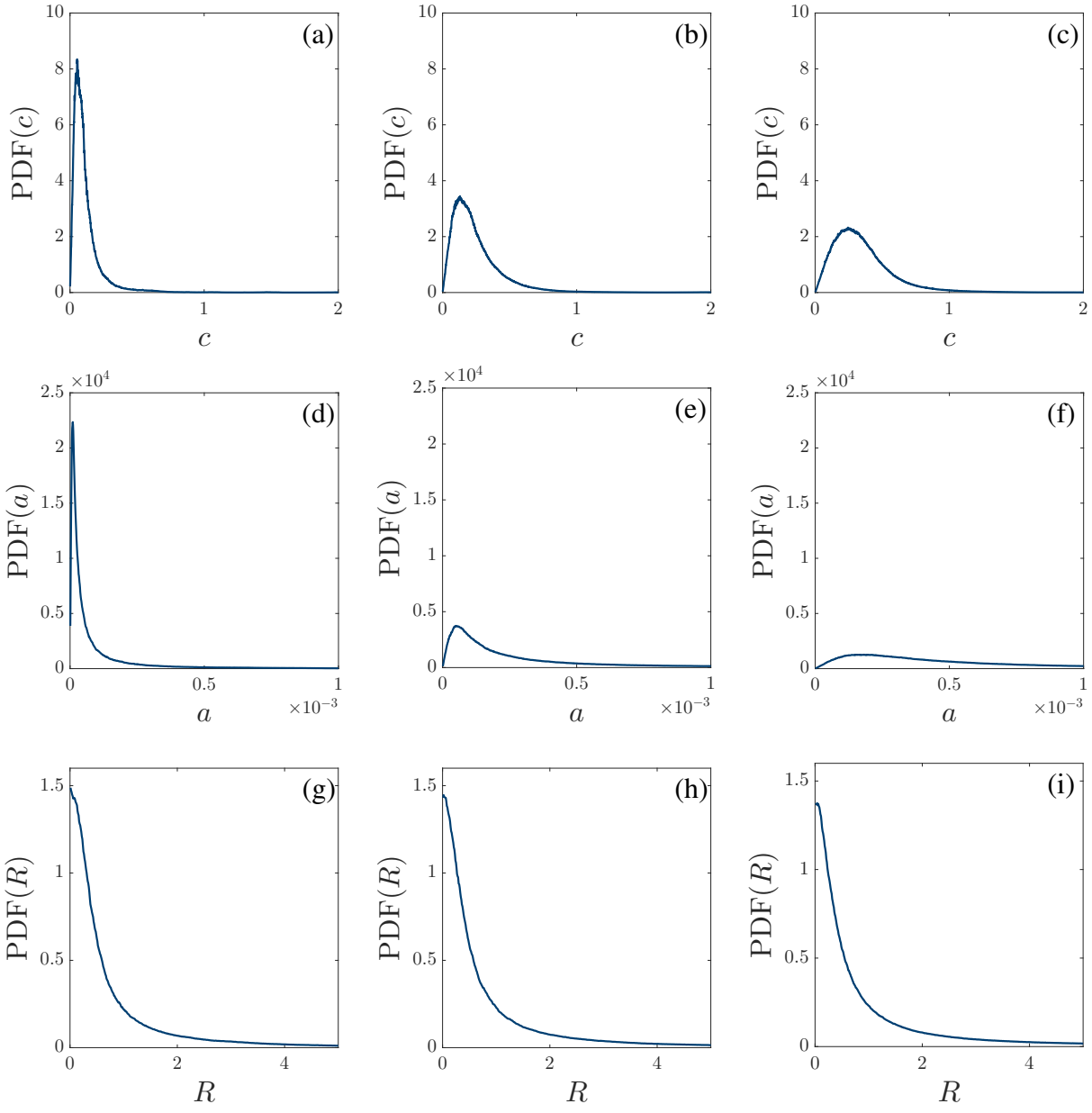

Figure 4.18: [Dimensionless units] Probability density function, for all tracer particles over all times, of speed (a-c), magnitude of acceleration (d-f), and curvature (g-i), for PVM simulations with 20 (a,d,g), 50 (b,e,h), and 100 (c,f,i) point vortices.

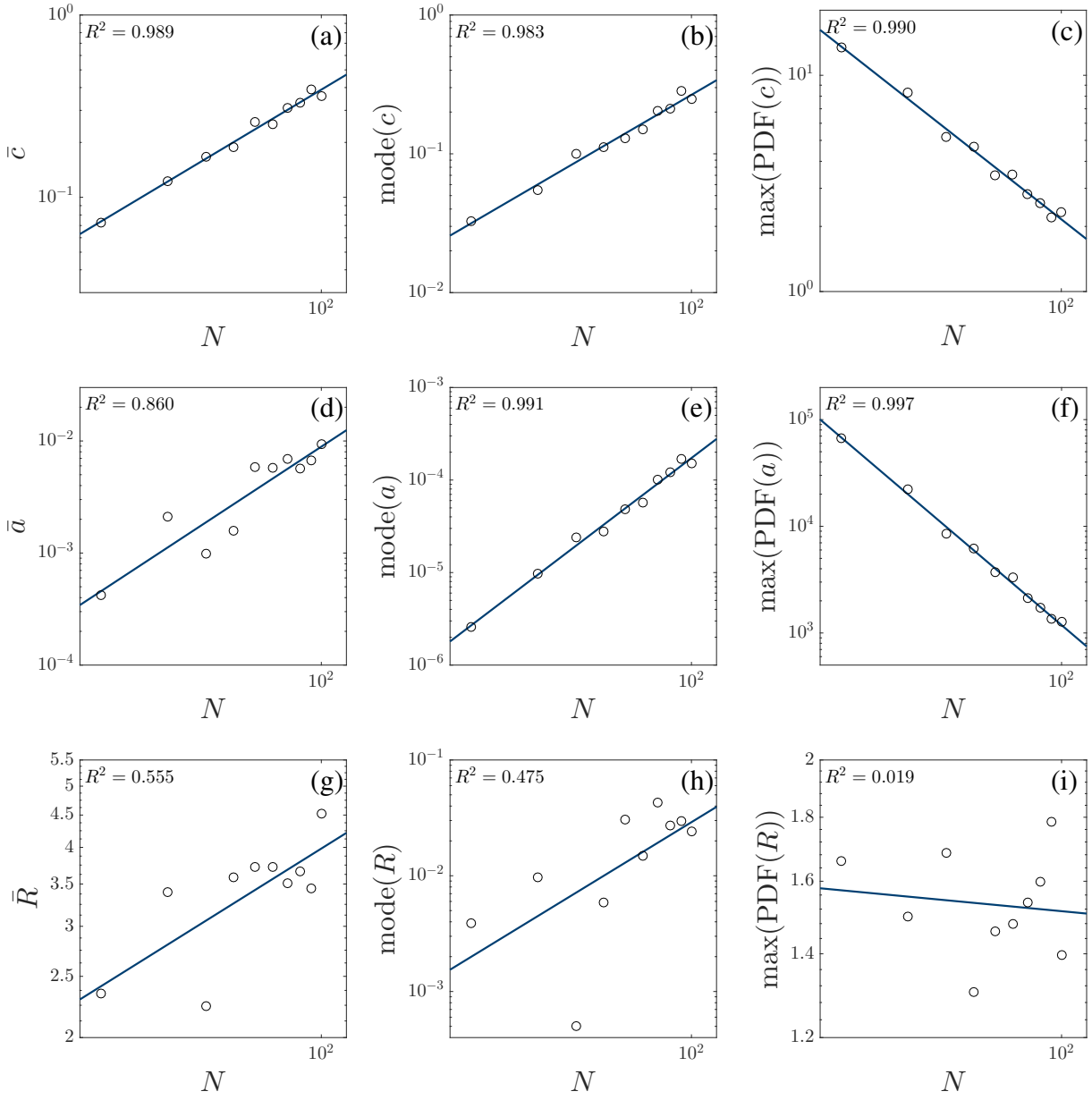

Figure 4.19: [Dimensionless units] Mean (a,d,g), mode (b,e,h), and maximum (c,f,i) of the distributions of speed (a-c), magnitude of acceleration (d-f), and curvature (g-i) of tracer particles vs. number of vortices, with linear regression to identify power laws, and coeffient of determination R^2.

Chapter 5

3-D Models

We describe the 3-D models which we use in the context of superfluid helium. There are a number of popular models of helium II in various contexts. In the zero temperature limit the superfluid component can be modelled phenomenologically by the GPE, as described in Sec. 2.2. At finite temperatures both fluids can be modelled using a hydrodynamic approach: the Hall-Vinen-Bekarevich-Khalatnikov (HVBK) equations [22, 310, 311] describe the evolution of the normal fluid by a Navier-Stokes-like equation, and the evolution of the superfluid by an Euler-like equation with the components coupled through a mutual friction term, thus:

$$\frac{D\mathbf{v}_\mathrm{n}}{Dt} = -\frac{\nabla P_\mathrm{n}}{\rho_\mathrm{n}} + \frac{\rho_\mathrm{s}}{\rho}\mathbf{F}_\mathrm{ns} + \nu\nabla^2\mathbf{v}_\mathrm{n} + \mathbf{F}_\mathrm{n}^\mathrm{ext},$$

$$\frac{D\mathbf{v}_\mathrm{s}}{Dt} = -\frac{\nabla P_s}{\rho_\mathrm{s}} - \frac{\rho_\mathrm{n}}{\rho}\mathbf{F}_\mathrm{ns} + \mathbf{F}_\mathrm{s}^\mathrm{ext}, \tag{5.1}$$

where P_n and P_s are the partial pressures of the normal and superfluid components, $\mathbf{F}_\mathrm{ns}$ is a mutual friction force, and $\mathbf{F}_\mathrm{n}^\mathrm{ext}$ and $\mathbf{F}_\mathrm{s}^\mathrm{ext}$ are external body forces. Then, the vortex filament method (VFM) describes the evolution of the quantised vortex lines embedded in the superfluid. This is a classical model, analogous to the point vortex approximation in 2-D, with the approximation of vortex filaments by infinitesimal lines justified by the small vortex core radius ($\sim 10^{-8}$ cm in ^{4}He at 0 K [312]) in comparison to the length scales typically relevant in simulations; the smallest length scales we resolve in our simulations are $\sim 10^{-4}$ cm. Additional physics relating to the normal fluid and finite temperature can be incorporated in the VFM by introducing a mutual friction correction.

In this work we use the VFM: we are interested in the emergent statistical properties of quantum turbulence in helium II, and so need to model the individual vortex lines, which the macroscopic HVBK-equations are not suitable for. Although the GPE captures the microscopic physics of the vortex filaments, we do not need to access the internal structure of them and would need huge computational power to simulate unneccessary details.

5.1 The Vortex Filament Method

The VFM treats vortex filaments embedded in the superfluid component of helium II as line defects, with a phase change of 2π around the core. All such vortices must either form closed loops or terminate at boundaries. The filaments are modelled as infinitesimal lines, although the core size does play a role in the dynamics. The velocity induced by the vortices, $\mathbf{v}_\mathrm{i}$, is then determined by the configuration of vortex filaments, defined by a set of parametric curves $\mathbf{s} = \mathbf{s}(\xi, t)$, and calculated using the Biot-Savart law [313]:

$$\mathbf{v}_\mathrm{i}(\mathbf{r}, t) = \frac{\kappa}{4\pi} \oint_{\mathcal{L}} \frac{(\mathbf{s} - \mathbf{r}) \times d\mathbf{s}}{|\mathbf{s} - \mathbf{r}|^3}, \tag{5.2}$$

where the integration is performed over all vortex lines, $\mathcal{L}$, and $\kappa = h/m$ is the quantum of circulation, with $\kappa = 9.97 \times 10^{-4}$ cm^2·s^{-1} for ^{4}He. A derivation is given in Appx. A.3. The mass of the core is negligible due to the small core size, and so the vortices move with the local superfluid velocity, so for the vortex filaments themselves we have:

$$\mathbf{v}_\mathrm{i}(\mathbf{s}, t) = \frac{\kappa}{4\pi} \oint_{\mathcal{L}} \frac{(\mathbf{s}_1 - \mathbf{s}) \times d\mathbf{s}_1}{|\mathbf{s}_1 - \mathbf{s}|^3}, \tag{5.3}$$

where $\mathbf{s}_1$ is a dummy variable. We discuss the handling of the singularity as $\mathbf{s} \to \mathbf{s}_1$ in Sec. 6.1.1. In Fig. 5.1 we show some flow patterns induced by simple vortex filament configurations.

Reconnections of vortex lines have been observed, both experimentally [25, 166] and in simulations of quantised vortex lines under the GPE [261, 314]. Moreover, reconnections are required for a system to reach a statistically steady state away from equilibrium under the VFM [315], as well as to enable the transfer of energy from 3-D hydrodynamic motion in the fluid to 1-D wave motion along the vortices [316], and to allow the topology of the vortex tangle to evolve [317]. However, the VFM does not naturally include vortex reconnections, so they are implemented algorithmically, with vortices being reconnected when they have a close approach. Several methods have been proposed to model reconnections [155, 186, 315, 318], although, for counterflow turbulence, all have been shown to produce very similar results [318]. A recent investigation [319] of reconnecting vortex filaments identified two scaling laws for their minimum separation before and after the reconnection event, and found evidence supporting this in both GPE and VFM simulations.

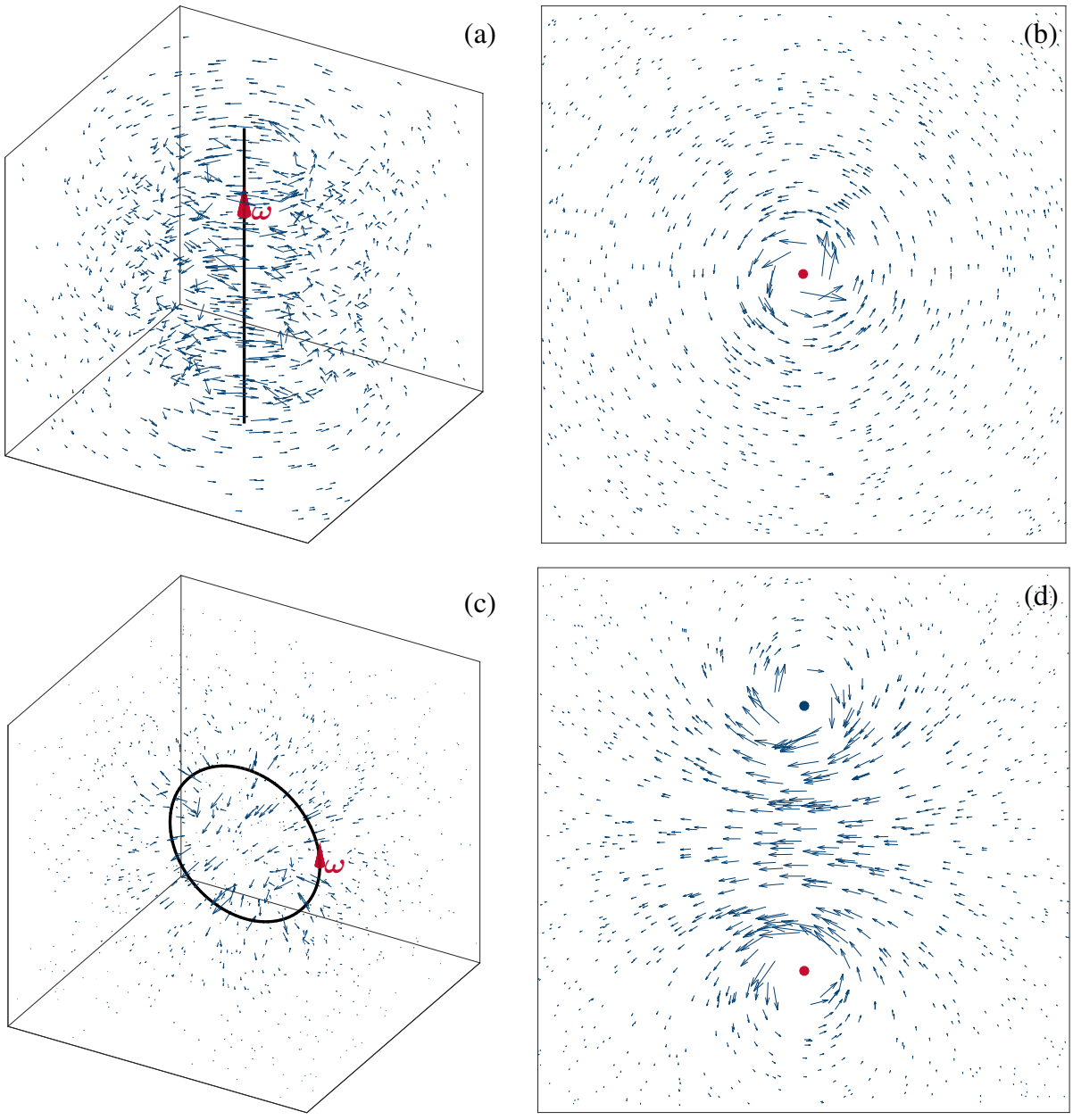

Figure 5.1: Vortex filament method. Flow induced around a straight line vortex (a) and velocity field in the plane perpendicular to the vortex (b), and flow around a vortex ring (c) and velocity field in a plane bisecting the ring (d).

5.2 Mutual Friction

The two fluid equations for the normal fluid and superfluid velocities, eq. (5.1), are coupled by a temperature-dependent mutual friction force, arising from ths scattering of quasiparticles which comprise the normal fluid by the vortex lines in the superfluid component [20, 320]. A frictional force $\mathbf{f}$ (per unit length) is exerted on the superfluid in the region of the vortex core when there is a net relative velocity between the normal fluid and the vortex line, which, through momentum-conservation arguments, leads to a velocity correction:

$$\mathbf{v} = \mathbf{v}_\mathrm{i} + \mathbf{v}_\mathrm{mf},$$

$$\mathbf{v}_\mathrm{mf} = \frac{\mathbf{s}' \times \mathbf{f}}{\rho_\mathrm{s}\kappa},$$

where $\mathbf{v}$ is the velocity of the vortex lines, $\mathbf{v}_\mathrm{i}$ is the self-induced velocity of the vortex lines, and the prime indicates the derivative with respect to arclength [313]. The form of the mutual friction has been measured [196, 321] as:

$$\frac{\mathbf{f}}{\rho_\mathrm{s}\kappa} = \alpha(\mathbf{v}_\mathrm{n} - \mathbf{v}_\mathrm{s} - \mathbf{v}_\mathrm{i}) - \alpha'\mathbf{s}' \times (\mathbf{v}_\mathrm{n} - \mathbf{v}_\mathrm{s} - \mathbf{v}_\mathrm{i}),$$

where α and α' are temperature-dependent mutual friction coefficients (See Appx. B), and $\mathbf{v}_\mathrm{s}$ and $\mathbf{v}_\mathrm{n}$ are respectively the background superfluid and normal fluid velocities. This immediately gives the Schwarz equation:

$$\mathbf{v}_\mathrm{mf} = \alpha\mathbf{s}' \times (\mathbf{v}_\mathrm{n} - \mathbf{v}_\mathrm{s} - \mathbf{v}_\mathrm{i}) - \alpha'\mathbf{s}' \times [\mathbf{s}' \times (\mathbf{v}_\mathrm{n} - \mathbf{v}_\mathrm{s} - \mathbf{v}_\mathrm{i})]\,. \tag{5.4}$$

The most apparent effects of this mutual friction correction are the damping of small-scale perturbations, shown in Fig. 5.2, and the growth and contraction of vortex lines, depending on the strength and direction of the relative flow $\mathbf{v}_\mathrm{n} - \mathbf{v}_\mathrm{s} - \mathbf{v}_\mathrm{i}$ in relation to the velocity of the vortex lines. A regular vortex ring at zero temperature moves with self-induced velocity in the direction binormal to the vortex ring, with speed:

$$v_\mathrm{i} = \frac{\kappa}{4\pi R}\left[\ln\left(\frac{8R}{a_0}\right) - \frac{1}{2}\right], \tag{5.5}$$

where R is the radius of the ring and a_0 is the radius of the core [322]. At finite temperatures, possibly also with some normal fluid and superfluid motion entirely aligned with the direction of the vortex ring's self-induced velocity, the speed becomes:

$$v = \frac{1 - \gamma_0^2/\left[\gamma_0^2 + (\rho_\mathrm{s}\kappa - \gamma_0')^2\right]}{1 - \gamma_0'^2/\rho_\mathrm{s}\kappa}(v_\mathrm{i} + v_\mathrm{s}) + \frac{\gamma_0^2/\left[\gamma_0^2 + (\rho_\mathrm{s}\kappa - \gamma_0')^2\right] - \gamma_0'^2/\rho_\mathrm{s}\kappa}{1 - \gamma_0'^2/\rho_\mathrm{s}\kappa}v_\mathrm{n}, \tag{5.6}$$

where

$$\gamma_0 = \rho_\mathrm{s}\kappa\frac{\alpha}{(1-\alpha')^2 + \alpha^2},$$

$$\gamma_0' = \rho_\mathrm{s}\kappa\frac{\alpha^2 - \alpha'(1-\alpha')}{(1-\alpha')^2 + \alpha^2},$$

and v_s and v_n are the magnitudes of the superfluid and normal fluid component velocities. The radius of the vortex ring then evolves according to:

$$\frac{dR}{dt} = \frac{\gamma_0^2 \rho_\mathrm{s}}{\gamma_0^2 + (\rho_\mathrm{s}\kappa - \gamma')^2}(v_\mathrm{n} - v_\mathrm{s} - v_\mathrm{i}), \tag{5.7}$$

which reduces to 0 as $T \to 0$ [320]. These analytic expressions are straightforward to evaluate, and provide a simple check for our numerics (Sec. 6.1.5). This effect is illustrated in Fig. 5.3.

This effect is directly analogous to the observed damping of vortex dynamics in 2-D superfluids at finite temperatures, originating from the scattering of quasiparticles by the vortex cores [323, 324]. In particular, vortices in 2-D comprising vortex-antivortex dipoles are driven together by this frictional force as they move through the superfluid, ultimately resulting in their mutual annihilation; cf. panel (b) of Fig. 5.3, in which a vortex ring in 3-D shrinks due to its own motion.

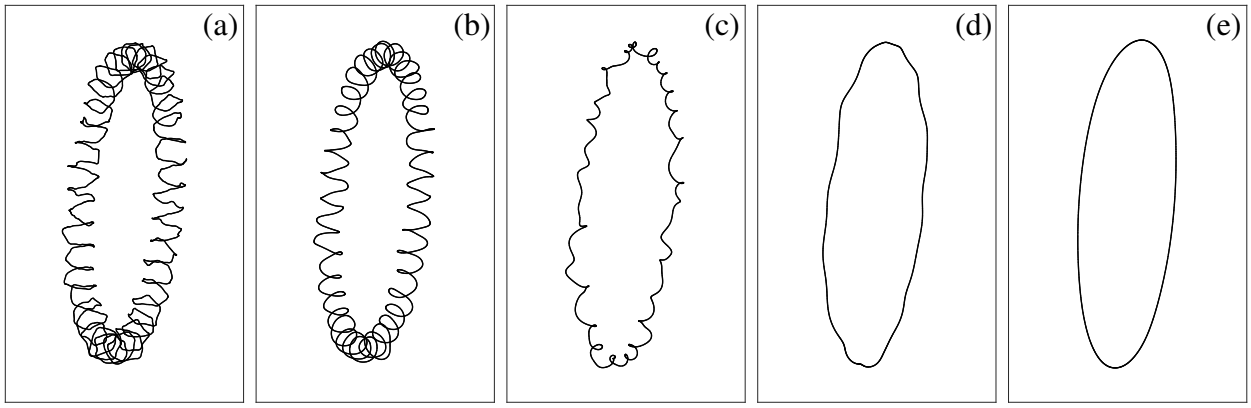

Figure 5.2: Evolution of a vortex loop of radius 0.1 cm with smaller oscillations and random noise under the VFM with mutual friction parameters $\alpha = 0.206$, $\alpha' = 8.34 \times 10^{-3}$ corresponding to 1.9 K. Panels show $t = 0$ s (a), $t = 0.05$ s (b), $t = 0.2$ s (c), $t = 0.5$ s (d), and $t = 2$ s (e).

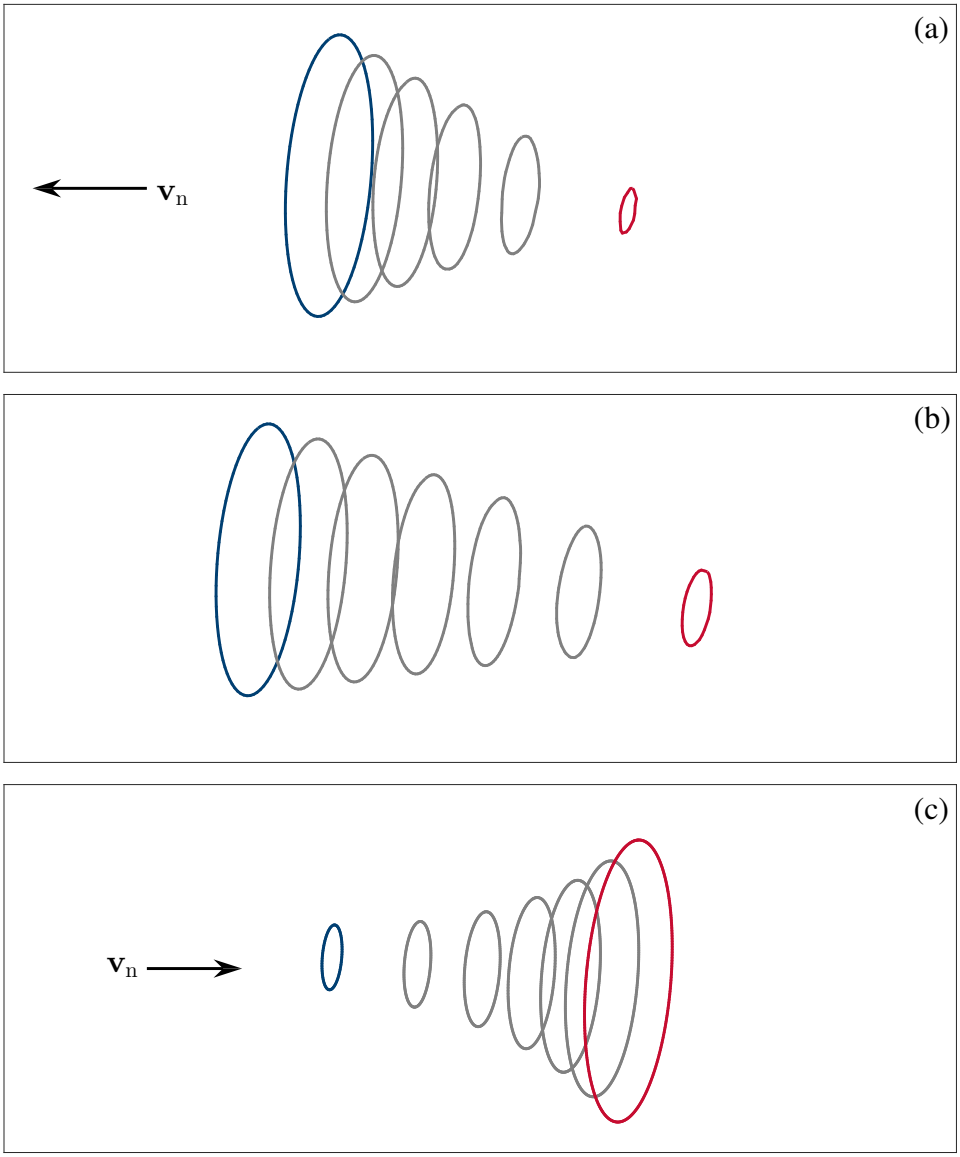

Figure 5.3: Illustration of the effect of normal fluid flow on a vortex ring of radius, from VFM simulation with parameters corresponding to 1.9 K. An initial vortex ring with radius 0.01 cm is shown in blue, with intermediate states shown in grey as it evolves toward a later state shown in red. The vortex ring is oriented such that it travels from left to right under its self-induced velocity. Panel (a) shows the evolution of the ring with the normal fluid flowing in opposition to the vortex ring, with $|\mathbf{v}_n| = 0.1$ cm/s, panel (b) with no normal fluid velocity, and (c) with the normal flow aligned with the ring's direction of motion, again with $|\mathbf{v}_n| = 0.1$ cm/s. Note that, in order to make the effect apparent, the time scales vary from panel to panel, with (a) covering a period of 0.1 s, (b) a period of 0.18 s, and (c) a period of 1.5 s.

5.3 Counterflow Turbulence & Vinen's Equation

Experiments with thermally driven counterflow in He II, flows in which the large-scale normal fluid motion is in opposition to the superfluid motion, have informed theory for seven decades, from investigation of the mutual friction force [19, 20, 325] to the comparison of classical and quantum turbulence [216, 326–328]. In the typical set-up, illustrated in Fig. 5.4, an insulated channel is immersed in a bath of He II, with one end open to the bath, and the other closed and containing a heat source. The heat source produces excess excited particles, leading to a flow of the normal fluid, as the sole carrier of entropy, away from the heater with velocity $\mathbf{v}_\mathrm{n}$ proportional to the heat flux. Conservation of mass then implies $\rho_\mathrm{n}\mathbf{v}_\mathrm{n} + \rho_\mathrm{s}\mathbf{v}_\mathrm{s} = \mathbf{0}$, and so $\mathbf{v}_\mathrm{s} = -(\rho_\mathrm{n}/\rho_\mathrm{s})\mathbf{v}_\mathrm{n}$; the superfluid component travels counter to the normal fluid component [329], with relative velocity $\mathbf{v}_\mathrm{ns} = \mathbf{v}_\mathrm{n} - \mathbf{v}_\mathrm{s}$.

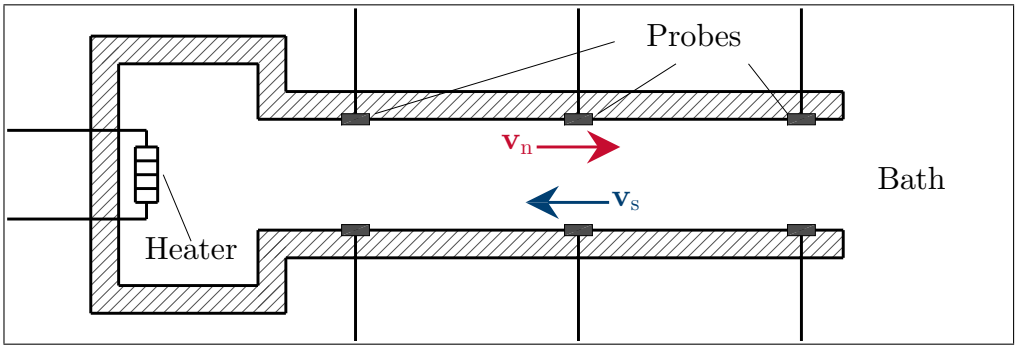

Figure 5.4: Schematic showing the typical set-up for a thermal counterflow experiment.

Above a critical counterflow velocity a turbulent tangle of quantised vortices develops in the superfluid component, seeded by the stretching of remanent vortices through the Donnelly-Glaberson instability [330]. Far from the heater and the boundaries, the tangle is homogeneous (though not necessarily isotropic), and the evolution of the vortex line density L can be described by Vinen's equation:

$$\frac{dL}{dt} = \chi_1 \frac{B}{2}\frac{\rho_\mathrm{n}}{\rho}|\mathbf{v}_\mathrm{ns}|L^{3/2} - \chi_2 \frac{\kappa}{2\pi}L^2, \tag{5.8}$$

where B is a mutual friction coefficient related to α by $B = (2\rho/\rho_\mathrm{n})\alpha$, and χ_1 and χ_2 are phenomenological constants of order unity [20, 331]. The first term on the RHS relates to the injection of energy through the interaction of the vortex lines with the normal fluid through the mutual friction, while the second corresponds to the dissipation of energy following reconnection events. For a statistically steady state with $(dL/dt) = 0$ this predicts that $L = \gamma^2|\mathbf{v}_\mathrm{ns}|^2$, where γ is a temperature-dependent parameter; the intensity of the vortex tangle is proportional to the square of the counterflow velocity, which has been experimentally verified [34, 332].

Having introduced the vortex filament method, we now move on to its numerical implementation.

Chapter 6

Numerical Methods II

We describe the numerical implementation of the vortex filament method, and test the accuracy of our implementation by comparing simulations to theoretical vortex dynamics. We also discuss some numerical procedures which are particular to our analysis.

6.1 The Vortex Filament Method

Vortex filament method (VFM) simulations are performed using QVORT [318, 333, 334]. We discuss the principle numerical routines involved in this section.

6.1.1 Discretisation & Evolution

Vortex filaments are smooth, continuous structures, described by spacecurves $\mathbf{s}(\xi, t)$ where ξ is arclength. In order to simulate them under the VFM we must approximate their structure by a set of discrete points, with each point connected to two neighbours, one in front and one behind on the filament, with the direction determining the sense of the vorticity along the filament. Each point then has an associated position and velocity in $\mathbb{R}^3$.

Discretising the filaments introduces a spatial resolution δ of the average distance between points, which will also determine the scales which we can access, as well as the appropriate temporal resolution. However, as vortices can stretch and contract this resolution is not automatically maintained, and so we remesh the discretisation at each time-step algorithmically: if the distance from a point to the point in front is greater than δ, then a new point is inserted between them, with position and velocity taken as their average, while if the distance between a point and the point two in front is less than δ, then the intermediate point is removed.

The configuration is evolved forward in time by a 3^{rd}-order Adams-Bashforth scheme, after a single Euler step, and a single 2^{nd}-order Adams-Bashforth step, as described in Sec. 6.1.2. All spatial derivatives are calculated using the methods discussed in Sec. 3.1.1. We calculate the velocities of points using two methods, depending on the context.

The local induction approximation (LIA), proposed by Schwarz [313], estimates the velocity of a point on a filament by a 1^{st}-order approximation (See Appx. A.4 for derivation) to the full Biot-Savart law:

$$\mathbf{v}_{\mathrm{i}}(\mathbf{s}) = \frac{\kappa}{4\pi} \ln\left(\frac{R}{a_0}\right) \mathbf{s}' \times \mathbf{s}'', \tag{6.1}$$

where $R = 1/\sqrt{\mathbf{s}'' \cdot \mathbf{s}''}$ is the local radius of curvature, primes denote derivatives w.r.t. the arclength, and κ and a_0 are the quantum of circulation and vortex core radius respectively.

As the evaluation of eq. (6.1) only requires the local derivative, this method's computation times scales as $\mathcal{O}(n)$, where n is the number of discretisation points. The speed of this method makes it ideal for exploratory simulations, or for initialising simulations before switching to a more accurate method. However, it is not a reliable method in many situations: it cannot include nonlocal interactions which also precludes the correct implementation of any boundaries implemented through 'ghost' vortices, it produces integrable systems which are not suitable for the study of weak Kelvin wave turbulence [335], and it has been observed [328] that counterflow simulations performed using the LIA produce vortex tangles that are denser and more anisotropic than those performed using the full Biot-Savart law.

The Biot-Savart law (derived in Appx. A.3) calculates the velocity as:

$$\mathbf{v}_{\mathrm{i}}(\mathbf{s}) = \frac{\kappa}{4\pi} \oint_{\mathcal{L}} \frac{(\mathbf{s}_1 - \mathbf{s}) \times d\mathbf{s}_1}{|\mathbf{s}_1 - \mathbf{s}|^3}, \tag{6.2}$$

with $\mathbf{s}$ some position on the curves describing the vortex filaments. When evaluating the velocity of the lines themselves a singularity emerges as $\mathbf{s}_1 \to \mathbf{s}$. This is handled by decomposing the velocity into local and nonlocal contributions (See Appx. A.3):

$$\mathbf{v}_{\mathrm{i}}(\mathbf{s}) = \frac{\kappa}{4\pi} \mathbf{s}' \times \mathbf{s}'' \ln\left(\frac{2\sqrt{\ell_+ \ell_-}}{e^{1/2} a_0}\right) + \frac{\kappa}{4\pi} \int_{\mathcal{L}'} \frac{(\mathbf{s}_1 - \mathbf{s}) \times d\mathbf{s}_1}{|\mathbf{s}_1 - \mathbf{s}|^3}, \tag{6.3}$$

where ℓ_+ and ℓ_- in the first, local, term are the distances from $\mathbf{s}$ to the points in front and behind, and the integral in the second, nonlocal, term now omits the line segments from $\mathbf{s}$ to the points in front and behind. Following [315], the contribution to the integral from the line segment between a point $\mathbf{s}_j$ and the point in front $\mathbf{s}_{j+1}$ is given by:

$$\Delta_j \mathbf{v}_{\mathrm{i}}(\mathbf{s}) = \frac{\kappa}{2\pi(4AC - B^2)} \left[\frac{2C + B}{\sqrt{A + B + C}} - \frac{B}{\sqrt{A}}\right] \mathbf{p} \times \mathbf{q}, \tag{6.4}$$

where $\mathbf{p} = \mathbf{s}_j - \mathbf{s}$, $\mathbf{q} = \mathbf{s}_{j+1} - \mathbf{s}_j$, $A = |\mathbf{p}|^2$, $B = 2\mathbf{p} \cdot \mathbf{q}$, and $C = |\mathbf{q}|^2$. The evaluation of the velocity for each point then requires integration over all other points, and so the computation time for this method scales as $\mathcal{O}(n^2)$. Simulations can typically contain $10^4 - 10^5$ points, making this a very costly procedure.

Drawing inspiration from N-body simulations in astrophysics and cosmology [336–338], the use of tree algorithms to improve the performance of VFM implementations has been gaining popularity in recent years [339, 340]. The basic idea of tree algorithms is to approximate the contribution to the velocity of a point from a region by some average over that region, with the size of the region which can be averaged over effectively determined by its distance from the point.

The first step is the construction of the tree describing the vortex configuration. The computational domain is divided into eight equal cubes, for each of which the total circulation $\mathbf{s}_\Sigma$ and the centre of circulation $\bar{\mathbf{s}}$ are calculated as:

$$\mathbf{s}_\Sigma = \sum_{j=1}^{n_\mathrm{c}} \mathbf{s}_{j+1} - \mathbf{s}_j, \qquad \bar{\mathbf{s}} = \frac{1}{n_\mathrm{c}} \sum_{j=1}^{n_\mathrm{c}} \mathbf{s}_j, \tag{6.5}$$

where n_c is the number of points within the cube. Each region is then recursively subdivided into eight further cubes, with the total circulation and centre of circulation again calculated, until a cube contains either no discretisation points or a single point, with the computation time for the construction of this tree scaling as $\mathcal{O}(n \log(n))$.

To calculate the velocity for some $\mathbf{s}$ we must then track through the tree, deciding which points are sufficiently far to use an averaged contribution. This decision is made using the opening angle θ, defined as $\theta = w/d$, where w is the width of the cube being queried, and d is the distance from $\bar{\mathbf{s}}$ to $\mathbf{s}$. If $\theta < \theta_\mathrm{c}$, where θ_c is some critical opening angle, or the cube contains at most one point, then we accept the cube and calculate its contribution to the nonlocal part of the velocity in eq. (6.3), using eq. (6.4), where $\mathbf{p}$ and $\mathbf{q}$ are now defined as $\mathbf{p} = \bar{\mathbf{s}} - \mathbf{s}$ and $\mathbf{q} = \mathbf{s}_\Sigma$. Otherwise, we go to the next level and repeat the test for each of the children cubes within the cube, with this process repeated recursively until the contributions from all cubes have been included.

The success of this method depends upon using a sensible choice for θ_c: if θ_c is too large the discrepancy between the tree algorithm and the full Biot-Savart integral is untenable, whereas if θ_c is too small the tree algorithm will recover the full Biot-Savart integral, making no improvement in computation time; indeed, it will be slower due to the additional overhead in creating and traversing the tree. Testing suggests that $\theta_\mathrm{c} = 0.2$ is a suitable choice for significant speed-up without great loss of accuracy [333].

Having calculated the velocity induced by the vortices themselves, if the simulation is performed at a finite temperature the mutual friction correction is then added:

$$\mathbf{v}(\mathbf{s}) = \mathbf{v}_\mathrm{i}(\mathbf{s}) + \mathbf{v}_\mathrm{mf}(\mathbf{s}), \tag{6.6}$$

where

$$\mathbf{v}_\mathrm{mf}(\mathbf{s}) = \alpha \mathbf{s}' \times (\mathbf{v}_\mathrm{n} - \mathbf{v}_\mathrm{s} - \mathbf{v}_\mathrm{i}) - \alpha' \mathbf{s}' \times [\mathbf{s}' \times (\mathbf{v}_\mathrm{n} - \mathbf{v}_\mathrm{s} - \mathbf{v}_\mathrm{i})], \tag{6.7}$$

where $\mathbf{v}_\mathrm{n}$ is some imposed normal flow, and $\mathbf{v}_\mathrm{s}$, taken to be $-\rho_\mathrm{n}/\rho_\mathrm{s}\mathbf{v}_\mathrm{n}$ in counterflows for mass conservation, is an imposed superflow - note that both may be zero, a situation which does not imply that $\mathbf{v}_\mathrm{mf}$ is zero. Finally, the vortices move with the superfluid, to give:

$$\mathbf{v}(\mathbf{s}) = \mathbf{v}_\mathrm{i}(\mathbf{s}) + \mathbf{v}_\mathrm{mf}(\mathbf{s}) + \mathbf{v}_\mathrm{s}(\mathbf{s}) \tag{6.8}$$

6.1.2 Adams-Bashforth Methods

We evolve our VFM solutions using a 3$^\mathrm{rd}$-order Adams-Basthforth method [341]. For a solution with positions $\mathbf{x}(t)$ and velocities $\mathbf{v}(t)$, we march forward in time using:

$$\mathbf{x}(t+\Delta t) = \mathbf{x}(t) + \Delta t \left[\frac{23}{12}\mathbf{v}(t) - \frac{16}{12}\mathbf{v}(t-\Delta t) + \frac{5}{12}\mathbf{v}(t-2\Delta t)\right] + \mathcal{O}((\Delta t)^4). \tag{6.9}$$

A detailed derivation is given in Appx. A.7. Note that this scheme requires knowledge of the velocities at the current time and at two previous points in time. When we initialise our simulations we only have knowledge of the velocity at the current time, so the first step is performed using Euler's method, and the second step is performed using a 2^{nd}-order Adams-Bashforth scheme:

$$\mathbf{x}(t+\Delta t) = \mathbf{x}(t) + \Delta t \left[\frac{3}{2}\mathbf{v}(t) - \frac{1}{2}\mathbf{v}(t-\Delta t)\right] + \mathcal{O}((\Delta t)^3), \tag{6.10}$$

with the third and all subsequent steps performed using the 3^{rd}-order scheme described.

6.1.3 Reconnections & Dissipation

Multiple algorithms for deciding when reconnection events should occur have been proposed [315, 318, 342], although no significant difference in the statistical properties of counterflow turbulence was observed between simulations using several methods [318]. We use the type II algorithm described in [318], which performs a reconnection only if doing so will decrease the total vortex line length; reconnections are dissipative and lead to phonon emission [343], and vortex line length acts as a proxy for their kinetic energy [28], so reconnections should not increase the total vortex line length.

In determining which points should reconnect, we first determine which points are close enough to reconnect, which we take to be those with a separation of less than $\Delta = \delta/2$, the smallest spatial resolution of the particular simulation. Rather than a brute force distance test, which scales as $\mathcal{O}(n^2)$, we use a simple tree algorithm: points are binned according to their x and y coordinates, with bins having a width of at least Δ, an $\mathcal{O}(n)$ process. The only points they can reconnect with are those in the same bin, or in the bins immediately surrounding it, and so we directly check the separations within each such subset, an $\mathcal{O}(n \log(n))$ process.

Then, having identified the points that are close enough to reconnect, we check that they satisfy several criteria. We exclude reconnections between points and their immediate neighbours as unphysical. We then check that the two reconnecting points are the nearest to each other (as opposed to another third point being nearer to either of them) which would lead to a decrease in the total line length, and which are not parallel, in order to preserve the orientation of vorticity, requiring that $\hat{\mathbf{s}}_i' \cdot \hat{\mathbf{s}}_j' < 0.965$, with $\hat{\mathbf{s}}_i'$ the unit tangent to the vortex filament at the point $\mathbf{s}_i$, which imposes a minimum angle of $\sim 15°$ between reconnecting filaments. Note that this algorithm does not prohibit the self-reconnection of filaments which have become twisted enough to do so.

Having identified points to reconnect, the reconnection itself is performed by appropriate changes to the pointers which describe which points are in front and behind the reconnecting points and their neighbours along the filaments, as illustrated in Fig. 6.1.

Loops containing fewer than five discretisation points are removed from simulations. This mimics the dissipation of energy through friction and phonon emission at the small-

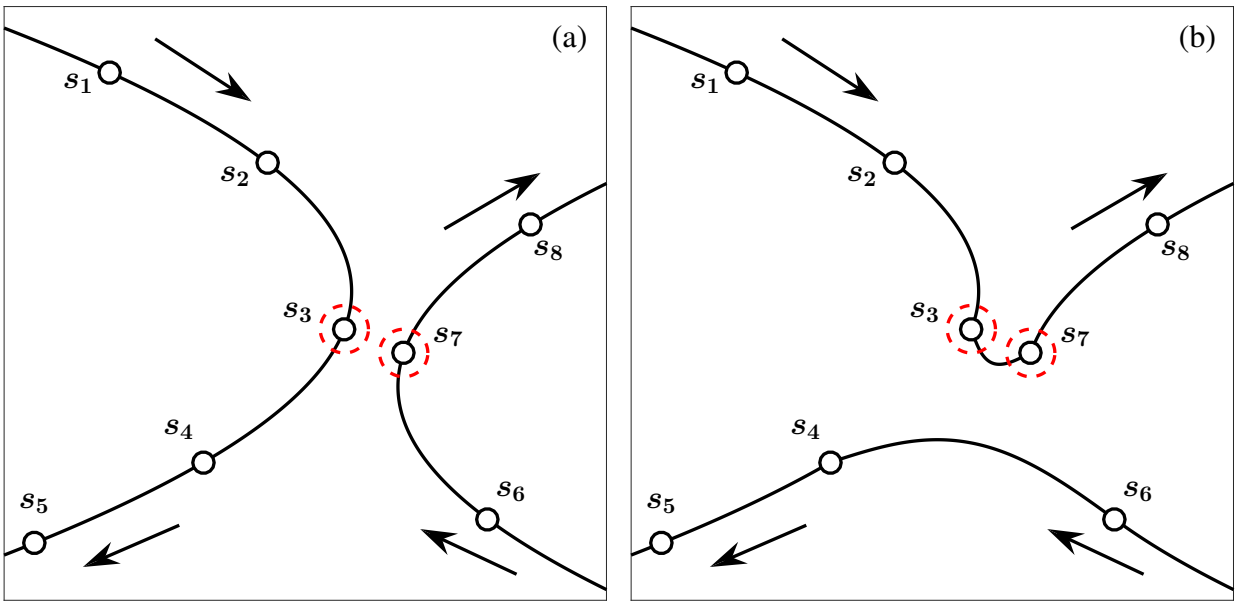

Figure 6.1: Schematic showing the change in connections along vortex filaments during a reconnection. Two filaments $\{\mathbf{s}_1, \mathbf{s}_2, \mathbf{s}_3, \mathbf{s}_4, \mathbf{s}_5\}$ and $\{\mathbf{s}_6, \mathbf{s}_7, \mathbf{s}_8\}$ reconnect at $\mathbf{s}_3$ and $\mathbf{s}_7$, resulting in two filaments $\{\mathbf{s}_1, \mathbf{s}_2, \mathbf{s}_3, \mathbf{s}_7, \mathbf{s}_8\}$ and $\{\mathbf{s}_6, \mathbf{s}_4, \mathbf{s}_5\}$.

est length scales, which occurs even at the lowest temperatures [167, 344]. From a numerical perspective, this treatment is also necessary to avoid unpredictable behaviour of small loops - when the discretisation is too coarse to capture the shape of a loop the calculation of $\mathbf{s}' \times \mathbf{s}''$ in the first term of eq. (6.3) suffers from noise, which can produce erratic trajectories.

6.1.4 Boundaries

As with the PVM, the VFM is a Lagrangian system which naturally resides in an infinite domain; in a similar manner we can impose a selection of boundaries.

Periodic boundaries can be imposed in one direction by repeating the vortex configuration, shifted by the desired period in the chosen direction, both ahead and behind. Repeating this in the other directions, as illustrated in Fig. 6.2, will result in a periodic box. Strictly speaking the configuration should be infinitely repeated, although this is neither feasible nor necessary, and we use a single layer to impose periodicity. When a discretisation point crosses a boundary it is removed and reinserted at the other side of the domain. Finally, note that care should be taken in the calculation of eq. (6.4): the vectors between points must be calculated as though they were physically next to each other, in particular when a filament passes through a boundary between one point and the next.

Some hard wall boundaries can be imposed by the use of image vortices. For planes, the real vortex configuration is reflected in the plane, with the reflected configuration having the opposite circulation (or, equivalently, being integrated over in the opposite direction), illustrated in Fig. 6.3.

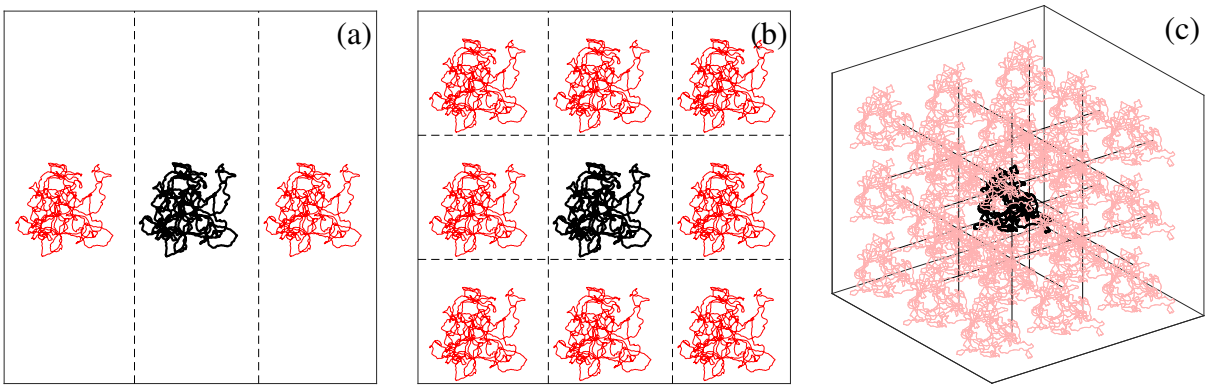

Figure 6.2: Illustration of the 'ghost' vortices used to enforce periodic boundary conditions. Panels (a) and (b) show a top-down projection of the real vortices in black, with 'ghost' vortices in red, producing periodic boundaries in x in (a), and periodic boundaries in x and y in (b), while (c) shows the layer of 26 repetitions of the real configuration used to produce a fully periodic box.

Cylindrical boundaries, illustrated in Fig. 6.4, can be imposed by generating an image vortex configuration according to:

$$\mathbf{s}_{\text{image}} = \left(\frac{a^2 \mathbf{s}_x}{\mathbf{s}_x^2 + \mathbf{s}_y^2}, \frac{a^2 \mathbf{s}_y}{\mathbf{s}_x^2 + \mathbf{s}_y^2}, \mathbf{s}_z \right),$$

where $\mathbf{s}_x$, $\mathbf{s}_y$, and $\mathbf{s}_z$ are the x-, y-, and z-components of point $\mathbf{s}$ of the original vortex filament, a is the radius of the cylinder, which is here aligned with the z-axis; arbitrarily oriented cylinders can be imposed by simple coordinate transformations.

Vortex filaments also reconnect with hard wall boundaries, when a point is within $\delta/2$ of the boundary, with the neighbouring point that is closest to the boundary also reconnecting, provided that performing the reconnection will reduce the total line length. A reconnected point is created on the boundary, with its position the projection of the reconnecting point onto the boundary, as shown in Fig. 6.5. We can treat boundaries as either perfectly rough, in which case the reconnection site is fixed, or as perfectly smooth, in which case the reconnection site tracks over the surface as the projection from the first discretisation point of the connected filament.

Finally, we note that many of these boundaries can be used in conjunction with each other, for instance, we could simulate a cylinder in a periodic domain by imposing a cylindrical hard wall boundary aligned with the z-axis, and then enforcing periodicity in the z-direction as discussed, with the image enforcing the cylinder also to be repeated.

6.1.5 Accuracy

In this section we will test the reliability of the VFM code, by comparing various known analytic results with numerical simulations.

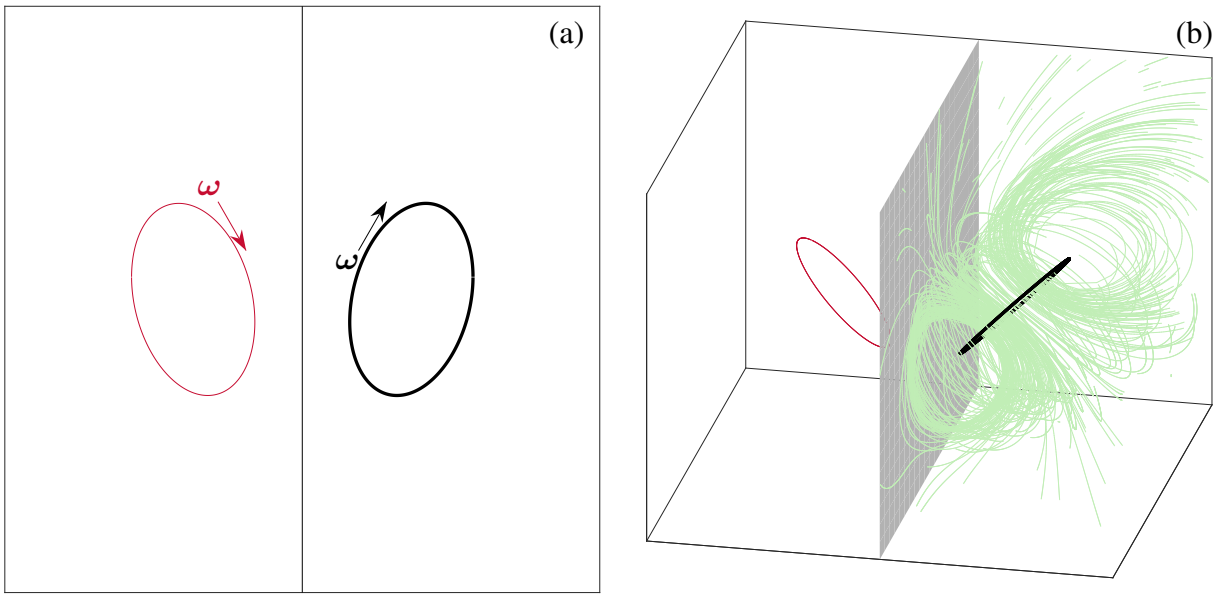

Figure 6.3: Illustration of a vortex ring interacting with a hard wall boundary imposed by an image vortex (red). Panel (a) gives a top-down projection, panel (b) shows some resulting streamlines (green); note that none pass through the boundary.

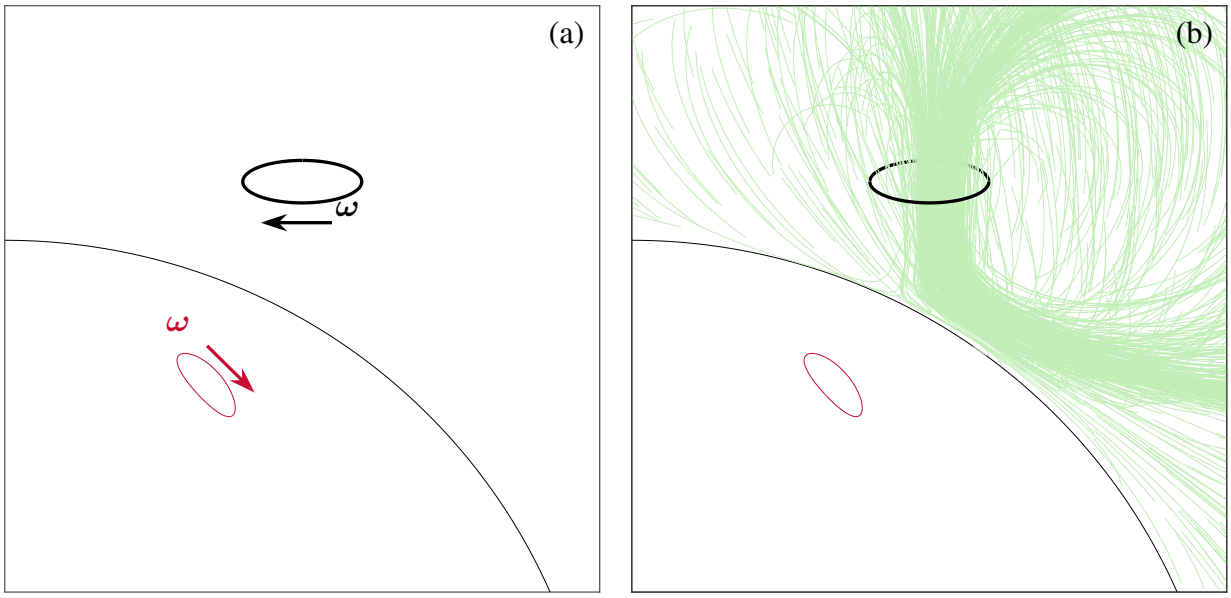

Figure 6.4: Top-down view of a vortex ring (black) and corresponding image vortex (red) imposing a cylindrical boundary, with some instantaneous streamlines (green) shown in (b).

A simple criterion for the maximum permissible time-step can be derived by considering Kelvin waves on the vortex filaments [333]. The angular frequency of Kelvin waves along straight vortex lines is given by:

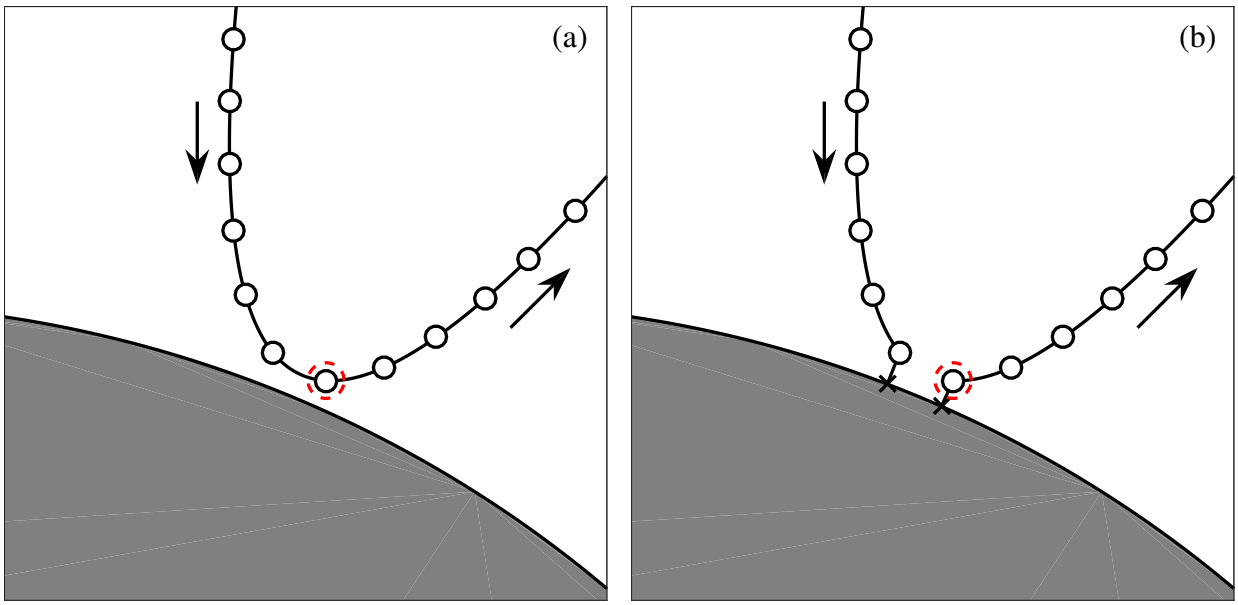

Figure 6.5: Schematic showing the topology of a vortex filament before (a) and after (b) reconnection with the surface of a cylinder. The circled point approaches within $\delta/2$ of the boundary, the neighbour of that point which is closest to the boundary is identified, and, having checked that performing the reconnection will reduce the total line length, a reconnection point is created beneath both points on the surface.

$$\omega \approx -\frac{\kappa k^2}{4\pi}\left[\ln\left(\frac{2}{ka_0}\right) - \gamma\right],$$

where $\gamma \simeq 0.5772$ is Euler's constant, provided $ka_0 \ll 1$ [345] (the long-wavelength approximation). The fastest motions, set by the maximum wavenumber $k_{\max} = 4\pi/\delta$, which is in turn set by our chosen spatial resoluion, are on a time scale of:

$$\omega_{\max}^{-1} \approx \frac{\delta^2}{4\pi\kappa\left[\ln\left(\frac{\delta}{2\pi a_0}\right) - \gamma\right]},$$

which suggests that a sensible time-step is:

$$\Delta t < \frac{\delta^2}{4\pi\kappa \ln\left(\frac{\delta}{2\pi a_0}\right)}. \tag{6.11}$$

We now consider the motion of regular vortex rings. At zero temperature a vortex ring in the xy-plane moves with self-induced velocity:

$$\mathbf{v}_{\mathrm{i}} = \begin{pmatrix} 0 \\ 0 \\ \frac{\kappa}{4\pi R}\left[\ln\left(\frac{8R}{a_0}\right) - \frac{1}{2}\right], \end{pmatrix}$$

where R is the radius of the vortex ring [322]. We compare the velocity of rings of a range of radii for three different spatial resolutions in Fig. 6.6. Note that the velocity reported is the instantaneous velocity, and so the choice of time-step does not affect this. The discrepancy between the theoretical and numerical values are minimal ($\sim$ 2%) for larger loops, while loops containing fewer than around 10 discretisation points suffer from increasing inaccuracy.

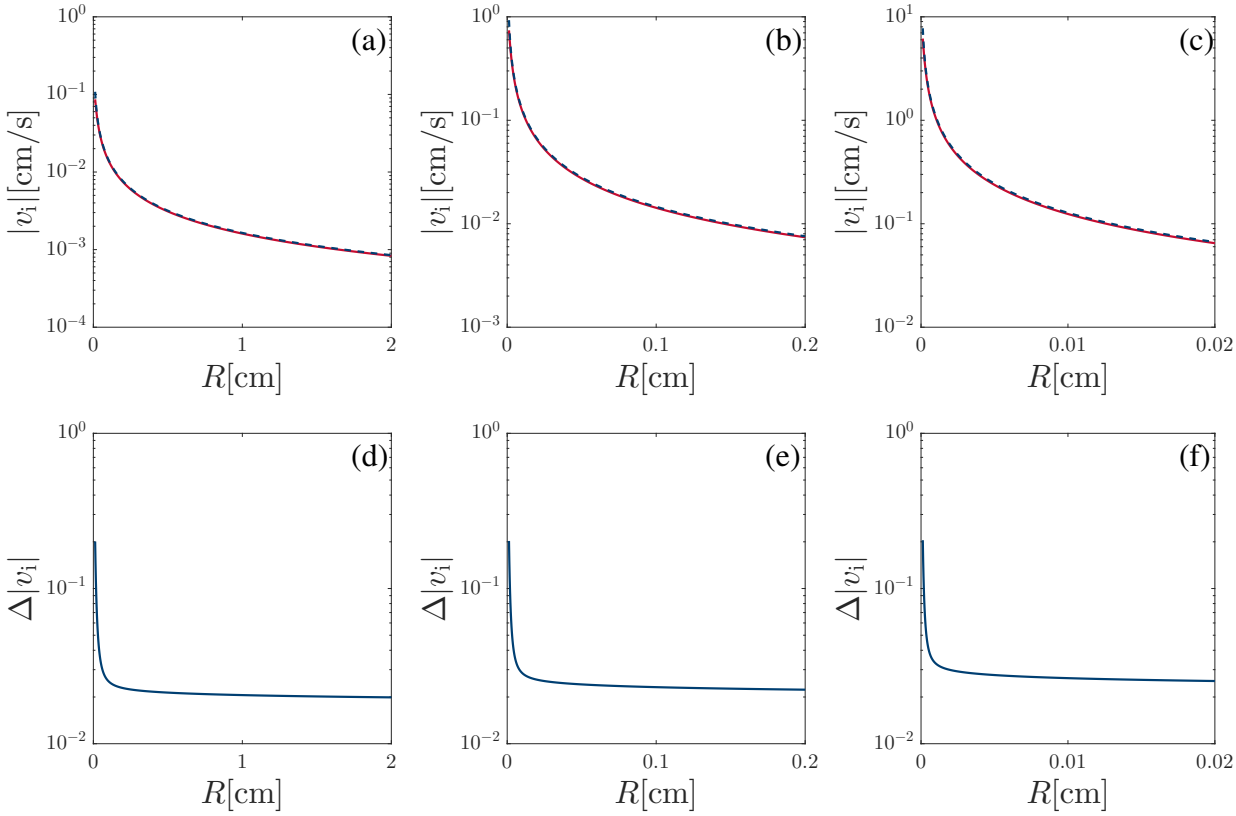

Figure 6.6: Comparison of theoretical and simulated velocities of regular vortex rings of radius R. Panels (a-c) show the theoretical (dashed blue) and simulated, under the tree algorithm, velocity of vortex rings, with (d-f) showing the relative error calculated as $\Delta|v_\mathrm{i}| = |(v_\mathrm{theory} - v_\mathrm{simulation})/v_\mathrm{theory}|$. Panels (a) and (d) correspond to $\delta = 10^{-2}$ cm, (b) and (e) to $\delta = 10^{-3}$ cm, (c) and (f) to $\delta = 10^{-4}$ cm.

At finite temperatures the velocity of a regular vortex ring is modified by mutual friction with the normal fluid according to eq. (5.6), while the evolution of the radius of a vortex ring is given by eq. (5.7). In Fig. 6.7 and Fig. 6.8 we compare theoretical and simulated values for selected temperatures, with the relative accuracy explored in Fig. 6.9. The simulated velocities are generally closest to theoretical values in an intermediate temperature range, with the values closest to the transition temperature the least reliable.

As a final test of the code, we now compare an analytic prediction for the growth due to the Donnelly-Glaberson instability [330] of a helical perturbation along a straight vortex line aligned with some normal flow, illustrated in Fig. 6.10, with the growth of the pertur-

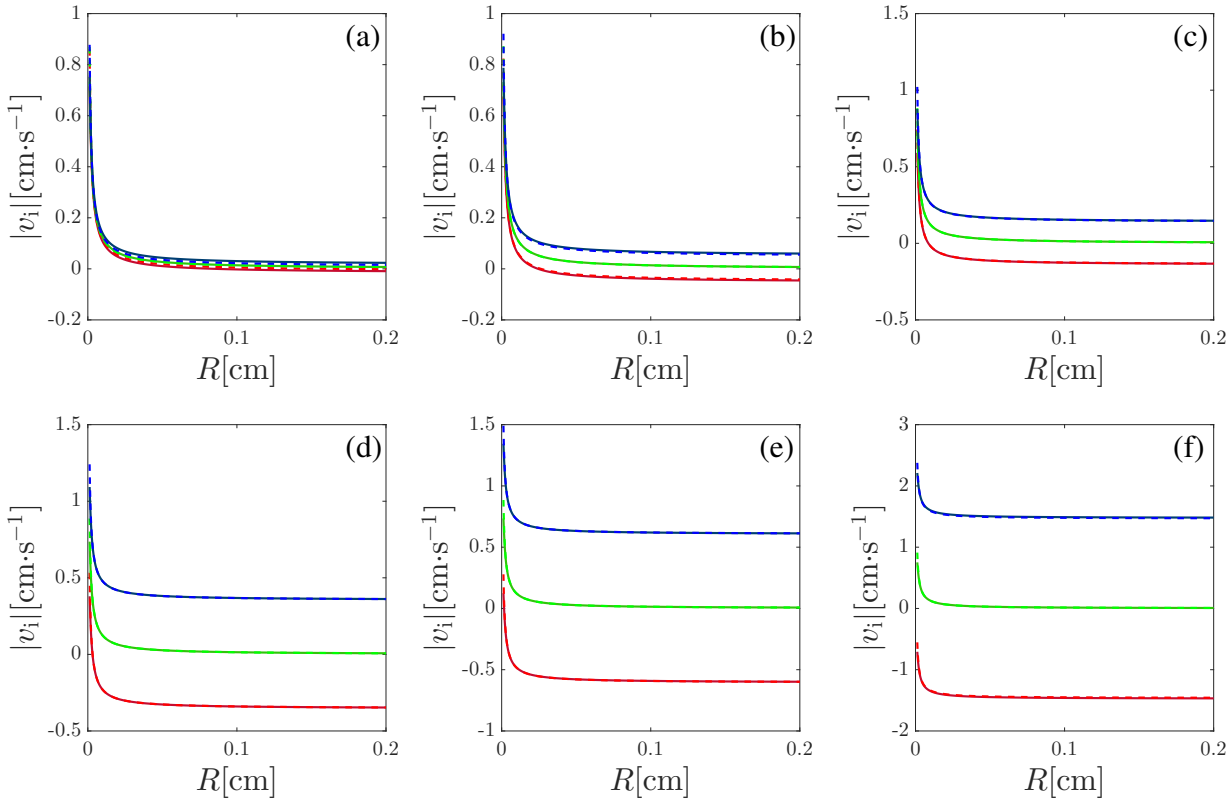

Figure 6.7: Comparison of theoretical (lighter dashed lines) and simulated (darker solid lines) velocities of regular vortex rings at (a) 1.3 K, (b) 1.5 K, (c) 1.7 K, (d) 1.9 K, (e) 2.0 K, (f) 2.1 K, with a spatial resolution of $\delta = 10^{-3}$ cm. Green lines correspond to no background fluid velocity, red lines correspond to a normal fluid velocity of 0.5 cm/s in the same direction as the motion of the vortex ring, and blue lines correspond to a normal fluid velocity of 0.5 cm/s in the opposite direction to the motion of the vortex ring.

bation in simulations. First, consider a straight vortex line, aligned with the x-direction and with a small helical perturbation of amplitude ε, with $\varepsilon \ll 1$:

$$\mathbf{s} = \begin{pmatrix} x \\ \varepsilon \cos(kx - \omega t) \\ \varepsilon \sin(kx - \omega t) \end{pmatrix}, \tag{6.12}$$

where k and ω are the wavenumber and angular frequency of the perturbation. The velocity of the filament according to the LIA, eq. (6.1), and the Schwarz equation, eq. (5.4), is given by:

$$\frac{d\mathbf{s}}{dt} = \beta \mathbf{s}' \times \mathbf{s}'' + \alpha \mathbf{s}' \times [\mathbf{v}_n - \beta \mathbf{s}' \times \mathbf{s}'' - \mathbf{v}_s], \tag{6.13}$$

where $\beta = (\kappa/4\pi)\ln(R/a_0)$, α is a mutual friction coefficient, $\mathbf{v}_n = (v_n, 0, 0)$ is our normal fluid velocity, $\mathbf{v}_s = (v_s, 0, 0)$ is our superfluid velocity, and we have neglected the second term in the Schwarz equation for simplicity.

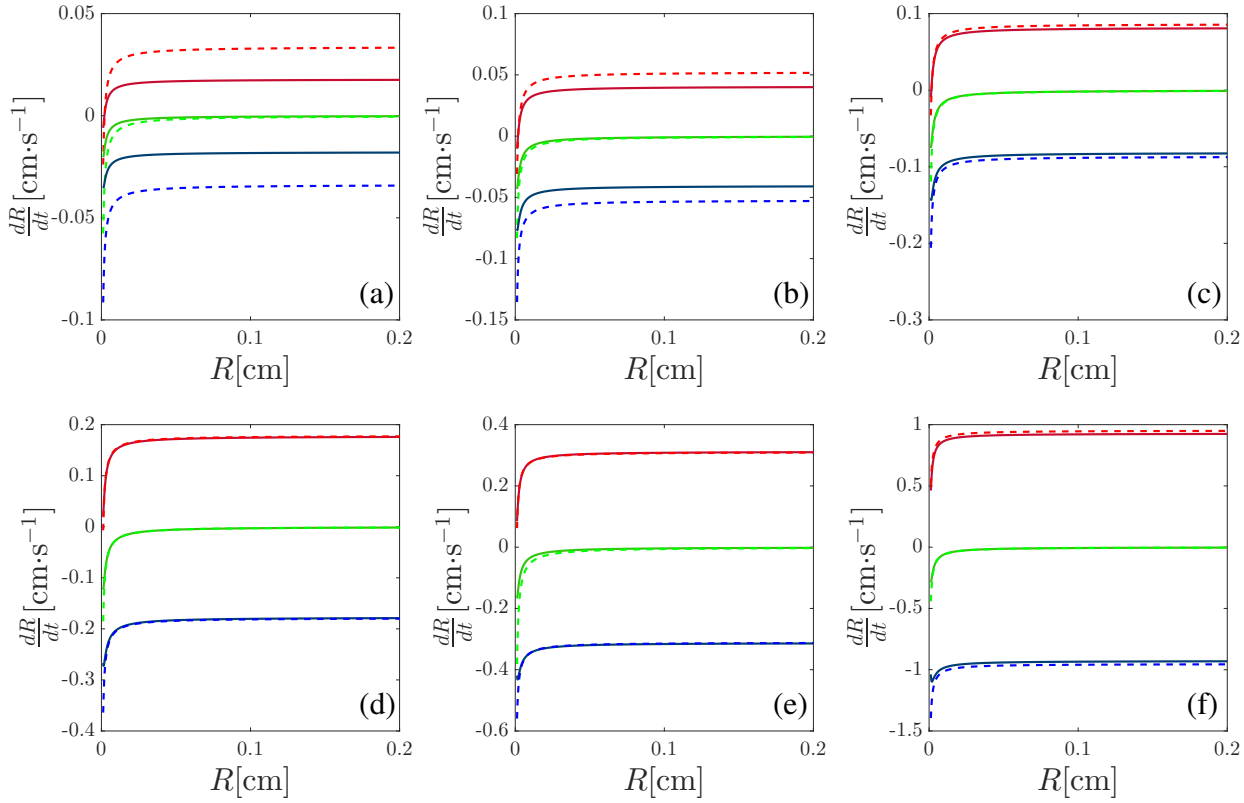

Figure 6.8: Comparison of theoretical (lighter dashed lines) and simulated (darker solid lines) rate of change of radius of regular vortex rings at (a) 1.3 K, (b) 1.5 K, (c) 1.7 K, (d) 1.9 K, (e) 2.0 K, (f) 2.1 K, with a spatial resolution of $\delta = 10^{-3}$ cm. Green lines correspond to no background fluid velocity, blue lines correspond to a normal fluid velocity of 0.5 cm/s in the same direction as the motion of the vortex ring, and red lines correspond to a normal fluid velocity of 0.5 cm/s in the opposite direction to the motion of the vortex ring.

We approximate $\mathbf{s}'$ and $\mathbf{s}''$ by derivatives of eq. (6.12) w.r.t. x (valid for small perturbations, as $x \simeq \xi$):

$$\mathbf{s}' \simeq \begin{pmatrix} 1 \\ -\varepsilon k \sin(kx - \omega t) \\ \varepsilon k \cos(kx - \omega t) \end{pmatrix}, \qquad \mathbf{s}'' \simeq \begin{pmatrix} 0 \\ -\varepsilon k^2 \cos(kx - \omega t) \\ -\varepsilon k^2 \sin(kx - \omega t) \end{pmatrix},$$

which then gives:

$$\mathbf{s}' \times \mathbf{s}'' = \begin{pmatrix} \varepsilon^2 k^3 \\ \varepsilon k^2 \sin(kx - \omega t) \\ -\varepsilon k^2 \cos(kx - \omega t) \end{pmatrix} \simeq \begin{pmatrix} 0 \\ \varepsilon k^2 \sin(kx - \omega t) \\ -\varepsilon k^2 \cos(kx - \omega t) \end{pmatrix}, \tag{6.14}$$

$$\mathbf{s}' \times (\mathbf{v}_\mathrm{n} - \beta \mathbf{s}' \times \mathbf{s}'') = \begin{pmatrix} 1 \\ -\varepsilon k \sin(kx - \omega t) \\ \varepsilon k \cos(kx - \omega t) \end{pmatrix} \times \begin{pmatrix} v_\mathrm{n} - \beta \varepsilon^2 k^3 - v_\mathrm{s} \\ \beta \varepsilon k^2 \sin(kx - \omega t) \\ -\beta \varepsilon k^2 \cos(kx - \omega t) \end{pmatrix}$$

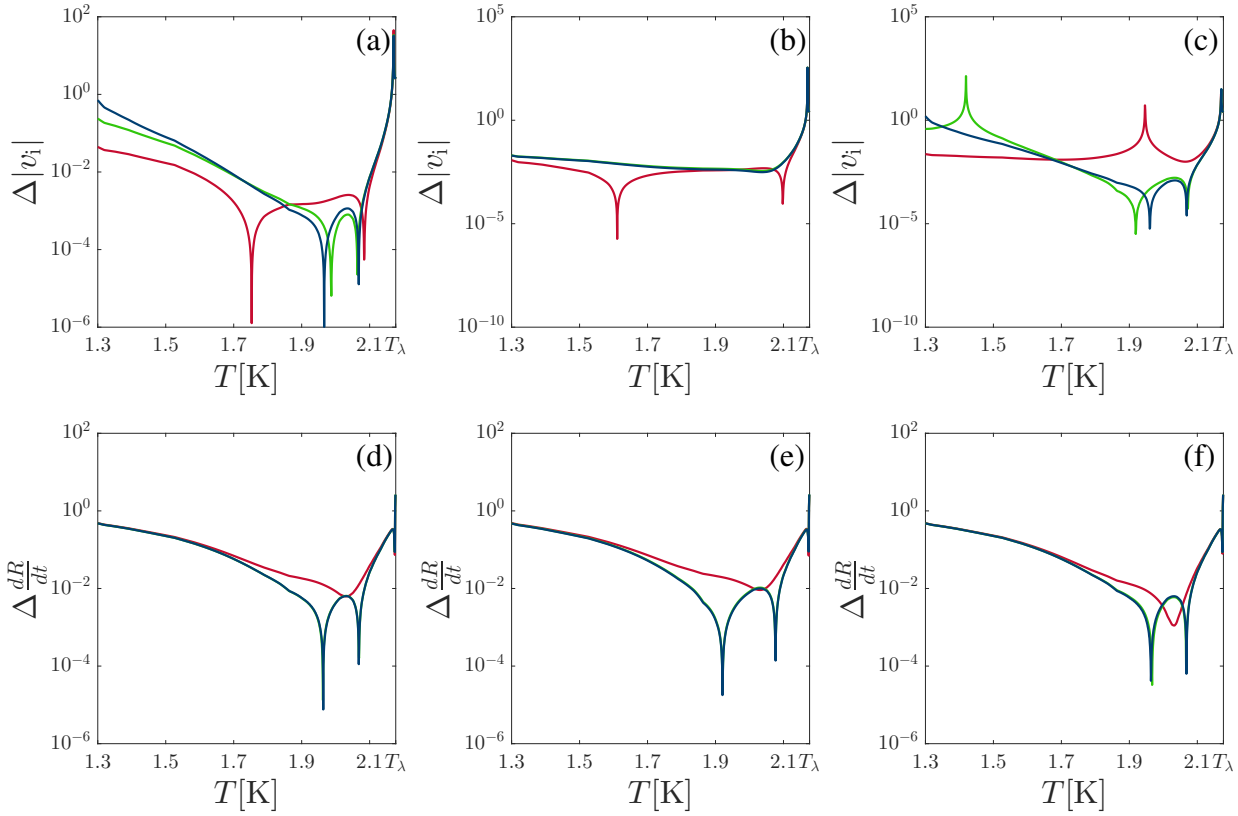

Figure 6.9: Relative error $\Delta f = |(f_{\text{theory}} - f_{\text{simulation}})/f_{\text{theory}}|$ in the velocity and rate of change of radius of regular vortex rings between 1.3 K and $T_\lambda \simeq 2.1768$ K, with a spatial resolution of $\delta = 10^{-3}$ cm. Red, green, and blue lines correspond to vortex rings of radius 0.01 cm, 0.1 cm, and 1 cm respectively. Panels (a) and (d) correspond to a relative fluid velocity $v_{\text{ns}} = 0.5$ cm/s in the same direction as the motion of the vortex ring, (b) and (e) to no normal fluid motion, and (c) and (f) to a relative fluid velocity $v_{\text{ns}} = 0.5$ cm/s in the opposite direction to the motion of the vortex ring.

$$= \begin{pmatrix} 0 \\ (v_{\text{n}} - \beta\varepsilon^2 k^3 - v_{\text{s}} - \beta\varepsilon k^2)\cos(kx - \omega t) \\ (v_{\text{n}} - \beta\varepsilon^2 k^3 - v_{\text{s}} - \beta\varepsilon k^2)\sin(kx - \omega t) \end{pmatrix}$$

$$\simeq \begin{pmatrix} 0 \\ (v_{\text{n}} - v_{\text{s}} - \beta\varepsilon k^2)\cos(kx - \omega t) \\ (v_{\text{n}} - v_{\text{s}} - \beta\varepsilon k^2)\sin(kx - \omega t) \end{pmatrix}, \tag{6.15}$$

where we have linearised in terms of ε, as $\varepsilon \ll 1$. Substituting eq. (6.14) and (6.15) into eq. (6.13) then gives:

$$\frac{d\mathbf{s}}{dt} = \begin{pmatrix} 0 \\ \beta\varepsilon k^2 \sin(kx - \omega t) + \alpha(v_{\text{n}} - \beta k - v_{\text{s}})\varepsilon\cos(kx - \omega t) \\ \beta\varepsilon k^2 \cos(kx - \omega t) + \alpha(v_{\text{n}} - \beta k - v_{\text{s}})\varepsilon\sin(kx - \omega t) \end{pmatrix}. \tag{6.16}$$

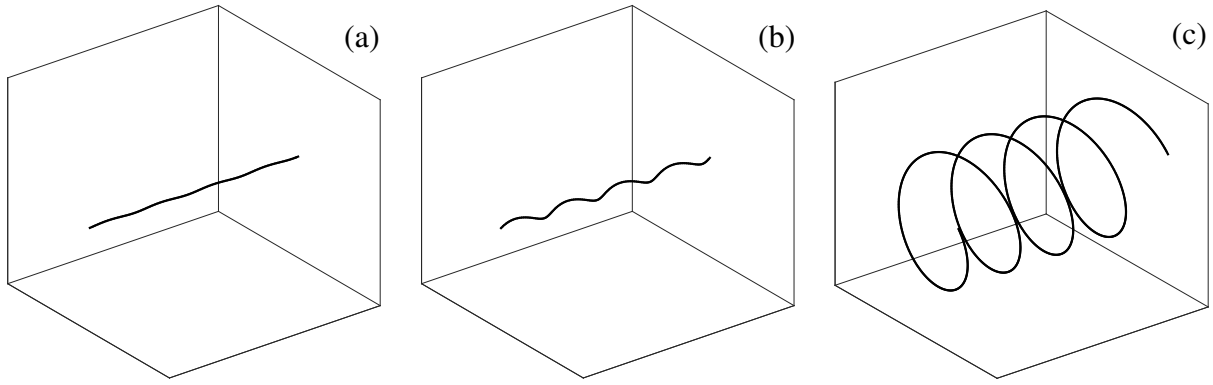

Figure 6.10: Growth of a helical perturbation in a linear flow, aligned with the initial vortex filament, due to the Donnelly-Glaberson instability, with time advancing from (a) to (b) to (c).

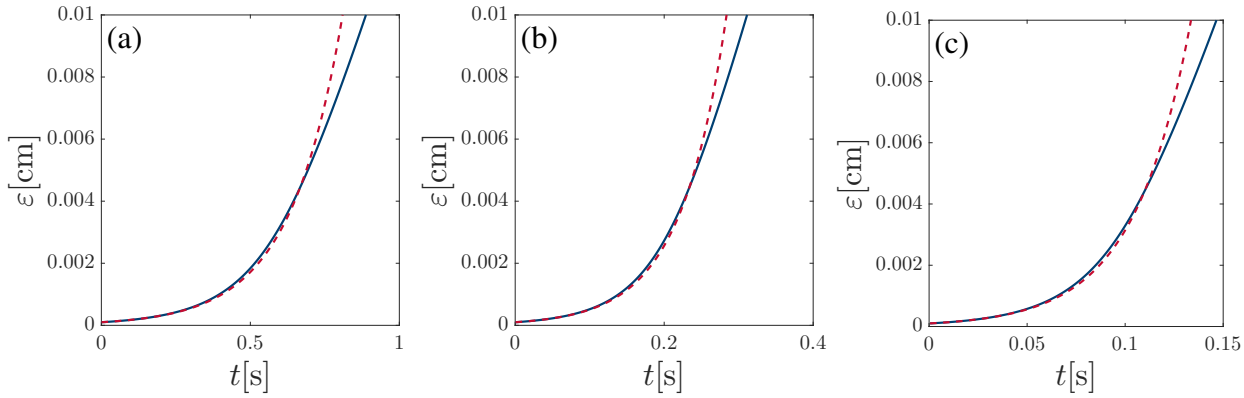

Figure 6.11: Theoretical (dashed red line) and simulated (solid blue line) growth of a helical perturbation with $\varepsilon(0) = 10^{-4}$, $k = 80\pi$, $v_{\mathrm{ns}} = 1$ cm/s at (a) 1.3 K, (b) 1.6 K, (c) 1.9 K. The simulation is performed in a $0.1 \times 0.1 \times 0.1$ cm^3 periodic box, with $\delta = 10^{-3}$ cm, $\Delta t = 10^{-5}$ s. Note the different time scales.

We can find a second expression for $(d\mathbf{s}/dt)$ by directly differentiating eq. (6.12) w.r.t. t, yielding:

$$\frac{d\mathbf{s}}{dt} = \begin{pmatrix} 0 \\ \varepsilon\omega \sin(kx - \omega t) + \frac{d\varepsilon}{dt}\cos(kx - \omega t) \\ -\varepsilon\omega \cos(kx - \omega t) + \frac{d\varepsilon}{dt}\sin(kx - \omega t) \end{pmatrix}.$$

Comparing the y-component of this expression with eq. (6.16):

$$\beta\varepsilon k^2 \sin(kx - \omega t) + \alpha(v_{\mathrm{n}} - \beta k - v_{\mathrm{s}})\varepsilon k \cos(kx - \omega t) = \varepsilon\omega \sin(kx - \omega t) + \frac{d\varepsilon}{dt}\cos(ks - \omega t).$$

Then comparing coefficients of $\cos(kx - \omega t)$ we find:

$$\frac{d\varepsilon}{dt} = \alpha(v_\mathrm{n} - \beta k - v_\mathrm{s})\varepsilon k$$

$$\implies \varepsilon(t) = \varepsilon(0)\exp\left[\alpha(v_\mathrm{n} - \beta k - v_\mathrm{s})kt\right],$$

where $\varepsilon(0)$ is the amplitude of our initial perturbation. We can then compare this analytic expression for the growth of a helical perturbation in a linear flow with simulations, shown in Fig. 6.11. It is apparent that the simulation is in good agreement with the theoretical prediction for almost two orders of magnitude of growth in the perturbation.

6.1.6 Reconstructing Trajectories

The calculation of the root-mean-square deviation, d_rms in Sec. 7.3 requires knowledge of the initial and current positions of discretisation points in our VFM simulations. This is complicated by the continual remeshing of the filaments necessary to maintain the selected spatial resolution: if we only include discretisation points that can be tracked through direct ancestors (see subsequent description of algorithm) since the first time-step we rapidly reach a situation where we have very little data to work with (Fig. 6.12(a)). If we are to include points that have been created during remeshing we need to determine where they originated. In this work we do this through an algorithmic procedure.

The configuration at the first time-step is stored as the origin of the points. We then compare the configuration at the next time-step to this. If a point has a clear ancestor at the previous time-step we assign the origin of that ancestor as the point's origin. We consider a point to have a clear ancestor if it has the same index in the array storing the points, and if either or both of the indices describing its immediate neighbours match the previous time-step. This leaves points where neither neighbour matches the neighbours of the point at the previous time-step, which can be the case when either both neighbours have newly been inserted, or both previous neighbours have been removed, or some combination of these, or when the point itself has been newly inserted (in which case its neighbours will most likely be null at the previous time-step; however the indices of removed points are reused for efficient memory usage, so we cannot rely on this).

In this case, we concatenate and store the origins of both neighbours as its origin, and take the average of the concatenated array as the value of the origin in calculations. If both neighbours are newly created points, this will be unable to assign an origin, but as this is a rare event, and is fixed at the next time-step (provided the same thing doesn't happen again by some fluke), we do not worry about this. This process is repeated for each subsequent time-step in turn, until the end of the simulation. To ensure that we are not taking an average of distant points as the origin of a point, we only accept the mean value of an origin array as the origin of the point if the standard deviation of the origin array is less than 2δ. This algorithm allows us to use $\sim$ 70% of the discretisation points after 2×10^5 time-steps (Fig. 6.12(b)). We illustrate the origins inferred by this algorithm in Fig. 6.13. We note that, referring to Fig. 6.1, points can be tracked through reconnections as they still retain one of their neighbours.

Having described our implementation of the vortex filament method and some relevant post-processing procedures, we now move on to the particular investigations of three-dimensional quantum turbulence which we have carried out.

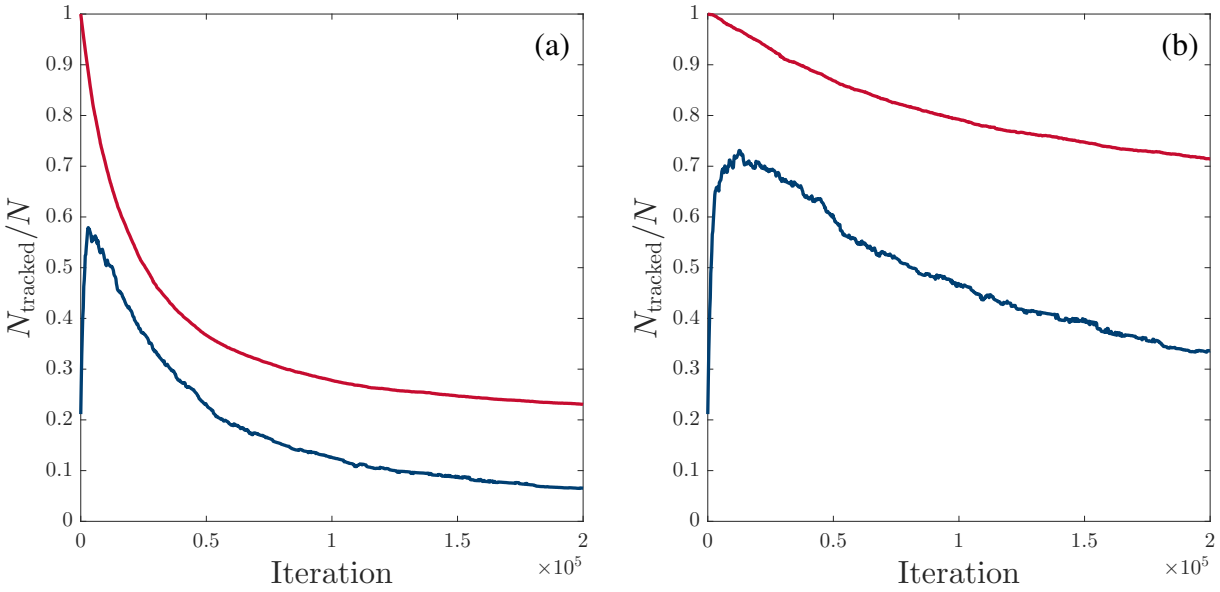

Figure 6.12: Proportion of points for which we infer an origin based on (a) direct ancestors and (b) the method described in this section. Red lines show the total proportion tracked, while blue lines show the proportion that are tracked, and which belong to vortex loops containing more than 200 discretisation points - loops containing fewer points are excluded from analysis, discussed in Sec. 7.3.1.

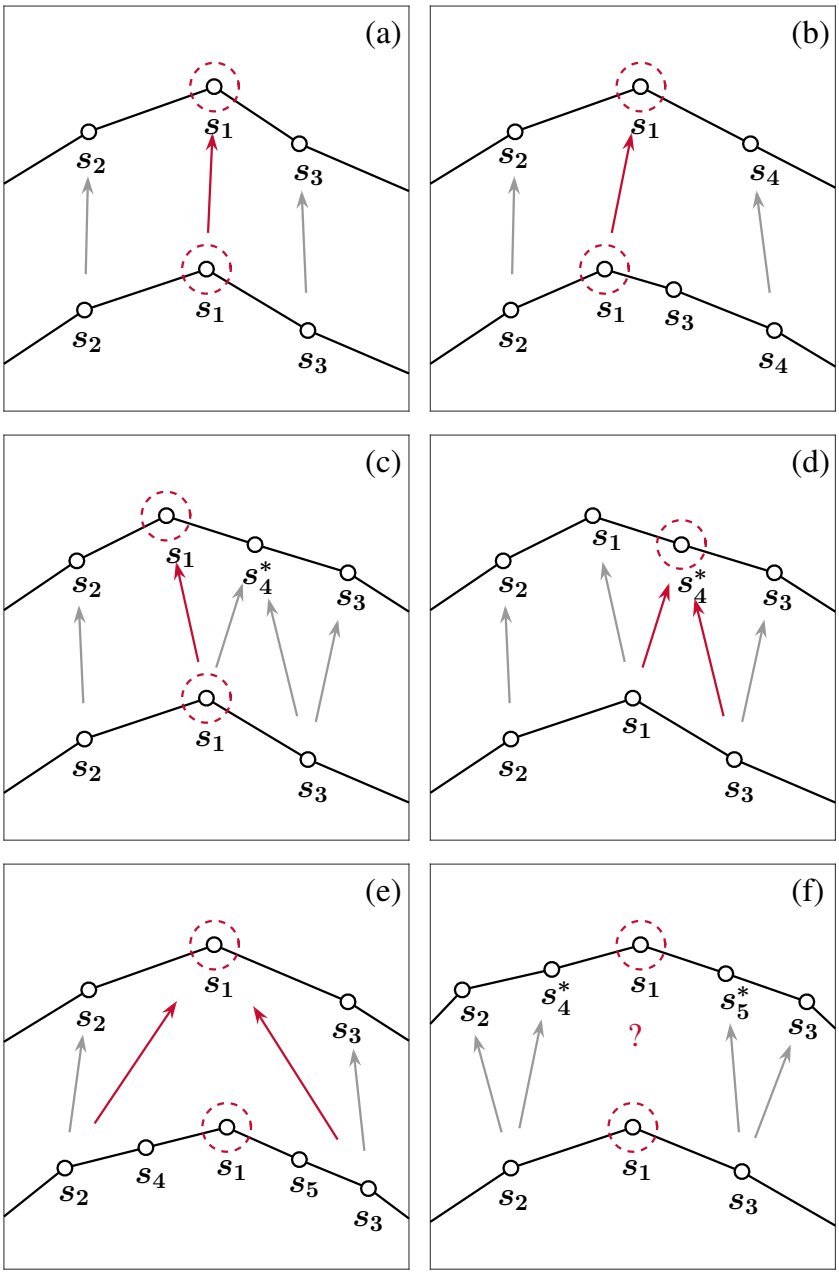

Figure 6.13: Schematic views of various point tracking possibilities, with time increasing from the bottom of the panels, and arrows indicating inheritance of origins. In (a-c) $\mathbf{s}_1$ has a clear ancestor, having at least one neighbour in common with the previous time-step, in (d), a new point has been created by remeshing, which then inherits ancestors from its neighbours, in (e), an existing point has both neighbours removed by remeshing, and its origin is inherited from its new neighbours, and in (f) new points are created by remeshing on either side of an existing point, and the point inherits no origin (for at least one time-step). Note that subscripts here refer to the position of the point in the numerical array, not the physical order along the filament.

Chapter 7

3-D Numerical Experiments & Results

In this chapter we shall probe some important properties of ultraquantum turbulence in ^{4}He through numerical simulations. In particular, we examine the parameter χ_2 in Vinen's equation, which relates the rate of dissipation of ultraquantum turbulence to the vortex line density, the parameter γ arising from Vinen's equation which relates the intensity of turbulence to the relative motion of the two fluid components, and the effective viscosity in quantum turbulence. We also address how localised quantum turbulence spreads into a surrounding vorticity free region, which is relevant to experiments that generate turbulence locally.

7.1 Steady-State Counterflow

In Sec. 5.3 we introduced Vinen's equation:

$$\frac{dL}{dt} = \chi_1 \frac{B}{2} \frac{\rho_\mathrm{n}}{\rho} |\mathbf{v}_\mathrm{ns}| L^{3/2} - \frac{\kappa}{2\pi} \chi_2 L^2,$$

which describes the evolution of the vortex line density (VLD) L in superfluid helium in the presence of a counterflow, where $B = (2\rho/\rho_\mathrm{n})\alpha$ is a mutual friction parameter, χ_1 and χ_2 are dimensionless parameters, and $\mathbf{v}_\mathrm{ns} = \mathbf{v}_\mathrm{n} - \mathbf{v}_\mathrm{s}$ is the counterflow velocity. Setting $(dL/dt) = 0$ produces a steady solution $L = \gamma^2 |\mathbf{v}_\mathrm{ns}|^2$, where γ is a temperature-dependent parameter. This scaling has been confirmed in multiple experiments [34, 346, 347], but only relatively recently have simulations at the individual vortex level been performed which well capture this [328] - pioneering simulations by Schwarz [262, 313, 315, 329] were reliant on the LIA due to computational limitations. In the presence of a counterflow, vortex filaments simulated using the LIA become increasingly aligned perpendicular to the flow, and aligned with other vortex filaments (see Fig. 7.1), resulting in an anomalously dense and anisotropic tangle [328]. Schwarz circumvented this behaviour by rotating randomly selected vortex lines through 90° to introduce some mixing and drive the system back towards an isotropic state, but this is clearly an extremely artificial procedure without physical justification. In [328], simulations performed using the full Biot-Savart law found values

of γ in good agreement with experimental values, without any phenomenological mixing procedure, with the anisotropy of vortices far less pronounced than under the LIA.

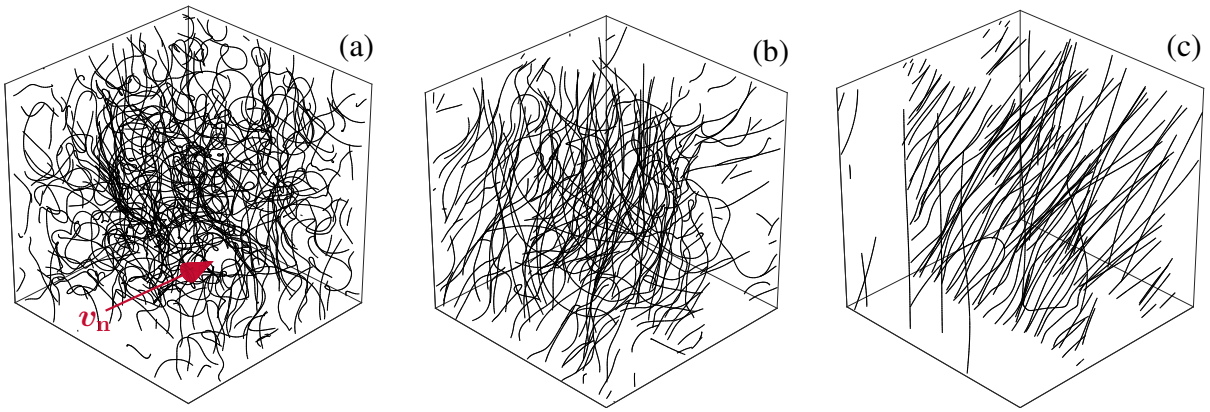

Figure 7.1: Snapshots of a counterflow simulation using the VFM and the LIA in a $0.05 \times 0.05 \times 0.05$ cm^3 periodic box, with the counterflow direction indicated. Panel (a) shows the simulation at 1 s, (b) at 2 s, (c) at 4 s. The vortex configuration becomes increasingly anisotropic as the simulation progresses, quantified by the anistropy parameter parallel to the flow (defined in main text) as $I_{||} = 0.795$ (a), $I_{||} = 0.905$ (b), and $I_{||} = 0.984$ (c).

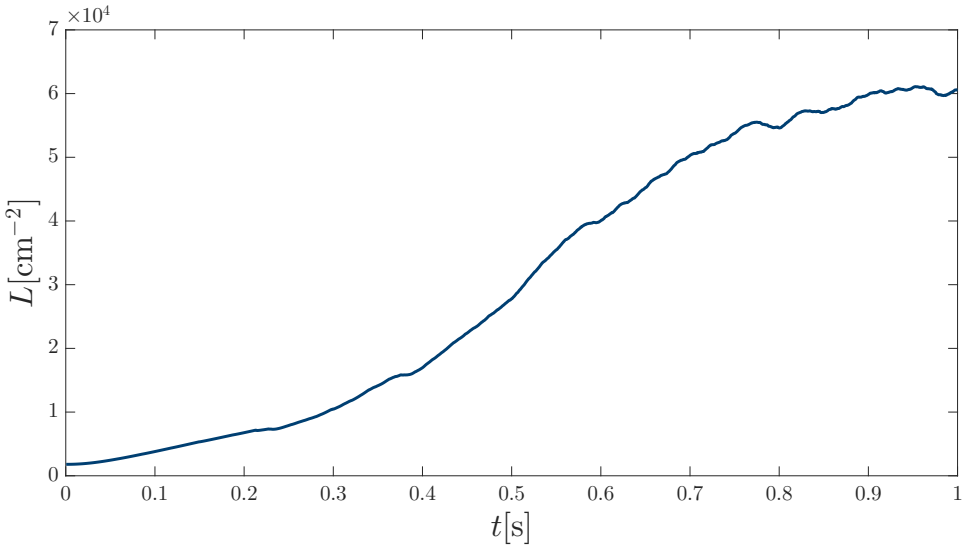

Figure 7.2: Growth of the vortex line density during initial evolution using the LIA. This particular example, typical of all temperatures and values of $|\mathbf{v}_{ns}|$, is for 1.7 K and $|\mathbf{v}_{ns}| = 1.4$ cm/s.

In this section we perform a large number of counterflow simulations with the aim of increasing the amount of available data on γ, as values have only been estimated for a handful of temperatures. Comparison with previous studies also acts as a final verification for the implementation of the VFM.

We use the VFM in a periodic box, which is enforced by a periodic wrapping as discussed in Sec. 6.1.4. A normal flow with speed $v_{\rm n}$ is imposed, and an opposing superflow with speed $v_{\rm s} = -\rho_{\rm n}/\rho_{\rm s} v_{\rm n}$ We initialise simulations with a small number of seed vortex rings, and evolve the system using the LIA until the VLD appears to saturate (Fig. 7.2). The initial rings grow or shrink depending on their orientation with respect to the counterflow, until they begin to reconnect with each other, redistributing the vortex lines into structures with smaller radius of curvature, which is turn grow and shrink, eventually filling the system - shown in Fig. 7.3. We then switch to the tree algorithm, and evolve the system until a statistically steady state is reached.

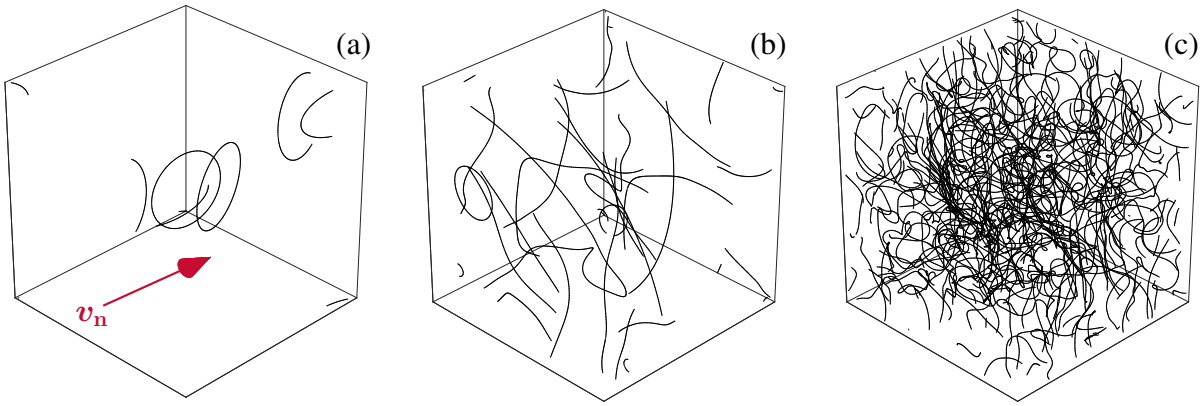

Figure 7.3: Snapshots of the development of a vortex tangle, in a $0.05 \times 0.05 \times 0.05$ cm^3 periodic box, from initial seed vortex rings, taken from the same simulation as Fig. 7.2, at the initial time (a), 0.25 s (b), and 1 s (c).

In order to expedite the simulations we select D, the length of a side of the periodic box, based on the expected intensity of the simulations. We can estimate L for a particular simulation based on the value of $|\mathbf{v}_{\rm ns}|$ and γ (using either values of γ from experiments if available or interpolating if not), which then gives an estimate of the typical intervortex distance as $\ell = 1/\sqrt{L}$. We then choose $D = 10\ell$, and $\delta = \ell/10$, to give a reasonable separation of length scales, with the time-step then set by eq. (6.11). Calculating the longitudinal velocity structure function:

$$f_x(r) = \frac{\langle v_x(\mathbf{r}) v_x(\mathbf{r} + r\hat{\mathbf{e}}_x)\rangle}{\langle v_x(\mathbf{r})^2\rangle},$$

which measures the correlation at a separation of r, at late times (with one example shown in Fig. 7.4), we find a typical values $f_x(\ell/2) \simeq 0.13$, $f_y(\ell/2) \simeq 0.19$, $f_z(\ell/2) \simeq 0.19$ (with the difference between $f_x(\ell/2)$ and the others due to the anisotropy). This is indicative of a lack of large-scale structure, as expected for ultraquantum turbulence, justifying the use of a small periodic box. Simulations are performed for 1.3 K, 1.4 K, 1.5 K, 1.6 K, 1.7 K, 1.8 K, and 1.9 K, at six different normal fluid velocities for each.

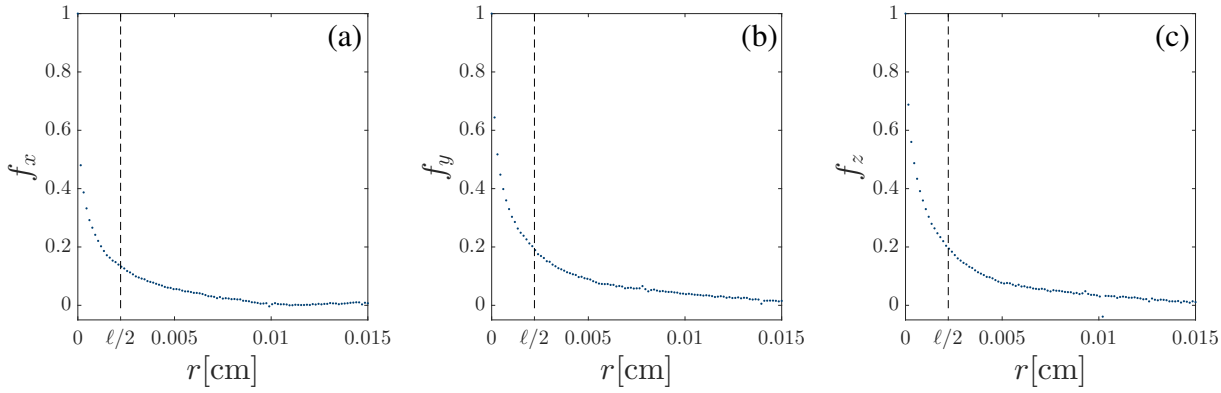

Figure 7.4: Velocity structure functions in the x (a), y (b), and z (c) directions, calculated for one snapshot of the developed vortex tangle for the simulation at $T = 1.9$ K with $|\mathbf{v}_{\rm ns}| = 1.4$ cm/s.

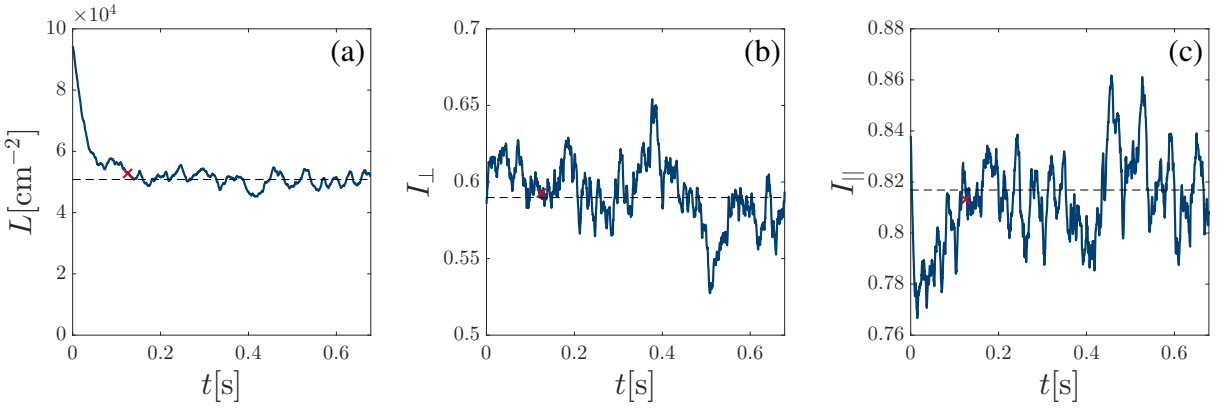

Figure 7.5: Evolution of the vortex line density (a) and anisotropy parameters (b,c) for one simulation at 1.9 K, $|\mathbf{v}_{\rm ns}| = 1.4$ cm/s after the switch from the LIA to the tree algorithm. In (a) we illustrate the removal of the transient initial period, as described in the main text, with only data to the right of the red cross considered in the final analysis. The mean values after this transient period are indicated by black dashed lines.

We will quantify the anisotropy of the vortex tangles using the following quantities [315]:

$$I_\parallel = \frac{1}{LD^3}\int_{\mathcal{L}} \left[1 - (\mathbf{s}' \cdot \hat{\mathbf{r}}_\parallel)^2\right] d\xi,$$

$$I_\perp = \frac{1}{LD^3}\int_{\mathcal{L}} \left[1 - (\mathbf{s}' \cdot \hat{\mathbf{r}}_\perp)^2\right] d\xi,$$

with $\hat{\mathbf{r}_\parallel}$ and $\hat{\mathbf{r}_\perp}$ respectively units vectors parallel and perpendicular to the counterflow, and $\mathcal{L}$ signifying integration over all vortex lines. For isotropic configurations $\langle I_\parallel \rangle = \langle I_\perp \rangle = 2/3$, while if the vortices lie entirely in the plane perpendicular to the counterflow $\langle I_\parallel \rangle = 1$,

$\langle I_\perp \rangle = 1/2$. We show the evolution of L and the anisotropy parameters for one typical simulation, after the switch to the tree algorithm, in Fig. 7.5. We observe that in all simulations the vortex line density decreases; this is expected from the anomalously high VLD generated by the LIA. In Fig. 7.6 we compare the VLD of two simulations at the same temperature and counterflow velocity. One is initialised using the procedure described, and the other is initialised with a few seed vortices and evolved using the tree algorithm for the entire simulation. The two simulations tend to the same saturated VLD, and we are satisfied that the eventual saturated value is not influenced by our initialisation; this also provides some evidence for the independence of the long-term structure of the vortex tangle from the initial configuration.

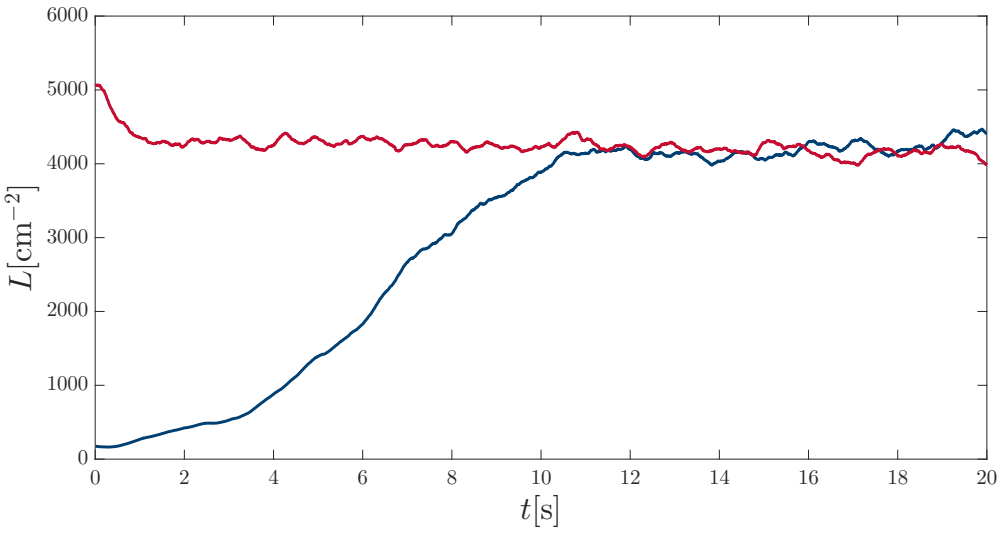

Figure 7.6: Evolution of the vortex line density for two simulations using the tree algorithm at 1.3 K, $|\mathbf{v}_{\mathrm{ns}}| = 1$ cm/s, initialised with a few seed vortex rings (blue) and with the tangle found using the LIA (red).

When calculating the mean value of L for statistically steady states we need to ensure that we do not include the initial transient period. We do this by calculating the mean of L for the portion of the simulation after switching to the tree algorithm, and identifying the first time at which L is below the mean. The data before this time is then disregarded in the analysis, as illustrated in Fig. 7.5.

We then estimate γ by linear regression to $\sqrt{L}$ vs. $|\mathbf{v}_{\mathrm{ns}}|$, shown in Fig. 7.7. The linear relation between $\sqrt{L}$ and $|\mathbf{v}_{\mathrm{ns}}|$ is evident, in agreement with theoretical predictions and previous experiments and simulations. The values of γ estimated from these fits, shown in Fig. 7.8, are in reasonable agreement with previous studies, although slightly higher, which we discuss in the next section.

We also examine the dependence of the anisotropy on the counterflow velocity (Fig. 7.9), and on the temperature (Fig. 7.10). In agreement with previous studies, we find the counterflow velocity does not significantly influence the anisotropy in the range of values under consideration, while the anisotropy is affected by the temperature, increasing as the temperature increases. The specific values of the anisotropy parameters we find are in good

agreement with previous studies.

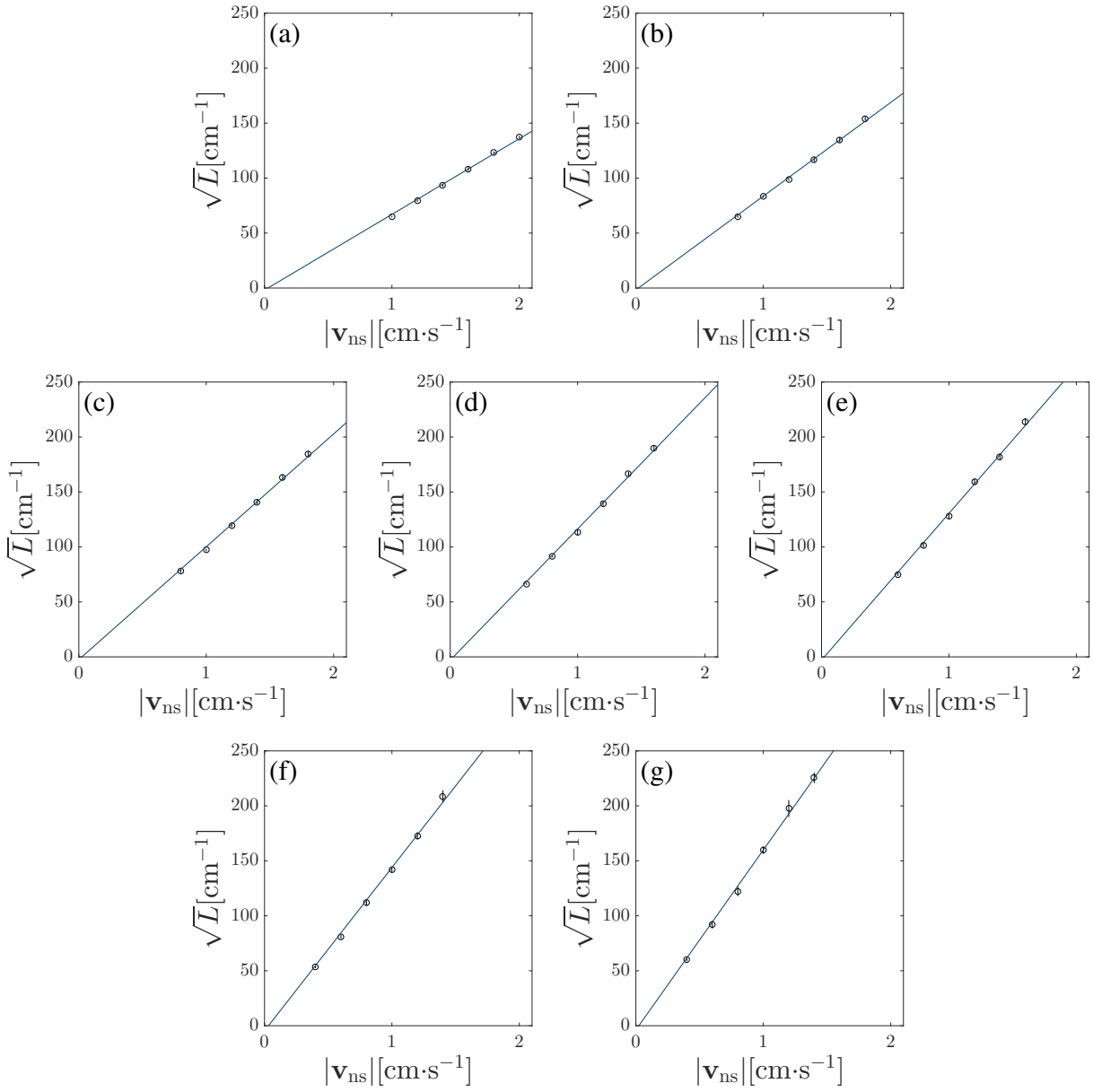

Figure 7.7: Values of $\sqrt{L}$ vs. the counterflow velocity at different temperatures: (a) 1.3 K, (b) 1.4 K, (c) 1.5 K, (d) 1.6 K, (e) 1.7 K, (f) 1.8 K, (g) 1.9 K, with linear regression shown.

7.1.1 Discussion

In this section we have probed values of the parameter γ which describes the balance between the generation and decay of vortex line density in counterflows. We use an established method, pioneered by Schwarz [262, 313, 315, 329], in which a few seed vortices in a periodic box with a constant counterflow are simulated (although we use the LIA initially

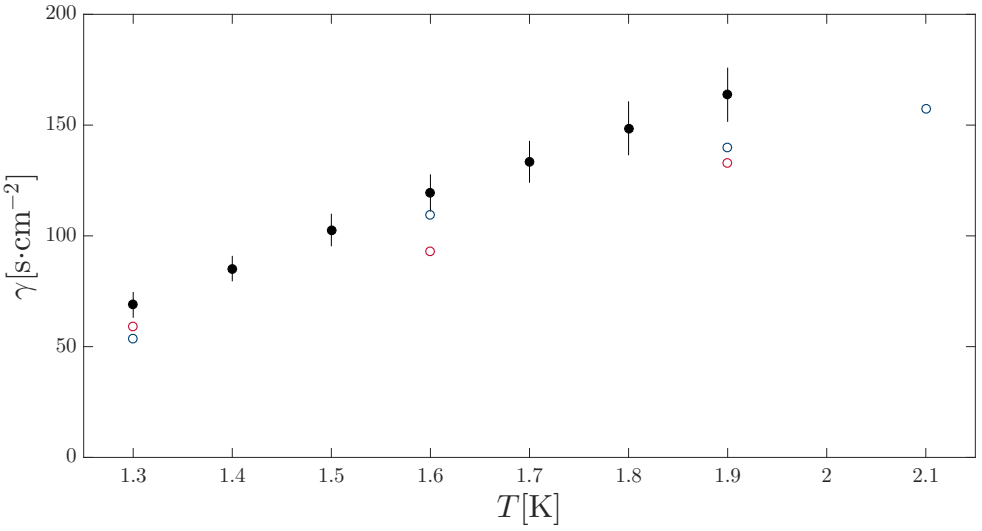

Figure 7.8: Values of the parameter γ estimated from these simulations (black) with 95% margin of error indicated. Values from previous simulations [328] are shown in red, and experimental values [34, 332] in blue.

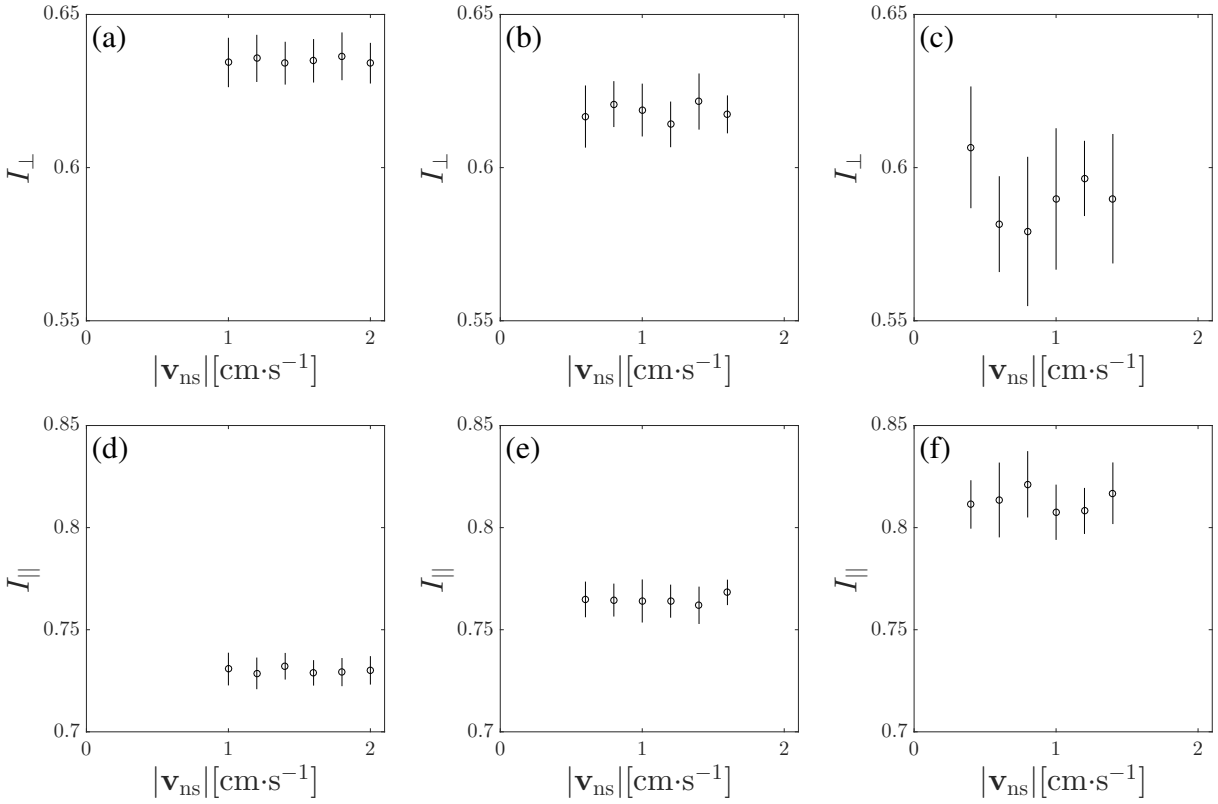

Figure 7.9: Mean value of anisotropy parameters for statistically steady states as a function of the counterflow velocity, for (a) 1.3 K, (b) 1.6 K, and (c) 1.9 K.

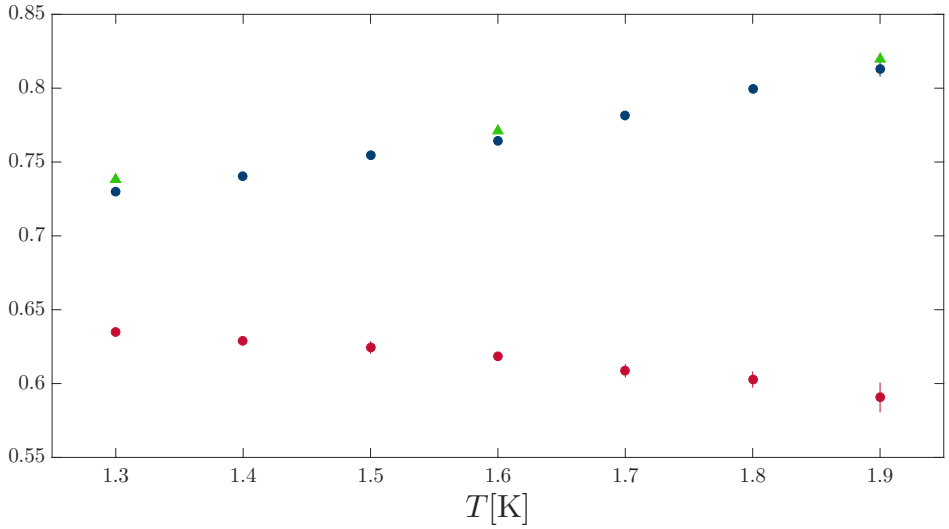

Figure 7.10: Mean value of anisotropy parameters $L_\perp$ (red) and $L_{||}$ (blue) for statistically steady states as a function of temperature, with values from previous numerical studies [328] (green).

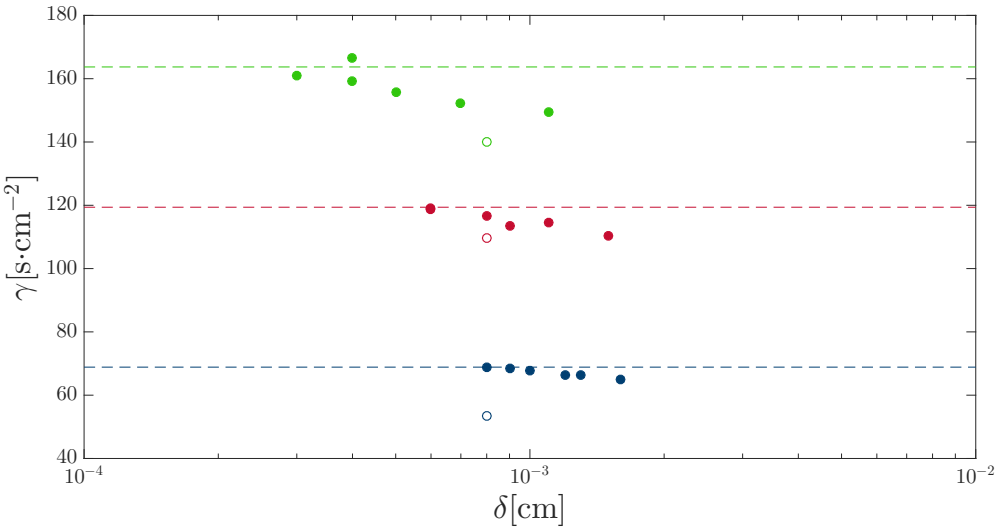

Figure 7.11: Comparison of γ with the spatial resolution δ, for $T = 1.3$ K (blue), $T = 1.6$ K (red), and $T = 1.9$ K (green). Hollow discs correspond to the simulations of Adachi *et al.* [328], and solid discs correspond to the simulations described in this work, with the dashed lines indicating the values of γ found by linear regression.

before switching to a tree algorithm for the full Biot-Savart law), resulting in a statistically steady state, from which γ can be inferred. However, whilst previous studies have used a fixed box size and numerical resolution, we choose these parameters based on the temperature and counterflow velocity of the particular simulation, with the aim of ensuring a rea-

sonable separation of scales, and avoiding the simulation of very large tangles - as the turbulence generated is in the ultraquantum regime there is no large-scale structure, so it is not necessary to simulate scales far above the intervortex spacing - indeed, even our target of $D = 10\ell$ may be excessive, as Fig. 7.4 shows the correlation is negligible at a separation of $D/2$. This approach also has potential for probing a wider range of values of $|\mathbf{v}_{\rm ns}|$, and for probing the structure of vortex tangles at temperatures close to T_λ.

In agreement with theoretical predictions and previous studies, the VLD clearly scales with $|\mathbf{v}_{\rm ns}|^2$. The specific values of γ found are comparable to previous studies, although somewhat higher. In Fig. 7.11 we consider values of γ found from selected individual simulations (calculated as $\gamma = \sqrt{\bar{L}}/|\mathbf{v}_{\rm ns}|$). Although they are all higher than those found by Adachi *et al.*, we note that the values increase as the numerical resolution improves; this may be related to the fractal nature [348, 349] of vortex tangles, and the improved capacity to capture such smaller features; further simulations at higher $|\mathbf{v}_{\rm ns}|$ and with correspondingly smaller δ could usefully explore this trend.

It should be emphasised that these simulations do not make any attempt to account for the back-reaction of the vortices on the normal fluid, and so truly relate to the TI regime, where the normal fluid flow is laminar. Experiments have been performed in this context [34, 35], as well as the related contexts of the TII regime, where both normal and superfluid components are believed to be turbulent [34], and pure superflow in channels with superleaks at both ends, with flow generated both mechanically [219] and thermally [347, 350]. We put the results of this study in this context in Fig. 7.12.

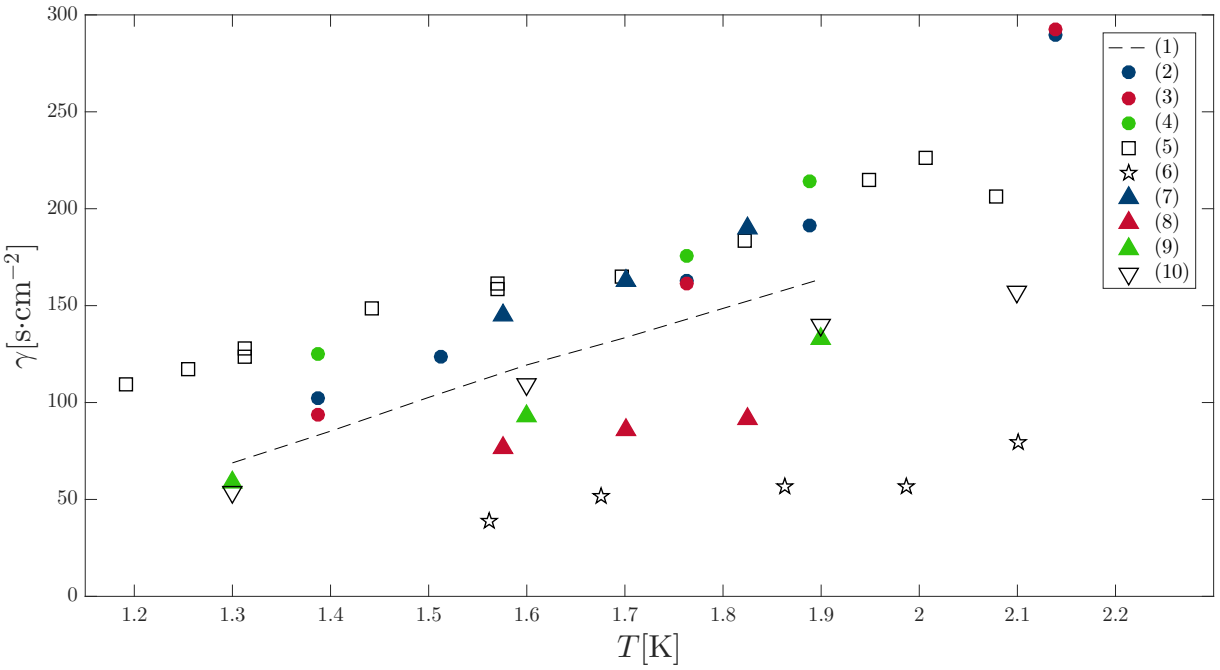

Figure 7.12: Comparison of γ calculated from experiments and simulations, adapted from [219]: (1) this work, (2) bellows-driven superflow in a 7 mm channel; (3) in a 7 mm channel without downstream superleak; (4) in a 10 mm channel [219], (5) thermally induced superflow in a 0.13 mm channel [347], (6) thermally induced superflow in a 7 mm channel [350], (7) counterflow in a 1 mm channel, TI regime; (8) TII regime [35], (9) counterflow in a 0.13 mm channel, TI regime [34], (10) numerical simulation [328].

7.2 Dissipation

A major source of the dissipation of kinetic energy in ultraquantum turbulence in helium at zero temperature is believed to be the emission of phonons by high-frequency Kelvin waves [163, 169], excited by reconnection events [166]. Although the scales at which this mechanism occurs are inaccessible to the vortex filament method with current computers, this dissipation is emulated by numerical dissipation due to the discretisation of vortex filaments. In Vinen's equation, eq. (5.8), the dissipation is modelled by the $-\chi_2(\kappa/2\pi)L^2$ term, with the square arising from the two-body nature of reconnections, and the dimensionless parameter χ_2 characterising the strength of dissipation.

In this section we shall probe values of χ_2 in the zero temperature limit, spurred on by several points. Firstly, in the subsequent section, "3-D Diffusion", one method for estimating the effective viscosity at 0 K requires knowledge of χ_2, prompting a revisition of this topic. A previous estimate found $\chi_2 \approx 0.3$ from the decay of a homogeneous tangle simulated with the LIA [186]; it is now feasible to repeat this investigation using a more accurate model, either the full Biot-Savart law or a tree algorithm. Furthermore, this method assumes that χ_2 does not depend on L, which may not be the case.

Secondly, in a recent paper [215] Gao *et al.* find values of χ_2 for temperatures between

1.4 K and 1.7 K by performing thermal counterflow simulations. By considering the energy per unit mass associated with a random tangle of vortices, and relating this through the quantum kinetic energy dissipation equation $(dE/dt) = -\nu'\kappa^2 L^2$, to Vinen's equation (without generation), they find an expression:

$$\chi_2 = \frac{\alpha c_2^2}{2} \ln\left[\frac{\ell}{\xi_0}\right], \tag{7.1}$$

where α is a mutual friction parameter, ℓ is the characteristic intervortex spacing $\ell = 1/\sqrt{L}$, ξ_0 is the vortex core parameter, and c_2 is a dimensionless parameter relating the mean-square curvature of the vortices to their density as:

$$\left\langle \left[\frac{1}{R^2}\right] \right\rangle = c_2^2 L,$$

where R is the local radius of curvature. Although this method is not applicable at zero temperature, as this condition precludes counterflow, this approach inspired us to seek a steady state approach to the zero temperature limit.

7.2.1 Decay Method

In the absence of a relative motion between the two fluids, or at 0 K, Vinen's equation reduces to:

$$\frac{dL}{dt} = -\chi_2 \frac{\kappa}{2\pi} L^2,$$

which, assuming χ_2 is constant, is separable, immediately giving:

$$L^{-1}(t) = L_0^{-1} + \chi_2 \frac{\kappa}{2\pi} t,$$

where L_0 is the vortex line density at $t = 0$ s. We can then estimate χ_2 by tracking the inverse line density of a decaying homogeneous tangle.

We generate an initial state by injecting randomly oriented and randomly translated vortex loops into a $1 \times 1 \times 1$ cm^3 periodic box at a constant rate until the vortex line density saturates. We then evolve the system with the tree algorithm for the Biot-Savart law and a 3$^{\text{rd}}$-order Adams-Bashforth scheme, with a spatial resolution of 0.02 cm and a time-step of 5×10^{-3} s. We confirm the homogeneity of the system by examining the vortex line density as a function of each cartesian direction, shown in Fig. 7.13. We test the isotropy of the configuration by comparing the projected line length onto the yz-, xz-, and xy-planes, respectively referred to as Λ_x, Λ_y, and Λ_z. For an isotropic tangle $\langle\Lambda_x\rangle = \langle\Lambda_y\rangle = \langle\Lambda_z\rangle$; we find $\Lambda_x \approx 49.8$ cm, $\Lambda_y \approx 50.0$ cm, $\Lambda_z \approx 50.9$ cm, and so are satisfied that our initial configuration is isotropic. Finally, we calculate the longitudinal velocity structure function in the x-direction (as the choice of direction is arbitrary if we accept that the system is isotropic), shown in Fig. 7.14, finding $f_x(\ell/2) \approx 0.1$; the lack of long-range correlation or structure is a clear indication that the tangle is random, consistent with ultraquantum turbulence.

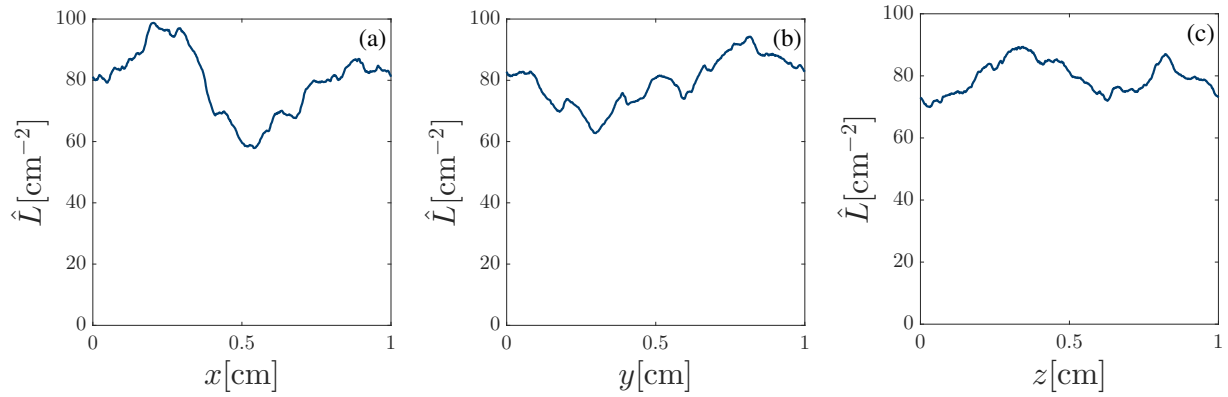

Figure 7.13: Local vortex line density of the initial configuration vs. x, y, and z, calculated over a region of 0.1 cm either side of the coordinate value under consideration to avoid noise from small-scale fluctuations.

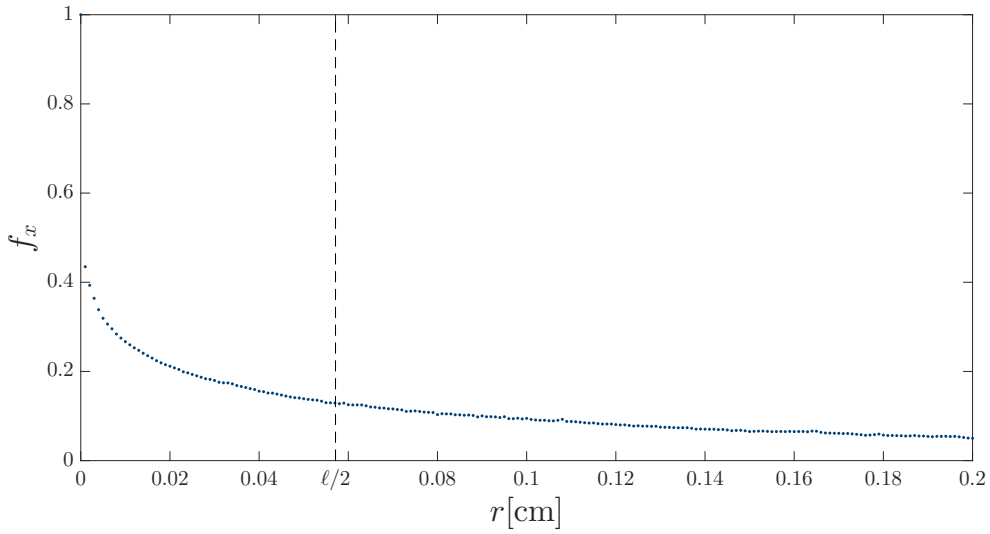

Figure 7.14: Longitudinal velocity structure function in the x-direction for the developed tangle formed by random injection of vortex loops, with half the characteristic intervortex spacing ℓ indicated.

Having satisfied ourselves that our initial condition is suitable we allow the configuration to evolve without forcing, with the configuration at three times shown in Fig. 7.15. We show the inverse line density as a function of time in Fig. 7.16, with a fitted line. For comparison we also show the inverse line density found by evolving the same initial configuration with the LIA. The slope of the fitted line estimates $(\kappa/2\pi)\chi_2$, and we estimate $\chi_2 \approx 0.596$ from the tree algorithm simulation, and $\chi_2 \approx 0.475$ from the LIA simulation.

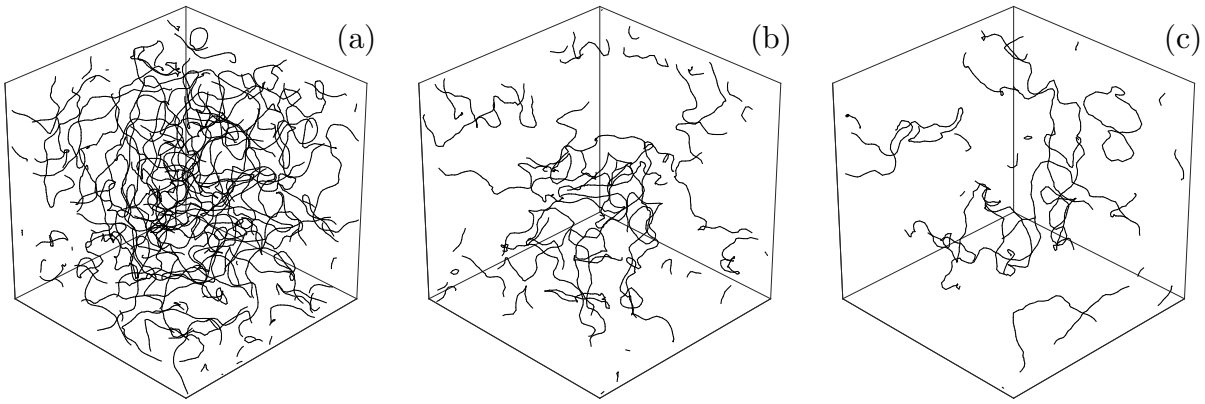

Figure 7.15: Visualisation of a decaying vortex tangle in a periodic box simulated with the tree algorithm for the VFM. The configuration in the full $1\times1\times1$ cm^3 periodic box is shown at the initial time (a), at 250 s (b), and at 500 s (c).

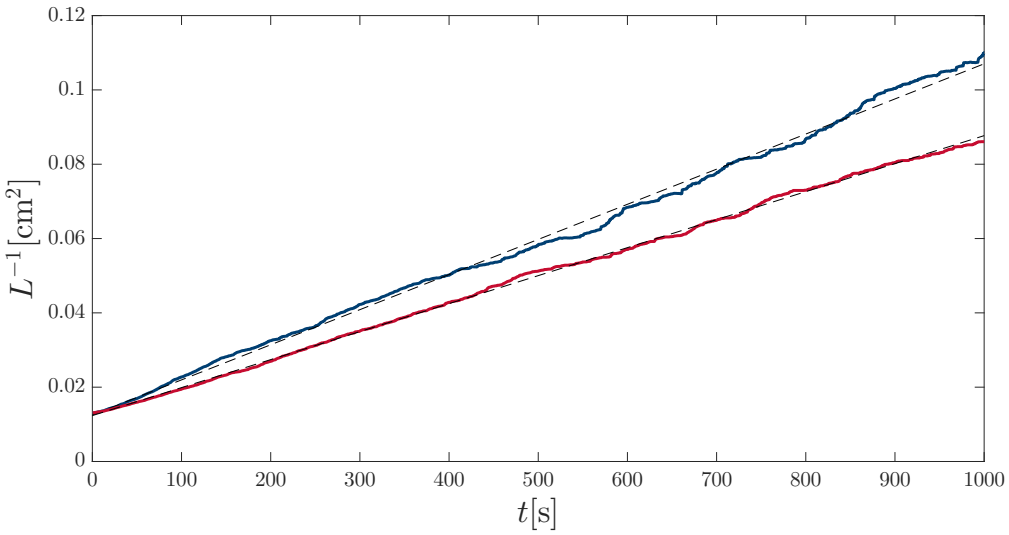

Figure 7.16: Inverse line density of a decaying homogeneous vortex tangle vs. t, for simulations using the LIA (red) and using the tree algorithm for the Biot-Savart law (blue), with linear regression (black dashed) to each.

7.2.2 Steady State Method

In steady state thermal counterflow, the vortex line length is increased by the stretching of vortices depending on their orientation with respect to the flow, balanced by the dissipation of vortex line length by reconnections. This dissipation still occurs at zero temperature, but the only steady state is the trivial zero density state as no counterflow can exist. We explore an alternative method for finding a non-trivial steady state, and use it to estimate values of χ_2 as a function of L.

Starting from an empty $1 \times 1 \times 1$ cm^3 periodic box, we inject randomly translated and randomly oriented vortex loops of radius 0.0334 cm at a constant rate while evolving the

system in time. The system is evolved using the tree algorithm, with the same spatial resolution and time-step as the decay simulations. As the loops begin to fill the box, they start to reconnect, forming a complicated vortex tangle which eventually reaches a statistically steady state, shown in Fig. 7.17, with the evolution of the vortex line density shown in Fig. 7.18.

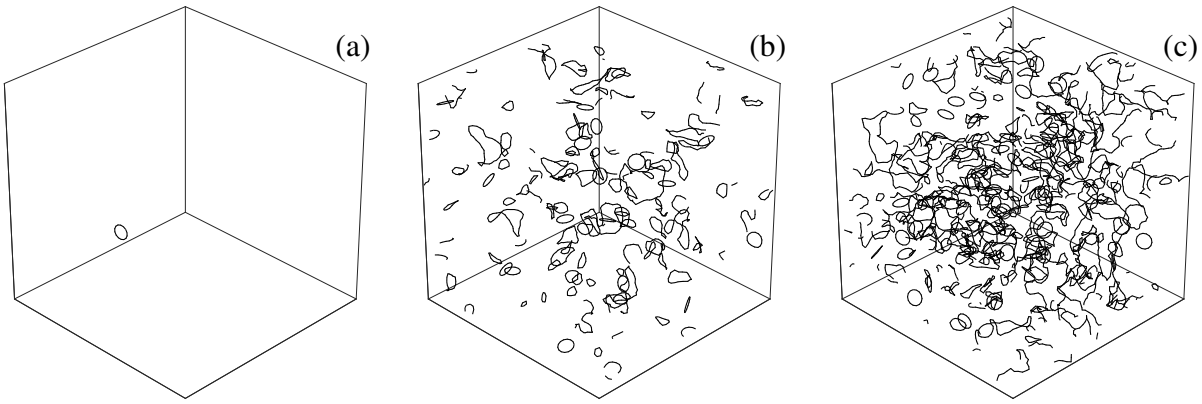

Figure 7.17: Development of a vortex tangle in a $1 \times 1 \times 1$ cm^3 periodic box by injection of vortex rings with radius 0.0334 cm every 0.1 s. Panel (a) shows the initial configuration, a single ring. Panel (b) shows the configuration at $t = 25$ s, by which time vortex rings have begun to collide and reconnect, forming more complicated structures. Panel (c) shows the configuration at $t = 1000$ s, by which time the vortex tangle has filled the periodic box and reached a statistically steady state.

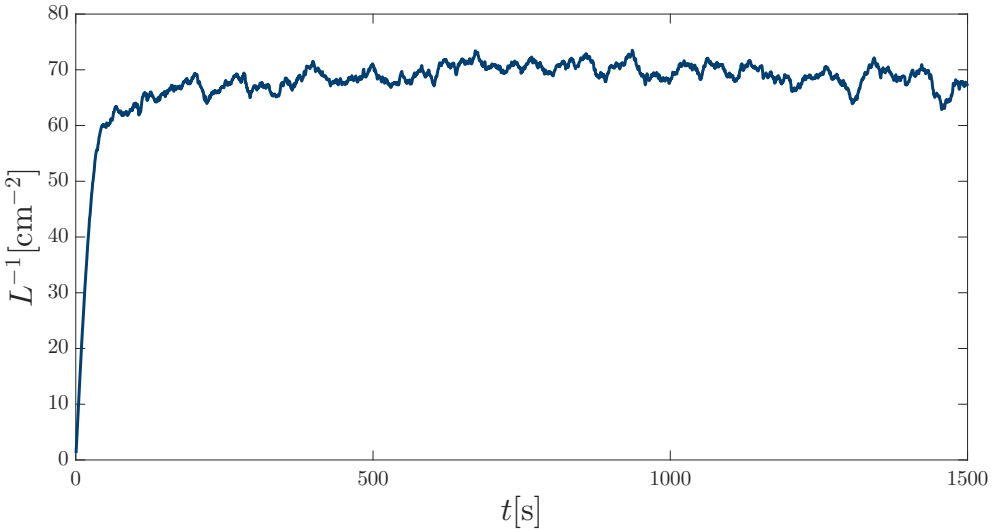

Figure 7.18: Evolution of the vortex line density for the simulation shown in Fig. 7.17 where vortex rings of radius 0.0334 cm are injected every 0.1 s.

As we are injecting vortices of the same size at a constant rate we can easily determine the

rate at which we are injecting vortex line density, denoted L_{inj}, which emulates the growth term in Vinen's equation, giving a modified version:

$$\frac{dL}{dt} = L_{\text{inj}} - \chi_2 \frac{\kappa}{2\pi} L^2.$$

For a statistically steady state the terms on the RHS must balance, and we find:

$$\chi_2 = \frac{2\pi}{\kappa} L_{\text{inj}} L^{-2}, \tag{7.2}$$

where L is the vortex line density of the statistically steady state.

The advantage of this approach over a decay approach is the ability to probe the dependence of χ_2 on L by varying the injection rate, through which we can achieve different steady state values for L. In Fig. 7.19 we show the steady state value of L as a function of L_{inj}, and in Fig. 7.20 we show the values of χ_2, calculated using eq. (7.2), as a function of L. The quantities are clearly related by power laws, which we find to be $L \approx 47.0(L_{\text{inj}})^{0.562}$, and $\chi_2 \approx 6.73 L^{-0.223}$.

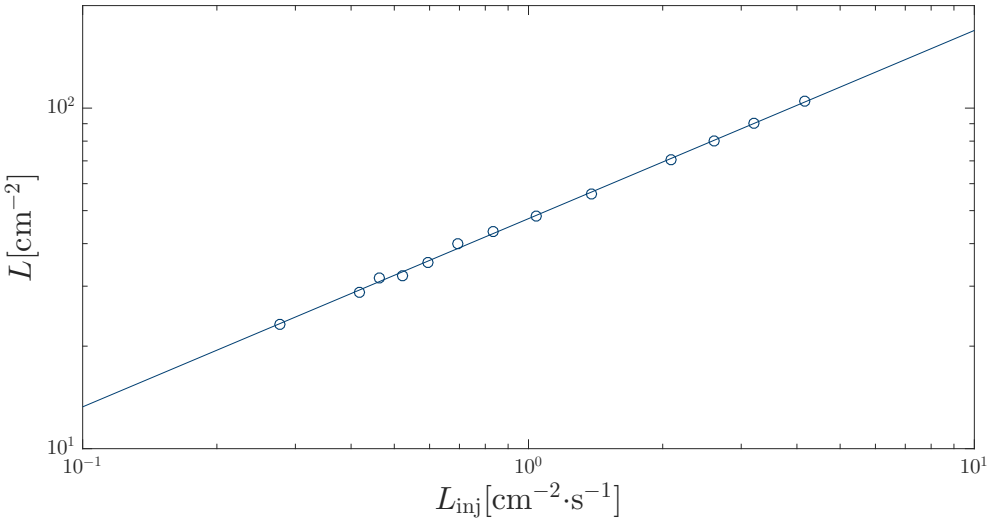

Figure 7.19: Mean vortex line density L of statistically steady states obtained by injecting vortex rings of radius 0.0334 cm, vs. the rate of injection of vortex line density L_{inj}, with fit $L \approx 47.0(L_{\text{inj}})^{0.562}$.

So far we have injected vortex loops of one fixed radius, and identified a relation between the rate of injection and the resulting vortex line density, and between the vortex line density and χ_2. However, the values of L_{inj} are not unique; we can reach the same value, by increasing the radius of the injected loops, while reducing the rate at which we inject them proportionally. Naturally, this prompts us to ask whether the resulting line density depends on the size of the injected rings, and moreover whether $\chi_2(L)$ is independent of their size - we note that a change in density alone may not be significant, if the

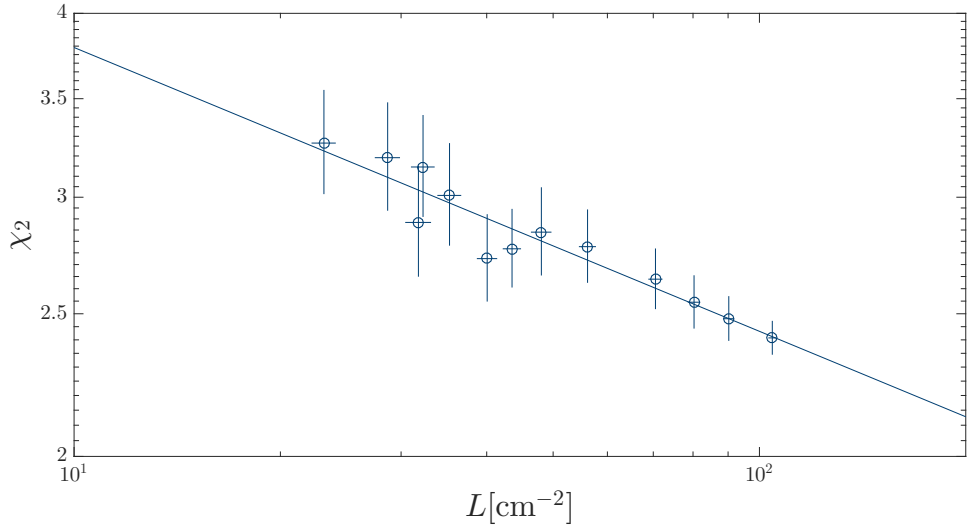

Figure 7.20: Values of χ_2 estimated from the values of L produced by particular injection rates, shown in Fig. 7.19, with fit $\chi_2 \approx 6.73 L^{-0.223}$.

value of χ_2 matches the value found at this particular density by the original set of simulations. With this in mind, we repeat the injection simulations, doubling the radius of injected rings and halving the frequency of injection, with the new values of L and χ_2 found shown in Fig. 7.21 and Fig. 7.22.

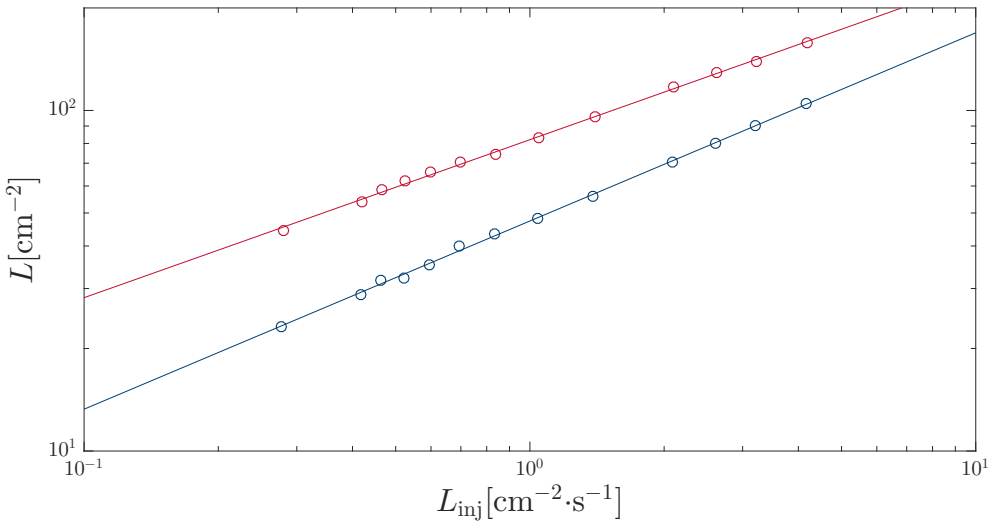

Figure 7.21: Mean vortex line density L of statistically steady states obtained by injecting vortex rings of radius 0.0334 cm (blue) and of radius 0.0668 cm (red), vs. the rate of injection of vortex line density L_{inj}, with fit $L \approx 79.3(L_{\mathrm{inj}})^{0.468}$ to the larger vortex rings.

Clearly, the change in injection size has drastically affected our estimates of χ_2. We find

lower values from the second set of simulations, and note that for our first set of simulations χ_2 appears to diverge as $L \to 0$, while χ_2 appears to tend to 0 in this limit in the

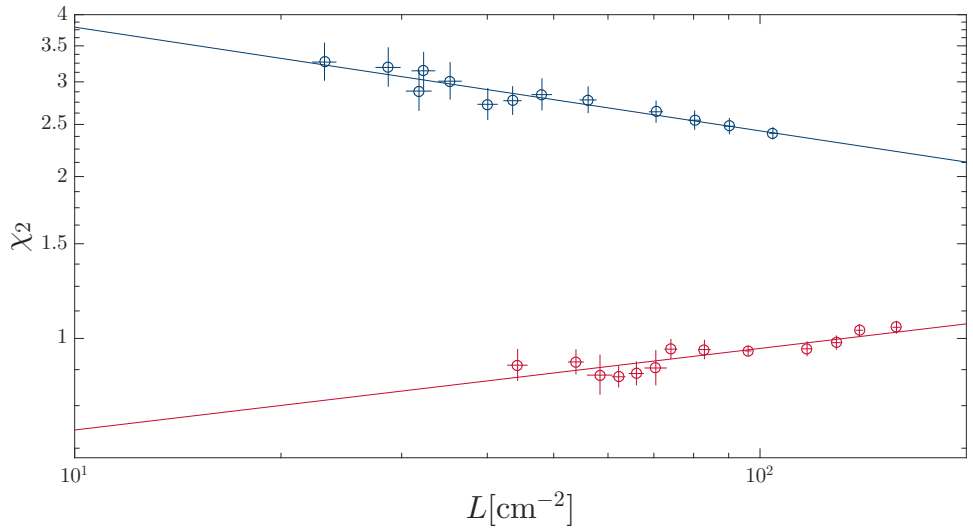

Figure 7.22: Values of χ_2 estimated from the values of L produced by particular injection rates of vortices with radius 0.0334 cm (blue), and with radius 0.0668 cm (red), with fit $\chi_2 \approx 0.553 L^{0.134}$ to the larger vortex rings.

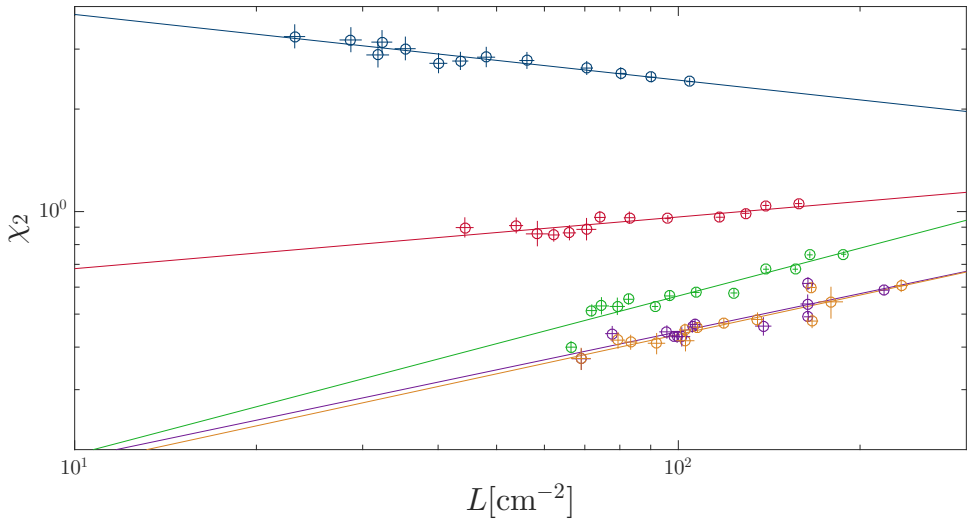

Figure 7.23: Values of χ_2 estimated from five sets of injection with increasing radius of the injected rings, while maintaining the same injection rates between the sets. Colours correspond to the radius of the injected rings, with radius 0.0334 cm (blue), 0.0668 cm (red), 0.134 cm (green), 0.267 cm (orange), and 0.534 cm (purple).

new set of simulations. To determine whether there is some general trend we perform three

further sets of simulations, each time doubling the radius of injected loops while holding L_{inj} the same, with estimates of χ_2 shown in Fig. 7.23. As we increase the size of the injected loops the estimated values of χ_2 converge, as shown by the fitted power laws, and we estimate $\chi_2(L) \approx 0.07L^{0.4}$.

7.2.3 Effective Viscosity

We can also use our estimates of χ_2 to estimate the effective viscosity. In classical fluids the rate of dissipation per unit mass is described by:

$$\frac{dE}{dt} = -\nu\omega^2,$$

which has quantum analogue:

$$\frac{dE}{dt} = -\nu'(\kappa L)^2. \tag{7.3}$$

The energy per unit mass can be written as $E = cL$, where c is a constant which we shall treat momentarily. Substituting this into eq. (7.3):

$$c\frac{dL}{dt} = -\nu'(\kappa L)^2 \implies \frac{dL}{dt} = -\frac{\nu'}{c}(\kappa L)^2.$$

From Vinen's equation, with no relative fluid motion, we have:

$$\frac{dL}{dt} = -\chi_2\frac{\kappa}{2\pi}L^2,$$

and hence we identify:

$$-\frac{\nu'}{c}(\kappa L)^2 = -\chi_2\frac{\kappa}{2\pi}L^2 \implies \frac{\nu'}{\kappa} = \chi_2\frac{c}{2\pi\kappa^2}. \tag{7.4}$$

We now consider the constant c. One can estimate the kinetic energy of a vortex per unit length, E', by considering a straight line vortex in the centre of a cylinder of radius b and unit height. The kinetic energy of the fluid is then:

$$\begin{aligned} E' &= \int_0^1 dz \int_0^{2\pi} d\theta \int_{a_0}^b \frac{\rho}{2}v^2 r dr, \qquad \text{where } v = \frac{\kappa}{2\pi r} \\ &= \rho\frac{\kappa^2}{4\pi}\int_{a_0}^b \frac{dr}{r} \\ &= \rho\frac{\kappa^2}{4\pi}\ln\left(\frac{b}{a_0}\right), \end{aligned}$$

where a_0 is the vortex core radius. Then:

$$\begin{aligned} E &= \frac{\text{kinetic energy}}{\text{mass}} = \frac{\text{kinetic energy}}{\rho \times \text{volume}} = \frac{\text{kinetic energy}}{\text{length}} \times \frac{\text{length}}{\text{volume}} \times \frac{1}{\rho} = E' \times L \times \frac{1}{\rho} \\ &= \frac{\kappa^2}{4\pi}\ln\left(\frac{\ell}{a_0}\right)L, \end{aligned}$$

where we have substituted $b = \ell = 1/\sqrt{L}$, the characteristic intervortex spacing, to give:

$$c = \frac{\kappa^2}{4\pi} \ln\left(\frac{\ell}{a_0}\right).$$

Substituting this into eq. (7.4) we find:

$$\frac{\nu'}{\kappa} = \frac{\chi_2}{8\pi^2} \ln\left(\frac{\ell}{a_0}\right). \tag{7.5}$$

In Fig. 7.24 we plot this estimate of ν'/κ based on our estimate of $\chi_2 = 0.596$ from the free decay of a vortex tangle, and based on our estimate $\chi_2 = 0.07L^{0.4}$ from the steady states found through injection.

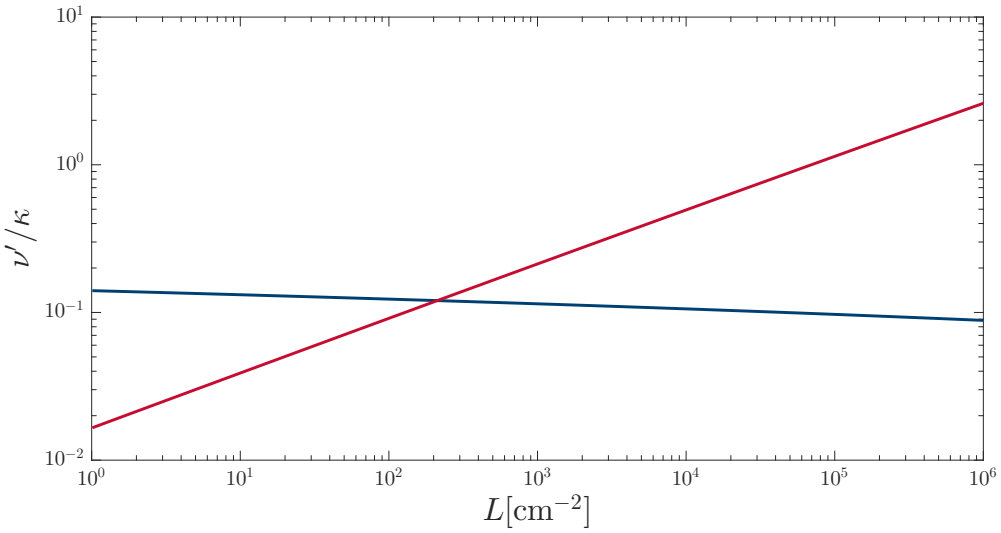

Figure 7.24: Estimates of ν'/κ as a function of L for $\chi_2 = 0.596$ (blue) and $\chi_2 = 0.07L^{0.4}$ (red).

7.2.4 Discussion

The most pressing point to address is the disparity between the form of χ_2 found when we inject vortices on different scales. For these simulations the relevant length scales are the box width D, the intervortex spacing ℓ, and the dissipation scale, which we take to be the radius R_0 of rings containing 5 or fewer discretisation points, which are removed algorithmically, with $R_0 \approx \delta/2$ based on our numerical resolution. In Fig. 7.25 we plot the steady state values of L found for selected values of L_{inj} as a function of the radius R_{inj} of the injected vortices, in units of R_0. We note that the radius of the smallest vortex rings is only three times the dissipation scale. Our understanding is that vortices injected at this scale are more readily dissipated than those further from the dissipation scale; this is reflected in the enhanced values of χ_2 found for this set of simulations.

The largest vortex rings injected, for which the estimates of χ_2 converge, are on a scale comparable to the box width. This is compatible with the mechanical generation of turbulence, where energy is injected at the largest length scales. However, it also invites further

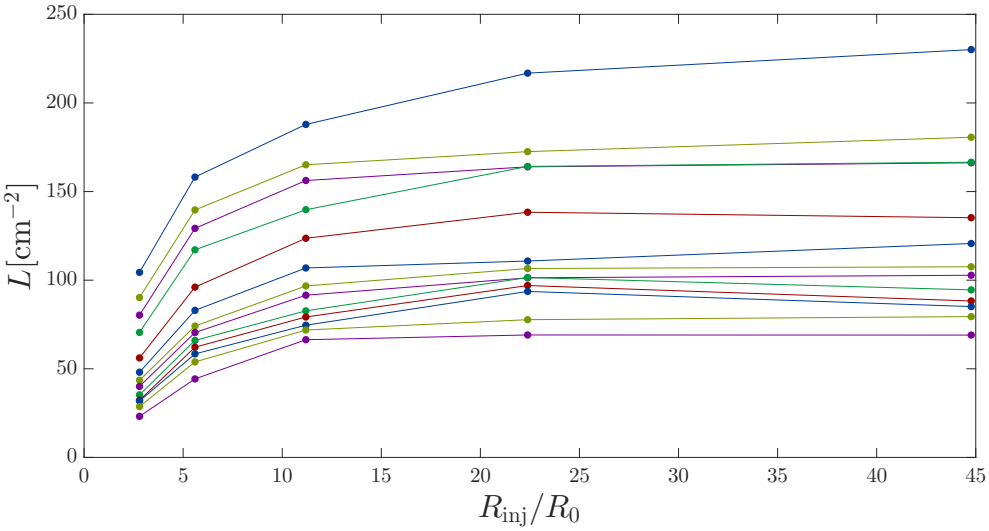

Figure 7.25: Steady state values of the vortex line density as a function of the radius of injected vortex rings, in units of the characteristic dissipation scale. Individual lines correspond to a particular rate of injection.

numerical investigation with parameters chosen to give a greater separation of scales between the dissipation scale and the injection scale, as it is not clear whether being far from the dissipation scale is sufficient for convergence, or whether it is also necessary for injection to occur close to the system size. With regard to the intervortex spacing, we observe that injecting vortex filaments of a particular size does not directly translate to injecting energy at that scale, as this depends on the configuration of the entire tangle; for a random tangle with the intervortex spacing less than the size of the injected vortices, the injected vortices almost immediately reconnect in multiple locations, and in effect injection introduces vortices at the intervortex length scale. In Fig. 7.26 we plot the intervortex spacing vs. the radius of injected loops for selected values of L_{inj}. It may be that the onset of convergence occurs when the injection radius is comparable to the intervortex spacing; again, simulations with a greater separation of scales would be necessary to confirm this.

The scales used for this investigation were chosen to match those of the diffusion investigation in the next section, but vortex line densities are typically much higher in experiments. Using the same approach as in the previous section, where we chose our length scales to make more extreme regimes accessible, would allow us to expand this work to more experimentally relevant densities.

The values of χ_2 found by the injection method are in reasonable agreement with the value found from decay simulations, yet there is a contradiction between the two results: the decay method relies on χ_2 being constant, while we have strong evidence from the injection method that it depends on L. However, the vortex line density is observed to decay like t^{-1}, which does not appear to be compatible with $\chi_2 = \chi_2(L)$. This issue may be masked by the slow variation in χ_2 over the range of L in the decay simulation, but this contradiction is not yet resolved.

We also produce two estimates of the effective viscosity from our estimates of χ_2. Both

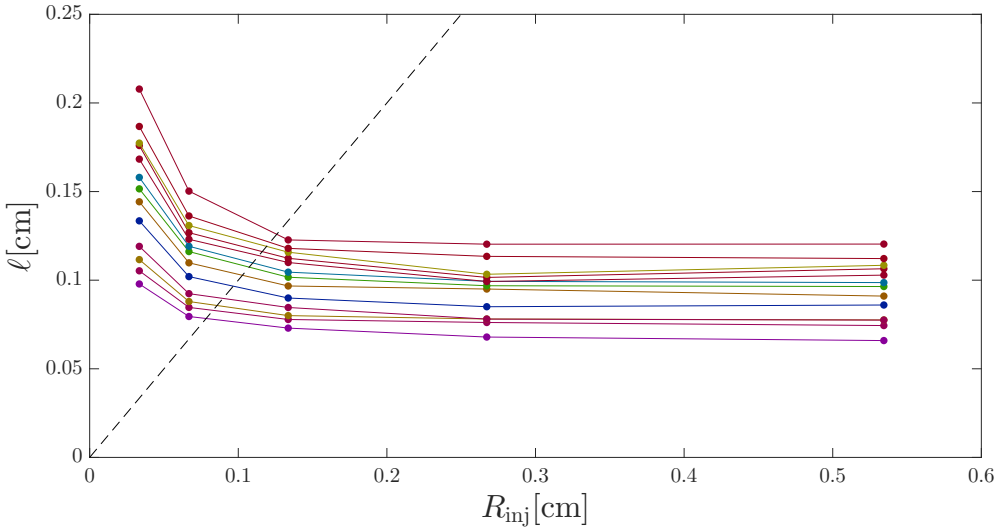

Figure 7.26: Steady state values of the characteristic intervortex spacing as a function of the radius of injected vortex rings, with the line $\ell = R_{\mathrm{inj}}$ superimposed (black dashed). Individual lines correspond to a particular rate of injection.

depend on L: the estimate from $\chi_2 = 0.596$ has logarithmic dependence, while the estimate from $\chi_2 = 0.07L^{0.4}$ is dominated by the power law dependence of χ_2 on L. The first estimate is consistent with previous estimates, which are most focussed around $\nu'/\kappa \approx 0.1$ [160], while the second is higher than previous estimates for larger values of L. However, we note that in the range of L probed by these simulations ($\sim 10^1$–10^2 cm^{-2}) the second estimate is consistent with previous estimates of ν'/κ, again motivating further simulations to probe higher vortex line densities.

As mentioned above, Gao *et al.* find values of χ_2 at finite temperatures using a different methodology. The method we propose here would be applicable at finite temperatures, and a direct comparison with their results could be made. Finally, we remark that this method could be used to probe the phenomena of anomalous dissipation. Even in the absence of viscosity, kinematic energy in classical turbulent flows is dissipated at a finite rate [351, 352]. Using an analogue to the Reynolds number appropriate to superfluid helium [353], $(1 - \alpha')/\alpha$, which encapsulates the balance between dissipative and inertial forces, one can find the injection rate needed to sustain a tangle at a given density for a given value of this analogue. As the vortex line length acts as a proxy for the energy for a random tangle, this then gives the dissipation as a function of the Reynolds number analogue; is the same behaviour observed as for classical turbulence, shown in Fig. 7.27?

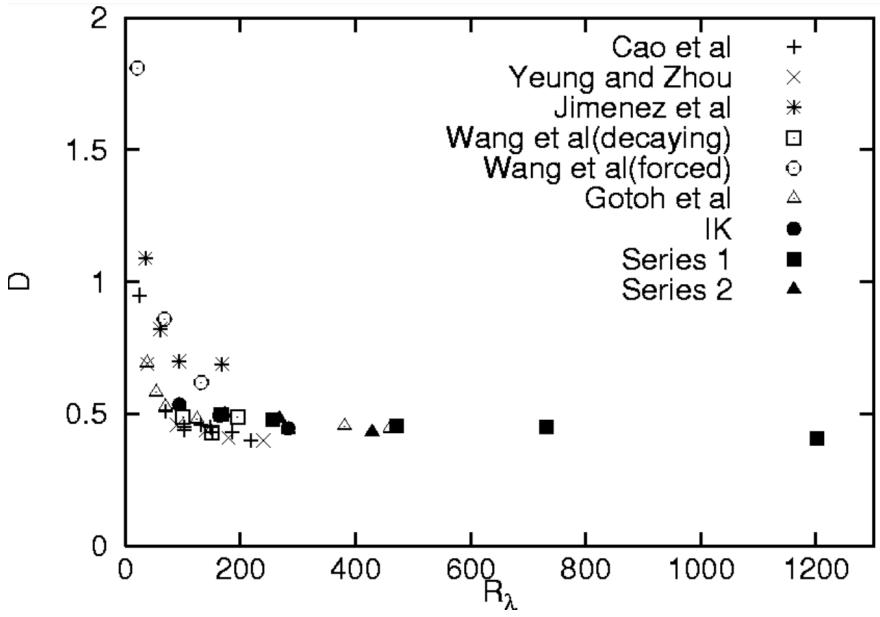

Figure 7.27: Normalised dissipation rate vs. R_λ for various direct numerical simulations of turbulence, reproduced from [351]

7.3 3-D Diffusion

In Sec. 4.1 we found that an initially localised region of quantum vorticity in 2-D, free to expand into empty space, did so through two processes: the formation and ballistic flight of vortex dipoles, and the gradual spread of the remaining vortices, with the spread governed by a diffusion process with the diffusion coefficient $D \sim \kappa$, the quantum of circulation. The obvious extension of this problem is to move from two dimensions to three dimensions, which introduces new effects, including vortex reconnections and Kelvin waves, as well as more complicated possible vortex configurations.

In a pioneering numerical study Tsubota *et al.* [194] reported a value of the effective viscosity of $\nu' \approx 0.1\kappa$, based on the diffusion of an initial configuration generated by thermal counterflow next to a wall, and analysed using a modified Vinen's equation, which requires knowledge of the dissipation parameter χ_2. We create an initial region of vorticity, in a system relevant to helium in the zero temperature limit, by inserting randomly oriented vortex loops, randomly translated according to a normal distribution about the origin. The evolution of this tangle, determined by the vortex filament method, is then analysed in terms of the root-mean-square deviation, $d_{\rm rms}$, of the vortex filaments from their origin, and in terms of a modified Vinen's equation to facilitate comparison with [194].

Studies of quantum turbulence typically focus on statistically steady, homogeneous, isotropic turbulence. However, many experiments generate turbulence locally, using ultrasound [354] and various vibrating structures [203, 355–357] in superfluid helium at rest. This localised turbulence may then spread to fill the experimental system, and an understanding of the processes governing this would be relevant to such experiments. Further, numerous experimental and numerical studies [33, 174, 186, 202, 208, 358] estimate the effective viscosity of superfluid helium, and this approach offers a new technique to do so, which could be exper-

imentally realised using current particle tracking techniques [24].

7.3.1 Set-Up and Methods

We generate our initial configuration by inserting randomly oriented vortex loops of radius 0.24 cm, randomly and independently translated in the x, y, and z directions according to a normal distribution with a standard deviation of 1 cm. To examine the effect of changing the initial vortex line density we produce two sets of initial configurations, one with 50 vortex rings, with $L \approx 70$ cm^{-2} at the origin, and one with 100 vortex rings, with $L \approx 140$ cm^{-2} at the origin, with 10 realisations of each. The vortex filaments are discretised with resolution $\delta = 0.02$ cm, their velocity is calculated by the tree algorithm for the full Biot-Savart law [333], and the system is integrated in time by a 3$^{\text{rd}}$-order Adams-Bashforth scheme with a time-step $\Delta t = 5 \times 10^{-3}$ s. We illustrate one typical lower density and one typical higher density initial configuration and their evolution in Fig. 7.28; we observe the formation and evaporation of small vortex rings, previously observed in [302], and the 3-D equivalent of the evaporating dipoles we observe in 2-D PVM and GPE simulations [233].

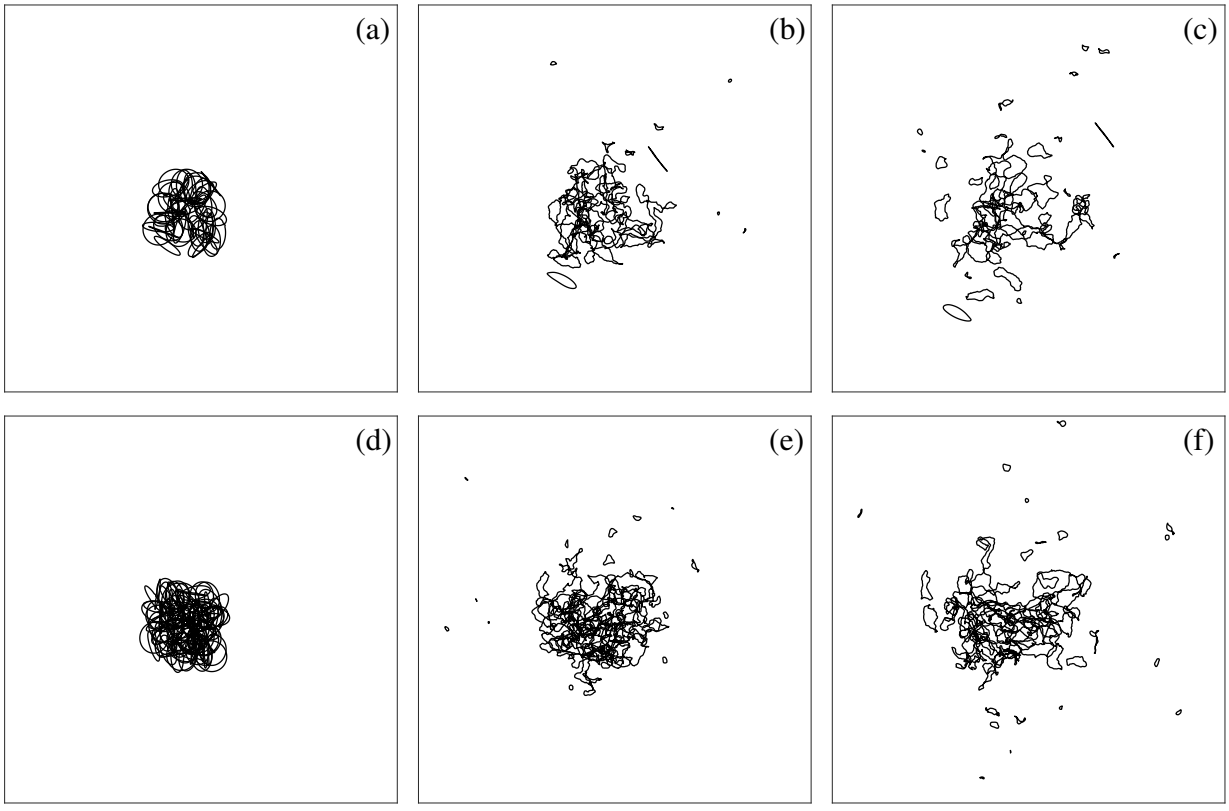

Figure 7.28: Vortex filament method simulations. The top row shows the initial configuration (a), configuration at $t = 100$ s (b), and configuration at $t = 200$ s (c) for a typical lower density simulation, while the bottom row shows a typical higher density simulation at the same times. All panels show the region -3 cm $\leq x, y \leq 3$ cm projected onto the $z = 0$ plane.

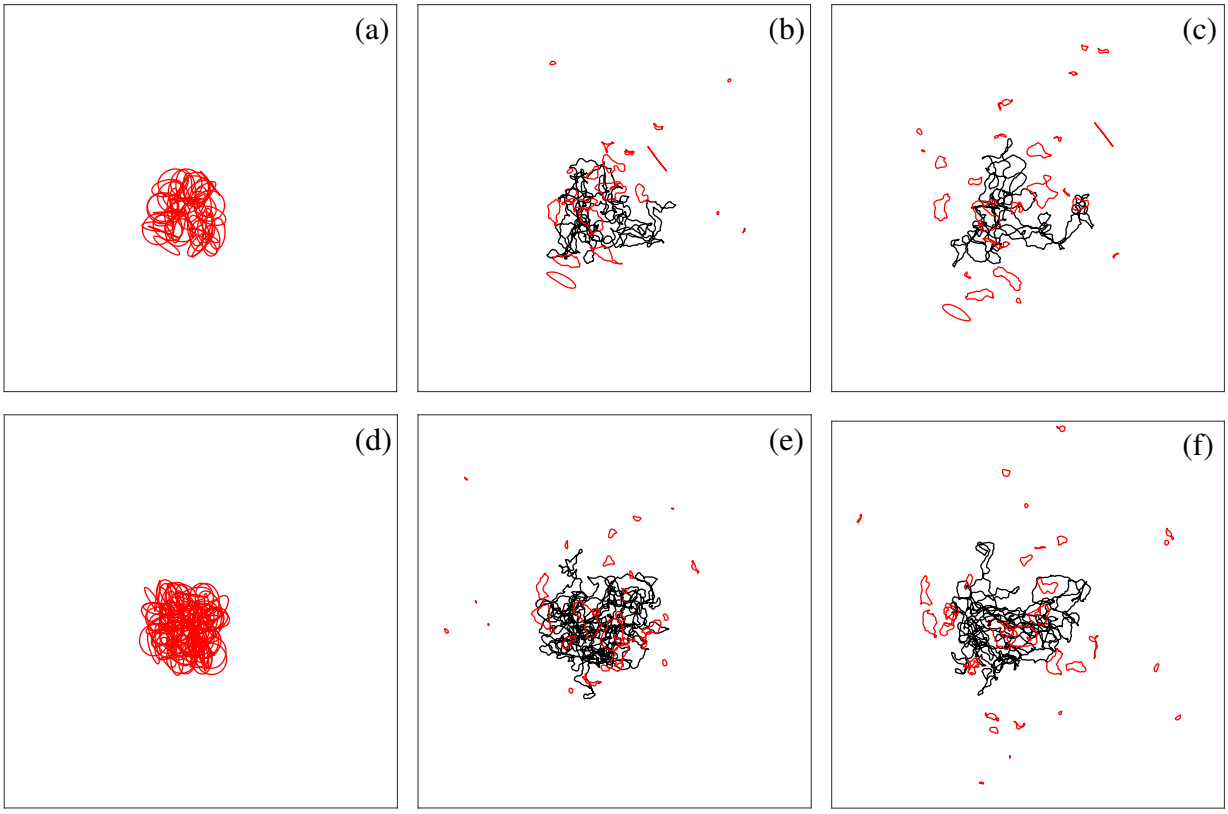

Figure 7.29: As for Fig. 7.28, but with vortex filaments containing fewer than 200 discretisation points highlighted in red.

The algorithm described in Sec. 3.4 for identifying vortex dipoles does not readily extend to vortex filaments embedded in 3-D systems, and we require another technique to distinguish the evaporating vortex rings from the main vortex tangle. We assume that all vortex filaments containing fewer than some number N_c of discretisation points are evaporating rings, while all vortex filaments containing at least N_c discretisation points are part of the main tangle. In Fig. 7.29 we apply this criterion with $N_c = 200$ to the configurations shown in Fig. 7.28, and visually it appears to be adept at distinguishing between the rings and the main tangle. The value of N_c is not chosen arbitrarily; it is chosen for the convergence of ν' as we shall discuss in the next section. In Fig. 7.30 we show the distribution of the radial position, speed, and local radius of curvature of the main tangle and of the rings at $t = 200$ s. The rings account for all of the vorticity furthest from the origin, with the peak beyond the edge of the tangle, in agreement with visual inspection of Fig. 7.29. It is interesting to note that the distribution of velocity and curvature is almost indistinguishable between the tangle and the rings, which we shall comment on in the discussion. In Fig. 7.31 we show the vortex line length of filaments in the tangle and filaments identified as evaporating loops as a proportion of the total vortex line length. After an initial period during which the proportion of line length belonging to the tangle increases as the small initial vortices reconnect to produce the tangle, the proportion of line length belonging to the tangle decreases until the end of the simulations. We note that more than 50% of the line length resides within the tangle even at the end of the simulation, so we have a large

number of data points for calculating statistics.

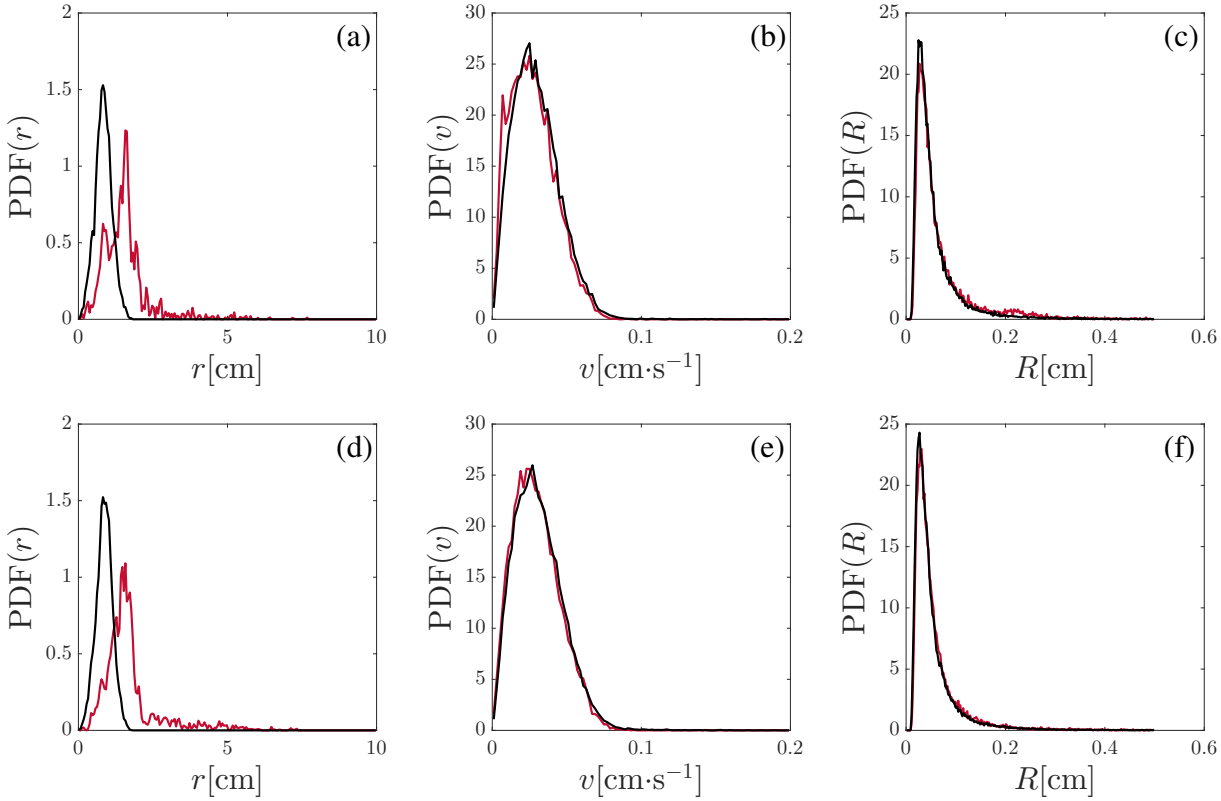

Figure 7.30: Probability density function of radial coordinate (a,d), speed (b,e), and radius of curvature (c,f), all at $t = 200$ s (corresponding to panels (c,f) in Fig. 7.29), for the lower density simulations (a-c) and higher density simulations (d-f). The black curves correspond to the vortex filaments containing 200 or more discretisation points, and the red curves to those containing fewer.

We analyse the simulations with two methods. Firstly, we use the same tools as for 2-D. We calculate the root-mean-square deviation, d_{rms} of vortex filaments comprising the main tangle from their origins, using their discretisation points as tracers:

$$d_{\mathrm{rms}}(t) = \sqrt{\frac{1}{N(t)} \sum_{i=1}^{N(t)} (x_i(t) - x_i(0))^2 + (y_i(t) - y_i(0))^2 + (z_i(t) - z_i(0))^2},$$

where $N(t)$ is the number of points tracked at time t which belong to the main tangle, and $(x_i(t), y_i(t), z_i(t))$ is the position of the i^{th} discretisation point at time t. As discretisation points are inserted and removed to maintain the spatial resolution we must infer the origin of newly inserted points, which we discuss in detail in Sec. 6.1.6. In Fig. 7.32 we compare the probability density functions of the radial position, speed, and local radius of curvature for tracked particles in the main tangle, and for all particles comprising tangles, concluding that the particles which we successfully track are representative of the tangle as a whole.

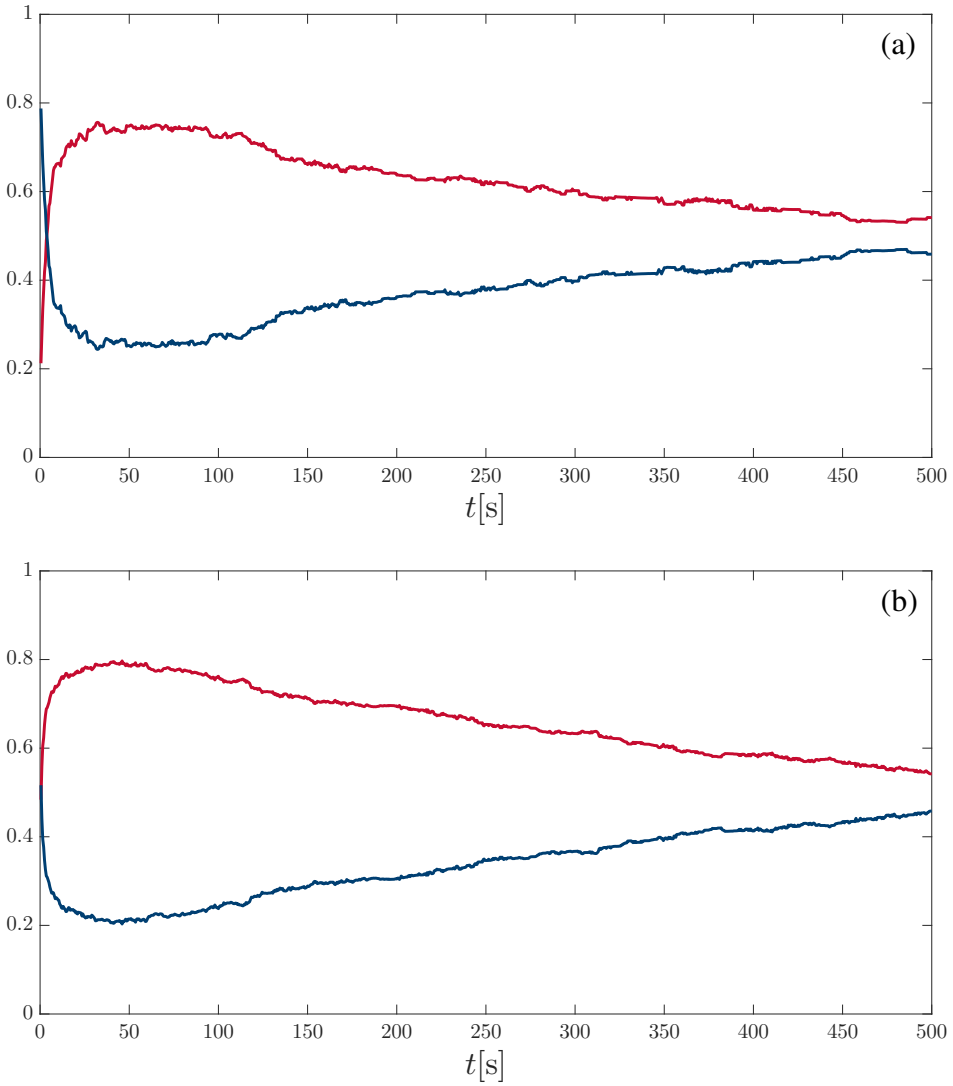

Figure 7.31: Proportion of the total vortex line length contained in the main tangle (red) and in the evaporating loops (blue) for the lower density simulations (a) and higher density simulations (b)

The diffusion coefficient for the diffusion process governing the spread of the tangle is then calculated as:

$$D(t) = \frac{d_{\text{rms}}}{4t}.$$

The second method we use is that of Tsubota *et al.*. They generalise Vinen's equation (with no generating term) to include a diffusive term:

$$\frac{dL}{dt} = -\chi_2 \frac{\kappa}{2\pi} L^2 + D\nabla^2 L, \tag{7.6}$$

which we solve in spherical coordinates, assuming spherical symmetry, using a 4^{th}-order finite difference scheme to estimate spatial derivatives, and a 3^{rd}-order Adams-Bashforth

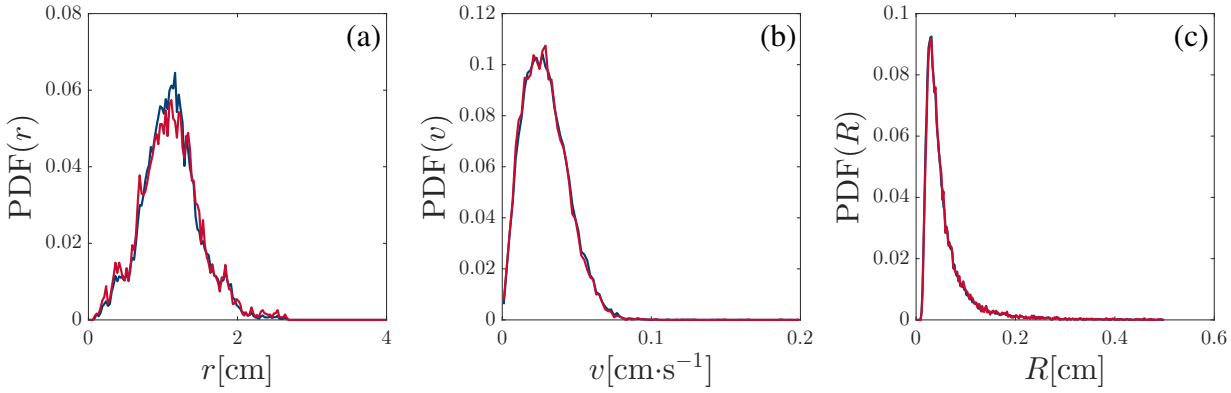

Figure 7.32: Probability density functions of the radial coordinate (a), speed (b), and local radius of curvature (c) for all points within the tangle (blue), and for all points which are successfully tracked within the tangle (red), at $t = 500$ s for the higher density simulations.

scheme to integrate forward in time, with spatial resolution $\Delta r = 0.02$ cm and a time-step $\Delta t = 0.01$ s. We take $\chi_2 = 0.07L^{0.4}$ as estimated in Sec. 7.2.2; we also use the constant value $\chi_2 = 0.3$ used in [194], and the constant value $\chi_2 = 0.596$ we estimate in Sec. 7.2.1 for comparison. Again assuming spherical symmetry, we estimate $L(r,t)$ by integrating over the vortex lines within spherical shells, using $L(r,0)$ as the initial condition for the modified Vinen's equation. We then estimate D by minimising the sum of square errors between $L(r,t)$ found from our VFM simulations, and our solution found through the integration of eq. (7.6).

7.3.2 Analysis

Before we calculate ν' we address the nature of the turbulence. Focusing on one of the higher density simulations, we calculate the transverse velocity correlation function $f_\perp(r,t) = \langle v_\perp(\mathbf{r},t)v_\perp(\mathbf{r}+r\hat{e}_\perp,t)\rangle/\langle v_\perp(\mathbf{r},t)^2\rangle$, and find that it quickly decreases as r increases, indicating that the turbulent velocity field is essentially random. At $t = 0$ s we find $f_\perp(\ell/2,0) \approx 0.27$, where ℓ is the characteristic intervortex spacing. This lack of long-range structure is consistent with Vinen (ultraquantum) turbulence [160].

We first analyse the data using the d_{rms} method. The ensemble averaged d_{rms} of tracked discretisation points in the main vortex tangle for both sets of simulations are shown in Fig. 7.33. At early times $d_{\mathrm{rms}} \sim t$, consistent with ballistic motion. After this transient initial period we find $d_{\mathrm{rms}} \sim t^{1/2}$, consistent with diffusion. We stress again that the early ballistic behaviour is not connected to the ballistic motion of the evaporating loops, which are excluded from this analysis. A possible interpretation of this behaviour is that the vortex filaments locally move in an almost linear way until they come close enough to other filaments for their motion to be dominated by them, deflecting them, with many interactions like this building up to a Brownian motion-like diffusion process; this is supported by the observation that the transition from a ballistic regime to a diffusive regime occurs at roughly the point at which d_{rms} becomes comparable with the initial intervortex spacing

($\sim$ 0.12 cm, and $\sim$ 0.08 cm at the centre of the lower density and higher density simulations, respectively).

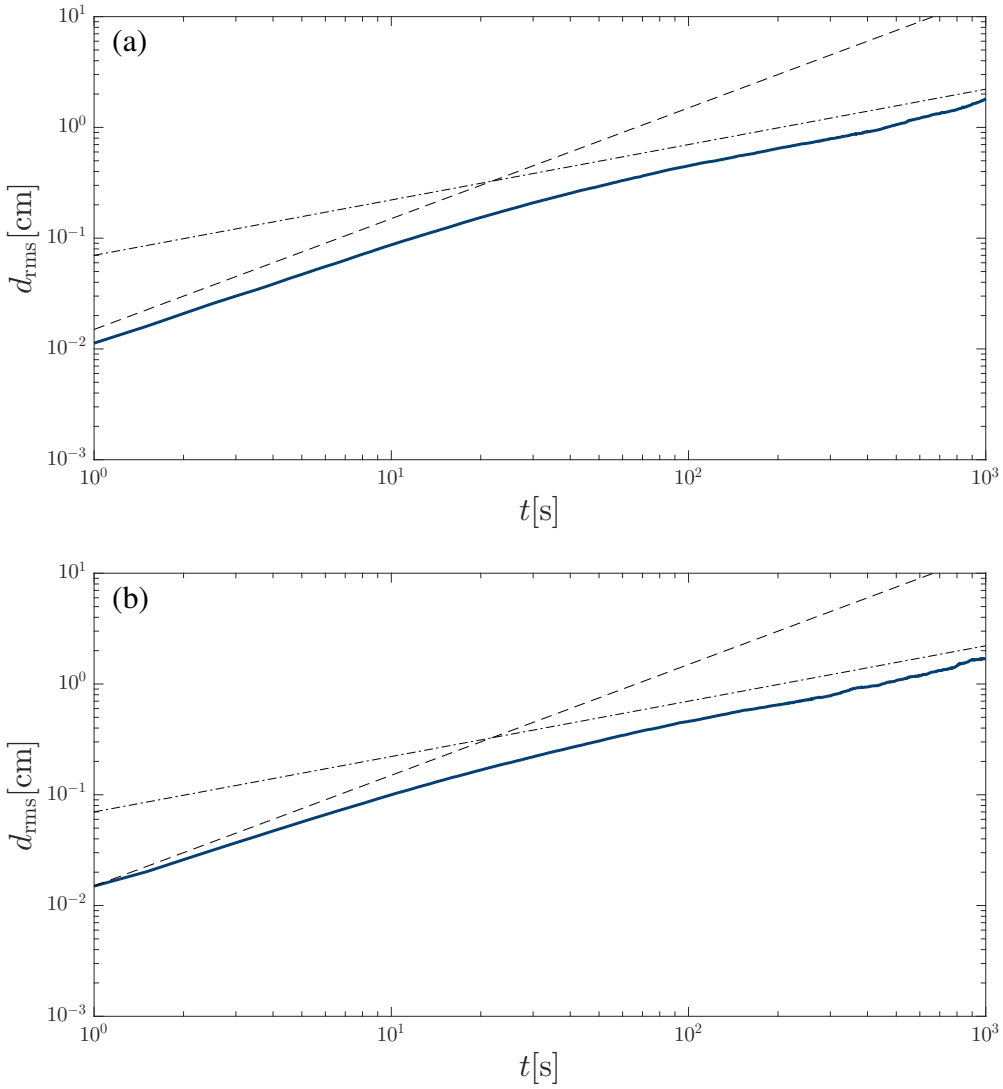

Figure 7.33: Ensemble average d_{rms} for lower density simulations (a) and higher density simulations (b), with $d_{\mathrm{rms}} \sim t$ scaling indicated by black dashed lines, and $d_{\mathrm{rms}} \sim t^{1/2}$ scaling indicated by black dot-dashed lines.

In Fig. 7.34 we show the ensemble average of the calculated value of ν', in units of the quantum of circulation, for a range of values for N_{c}, the criterion for identifying individual filaments as either part of the main tangle or evaporating loops. We see that for small values of N_{c} the value of ν' does not settle in time, whereas for large N_{c} the value of ν' does settle, and converges to a values of $\nu' \approx 0.5$ as N_{c} reaches 200, for both sets of simulations. We take this, in combination with the visual confirmation and radial position distribution in the previous section, to demonstrate that this method for distinguishing the tangle from the evaporating loops is effective.

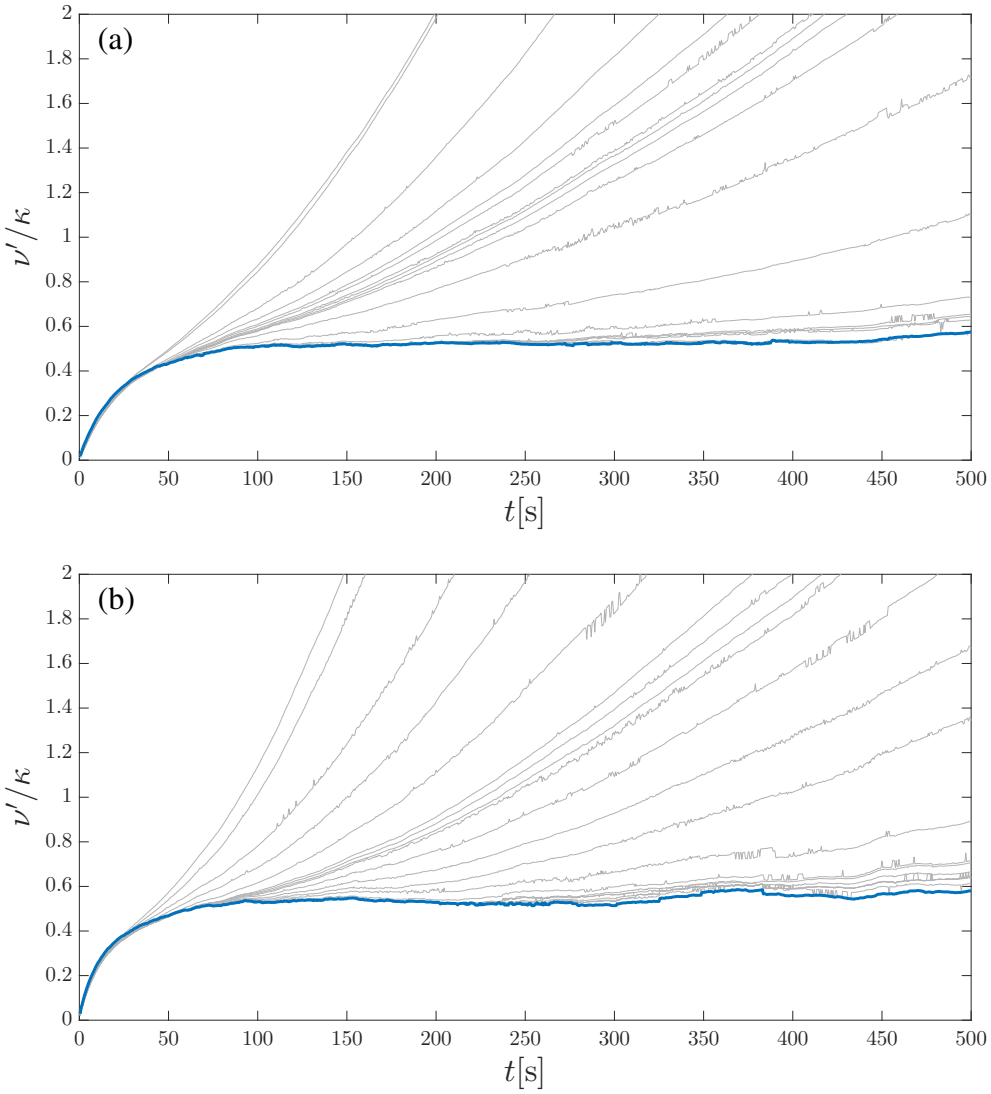

Figure 7.34: Ensemble average ν', in units of the quantum of circulation κ, for the lower density simulations (a) and the higher density simulations (b). Blue lines show the value found when $N_c = 200$, while the grey lines show values found as N_c is increased from 0 (grey line which reaches maximum value earliest) to 200.

We now use the modified Vinen's equation to estimate ν' independently. We fit solutions to the equation with three candidates for χ_2, and both including and excluding the ballistic loops that are disregarded in the d_{rms} analysis. In Fig. 7.35 we show the ensemble averaged vortex line density from the full VFM simulations, with solutions to the modified Vinen's equation superimposed, where we have taken the ensemble average initial density as our initial condition, and the mean estimate of ν' over the ten realisations. We summarise the values of ν'/κ found for both methods in Table 7.1.

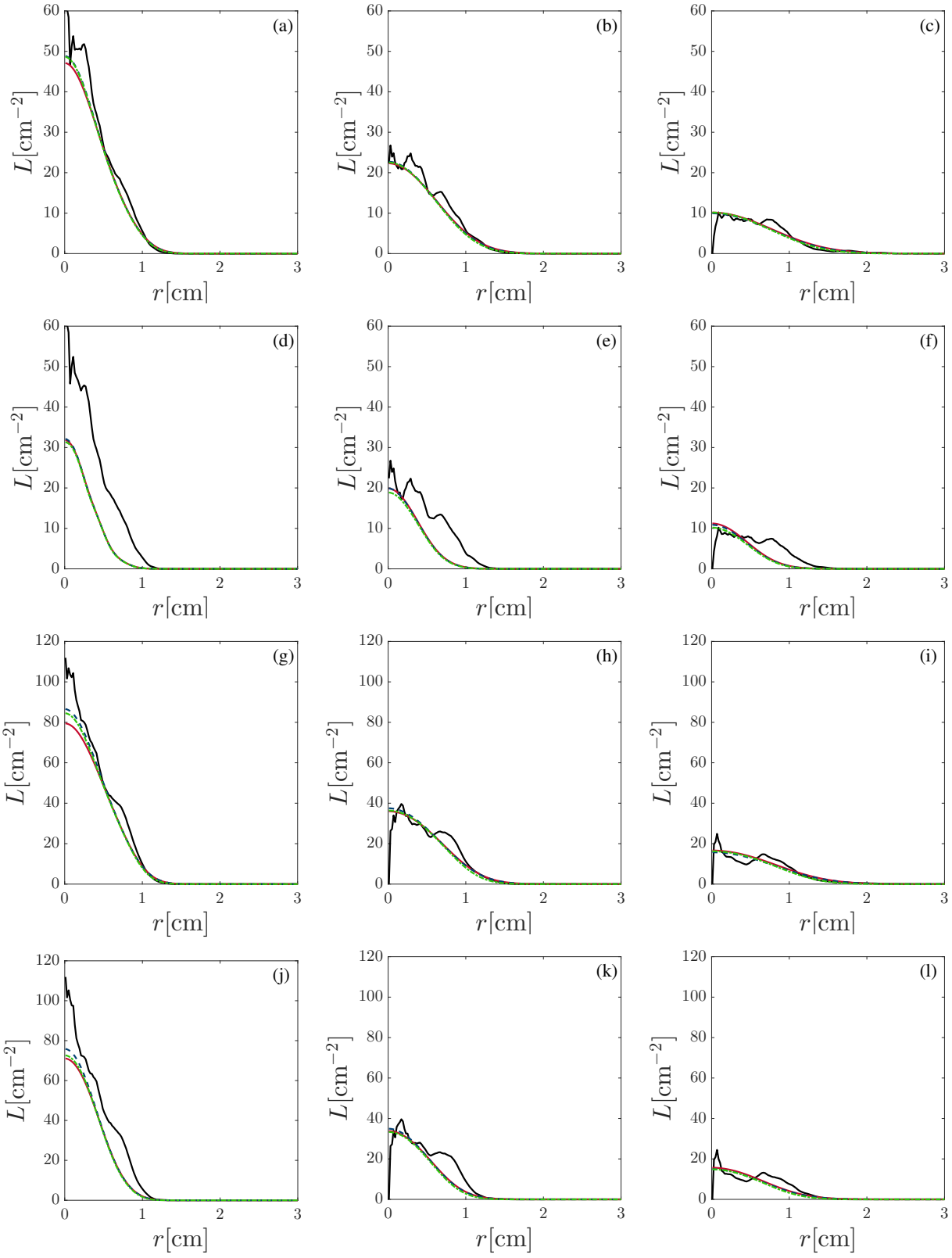

Figure 7.35: Vortex line density, as a function of radius, from VFM simulations (black) and modified Vinen's equation with $\chi_2 = 0.3$ (blue), $\chi_2 = 0.596$ (green), $\chi_2 = 0.07L^{0.4}$ (red), for lower density simulations with (1^{st} row) and without (2^{nd}) ballistic loops, higher density with (3^{rd}) and without (4^{th}), at times $t = 50$ s (1^{st} column), $t = 200$ s (2^{nd}), and $t = 500$ s (3^{rd}).

Method	ν'/κ
d_{rms}, lower density	0.526 ± 0.064
d_{rms}, higher density	0.530 ± 0.065
Modified Vinen's eq., lower density, $\chi_2 = 0.3$	0.315 ± 0.196
Modified Vinen's eq., lower density, small loops excluded, $\chi_2 = 0.3$	0.053 ± 0.095
Modified Vinen's eq., lower density, $\chi_2 = 0.596$	0.237 ± 0.193
Modified Vinen's eq., lower density, small loops excluded, $\chi_2 = 0.596$	0.028 ± 0.090
Modified Vinen's eq., lower density, $\chi_2 = 0.07L^{0.4}$	0.341 ± 0.195
Modified Vinen's eq., lower density, small loops excluded, $\chi_2 = 0.07L^{0.4}$	0.068 ± 0.095
Modified Vinen's eq., higher density, $\chi_2 = 0.3$	0.307 ± 0.105
Modified Vinen's eq., higher density, small loops excluded, $\chi_2 = 0.3$	0.198 ± 0.083
Modified Vinen's eq., higher density, $\chi_2 = 0.596$	0.162 ± 0.112
Modified Vinen's eq., higher density, small loops excluded, $\chi_2 = 0.596$	0.112 ± 0.093
Modified Vinen's eq., higher density, $\chi_2 = 0.07L^{0.4}$	0.304 ± 0.107
Modified Vinen's eq., higher density, small loops excluded, $\chi_2 = 0.07L^{0.4}$	0.201 ± 0.084

Table 7.1: Values of ν'/κ estimated from the two methods described in this section, for the lower and higher density sets of simulations, and in the case of the modified Vinen's equation, either retaining or excluding the small evaporating loops, and for various proposed values of χ_2. Values are quoted as mean ± 1 standard deviation.

7.3.3 Discussion

We find that an initially localised region of vortex filaments, with structure consistent with the ultraquantum regime, spreads out in space through two processes: the formation and ballistic flight of small vortex rings, and the slower spread of the remaining tangle. The latter can be modelled as a diffusion process, and by a standard approach analysing the root-mean-square deviation of vortices within the main tangle we find $\nu'/\kappa \approx 0.5$, consistent with the values in the range $0.3 < \nu'/\kappa < 0.5$ we obtained for a 2-D trapped Bose-Einstein condensate using the Gross-Pitaevskii equation and the point vortex model, bearing in mind that the value of ν'/κ in these trapped systems appears to be suppressed by boundary effects. We also obtain values of ν'/κ by fitting solutions to a modified Vinen's equation, with a dissipative term and a diffusive term, pioneered by Tsubota *et al.* [194]. Comparing the results of the two methods, with reference to Table 7.1, we make the following observations: the d_{rms} method does not require knowledge of χ_2, but the modified Vinen's equation does, and the result obtained is strongly dependent on the value (or functional dependence) of χ_2 used. Excluding ballistic loops lowers the values obtained - this in itself is not surprising, as the ballistic loops are the fastest spreading components of the configuration, but it does increase the difference between the estimate of ν' with this method and with d_{rms}, and it seems hard to justify including them when they are evidently ballistic, not diffusive. As well as depending on χ_2, the value found has some dependence on the vortex line density, although only significant when the ballistic loops are excluded from the analysis. Finally, we note that the variance, particularly in proportion to the

mean value, is far smaller for the $d_{\rm rms}$ method.

In their original paper Tsubota *et al.* find $\nu'/\kappa \approx 0.1$, a value somewhat lower than those we find , but not in total disagreement. There are a number of factors which could contribute to the difference observed. We work in an infinite open domain, while they used a domain with a hard wall boundary, and periodic boundary conditions in directions perpendicular to the wall. Then, they used an initial condition generated by thermal counterflow with dynamics given by the local induction approximation, which is known to generate anomalously anisotropic vortex tangles with large-scale structures [328]. The values we find when ballistic loops are excluded are closer to 0.1κ, it may be the case that the proportion of vortices in the main tangle was greater in their simulation, with the ballistic loops exerting less influence on the value of ν' obtained. We note also that Nemirovskii developed theory drawing on the simulations of Tsubota *et al.* [359], which yields a value four times greater than ours, $\nu'/\kappa \approx 2.2$. Both this theory and the modified Vinen's equation assume the existence of a diffusion process, while the scaling of $d_{\rm rms} \sim t^{1/2}$ in our analysis shows that such a process occurs.

We observe that the local curvature and velocity statistics of the vortices comprising the main tangle are almost indistinguishable from those of the evaporating loops: in effect, the tangle behaves like a collection of small vortex rings, although we stress that the tangle is a far more complicated and knotted structure than isolated vortex rings. It is clear that the behaviour of the tangle is not ballistic, as shown by the $d_{\rm rms} \sim t^{1/2}$ scaling, and by comparison of $d_{\rm rms}$ at later times with the deviation that would arise if the vortices were travelling ballistically. With an average speed of ~ 0.03 cm/s, we would expect $d_{\rm rms} \approx 30$ cm at $t = 1000$ s; the observed value of $d_{\rm rms}$ at this time is an order of magnitude lower. However, the diffusion process may originate in this local structure, with local sections of the tangle moving ballistically until deflected by other vortices in the tangle, as supported by the transition from the ballistic $d_{\rm rms} \sim t$ regime to the diffusive $d_{\rm rms} \sim t^{1/2}$ regime when $d_{\rm rms} \sim \ell$.

The effective viscosity of a superfluid is also inferred in the related problem of the decay of superfluid turbulence. Experimental and numerical values are found in the approximate range $0.01 < \nu'/\kappa < 1$, but most concentrated around 0.1 [33, 190, 200, 202, 215]. Finally, we reiterate that the $d_{\rm rms}$ method used to estimate ν'/κ here is Lagrangian, and could thus be used in future experimental studies using visualisation techniques based on tracking excited helium molecules [24, 37, 38].

Chapter 8

Conclusions

In this thesis we set out to describe how quantum turbulence spreads into vorticity free regions through numerical experiments, motivated by experiments in which quantum turbulence is generated locally within a larger experimental cell [31, 159, 195, 206, 207, 220, 221].

We first consider 2-D systems, which are relevant to Bose-Einstein condensates (BECs) in geometries with tight confinement in one direction. We use two models, the point vortex model (PVM) in an infinite domain which captures only the core of vortex dynamics, and the Gross-Pitaevskii equation (GPE), in a disc trap, which captures the physics of BECs at zero temperature. Under both models we observed the formation of vortex-antivortex dipoles, which move ballistically out from the region of vorticity. We also observe the spread of the remaining vortices, which we analyse in terms of the root-mean-square deviation, d_{rms}, of these vortices from their initial positions. After a transient period when $d_{\mathrm{rms}} \sim t$, consistent with ballistic dynamics, we find $d_{\mathrm{rms}} \sim t^{1/2}$, consistent with a diffusion process. We postulate that this diffusion emerges from vortex trajectories being deflected as they approach other vortices close enough for a single vortex to dominate their velocity, with many such events building up to act similarly to a random walk. This is supported by the observation that the transition from a ballistic regime to a diffusion regime occurs when d_{rms} is comparable to the initial characteristic intervortex spacing. In our initial simulations we find the diffusion coefficient to be $D \approx \kappa$, where κ is the quantum of circulation, under the PVM, and $D \approx 0.3\kappa$ under the GPE. Implementing a similar hard wall disc boundary in the PVM, and varying the initial vortex density, we find that the diffusion coeficient is suppressed by the presence of boundaries and low vortex density, and attribute the observed difference in D between the two models to this rather than to the physics modelled by the GPE but not the PVM.

We then consider 3-D systems, which we model using the vortex filament method (VFM) which is relevant to quantum turbulence in helium II. We observe the formation of small vortex rings, analogous to the dipoles observed in 2-D, which move ballistically out from the central region of vorticity. We analyse the spread of the remaining vorticity in terms of the d_{rms}, using the discretisation points of the vortex filaments as tracer particles. The results closely mirror those in 2-D: after a transient period during which $d_{\mathrm{rms}} \sim t$, we find $d_{\mathrm{rms}} \sim t^{1/2}$, with the transition occurring when $d_{\mathrm{rms}} \sim \ell$, the characteristic intervortex spacing. This is indicative of a diffusion process, and we find $D \approx 0.5\kappa$ for each of two sets of simulations with different initial densities. This value is somewhat higher than, but

not incomparable with, the value of $D \approx 0.1\kappa$ found by Tsubota *et al.* [194] analysing the spread of a region of vorticity next to a wall, in terms of a modified Vinen's equation which introduced a diffusion term to the usual Vinen's equation. Analysing our data using this method we find $D \approx 0.3\kappa$. However, there is a lot more variability in this method, and it requires independent knowledge of the dissipation parameter χ_2 which the d_{rms} method does not.

In classical fluids the vorticity transport equation describes the spread of vortices as a nonlinear diffusion process, with the kinematic viscosity acting as the diffusion coefficient. It is noteworthy that in quantum turbulence, vorticity still spreads through a diffusion process despite the lack of viscosity, suggesting that the diffusion coefficient found in our simulations of spreading quantum vortices may be a suitable candidate for the effective viscosity in quantum fluids. The effective viscosity of He II is the subject of a wealth of numerical and physical experiments, the results of which are summarised in Fig. 8.1. We discuss this shortly, after introducing a second estimate of the effective viscosity.

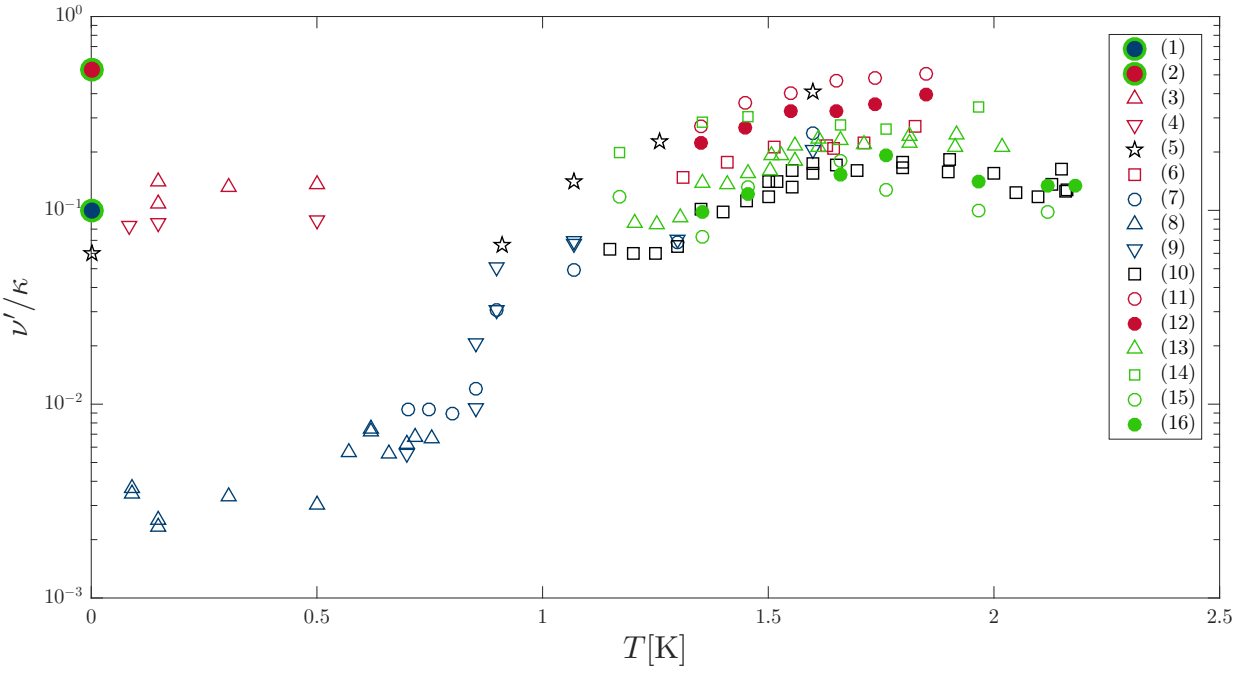

Figure 8.1: Estimates of the effective viscosity of He II: (1) this work, steady state injection simulations, Sec. 7.2, (2) this work, diffusion simulations, Sec. 7.3,(3) charged vortex rings measured vertically and (4) measured horizontally [160] (5) counterflow experiments [19, 20, 149, 150] (6) counterflow simulations [186] (7) ion jet [160] (8) spin down sampled by charged vortex rings and (9) sampled by free ions [33] (10) towed grid [187] (11) & (12) counterflow decay [192] (13) grid turbulence [188] (14) steady state grid turbulence [191] (15) steady state grid turbulence and (16) steady state turbulence [190].

In order to estimate the diffusion coefficient using the method of Tsubota *et al.* we need to estimate the dissipation parameter χ_2 in Vinen's equation. We do this using two meth-

ods: we first revisit estimation based on the decay of the vortex line density in homogeneous, isotropic, ultraquantum turbulence. This has previously been performed using the local induction approximation (LIA) in studies which find $\chi_2 \approx 0.3$ [186]; using the tree algorithm for the full Biot-Savart law, which includes long-range interactions absent in the LIA we find $\chi_2 \approx 0.596$. We also estimate χ_2 by using the injection of randomly oriented and randomly translated vortex rings at constant rates in a period box to achieve statistically steady states, finding $\chi_2 \approx 0.07 L^{0.4}$. By analogy to the classical energy dissipation equation we estimate the effective viscosity as:

$$\frac{\nu'}{\kappa} = \frac{\chi_2}{8\pi^2} \ln\left(\frac{\ell}{a_0}\right).$$

Using the constant value of $\chi_2 = 0.596$ we find $\nu' \approx 0.1\kappa$, with weak logarithmic dependence on the vortex line density. We include this data point in Fig. 8.1, which summarises estimates of the effective viscosity.

Below about 1 K two branches are evident in Fig. 8.1, with the lower branch corresponding to systems in the quasiclassical regime of turbulence, and the higher branch to systems in the ultraquantum regime of turbulence. Our estimate from the steady state injection simulations is in good agreement with previous estimates of the effective viscosity for ultraquantum turbulence in ^{4}He, which are focussed around $\nu' = 0.1\kappa$ at 0 K. Our estimate from the diffusion of quantum vorticity is somewhat higher, though still in order of magnitude agreement. We note that the estimate from steady state injection is based, as are previous studies, on the dissipation of energy, while the estimate from the diffusion of vorticity is made by analogy to the classical vorticity transport equation.

This is perhaps similar in spirit to the concept of eddy viscosity for classical fluids, which pertains to the momentum transport. Viscosity can be interpreted as the material property which determines momentum transport in a fluid, with Newton's law of viscosity:

$$\tau = \mu \frac{\partial u}{\partial y}$$

relating the shear stress τ to the velocity gradient through the dynamic viscosity μ. This is exact for laminar flow, however, this does not account for addition momentum transport done by vortices in turbulent flows. The eddy viscosity then attempts to describe this additional momentum transport as:

$$\tau = \mu \frac{\partial u}{\partial y} + \eta \frac{\partial u}{\partial y},$$

where η is the eddy viscosity. This is then an effective viscosity, as it does not arise solely from the microscopic behaviour of the fluid, but rather from the flow. Values of η are typically identified by comparison to known flows, and so the eddy viscosity is a phenomenological attempt to include additional momentum transport in models, analogous to ν' in our diffusion simulations characterising the transport of vortices.

As both ν' estimated from dissipation and estimated from vorticity transport are based on the dynamics of vortices in the fluid, they clearly also arise from the particular form

of the flow, and not just the fluid's material properties. This can be seen for the dissipation ν' in Fig. 8.1, as different values emerge for the two turbulent regimes, corresponding to the two branches seen below 1 K; for the diffusion transport ν' this can be seen in the change in value induced by boundaries in 2-D. However, in contrast to the eddy viscosity, which stems from vortex motion on all scales, in the ultraquantum regime the dissipation ν' arises from the motion at the smallest scales, while the vorticity transport ν' arises principally from motions at the intervortex scale. The suppression of the dissipation ν' in the Kolmogorov regime is due to the increased alignment of vortices in bundles suppressing the reconnections which drive the various dissipation mechanisms. This suggests that future work could usefully explore what difference, if any, is seen in the vorticity diffusion ν' between the Vinen and Kolmogorov regimes. We note that the vortex line density, and hence intervortex scale, does not affect ν' in our 3-D diffusion simulations. Future work should establish the dependence on other properties, including the temperature and external flow, and whether it is the intrinsic or extrinsic properties which influence ν' most.

The diffusion simulation could certainly be undertaken in an experimental setting, in both 2-D BECs and 3-D ^{4}He. Vortices can be generated locally in both systems [29, 31, 32, 83, 99, 100, 102], and then tracked, by the use of non-destructive imaging in BECs [85] and tracer particles in ^{4}He [24,25,37,38]. Although the systems currently experimentally achievable in BECs are not large enough to avoid the suppression of ν' by boundary effects, the formation of dipoles and spread of the remaining vortices should still be observable.

The investigations undertaken in this thesis primarily relate to ultraquantum turbulence at zero temperatures. However, the methods described are often also applicable at finite temperatures, and in the quasiclassical regime of turbulence. In particular, the effective viscosity of He II could be estimated from the diffusion of vortices in simulations and experiments at finite temperatures, and in the quasiclassical regime, provided that a diffusion process again emerges from the interaction of vortices. The estimation of χ_2, and the resulting estimate of ν'/κ, by the injection of vortex rings could be performed in finite temperature simulations of ultraquantum turbulence, moreover, if the rate at which vorticity is injected, by mechanical or other means, could be controlled with sufficient precision, this technique could also be used to experimentally determine the dissipation parameter.

Appendices

Appendix A

Derivations

A.1 Point Vortex Model

We follow the derivation given in [360]. Consider an inviscid, incompressible fluid with an associated velocity field $\mathbf{u}$ described by the Euler equation:

$$\frac{\partial \mathbf{u}}{\partial t} + (\mathbf{u} \cdot \nabla)\mathbf{u} = -\frac{\nabla p}{\rho} + \mathbf{f}, \tag{A.1}$$

and incompressibility condition:

$$\nabla \cdot \mathbf{u} = 0, \tag{A.2}$$

where p is the pressure and $f = -\nabla A$ for some conservative body force A. The vorticity is defined as:

$$\boldsymbol{\omega} = \boldsymbol{\nabla} \times \mathbf{u}, \tag{A.3}$$

and taking the curl of eq. (A.1) we obtain a vorticity transport equation:

$$\frac{\partial \boldsymbol{\omega}}{\partial t} + (\mathbf{u} \cdot \nabla)\boldsymbol{\omega} = 0, \tag{A.4}$$

which can be interpreted physically as vorticity being preserved along the flow lines.

We seek to describe the velocity field $\mathbf{u}$ that generates a chosen $\boldsymbol{\omega}$. Restricting ourselves to two dimensions, we consider point vortex fields $\boldsymbol{\omega}(\mathbf{r})$ where the vorticity is confined to points; i.e. point vortices are singularities in $\boldsymbol{\omega}$, and the velocity field associated with a configuration of N point vortices is

$$\boldsymbol{\omega}(\mathbf{r}) = \sum_{i=1}^{N} \Gamma_i \delta(\mathbf{r} - \mathbf{r}_i), \tag{A.5}$$

where Γ_i is the circulation about the i^{th} vortex, $\mathbf{r}_i$ is the position of the i^{th} vortex, and δ is the Dirac delta function. We can see that Γ_i corresponds to the circulation of the i^{th} vortex by considering the definition of circulation around a region R containing only the i^{th} vortex:

$$\Gamma_C = \oint_C \mathbf{u} \cdot d\mathbf{l}. \tag{A.6}$$

Using Stoke's theorem:

$$\Gamma_C = \iint_S (\nabla \times \mathbf{u}) \cdot \mathbf{n} d\mathbf{S} = \iint_S \boldsymbol{\omega} \cdot d\mathbf{S} \tag{A.7}$$

Using eq. (A.3) and substituting our particular velocity field eq. (A.5) we have:

$$\Gamma_C = \iint_S \left[\sum_{i=1}^{N} \Gamma_i \delta(\mathbf{r} - \mathbf{r}_i) \right] \cdot d\mathbf{S} = \Gamma_i, \tag{A.8}$$

as stated. Let us now introduce the auxiliary stream function Ψ satisfying:

$$\frac{dx}{dt} = \frac{\partial \Psi}{\partial y}, \qquad \frac{dy}{dt} = -\frac{\partial \Psi}{\partial x}, \tag{A.9}$$

and note that that this is guaranteed to satisfy eq. (A.2). Substituting eq. (A.9) into eq. (A.3) yields:

$$\nabla^2 \Psi(\mathbf{r}) = -\boldsymbol{\omega}(\mathbf{r}); \tag{A.10}$$

Poisson's equation with $\boldsymbol{\omega}$ as a source. We can solve for Ψ by inverting this:

$$\Psi(\mathbf{r}) = \int G(\mathbf{r}, \mathbf{r}') \boldsymbol{\omega}(\mathbf{r}') d\mathbf{r}', \tag{A.11}$$

where G is the Green's function solution to $\nabla^2 G(x, y) = -\delta(x, y)$. For the 2-D plane this is:

$$G(\mathbf{r},\mathbf{r}') = -\frac{1}{4\pi}\ln(|\mathbf{r}-\mathbf{r}'|^2), \tag{A.12}$$

from [361]. Combining eq. (A.5), (A.11), and (A.12) we have:

$$\begin{aligned}\Psi(\mathbf{r}) &= -\frac{1}{4\pi}\int \ln(|\mathbf{r}-\mathbf{r}'|^2)\left[\sum_{i=1}^{N}\Gamma_i\delta(\mathbf{r}'-\mathbf{r}_i)\right]d\mathbf{r}' \\ &= -\frac{1}{4\pi}\sum_{i=1}^{N}\Gamma_i\ln(|\mathbf{r}-\mathbf{r}_i|^2),\end{aligned} \tag{A.13}$$

which gives, through eq. (A.9):

$$\frac{dx}{dt} = -\frac{1}{2\pi}\sum_{i=1}^{N}\frac{\Gamma_i(y-y_i)}{|\mathbf{r}-\mathbf{r}_i|^2}, \qquad \frac{dy}{dt} = \frac{1}{2\pi}\sum_{i=1}^{N}\frac{\Gamma_i(x-x_i)}{|\mathbf{r}-\mathbf{r}_i|^2} \tag{A.14}$$

These are the components of the velocity field generated by the specified configuration of point vortices. As vortices move with the fluid [362], the equations of motion for the vortices themselves are recovered by substituting their (x, y) coordinates into eq. (A.14), and omitting the singular term.

A.2 Gross-Pitaevskii Equation

We give a derivation of the GPE, following the more detailed derivation given in [249]. We first examine the quantum field theory description of a many-body quantum system [363]. An N-body wavefunction $\tilde{\Psi}(\mathbf{r}_1...\mathbf{r}_N, t)$ describes such a system, with $\tilde{\Psi}$ obeying the Schrödinger equation:

$$i\hbar\frac{\partial}{\partial t}\tilde{\Psi}(\mathbf{r}_1...\mathbf{r}_N,t) = \hat{H}\tilde{\Psi}(\mathbf{r}_1...\mathbf{r}_N,t), \tag{A.15}$$

where $\mathbf{r}_i$ describes the location of the i^{th} body. We can describe a dilute, weakly interacting Bose gas of N atoms under this formalism with such a wavefunction, and a Hamiltonian:

$$\hat{H} = \sum_{i=1}^{N}\hat{h}_0(\mathbf{r}_i,t) + \frac{1}{2}\sum_{i,j=1}^{N}\hat{V}(\mathbf{r}_i,\mathbf{r}_j), \tag{A.16}$$

where $\hat{h}_0 = -\frac{\hbar}{2m}\nabla^2 + V_{\text{ext}}(\mathbf{r},t)$ arises from the effects of a single atom in an external potential field, and $\hat{V}(\mathbf{r}_i,\mathbf{r}_j)$ describes collisions between two particles. As the gas is dilute we assume that all collisions are binary. The factor of $\frac{1}{2}$ is included to account for double counting of two-body interactions.

We proceed by reformulating the problem in a different representation, the occupation number representation. The indistinguishability of particles is exploited to reduce the representation of the system to the number of particles n_i in each energetically accessible state i. The usual complete orthonormal basis of single-particle wavefunctions used to expand the many-body wavefunction is then replaced by a new complete orthonormal basis set $|n_1...n_\infty\rangle$. Although this basis set is infinite, there can be at most N populated states.

The N-body wavefunction is then mapped into this new occupation number basis via:

$$\tilde{\Psi}(\mathbf{r}_1...\mathbf{r}_\infty, t) \rightarrow |\tilde{\Psi}(t)\rangle = \sum_{n_1...n_\infty} c(n_1...n_\infty)|n_1...n_\infty\rangle, \tag{A.17}$$

where $c(n_1...n_\infty)$ are appropriate (complex-valued) expansion coefficients, that must be normalised such that the probability of finding the particular system in configuration space is 1, and must obey the relevant particle statistics; for bosons this means being symmetric with respect to the interchange of quantum numbers. For our system this leads to:

$$\int |\tilde{\Psi}|^2 d\mathbf{r} = 1 \rightarrow \sum_{n_1...n_\infty} |c(n_1...n_\infty)|^2 \frac{N!}{n_1!...n_\infty!} = 1. \tag{A.18}$$

The factor $N!/(n_1!...n_\infty!)$ accounts for the correspondence of some sets of occupation numbers to multiple N-particle states due to the indistinguishability of particles. The expressions for the expansion coefficients $c(n_1...n_\infty)$ describe the probability of a particle changing its energy by moving from one level, say i, to another, say j. This can be described mathematically as the simultaneous destruction of a particle in level i and creation of a particle in level j. We encode this using the single-particle annihilation ($\hat{a}$) and creation ($\hat{a}^\dagger$) operators [364] :

$$\hat{a}_i|n_1...n_j...n_i...n_\infty\rangle = \sqrt{n_i}|n_1...n_j...(n_i-1)...n_\infty\rangle, \tag{A.19}$$

$$\hat{a}_j^\dagger|n_1...n_j...n_i...n_\infty\rangle = \sqrt{n_j+1}|n_1...(n_j+1)...n_i...n_\infty\rangle, \tag{A.20}$$

which obey the bosonic commutation relations:

$$\left[\hat{a}_i, \hat{a}_j^\dagger\right] = \delta_{ij}, \qquad \left[\hat{a}_i, \hat{a}_j\right] = \left[\hat{a}_i^\dagger, \hat{a}_j^\dagger\right] = 0. \tag{A.21}$$

We can now describe any particle changing state through these operators; in particular a particle moving from state i to state j can be described by a product of a single-particle annihilation operator and a single-particle creation operator: $\hat{a}_j^\dagger\hat{a}_i$. Likewise, we can describe two-particle interactions where one moves from state i to state j, and the other from state k to state l with the product $\hat{a}_j^\dagger\hat{a}_l^\dagger\hat{a}_i\hat{a}_k$. The formulation in eq. (A.15) and (A.16) can now be expressed as:

$$i\hbar\frac{\partial}{\partial t}|\tilde{\Psi}\rangle = \hat{H}|\tilde{\Psi}\rangle, \tag{A.22}$$

with the Hamiltonian:

$$\hat{H} = \sum_{ij}\langle j|\hat{h}_0|i\rangle\hat{a}_j^\dagger\hat{a}_i + \frac{1}{2}\sum_{ijkl}\langle jl|\hat{V}|ik\rangle\hat{a}_j^\dagger\hat{a}_l^\dagger\hat{a}_i\hat{a}_k \tag{A.23}$$

where

$$\langle j|\hat{h}_0|i\rangle = \int \phi_j^*(\mathbf{r})\hat{h}_0\phi_i(\mathbf{r})d\mathbf{r}, \tag{A.24}$$

$$\langle jl|\hat{V}|ik\rangle = \frac{1}{2}\left[(jl|\hat{V}|ik) + (jl|\hat{V}|ki)\right] \tag{A.25}$$

$$(jl|\hat{V}|ik) = \iint \phi_j^*(\mathbf{r})\phi_l^*(\mathbf{r}')\hat{V}(\mathbf{r}-\mathbf{r}')\phi_i(\mathbf{r}')\phi_k(\mathbf{r})d\mathbf{r}'d\mathbf{r}, \tag{A.26}$$

and $\phi_i(\mathbf{r})$ are solutions of the usual Schrödinger equation, with no interaction term.

For the sake of brevity it is now convenient to introduce the Bose field operators:

$$\hat{\Psi}(\mathbf{r},t) = \sum_i \hat{a}_i(t)\phi_i(\mathbf{r},t), \tag{A.27}$$

$$\hat{\Psi}^\dagger(\mathbf{r},t) = \sum_i \hat{a}_i^\dagger(t)\phi_i^*(\mathbf{r},t), \tag{A.28}$$

with $\hat{\Psi}(\mathbf{r},t)$ representing the removal of a particle at position $\mathbf{r}$ and time t, and $\hat{\Psi}^\dagger(\mathbf{r},t)$ the addition of a particle at position $\mathbf{r}$ and time t. These operators, known respectively as the annihilation and creation operators, satisfy the commutation relations

$$\left[\hat{\Psi}(\mathbf{r},t),\hat{\Psi}^\dagger(\mathbf{r}',t)\right] = \delta(\mathbf{r}-\mathbf{r}'), \qquad \left[\hat{\Psi}(\mathbf{r},t),\hat{\Psi}(\mathbf{r}',t)\right] = \left[\hat{\Psi}^\dagger(\mathbf{r},t),\hat{\Psi}^\dagger(\mathbf{r}',t)\right] = 0 \tag{A.29}$$

for bosonic particles. Using these operators we can rewrite eq. (A.23) as:

$$\hat{H} = \int \hat{\Psi}^\dagger(\mathbf{r},t)\hat{h}_0\hat{\Psi}(\mathbf{r},t)d\mathbf{r} + \frac{1}{2}\iint \hat{\Psi}^\dagger(\mathbf{r},t)\hat{\Psi}^\dagger(\mathbf{r}',t)V(\mathbf{r}-\mathbf{r}')\hat{\Psi}(\mathbf{r}',t)\hat{\Psi}(\mathbf{r},t)d\mathbf{r}'d\mathbf{r}, \tag{A.30}$$

where $V(\mathbf{r}-\mathbf{r}')$ is the two-body interaction potential.

At this point in the derivation the Hamiltonian includes thermal effects and quantum fluctuations, beyond the theory contained in the GPE we will arrive at; the point at which this derivation deviates from approaches containing these effects will be made apparent. For now, we focus on the two-particle interactions. The typical approach is to approximate the two-body interaction potential as a contact interaction:

$$V(\mathbf{r}-\mathbf{r}') = g\delta(\mathbf{r}-\mathbf{r}'), \tag{A.31}$$

that is, we assume that the collisions are local and perfectly elastic, with a strength $g = 4\pi\hbar^2 a_s/m$ as a leading order approximation [365], where a_s is the s-wave scattering length, which can be determined in the laboratory for a particular atomic species.

Inserting this into eq. (A.30) gives the Hamiltonian:

$$\hat{H} = \int \hat{\Psi}^\dagger(\mathbf{r},t)\hat{h}_0\hat{\Psi}(\mathbf{r},t)d\mathbf{r} + \frac{g}{2}\int \hat{\Psi}^\dagger(\mathbf{r},t)\hat{\Psi}^\dagger(\mathbf{r},t)\hat{\Psi}(\mathbf{r},t)\hat{\Psi}(\mathbf{r},t)d\mathbf{r}. \tag{A.32}$$

The Heisenberg equation of motion:

$$i\hbar\frac{\partial}{\partial t}\hat{\Psi}(\mathbf{r},t) = \left[\hat{\Psi}(\mathbf{r},t), \hat{H}\right] \tag{A.33}$$

describes the evolution of the Bose field operator $\hat{\Psi}(\mathbf{r},t)$. Expanding out the commutator and simplifying by using eq. (A.29) and standard commutator identities, then integrating out delta functions, yields:

$$\begin{aligned} i\hbar\frac{\partial\hat{\Psi}(\mathbf{r},t)}{\partial t} &= \int\left[\hat{\Psi},\hat{\Psi}^\dagger\hat{h}_0\hat{\Psi}\right]d\mathbf{r} + \frac{g}{2}\int\left[\hat{\Psi},\hat{\Psi}^\dagger\hat{\Psi}^\dagger\hat{\Psi}\hat{\Psi}\right]d\mathbf{r} \\ &= \int\left[\hat{\Psi},\hat{\Psi}^\dagger\right]\hat{h}_0\hat{\Psi} + \hat{\Psi}^\dagger\left[\hat{\Psi},\hat{h}_0\hat{\Psi}\right]d\mathbf{r} + \frac{g}{2}\int\left[\hat{\Psi},\hat{\Psi}^\dagger\right]\hat{\Psi}^\dagger\hat{\Psi}\hat{\Psi} + \hat{\Psi}^\dagger\left[\hat{\Psi},\hat{\Psi}^\dagger\right]\hat{\Psi}\hat{\Psi} + \hat{\Psi}^\dagger\hat{\Psi}^\dagger\left[\hat{\Psi},\hat{\Psi}\hat{\Psi}\right]d\mathbf{r} \\ &= \hat{h}_0\hat{\Psi}(\mathbf{r},t) + g\hat{\Psi}^\dagger(\mathbf{r},t)\hat{\Psi}(\mathbf{r},t)\hat{\Psi}(\mathbf{r},t) \end{aligned} \tag{A.34}$$

For a Bose-Einstein condensate, with one particular state of the system macroscopically occupied, it is natural to consider a mean field approach [366], splitting the Bose field operator as:

$$\hat{\Psi}(\mathbf{r},t) = \hat{\psi}(\mathbf{r},t) + \hat{\delta}(\mathbf{r},t), \tag{A.35}$$

where $\hat{\psi}(\mathbf{r},t)$ is a field operator for the condensed atoms, in the macroscopically occupied state, and $\hat{\delta}(\mathbf{r},t)$ is a field operator for the non-condensed atoms, that is, atoms in thermally excited states, those promoted from the condensate state by interactions between atoms, and quantum mechanical fluctuations.

We now make the Bogoliubov approximation [71], resulting in the replacement of the operator $\hat{\psi}(\mathbf{r},t)$ in eq. (A.35) by a complex number, usually referred to as the condensate wavefunction, $\psi(\mathbf{r},t) = \sqrt{N_0}\varphi(\mathbf{r},t)$, where N_0 is the number of particles in the condensate. Note that in this definition, $\varphi(\mathbf{r},t)$ is a classical field.

This is a fairly substantial approximation, which immediately results in the breaking of the $U(1)$ global phase symmetry, and the loss of conservation of total particle number. It is assumed that the addition or removal of a particle does not change the state of the system, that is, $N_0 \pm 1 \approx N_0$ for large N_0. Equivalently, the ensemble average of the Bose field operator is well defined and nonzero; $\langle\hat{\Psi}(\mathbf{r},t)\rangle = \psi(\mathbf{r},t) \neq 0$. In this context we identify $\psi(\mathbf{r},t)$ with the condensate, but in principle excitations can be included, provided quantum fluctuations are negligible and the excited states have occupation $n_i \gg 1$.

Finally, in the $T = 0$ limit all of the particles are in the condensed state, and the non-condensate operator $\hat{\delta}(\mathbf{r},t)$ can be neglected, so $\hat{\Psi}(\mathbf{r},t) \to \psi(\mathbf{r},t)$. Thus, $\hat{\Psi}^\dagger(\mathbf{r},t) \to \psi^*(\mathbf{r},t)$, and eq. (A.34) reduces to the Gross-Pitaevskii equation [367, 368]:

$$\begin{aligned} i\hbar\frac{\partial\psi(\mathbf{r},t)}{\partial t} &= \left[\hat{h}_0(\mathbf{r},t) + g|\psi(\mathbf{r},t)|^2\right]\psi(\mathbf{r},t) \\ &= \left[-\frac{\hbar^2}{2m}\nabla^2 + V_{\text{ext}}(\mathbf{r},t) + g|\psi(\mathbf{r},t)|^2\right]\psi(\mathbf{r},t). \end{aligned} \tag{A.36}$$

A.3 Vortex Filament Method

As with the derivation of the point vortex model, the aim here is to find an expression for the velocity field from the vorticity. Given the vorticity $\boldsymbol{\omega} = \nabla\times\mathbf{v}$, we consider an

incompressible flow $\nabla \cdot \mathbf{v} = 0$. We can satisfy this by choosing $\mathbf{v} = \nabla \times \mathbf{A}$, where $\mathbf{A}$ is the vector potential. Furthermore, we can choose $\mathbf{A}$ such that $\nabla \cdot \mathbf{A} = 0$. Then:

$$\begin{aligned} \boldsymbol{\omega} &= \nabla \times \mathbf{v} \\ &= \nabla \times (\nabla \times \mathbf{A}) \\ &= \nabla(\cancelto{0}{\nabla \cdot \mathbf{A}}) - \nabla^2 \mathbf{A} \\ \implies \boldsymbol{\omega} &= -\nabla^2 \mathbf{A} \end{aligned}$$

The Green's Function solution to this Poisson equation is then:

$$\mathbf{A} = -\frac{1}{4\pi} \int_V \frac{\boldsymbol{\omega}(\mathbf{s})}{|\mathbf{s} - \mathbf{r}|} dV, \tag{A.37}$$

where $\mathbf{r}$ is a position vector and $\mathbf{s}$ is a point on the infinitesimally thin spacecurve describing the vorticity. Since $\boldsymbol{\omega}$ is confined to these lines we can rewrite eq. (A.37) as:

$$\mathbf{A} = -\frac{\kappa}{4\pi} \oint \frac{d\mathbf{s}}{|\mathbf{s} - \mathbf{r}|},$$

with $\boldsymbol{\omega}(\mathbf{s})dV = \kappa d\mathbf{s}$ and κ the circulation about a vortex. Then:

$$\frac{d\mathbf{A}}{d\mathbf{s}} = -\frac{\kappa}{4\pi} \frac{d\mathbf{s}}{|\mathbf{s} - \mathbf{r}|}.$$

Taking the curl gives:

$$\nabla \times \frac{d\mathbf{A}}{d\mathbf{s}} = -\frac{\kappa}{4\pi} \nabla \times \left(\frac{d\mathbf{s}}{|\mathbf{s} - \mathbf{r}|} \right)$$

$$\begin{aligned} \implies \frac{d}{d\mathbf{s}} \nabla \times \mathbf{A} = \frac{d\mathbf{v}}{d\mathbf{s}} &= -\frac{\kappa}{4\pi} \nabla \times \left(\frac{d\mathbf{s}}{|\mathbf{s} - \mathbf{r}|} \right) \\ &= -\frac{\kappa}{4\pi} \left[\frac{1}{|\mathbf{s} - \mathbf{r}|} \nabla \times d\mathbf{s} + \left(\nabla \frac{1}{|\mathbf{s} - \mathbf{r}|} \right) \times d\mathbf{s} \right], \end{aligned}$$

using $\nabla \times (\psi \mathbf{A}) = \psi \nabla \times \mathbf{A} + (\nabla \psi) \times \mathbf{A}$, to give:

$$\mathbf{v}(\mathbf{r}) = -\frac{\kappa}{4\pi} \oint \left(\nabla \frac{1}{|\mathbf{s} - \mathbf{r}|} \right) \times d\mathbf{s}.$$

Then, noting that:

$$\begin{aligned} \nabla |\mathbf{s} - \mathbf{r}|^{-1} &= -|\mathbf{s} - \mathbf{r}|^{-2} \nabla |\mathbf{s} - \mathbf{r}| \\ &= -|\mathbf{s} - \mathbf{r}|^{-2} (\mathbf{s} - \mathbf{r}) |\mathbf{s} - \mathbf{r}|^{-1} \\ &= -(\mathbf{s} - \mathbf{r}) |\mathbf{s} - \mathbf{r}|^{-3} \end{aligned}$$

yields the Biot-Savart law:

$$\mathbf{v}(\mathbf{r}) = \frac{\kappa}{4\pi} \oint_{\mathcal{L}} \frac{(\mathbf{s}-\mathbf{r}) \times d\mathbf{s}}{|\mathbf{s}-\mathbf{r}|^3},$$

with the integration over all vortex lines $\mathcal{L}$.

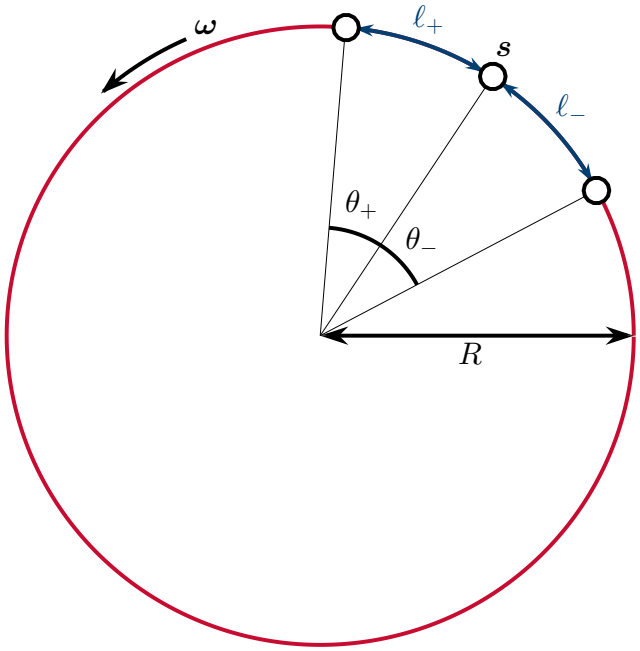

Figure A.1: Schematic of the decomposition of the Biot-Savart integral for a vortex ring into local (blue) and nonlocal (red) parts.

We now derive the desingularisation of the Biot-Savart law. The velocity of a superfluid vortex ring of radius R is experimentally observed [369, 370] to be described by:

$$\mathbf{v}_{\text{ring}}(\mathbf{s}) = \frac{\kappa}{4\pi R}\left[\ln\left(\frac{8R}{a_0}\right) - \frac{1}{2}\right]\mathbf{e}_{\perp}, \tag{A.38}$$

where $\mathbf{e}_{\perp}$ is a unit vector normal to the plane of the vortex ring, equivalent to the motion of a classical vortex ring with a hollow core of radius a_0. This can then be decomposed into a local and nonlocal contribution:

$$\mathbf{v}_{\text{ring}}(\mathbf{s}) = \mathbf{v}_{\text{ring}}^{\text{local}}(\mathbf{s}) + \mathbf{v}_{\text{ring}}^{\text{non}}(\mathbf{s}),$$

where

$$\mathbf{v}_{\text{ring}}^{\text{non}}(\mathbf{s}) = \frac{\kappa}{4\pi} \oint_{\mathcal{L}'} \frac{(\mathbf{s}_1-\mathbf{s}) \times d\mathbf{s}_1}{|\mathbf{s}_1-\mathbf{s}|^3} \tag{A.39}$$

is the standard Biot-Savart integral over the ring, with the prime indicating the omission of a small arclength either side of $\mathbf{s}$, as depicted in Fig. A.1, and with the local component to be determined. Equation (A.39) evaluates to [371]:

$$\mathbf{v}_{\text{ring}}^{\text{non}}(\mathbf{s}) = -\frac{\kappa}{8\pi R}\ln\left[\tan\left(\frac{\theta_+}{4}\right)\tan\left(\frac{\theta_-}{4}\right)\right]\mathbf{e}_\perp,$$

where $\theta_\pm$ are angles subtended by the local section as illustrated in Fig. A.1. As $|\theta_\pm| \ll 1$ we can approximate $\tan(\theta_\pm/4)$ by $\theta_\pm/4 = \ell_\pm/4R$, where $\ell_\pm$ are the arclengths from $\mathbf{s}$ to the nonlocal section. Then, absorbing a factor of $1/2$ into the logarithm, we have:

$$\mathbf{v}_{\text{ring}}^{\text{non}}(\mathbf{s}) = -\frac{\kappa}{4\pi R}\ln\left(\frac{\sqrt{\ell_+\ell_-}}{4R}\right)\mathbf{e}_\perp.$$

Subtracting this from eq. (A.38) yields an expression for the local contribution:

$$\mathbf{v}_{\text{ring}}^{\text{local}}(\mathbf{s}) = \frac{\kappa}{4\pi R}\ln\left(\frac{2\sqrt{\ell_+\ell_-}}{e^{1/2}a_0}\right)\mathbf{e}_\perp.$$

As this contribution only depends on the local structure, this expression is appropriate for the desingularisation of the Biot-Savart integral for general vortex structures; the final remaining component is the generalisation of the $\mathbf{e}_\perp$ vector.

We first note that $\mathbf{s}' \times \mathbf{s}''$ is normal to the plane containing $\mathbf{s}'$ and $\mathbf{s}''$, and so $\mathbf{s}' \times \mathbf{s}'' \parallel \mathbf{e}_\perp$ as illustrated in Fig. A.2. Since $\mathbf{s}'$ is a unit vector with $|\mathbf{s}'| = 1$, and $|\mathbf{s}''| = R^{-1}$, as $R = 1/\sqrt{\mathbf{s}''\cdot\mathbf{s}''}$, we have $|\mathbf{s}' \times \mathbf{s}''| = R^{-1}$. It is now apparent that $\mathbf{e}_\perp = R\mathbf{s}' \times \mathbf{s}''$, and so:

$$\mathbf{v}^{\text{local}}(\mathbf{s}) = \frac{\kappa}{4\pi}\ln\left(\frac{2\sqrt{\ell_+\ell_-}}{e^{1/2}a_0}\right)\mathbf{s}' \times \mathbf{s}'',$$

to give:

$$\mathbf{v}(\mathbf{s}) = \frac{\kappa}{4\pi}\ln\left(\frac{2\sqrt{\ell_+\ell_-}}{e^{1/2}a_0}\right)\mathbf{s}' \times \mathbf{s}'' + \frac{\kappa}{4\pi}\oint_{\mathcal{L}'}\frac{(\mathbf{s}_1 - \mathbf{s}) \times d\mathbf{s}_1}{|\mathbf{s}_1 - \mathbf{s}|^3}.$$

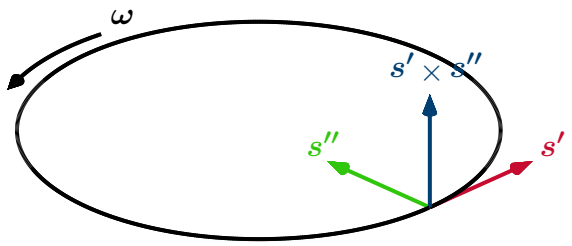

Figure A.2: Schematic of the orthogonal set of vectors $\mathbf{s}'$, $\mathbf{s}''$, and $\mathbf{s}' \times \mathbf{s}''$.

A.4 Local Induction Approximation

We follow the derivation of [372]. Starting with the Biot-Savart law for the self-induced velocity $\mathbf{v}(\mathbf{s})$ of a vortex filament:

$$\mathbf{v}(\mathbf{s}) = \frac{\kappa}{4\pi} \oint \frac{(\mathbf{s}_1 - \mathbf{s}) \times d\mathbf{s}_1}{|\mathbf{s}_1 - \mathbf{s}|^3}, \tag{A.40}$$

where $\mathbf{s} = \mathbf{s}(\xi)$ is a spacecurve (or set of spacecurves) describing the vortex filaments, with $\mathbf{s}$ a point on the curve, ξ the arclength from $\mathbf{s}_1$ to $\mathbf{s}$, and κ the circulation, we consider a Taylor series expansion about $\mathbf{s}$:

$$\mathbf{s}_1 \simeq \mathbf{s} + \xi\mathbf{s}' + \frac{1}{2}\xi^2\mathbf{s}'' + ..., \text{ or}$$

$$\mathbf{s}_1 - \mathbf{s} \simeq \xi\mathbf{s}' + \frac{1}{2}\xi^2\mathbf{s}'' + ... \tag{A.41}$$

Differentiation w.r.t. ξ gives:

$$\frac{d\mathbf{s}_1}{d\xi} \simeq \mathbf{s}' + \xi\mathbf{s}'' + ...$$

$$\implies d\mathbf{s}_1 \simeq (\mathbf{s}' + \xi\mathbf{s}'' + ...)d\xi \tag{A.42}$$

Substituting eq. (A.41) and (A.42) into eq. (A.40):

$$\mathbf{v}(\mathbf{s}) \simeq \frac{\kappa}{4\pi} \oint \frac{(\xi\mathbf{s}' + \frac{1}{2}\xi^2\mathbf{s}'' + ...) \times (\mathbf{s}' + \xi\mathbf{s}'' + ...)d\xi}{|\xi\mathbf{s}' + \frac{1}{2}\xi^2\mathbf{s}'' + ...|^3}. \tag{A.43}$$

Consider the denominator:

$$\begin{aligned}
|\xi\mathbf{s}' + \frac{1}{2}\xi^2\mathbf{s}'' + ...|^3 &= (|\xi||\mathbf{s}' + \frac{1}{2}\xi\mathbf{s}'' + ...|)^3 \\
&= |\xi|^3|\mathbf{s}' + \frac{1}{2}\mathbf{s}'' + ...|^3 \\
&= |\xi|^3 \left[(\mathbf{s}' + \frac{1}{2}\xi\mathbf{s}'' + ...) \cdot (\mathbf{s}' + \frac{1}{2}\xi\mathbf{s}'' + ...)\right]^{\frac{3}{2}} \text{ (using } |\mathbf{a}|^2 = \mathbf{a}\cdot\mathbf{a}) \\
&= |\xi|^3[\mathbf{s}'\cdot\mathbf{s}' + \xi\mathbf{s}'\cdot\mathbf{s}'' + \frac{1}{4}\xi^2\mathbf{s}''\cdot\mathbf{s}'' + ...]^{\frac{3}{2}} \\
&= |\xi|^3[|\mathbf{s}'|^2 + \frac{1}{4}\xi^2|\mathbf{s}''|^2 + ...]^{\frac{3}{2}}, \text{ since } \mathbf{s}' \perp \mathbf{s}'' \\
&= |\xi|^3 \left[1 + \frac{\xi}{4R^2}\right],
\end{aligned} \tag{A.44}$$

as $|\mathbf{s}'| = 1$ and $|\mathbf{s}''| = R^{-1}$ where R is the local radius of curvature. Now the numerator:

$$(\xi\mathbf{s}' + \frac{1}{2}\xi^2\mathbf{s}'' + ...) \times (\mathbf{s}' + \xi\mathbf{s}'' + ...) = \xi\mathbf{s}' \times \mathbf{s}' + \xi^2\mathbf{s}' \times \mathbf{s}'' + \frac{1}{2}\xi^2\mathbf{s}'' \times \mathbf{s}' + \frac{1}{2}\xi^3\mathbf{s}'' \times \mathbf{s}'$$

$$= \xi^2\mathbf{s}' \times \mathbf{s}'' - \frac{1}{2}\xi^2\mathbf{s}' \times \mathbf{s}''$$

$$= \frac{1}{2}\xi^2\mathbf{s}' \times \mathbf{s}'' \tag{A.45}$$

(using $\mathbf{a} \times \mathbf{b} = -\mathbf{b} \times \mathbf{a}, \mathbf{a} \times \mathbf{a} = \mathbf{0}$).

Substituting this and eq. (A.44) into eq. (A.43) gives:

$$\mathbf{v}(\mathbf{s}) \simeq \frac{\kappa}{8\pi}\mathbf{s}' \times \mathbf{s}'' \oint |\xi|^{-1} \left(1 + \frac{\xi}{4R^2} + ...\right)^{-\frac{3}{2}}$$

$$= \frac{\kappa}{8\pi}\mathbf{s}' \times \mathbf{s}'' \oint |\xi|^{-1} \left(1 - \frac{3\xi}{8R^2} + \frac{15\xi^4}{128R^4} - ...\right).$$

using a binomial expansion. Neglecting $\mathcal{O}(\xi^2)$ and higher-order terms we have:

$$\mathbf{v}(\mathbf{s}) \simeq \frac{\kappa}{8\pi}\mathbf{s}' \times \mathbf{s}'' \oint |\xi|^{-1}[1 + \mathcal{O}(\xi^2)]d\xi$$

$$= \frac{\kappa}{8\pi}\mathbf{s}' \times \mathbf{s}'' \oint |\xi|^{-1}d\xi$$
$$= \frac{\kappa}{8\pi}\mathbf{s}' \times \mathbf{s}'' \int_{\infty}^{\infty} |\xi|^{-1}d\xi$$
$$= \frac{\kappa}{4\pi}\mathbf{s}' \times \mathbf{s}'' \int_{0}^{\infty} \xi^{-1}d\xi, \text{ as } |\xi|^{-1} \text{ is even.}$$

Since $\ln(\xi)$ diverges as $\xi \to 0$ and as $\xi \to \infty$ we impose new limits on this integral, using the relevant length scales a_0 (the core radius) and R:

$$\mathbf{v}(\mathbf{s}) \simeq \frac{\kappa}{4\pi}\mathbf{s}' \times \mathbf{s}'' \int_{a_0}^{R} \xi^{-1}d\xi.$$

which gives the local induction approximation:

$$\mathbf{v}(\mathbf{s}) = \frac{\kappa}{4\pi}\mathbf{s}' \times \mathbf{s}'' \ln\left(\frac{R}{a_0}\right).$$

A.5 Finite Difference Methods

A.5.1 Regular Grids

We seek numerical approximations of spatial derivatives of scalar fields defined on regular grids. Consider a scalar field F defined on such a grid, with known values of F: F_0, F_1, $F_2, ..., F_{n-2}, F_{n-1}, F_n$ at points $x_0, x_1, x_2, ..., x_{n-2}, x_{n-1}, x_n$, with $\Delta x = x_i - x_{i-1}$. We will make repeated use of the following Taylor expansions about F_i in these derivations:

$$F_{i+1} = F_i + \Delta x \left.\frac{dF}{dx}\right|_{x=x_i} + \frac{(\Delta x)^2}{2} \left.\frac{d^2F}{dx^2}\right|_{x=x_i} + \mathcal{O}((\Delta x)^3)) \tag{A.46}$$

$$F_{i+1} = F_i + \Delta x \left.\frac{dF}{dx}\right|_{x=x_i} + \frac{(\Delta x)^2}{2} \left.\frac{d^2F}{dx^2}\right|_{x=x_i} + \frac{(\Delta x)^3}{3!} \left.\frac{d^3F}{dx^3}\right|_{x=x_i} + \frac{(\Delta x)^4}{4!} \left.\frac{d^4F}{dx^4}\right|_{x=x_i} + \mathcal{O}((\Delta x)^5)) \tag{A.47}$$

$$F_{i-1} = F_i - \Delta x \left.\frac{dF}{dx}\right|_{x=x_i} + \frac{(\Delta x)^2}{2} \left.\frac{d^2F}{dx^2}\right|_{x=x_i} + \mathcal{O}((\Delta x)^3)) \tag{A.48}$$

$$F_{i-1} = F_i - \Delta x \left.\frac{dF}{dx}\right|_{x=x_i} + \frac{(\Delta x)^2}{2} \left.\frac{d^2F}{dx^2}\right|_{x=x_i} - \frac{(\Delta x)^3}{3!} \left.\frac{d^3F}{dx^3}\right|_{x=x_i} + \frac{(\Delta x)^4}{4!} \left.\frac{d^4F}{dx^4}\right|_{x=x_i} + \mathcal{O}((\Delta x)^5)) \tag{A.49}$$

$$F_{i+2} = F_i + 2\Delta x \left.\frac{dF}{dx}\right|_{x=x_i} + \frac{(2\Delta x)^2}{2} \left.\frac{d^2F}{dx^2}\right|_{x=x_i} + \frac{(2\Delta x)^3}{3!} \left.\frac{d^3F}{dx^3}\right|_{x=x_i} + \frac{(2\Delta x)^4}{4!} \left.\frac{d^4F}{dx^4}\right|_{x=x_i} + \mathcal{O}((\Delta x)^5)) \tag{A.50}$$

$$F_{i-2} = F_i - 2\Delta x \left.\frac{dF}{dx}\right|_{x=x_i} + \frac{(2\Delta x)^2}{2} \left.\frac{d^2F}{dx^2}\right|_{x=x_i} - \frac{(2\Delta x)^3}{3!} \left.\frac{d^3F}{dx^3}\right|_{x=x_i} + \frac{(2\Delta x)^4}{4!} \left.\frac{d^4F}{dx^4}\right|_{x=x_i} + \mathcal{O}((\Delta x)^5)) \tag{A.51}$$

For 2nd-order approximations of first derivatives we rearrange eq. (A.46) and (A.48) to isolate terms containing $(dF/dx)|_{x=x_i}$ on the LHS:

$$\Delta x \left.\frac{dF}{dx}\right|_{x=x_i} = F_{i+1} - F_i - \frac{(\Delta x)^2}{2} \left.\frac{d^2F}{dx^2}\right|_{x=x_i} + \mathcal{O}((\Delta x)^3), \tag{A.52}$$

$$\Delta x \left.\frac{dF}{dx}\right|_{x=x_i} = -F_{i-1} + F_i + \frac{(\Delta x)^2}{2} \left.\frac{d^2F}{dx^2}\right|_{x=x_i} + \mathcal{O}((\Delta x)^3). \tag{A.53}$$

Summing eq. (A.52) & (A.53):

$$2\Delta x \left.\frac{dF}{dx}\right|_{x=x_i} = F_{i+1} - F_{i-1} + \mathcal{O}((\Delta x)^3)$$

$$\implies \left.\frac{dF}{dx}\right|_{x=x_i} = \frac{-F_{i-1} + F_{i+1}}{2\Delta x} + \mathcal{O}((\Delta x)^2). \tag{A.54}$$

For 4th-order approximations of first derivatives we rearrange eq. (A.47), (A.49), (A.50), and (A.51) to isolate terms containing $(dF/dx)|_{x=x_i}$ on the LHS:

$$\Delta x \left.\frac{dF}{dx}\right|_{x=x_i} = -F_i + F_{i+1} - \frac{(\Delta x)^2}{2} \left.\frac{d^2F}{dx^2}\right|_{x=x_i} - \frac{(\Delta x)^3}{3!} \left.\frac{d^3F}{dx^3}\right|_{x=x_i} - \frac{(\Delta x)^4}{4!} \left.\frac{d^4F}{dx^4}\right|_{x=x_i} + \mathcal{O}((\Delta x)^5), \tag{A.55}$$

$$\Delta x \left.\frac{dF}{dx}\right|_{x=x_i} = F_i - F_{i-1} + \frac{(\Delta x)^2}{2} \left.\frac{d^2F}{dx^2}\right|_{x=x_i} - \frac{(\Delta x)^3}{3!} \left.\frac{d^3F}{dx^3}\right|_{x=x_i} + \frac{(\Delta x)^4}{4!} \left.\frac{d^4F}{dx^4}\right|_{x=x_i} + \mathcal{O}((\Delta x)^5), \tag{A.56}$$

$$2\Delta x \left.\frac{dF}{dx}\right|_{x=x_i} = -F_i + F_{i+2} - \frac{(2\Delta x)^2}{2} \left.\frac{d^2F}{dx^2}\right|_{x=x_i} - \frac{(2\Delta x)^3}{3!} \left.\frac{d^3F}{dx^3}\right|_{x=x_i} - \frac{(2\Delta x)^4}{4!} \left.\frac{d^4F}{dx^4}\right|_{x=x_i} + \mathcal{O}((\Delta x)^5), \tag{A.57}$$

$$2\Delta x \left.\frac{dF}{dx}\right|_{x=x_i} = F_i - F_{i-2} + \frac{(2\Delta x)^2}{2} \left.\frac{d^2F}{dx^2}\right|_{x=x_i} - \frac{(2\Delta x)^3}{3!} \left.\frac{d^3F}{dx^3}\right|_{x=x_i} + \frac{(2\Delta x)^4}{4!} \left.\frac{d^4F}{dx^4}\right|_{x=x_i} + \mathcal{O}((\Delta x)^5), \tag{A.58}$$

We seek a linear combination of eq. (A.55), (A.56), (A.57), and (A.58), such that all terms of order $(\Delta x)^2$ and above cancel:

$$c_1(A.55) + c_2(A.56) + c_3(A.57) + c_4(A.58) \text{ s.t.} \tag{A.59}$$

$$-c_1 + c_2 - 4c_3 + 4c_4 = 0, \tag{A.60}$$

$$-c_1 - c_2 - 8c_3 - 8c_4 = 0, \tag{A.61}$$

$$-c_1 + c_2 - 16c_3 + 16c_4 = 0, \tag{A.62}$$

We also require that the LHS be nonzero, which we encode as the final linear equation:

$$c_1 + c_2 + 2c_3 + 2c_4 = 1. \tag{A.63}$$

Subtracting eq. (A.60) from eq. (A.62) yields:

$$-12c_3 + 12c_4 = 0 \implies c_3 = c_4. \tag{A.64}$$

Substituting eq. (A.64) into eq. (A.60) then gives:

$$-c_1 + c_2 = 0 \implies c_1 = c_2. \tag{A.65}$$

We then substitute eq. (A.64) and (A.65) into eq. (A.61):

$$-c_1 - c_1 - 8c_3 - 8c_3 = 0 \implies c_3 = -\frac{c_1}{8}, \tag{A.66}$$

which we substitute into eq. (A.63):

$$c_1 + c_1 - \frac{2c_1}{8} - \frac{2c_1}{8} = 1 \implies c_1 = \frac{2}{3},$$

which immediately leads to $c_2 = 2/3$, $c_3 = -1/12$, $c_4 = -1/12$. Substituting this all into eq. (A.59) gives:

$$\Delta x \left.\frac{dF}{dx}\right|_{x=x_i} = \frac{2}{3}F_{i+1} - \frac{2}{3}F_{i-1} - \frac{1}{12}F_{i+2} + \frac{1}{12}F_{i-2} + \mathcal{O}((\Delta x)^5)$$

$$\implies \left.\frac{dF}{dx}\right|_{x=x_i} = \frac{\frac{1}{12}F_{i-2} - \frac{2}{3}F_{i-1} + \frac{2}{3}F_{i+1} - \frac{1}{12}F_{i+2}}{\Delta x} + \mathcal{O}((\Delta x)^4). \tag{A.67}$$

For 2nd-order approximations of second derivatives we first rearrange eq. (A.46) and (A.48) to isolate terms containing $(d^2F/dx^2)|_{x=x_i}$ on the LHS:

$$\left.\frac{(\Delta x)^2}{2}\,\frac{d^2F}{dx^2}\right|_{x=x_i} = -F_i + F_{i+1} - \Delta x \left.\frac{dF}{dx}\right|_{x=x_i} + \mathcal{O}((\Delta x)^3), \tag{A.68}$$

$$\left.\frac{(\Delta x)^2}{2}\,\frac{d^2F}{dx^2}\right|_{x=x_i} = -F_i + F_{i-1} + \Delta x \left.\frac{dF}{dx}\right|_{x=x_i} + \mathcal{O}((\Delta x)^3), \tag{A.69}$$

Summing eq. (A.68) and (A.69) yields:

$$\left.(\Delta x)^2\,\frac{d^2F}{dx^2}\right|_{x=x_i} = -2F_i + F_{i+1} + F_{i-1} + \mathcal{O}((\Delta x)^3)$$

$$\implies \left.\frac{d^2F}{dx^2}\right|_{x=x_i} = \frac{F_{i-1} - 2F_i + F_{i+1}}{(\Delta x)^2} + \mathcal{O}(\Delta x). \tag{A.70}$$

However, if we consider the next term in the Taylor series expansions eq. (A.46) and (A.48):

$$\left.\frac{(\Delta x)^3}{3!}\,\frac{d^3F}{dx^3}\right|_{x=x_i}, \qquad \left.-\frac{(\Delta x)^3}{3!}\,\frac{d^3F}{dx^3}\right|_{x=x_i}, \tag{A.71}$$

respectively, substituting into the numerator of the RHS of eq. (A.70) we have:

$$\left.-\frac{(\Delta x)^3}{3!}\,\frac{d^3F}{dx^3}\right|_{x=x_i} + \left.\frac{(\Delta x)^3}{3!}\,\frac{d^3F}{dx^3}\right|_{x=x_i} = 0, \tag{A.72}$$

and so the truncation error is in fact $\mathcal{O}((\Delta x)^2)$:

$$\left.\frac{d^2F}{dx^2}\right|_{x=x_i} = \frac{F_{i-1} - 2F_i + F_{i+1}}{(\Delta x)^2} + \mathcal{O}((\Delta x)^2). \tag{A.73}$$

For 4th-order approximations of second derivatives we rearrange eq. (A.47), (A.49), (A.50), and (A.51) to isolate terms containing $(d^2F/dx^2)|_{x=x_i}$ on the LHS:

$$\left.\frac{(\Delta x)^2}{2}\,\frac{d^2F}{dx^2}\right|_{x=x_i} = -F_i + F_{i+1} - \Delta x \left.\frac{dF}{dx}\right|_{x=x_i} - \left.\frac{(\Delta x)^3}{3!}\,\frac{d^3F}{dx^3}\right|_{x=x_i} - \left.\frac{(\Delta x)^4}{4!}\,\frac{d^4F}{dx^4}\right|_{x=x_i} + \mathcal{O}((\Delta x)^5), \tag{A.74}$$

$$\left.\frac{(\Delta x)^2}{2}\,\frac{d^2F}{dx^2}\right|_{x=x_i} = -F_i + F_{i-1} + \Delta x \left.\frac{dF}{dx}\right|_{x=x_i} + \left.\frac{(\Delta x)^3}{3!}\,\frac{d^3F}{dx^3}\right|_{x=x_i} - \left.\frac{(\Delta x)^4}{4!}\,\frac{d^4F}{dx^4}\right|_{x=x_i} + \mathcal{O}((\Delta x)^5), \tag{A.75}$$

$$\left.\frac{(2\Delta x)^2}{2}\,\frac{d^2F}{dx^2}\right|_{x=x_i} = -F_i + F_{i+2} - 2\Delta x \left.\frac{dF}{dx}\right|_{x=x_i} - \left.\frac{(2\Delta x)^3}{3!}\,\frac{d^3F}{dx^3}\right|_{x=x_i} - \left.\frac{(2\Delta x)^4}{4!}\,\frac{d^4F}{dx^4}\right|_{x=x_i} + \mathcal{O}((\Delta x)^5), \tag{A.76}$$

$$\frac{(2\Delta x)^2}{2}\left.\frac{d^2F}{dx^2}\right|_{x=x_i} = -F_i + F_{i-2} + 2\Delta x \left.\frac{dF}{dx}\right|_{x=x_i} + \frac{(2\Delta x)^3}{3!}\left.\frac{d^3F}{dx^3}\right|_{x=x_i} - \frac{(2\Delta x)^4}{4!}\left.\frac{d^4F}{dx^4}\right|_{x=x_i} + \mathcal{O}((\Delta x)^5). \tag{A.77}$$

We again seek a linear combination:

$$c_1(A.74) + c_2(A.75) + c_3(A.76) + c_4(A.77) \tag{A.78}$$

such that the LHS is nonzero, and terms containing Δx, $(\Delta x)^3$, and $(\Delta x)^4$ cancel, giving us the system of linear equations:

$$c_1 + c_2 + 4c_3 + 4c_4 = 1, \tag{A.79}$$

$$-c_1 + c_2 - 2c_3 + 2c_4 = 0, \tag{A.80}$$

$$-c_1 + c_2 - 8c_3 + 8c_4 = 0, \tag{A.81}$$

$$-c_1 - c_2 - 16c_3 - 16c_4 = 0. \tag{A.82}$$

Subtracting eq. (A.80) from eq. (A.81):

$$-6c_3 + 6c_4 = 0 \implies c_3 = c_4. \tag{A.83}$$

Substituting eq. (A.83) into eq. (A.81):

$$-c_1 + c_2 = 0 \implies c_1 = c_2. \tag{A.84}$$

Now substituting eq. (A.83) and (A.84) into eq. (A.82):

$$-c_1 - 16c_3 = 0 \implies c_3 = -\frac{c_1}{16}. \tag{A.85}$$

Finally, substituting eq. (A.83), (A.84), and (A.85) into eq. (A.79):

$$c_1 - \frac{c_1}{4} = 1 \implies c_1 = \frac{4}{3},$$

which immediately gives $c_2 = 4/3$, $c_3 = -1/12$, $c_4 = -1/12$. Substituting this all into eq. (A.78) yields:

$$(\Delta x)^2 \left.\frac{d^2F}{dx^2}\right|_{x=x_i} = -\frac{5}{2}F_i + \frac{4}{3}F_{i+1} + \frac{4}{3}F_{i-1} - \frac{1}{12}F_{i+2} - \frac{1}{12}F_{i-1} + \mathcal{O}((\Delta x)^5)$$

$$\implies \left.\frac{d^2F}{dx^2}\right|_{x=x_i} = \frac{-\frac{1}{12}F_{i-2} + \frac{4}{3}F_{i-1} - \frac{5}{2}F_i + \frac{4}{3}F_{i+1} - \frac{1}{12}F_{i+2}}{(\Delta x)^2} + \mathcal{O}((\Delta x)^3). \tag{A.86}$$

Again, we consider the next terms in the Taylor series expansions, eq. (A.47), (A.49), (A.50), and (A.51):

$$\frac{(\Delta x)^5}{5!}\left.\frac{d^5F}{dx^5}\right|_{x=x_i}, \quad -\frac{(\Delta x)^5}{5!}\left.\frac{d^5F}{dx^5}\right|_{x=x_i}, \quad \frac{(2\Delta x)^5}{5!}\left.\frac{d^5F}{dx^5}\right|_{x=x_i}, \quad -\frac{(2\Delta x)^5}{5!}\left.\frac{d^5F}{dx^5}\right|_{x=x_i}, \tag{A.87}$$

respectively, and substituting into the numerator of the RHS of eq. (A.86) we have:

$$-\frac{1}{12}\frac{(\Delta x)^5}{5!}\left.\frac{d^5F}{dx^5}\right|_{x=x_i}-\frac{4}{3}\frac{(2\Delta x)^5}{5!}\left.\frac{d^5F}{dx^5}\right|_{x=x_i}+\frac{4}{3}\frac{(\Delta x)^5}{5!}\left.\frac{d^5F}{dx^5}\right|_{x=x_i}+\frac{1}{12}\frac{(2\Delta x)^5}{5!}\left.\frac{d^5F}{dx^5}\right|_{x=x_i}=0; \tag{A.88}$$

the truncation error is in fact $\mathcal{O}((\Delta x)^4)$:

$$\left.\frac{d^2F}{dx^2}\right|_{x=x_i}=\frac{-\frac{1}{12}F_{i-2}+\frac{4}{3}F_{i-1}-\frac{5}{2}F_i+\frac{4}{3}F_{i+1}-\frac{1}{12}F_{i+2}}{(\Delta x)^2}+\mathcal{O}((\Delta x)^4). \tag{A.89}$$

A.5.2 Irregular Grids

We derive here 3rd-order derivatives using finite difference methods on irregular grids, following the method of [373] - details for other orders can be found in their paper, with the derivation much the same as is given here.

Suppose we have a function F with known values F_0, F_1, F_2, ..., F_{n-2}, F_{n-1}, F_n, at positions x_0, x_1, x_2,...,x_{n-2}, x_{n-1}, x_n, where the interval between x_i and x_{i+1} is not necessarily constant. We define $\Delta_{+i} = x_{i+1} - x_i$, $\Delta_{-i} = x_i - x_{i-1}$, with Δ_i whichever of the two is greater.

We first seek a 3rd-order approximation for the first derivative of the form:

$$\left.\frac{dF}{dx}\right|_{x=x_i}=A_iF_{i-1}+B_iF_i+C_iF_{i+1}+\mathcal{O}(\Delta_i^3), \tag{A.90}$$

where A_i, B_i, C_i are coefficients to be determined. Consider the Taylor series expansions:

$$F_{i-1}=F_i-\Delta_{-i}\left.\frac{dF}{dx}\right|_{x=x_i}+\frac{\Delta_{-i}^2}{2!}\left.\frac{d^2F}{dx^2}\right|_{x=x_i}+\mathcal{O}(\Delta_{-i}^3), \tag{A.91}$$

$$F_{i+1}=F_i+\Delta_{+i}\left.\frac{dF}{dx}\right|_{x=x_i}+\frac{\Delta_{+i}^2}{2!}\left.\frac{d^2F}{dx^2}\right|_{x=x_i}+\mathcal{O}(\Delta_{+i}^3), \tag{A.92}$$

In order to match coefficients in eq. (A.90) we require that:

$$A_i+B_i+C_i=0, \tag{A.93}$$

$$-\Delta_{-i}A_i+\Delta_{+i}C_i=1, \tag{A.94}$$

$$\frac{\Delta_{-i}^2}{2!}A_i+\frac{\Delta_{+i}^2}{2!}C_i=0. \tag{A.95}$$

Rearranging eq. (A.95):

$$A_i=-\frac{\Delta_{+i}^2}{\Delta_{-i}^2}C_i. \tag{A.96}$$

Substituting this into eq. (A.94) and rearranging yields:

$$C_i=\frac{\Delta_{-i}}{\Delta_{+i}(\Delta_{+i}+\Delta_{-i})}. \tag{A.97}$$

Substituting this back into eq. (A.96) we have:

$$A_i = -\frac{\Delta_{+i}}{\Delta_{-i}(\Delta_{+i} + \Delta_{-i})}, \tag{A.98}$$

and substituting these into eq. (A.93):

$$B_i = -\frac{(\Delta_{+i}^2 + \Delta_{-i}^2)}{\Delta_{+i}\Delta_{-i}(\Delta_{+i} + \Delta_{-i})}. \tag{A.99}$$

Then by construction our 3$^{\text{rd}}$-order scheme is:

$$\left.\frac{dF}{dx}\right|_{x=x_i} = \frac{-\Delta_{+i}^2 F_{i-1} - (\Delta_{+i}^2 + \Delta_{-i}^2)F_i + \Delta_{-i}^2 F_{i+1}}{\Delta_{+i}\Delta_{-i}(\Delta_{+i} + \Delta_{-i})} + \mathcal{O}(\Delta_i^3). \tag{A.100}$$

Similarly, we seek a 3$^{\text{rd}}$-order approximation for the second derivative of the form:

$$\left.\frac{d^2F}{dx^2}\right|_{x=x_i} = A_i F_{i-1} + B_i F_i + C_i F_{i+1} + \mathcal{O}(\Delta_i^3), \tag{A.101}$$

where A_i, B_i, C_i are coefficients to be determined. To match coefficients of the Taylor series expansions we now require:

$$A_i + B_i + C_i = 0, \tag{A.102}$$

$$-\Delta_{-i}A_i + \Delta_{+i}C_i = 0, \tag{A.103}$$

$$\frac{\Delta_{-i}^2}{2!}A_i + \frac{\Delta_{+i}^2}{2!}C_i = 1. \tag{A.104}$$

Rearranging eq. (A.103):

$$A_i = \frac{\Delta_{+i}}{\Delta_{-i}}C_i. \tag{A.105}$$

Substituting this into eq. (A.104) and rearranging:

$$C_i = \frac{1}{\Delta_{-i}(\Delta_{+i} + \Delta_{-i})}, \tag{A.106}$$

and substituting this back into eq. (A.103):

$$A_i = \frac{1}{\Delta_{+i}(\Delta_{+i} + \Delta_{-i})}. \tag{A.107}$$

Substituting these into eq. (A.102):

$$B_i = -\frac{1}{\Delta_{+i}\Delta_{-i}}, \tag{A.108}$$

and so by construction our 3$^{\text{rd}}$-order scheme is:

$$\left.\frac{d^2F}{dx^2}\right|_{x=x_i} = \frac{\Delta_{-i}F_{i-1} - (\Delta_{+i} + \Delta_{-i})F_i + \Delta_{+i}F_{i+1}}{\Delta_{+i}\Delta_{-i}(\Delta_{+i} + \Delta_{-i})} + \mathcal{O}(\Delta_i^3). \tag{A.109}$$

A.6 Runge-Kutta Method

We give a derivation of the family of (globally) 2nd-order Runge-Kutta methods of quadrature, with the extensions required for proof of higher-order methods indicated.

Let an initial value problem be specified as:

$$\frac{dy}{dt} = f(y(t), t), \qquad y(t_0) = y_0, \tag{A.110}$$

where $t_n = n\Delta t$, Δt is the chosen time-step, and $f(y(t), t)$ is known. We seek an approximation of the solution $y(t_n)$ from the initial condition $y(t_0) = y_0$ through progressive approximation of the solution at intermediate times. A single step from a known $y(t_n)$ to an unknown $y_(t_{n+1})$ can be written as:

$$y(t_{n+1}) = y(t_n) + [y(t_{n+1}) - y(t_n)]$$

$$= y(t_n) + \int_{t_n}^{t_{n+1}} f(y(t'), t')dt'. \tag{A.111}$$

We now choose to substitute a numerical approximation for the exact integral $\int_{t_n}^{t_{n+1}} f(y(t'), t')dt'$, assuming we are in a situation where the exact evaluation of this is impossible or extremely difficult, of the form:

$$y(t_{n+1}) \approx y(t_n) + \Delta t \sum_{i=1}^{N} \left[b_i f\left(y\left(t_n + c_i\Delta t\right), t_n + c_i\Delta t\right)\right], \tag{A.112}$$

where N is the number of stages to be used in the scheme, and b_i and c_i are weights to be determined. The number of stages required is related to the desired order of accuracy in a way which is not yet fully understand; for the sake of this proof it is sufficient to note that the minimum number of stages required is equal to the order desired for schemes of up to 4th-order.

We aim to derive a 2nd-order scheme, so choose $N = 2$. We take our first substep at $c_1 = 0$, so the first term in eq. (A.112), excluding the weight b_i, which we label k_1, becomes:

$$k_1 = f(y(t_n), t_n), \tag{A.113}$$

which is straightforward to calculate. We then approximate k_2 as:

$$k_2 = f(y(t_n + c_2\Delta t), t_n + c_2\Delta t) \approx f(y(t_n) + a_{21}k_1\Delta t, t_n + c_2\Delta t), \tag{A.114}$$

with a_{21} another weight to be determined, and with the further substeps necessary for higher-order schemes approximated by:

$$k_i \approx f\left(y(t_n) + \Delta t \sum_{j=1}^{i-1} a_{ij}k_j, t_n + c_i\Delta t\right) \tag{A.115}$$

To 2nd-order the quadrature equation eq. (A.112) becomes:

$$y(t_{n+1}) \approx y(t_n) + \Delta t(b_1 k_1 + b_2 k_2). \tag{A.116}$$

Now consider the Taylor expansion:

$$y(t_{n+1}) = y(t_n) + \Delta t \left.\frac{dy}{dt}\right|_{t=t_n} + \frac{(\Delta t)^2}{2} \left.\frac{d^2y}{dt^2}\right|_{t=t_n} + \mathcal{O}((\Delta t)^3), \tag{A.117}$$

where for higher-order derivations additional terms would be retained. Substituting this into the LHS of eq. (A.116) and cancelling $f(t_n)$ gives:

$$\Delta t \left.\frac{dy}{dt}\right|_{t=t_n} + \frac{(\Delta t)^2}{2} \left.\frac{d^2y}{dt^2}\right|_{t=t_n} + \mathcal{O}((\Delta t)^3) = \Delta t(b_1 k_1 + b_2 k_2). \tag{A.118}$$

Furthermore:

$$\frac{dy}{dt} = f, \tag{A.119}$$

$$\frac{d^2y}{dt^2} = \frac{\partial f}{\partial t} + f\frac{\partial f}{\partial y}. \tag{A.120}$$

Combining eq. (A.114), (A.118), (A.119), and (A.120) yields:

$$hf + \frac{(\Delta t)^2}{2}\left(\frac{\partial f}{\partial t} + f\frac{\partial f}{\partial y}\right) + \mathcal{O}((\Delta t)^3) = \Delta t(b_1 f + b_2 f(y(t_n) + a_{21}k_1\Delta t, t_n + c_2\Delta t)), \tag{A.121}$$

where we have suppressed the arguments of f for notational convenience whenever the arguments are to be $y(t_n)$, t_n. We take the Taylor expansion of the final term of the RHS, again retaining further terms for higher-order derivations, to give:

$$\Delta t f + \frac{(\Delta t)^2}{2}\left(\frac{\partial f}{\partial t} + f\frac{\partial f}{\partial y}\right) + \mathcal{O}((\Delta t)^3) = \Delta t(b_1 f + b_2\left(f + c_2\Delta t\frac{\partial f}{\partial t} + a_{21}\Delta t f\frac{\partial f}{\partial y}\right)) + \mathcal{O}((\Delta t)^3) \tag{A.122}$$

By matching terms of the same order in Δt we find that the following must be satisfied for the scheme to be consistent:

$$b_1 + b_2 = 1 \tag{A.123}$$

$$b_2 c_2 = \frac{1}{2} \tag{A.124}$$

$$b_2 a_{21} = \frac{1}{2} \tag{A.125}$$

The canonical choice is $b_1 = b_2 = \frac{1}{2}$, $c_2 = a_{21} = 1$, and the full scheme is then

$$y(t_{n+1}) = y(t_n) + \Delta t\left(\frac{k_1}{2} + \frac{k_2}{2}\right) + \mathcal{O}((\Delta t)^3), \tag{A.126}$$

with

$$k_1 = f(y(t_n), t_n), \tag{A.127}$$
$$k_2 = f(y(t_n) + k_1\Delta t, t_n + \Delta t). \tag{A.128}$$

Higher-order derivations will lead to a larger system of equations to satisfy. A 4^{th}-order scheme [281] is given by:

$$y(t_{n+1}) = y(t_n) + \Delta t\left(\frac{k_1}{6} + \frac{k_2}{3} + \frac{k_3}{3} + \frac{k_4}{6}\right) + \mathcal{O}((\Delta t)^5), \tag{A.129}$$

$$k_1 = f(y(t_n), t_n), \tag{A.130}$$
$$k_2 = f\left(y(t_n) + \frac{\Delta t}{2}k_1, t_n + \frac{\Delta t}{2}\right), \tag{A.131}$$
$$k_3 = f\left(y(t_n) + \frac{\Delta t}{2}k_2, t_n + \frac{\Delta t}{2}\right), \tag{A.132}$$
$$k_4 = f(y(t_n) + k_3\Delta t, t_n + \Delta t). \tag{A.133}$$

A 6^{th}-order scheme [374] is given by:

$$y(t_{n+1}) = y(t_n) + \Delta t\left(\frac{61}{864}k_1 + \frac{98415}{321776}k_3 + \frac{16807}{146016}k_4 + \frac{1375}{7344}k_5 + \frac{1375}{5408}k_6 - \frac{37}{1120}k_7 - \frac{1}{10}k_8\right) + \mathcal{O}((\Delta t)^7), \tag{A.134}$$

with

$$k_1 = f(y(t_n), t_n), \tag{A.135}$$
$$k_2 = f\left(y(t_n) + \Delta t\frac{1}{10}k_1, t_n + \Delta t\frac{1}{10}\right), \tag{A.136}$$
$$k_3 = f\left(y(t_n) + \Delta t\left(-\frac{2}{81}k_1 + \frac{20}{81}k_2\right), t_n + \frac{2}{9}\Delta t\right), \tag{A.137}$$
$$k_4 = f\left(y(t_n) + \Delta t\left(\frac{615}{1372}k_1 - \frac{270}{343}k_2 + \frac{1053}{1372}k_3\right), t_n + \frac{3}{7}\Delta t\right), \tag{A.138}$$
$$k_5 = f\left(y(t_n) + \Delta t\left(\frac{3243}{5500}k_1 - \frac{54}{55}k_2 + \frac{50949}{71500}k_3 + \frac{4998}{17875}k_4\right), t_n + \frac{3}{5}\Delta t\right), \tag{A.139}$$
$$k_6 = f\left(y(t_n) + \Delta t\left(-\frac{26492}{37125}k_1 + \frac{72}{55}k_2 + \frac{2808}{23375}k_3 - \frac{24206}{37125}k_4 + \frac{338}{459}k_5\right), t_n + \frac{4}{5}\Delta t\right), \tag{A.140}$$
$$k_7 = f\left(y(t_n) + \Delta t\left(\frac{5561}{2376}k_1 - \frac{35}{11}k_2 - \frac{24117}{31603}k_3 + \frac{899983}{200772}k_4 - \frac{5225}{1836}k_5 + \frac{3925}{4056}k_6\right), t_n + \Delta t\right), \tag{A.141}$$
$$k_8 = f\Big(y(t_n) + \Delta t\Big(\frac{465467}{266112}k_1 - \frac{2945}{1232}k_2 - \frac{5610201}{14158144}k_3 + \frac{10513573}{3212352}k_4 - \frac{424325}{205632}k_5 + \frac{376225}{454272}k_6\Big), t_n + \Delta t\Big). \tag{A.142}$$

A.7 Adams-Bashforth Method

Given an initial value problem of the form:

$$\frac{dy}{dt} = f(t, y), \qquad y(0) = y_0,$$

we seek the solution y_{n+1} at some time $t_{n+1} = (n+1)\Delta t$ for some $n \in \mathbb{Z}$ and with $\Delta t > 0$ a (constant) time-step. If we have knowledge of y_n then the equation:

$$y_{n+1} = y_n + \int_{t_n}^{t_{n+1}} f(t', y(t'))dt' \tag{A.143}$$

is exact. We aim to approximate the given integral by polynomial interpolation of f at the times $t_{n+1-s}, t_{n+2-s}, ..., t_n$, where s is the (global) order of the method, and the polynomial interpolation is of degree $s-1$. Note that this assumes knowledge of f at s previous time-steps; if $s > 1$ another method must first be used to generate these values, typically a lower-order Adams-Bashforth scheme. We consider the case $s = 3$ - the extension of this derivation to higher-order schemes is straightforward.

The interpolating polynomial (in the Lagrange form) for $f(t', y(t'))$ which passes through the points $(t_{n-2}, f_{n-2}), (t_{n-1}, f_{n-1}), (t_n, f_n)$ is:

$$F_3(t') = f_{n-2}\ell_{n-2}(t') + f_{n-1}\ell_{n-1}(t') + f_n\ell_n(t'), \tag{A.144}$$

with the Lagrange polynomials:

$$\ell_{n-2}(t') = \frac{(t'-t_{n-1})(t'-t_n)}{(t_{n-2}-t_{n-1})(t_{n-2}-t_n)} = \frac{1}{2(\Delta t)^2}(t'-t_{n-1})(t'-t_n),$$

$$\ell_{n-1}(t') = \frac{(t'-t_{n-2})(t'-t_n)}{(t_{n-1}-t_{n-2})(t_{n-1}-t_n)} = -\frac{1}{(\Delta t)^2}(t'-t_{n-2})(\tau-t_n),$$

$$\ell_n(t') = \frac{(t'-t_{n-2})(t't_{n-1})}{(t_n-t_{n-2})(t_n-t_{n-1})} = \frac{1}{2(\Delta t)^2}(t'-t_{n-2})(t'-t_{n-1}).$$

If we substitute eq. (A.144) into eq. (A.143) we find:

$$\begin{aligned} y_{n+1} &\approx y_n + \int_{t_n}^{t_{n+1}} L_3(t')dt' \\ &\approx y_n + f_{n-2}\int_{t_n}^{t_{n+1}} \ell_{n-2}(t')dt' + f_{n-1}\int_{t_n}^{t_{n+1}} \ell_{n-1}(t')dt' + f_n\int_{t_n}^{t_{n+1}} \ell_n(t')dt'. \end{aligned} \tag{A.145}$$

Introducing $u = \dfrac{t'-t_n}{\Delta t}$, $0 \le u \le 1$, we then have:

$$t' = t_n + u\Delta t, \qquad dt' = du\Delta t,$$

$$t'-t_n = u\Delta t, \qquad t'-t_{n-1} = u\Delta t + \Delta t, \qquad t'-t_{n-2} = u\Delta t + 2\Delta t.$$

Substituting these into the Lagrange polynomials yields:

$$\ell_{n-2}(u) = \frac{1}{2}u(u+1),$$

$$\ell_{n-1}(u) = -u(u+2),$$

$$\ell_n(u) = \frac{1}{2}(u+1)(u+2).$$

We can now integrate eq. (A.145):

$$\int_{t_n}^{t_{n+1}} \ell_{n-2}(t') = \Delta t \int_0^1 \ell_{n-2}(u)du = \frac{\Delta t}{2}\int_0^1 u(u+1)du = \frac{5}{12}\Delta t,$$

$$\int_{t_n}^{t_{n+1}} \ell_{n-1}(t') = \Delta t \int_0^1 \ell_{n-1}(u)du = -\Delta t \int_0^1 u(u+2)du = -\frac{4}{3}\Delta t,$$

$$\int_{t_n}^{t_{n+1}} \ell_n(t') = \Delta t \int_0^1 \ell_n(u)du = \frac{\Delta t}{2}\int_0^1 (u+1)(u+2)du = \frac{23}{12}\Delta t,$$

to give:

$$y_{n+1} \approx y_n + \frac{\Delta t}{12}(5f_{n-2} - 16f_{n-1} + 23f_n)$$

with the truncation error given by the error in the interpolation, in this case $\mathcal{O}((\Delta t)^4)$.

Appendix B

Selected Properties Of He II

We summarise the physical properties of ^{4}He at saturated vapour pressure relevant to our vortex filament method simulations, as informed by [196].

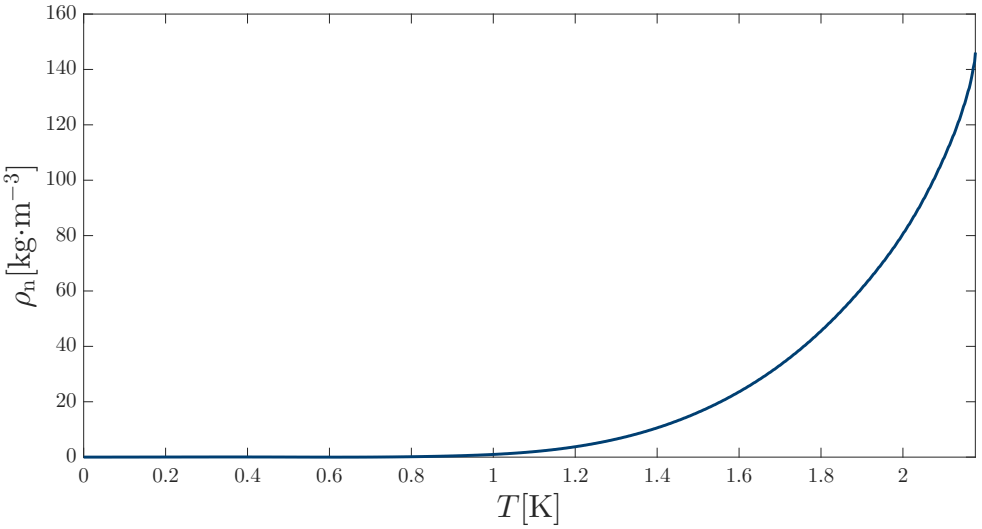

Figure B.1: Density of the normal fluid component of ^{4}He below the lambda transition.

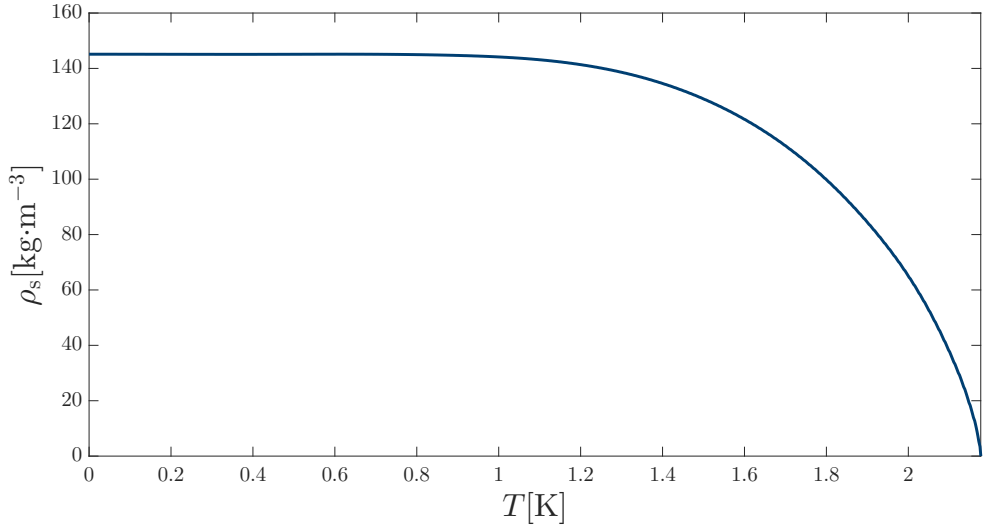

Figure B.2: Density of the superfluid component of ^{4}He below the lambda transition.

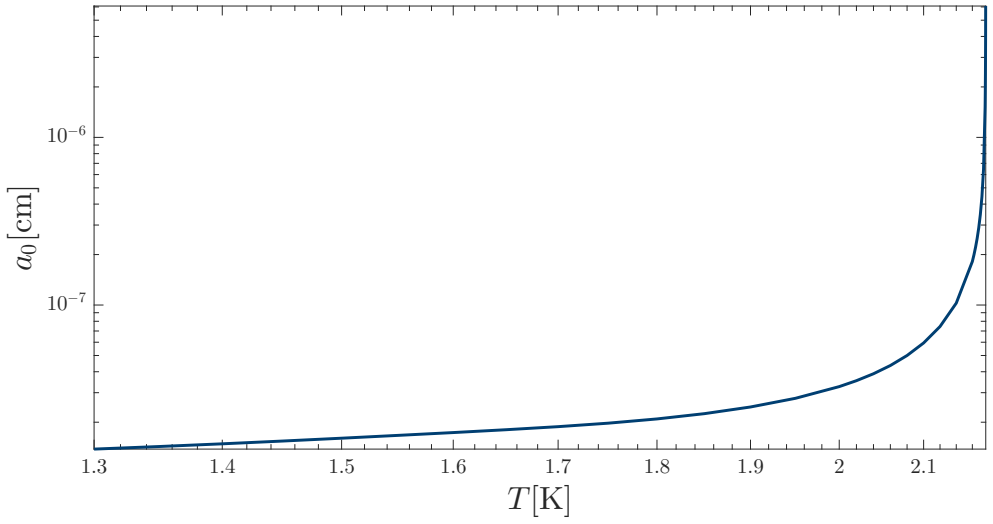

Figure B.3: Vortex core parameter a_0 for quantised vortices in ^{4}He below the lambda transition.

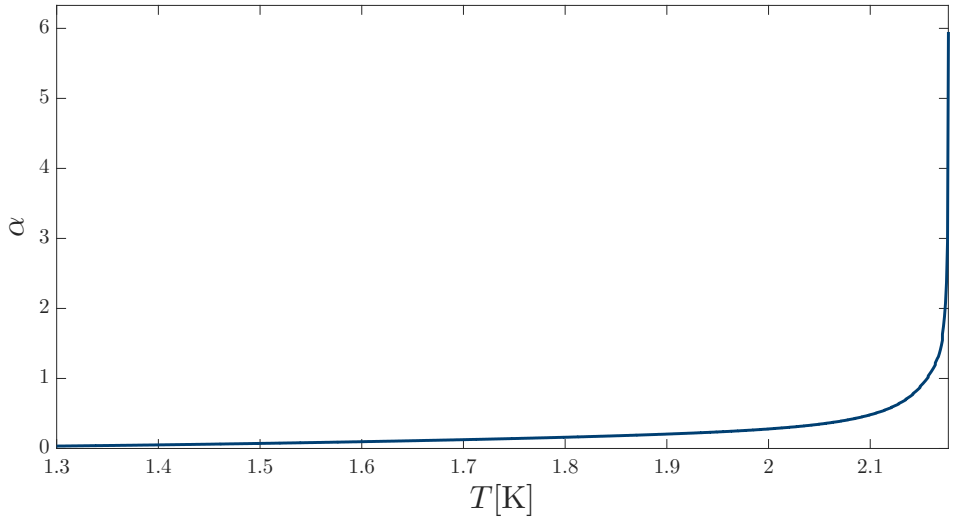

Figure B.4: Recommended values of the dimensionless mutual friction coefficient α - see Sec. 5.2

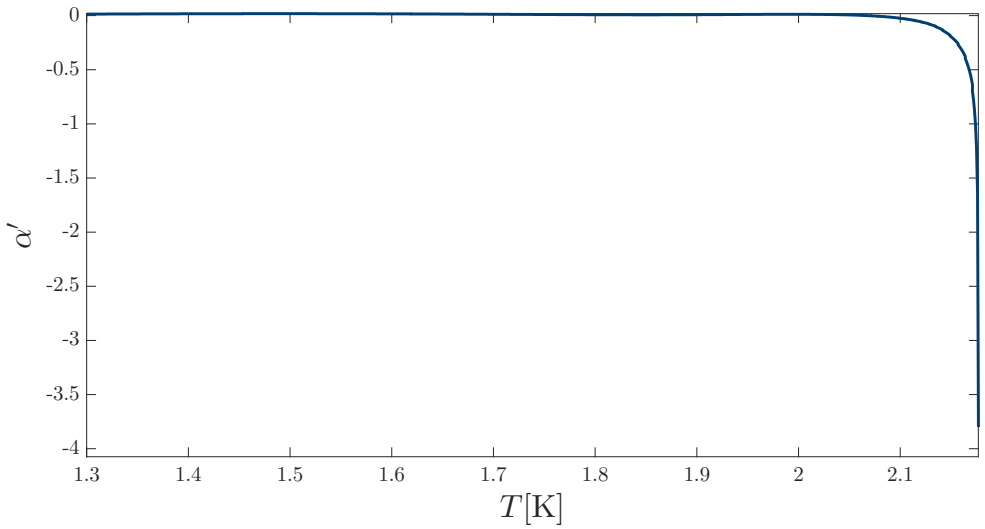

Figure B.5: Recommended values of the dimensionless mutual friction coefficient α' - see Sec. 5.2

Bibliography

[1] F. Hyndman. The Liquefying of Helium. *Nature*, **78**(2025), 1908.

[2] A. T. A. M. de Waele. Basics of Joule-Thomson Liquefaction and JT Cooling. *Journal of Low Temperature Physics*, **186**(5-6), 2017.

[3] D. van Delft and P. Kes. The Discovery of Superconductivity. *Physics Today*, **63**(9), 2010.

[4] C. F. Barenghi and N. G. Parker. *A Primer on Quantum Fluids*. Springer, 2016.

[5] P. Kapitza. Viscosity of Liquid Helium Below the λ-Point. *Nature*, **141**(3558), 1938.

[6] J. F. Allen and A. D. Misener. Flow of Liquid Helium II. *Nature*, **141**(3558), 1938.

[7] H. Kojima, W. Veith, E. Guyon, and I. Rudnick. Persistent Current States in Rotating Superfluid Helium. *Journal of Low Temperature Physics*, **8**(3-4), 1972.

[8] K. K. Darrow. Helium the Superfluid. *Reviews of Modern Physics*, **12**(3), 1940.

[9] J. F. Allen and H. Jones. New Phenomena Connected with Heat Flow in Helium II. *Nature*, **141**(3562), 1938.

[10] F. London. The λ-Phenomenon of Liquid Helium and the Bose-Einstein Degeneracy. *Nature*, **141**(3571), 1938.

[11] S. Balibar. The Discovery of Superfluidity. *Journal of Low Temperature Physics*, **146**(5-6), 2007.

[12] L. Tisza. Transport Phenomena in Helium II. *Nature*, **141**(3577), 1938.

[13] L. D. Landau. Theory of the Superfluidity of Helium II. *Physical Review*, **60**(4), 1941.

[14] W. F. Vinen. The Physics of Superfluid Helium. In *CAS - CERN Accelerator School on Superconductivity and Cryogenics for Accelerators and Detectors*. 2004.

[15] Y. Castin, A. Sinatra, and H. Kurkjian. Landau Phonon-Roton Theory Revisited for Superfluid ^{4}He and Fermi Gases. *Physical Review Letters*, **119**(26), 2017.

[16] R. M. Brady, E. T. Samulski, and D. H. P. Turban. Evidence that Rotons in Helium II are Interstitial Atoms. *arXiv preprint arXiv:1706.10149*, 2017.

[17] A. Nicolis and R. Penco. Mutual Interactions of Phonons, Rotons, and Gravity. *Physical Review B*, **97**(13), 2018.

[18] H. Palevsky, K. Otnes, and K. E. Larsson. Excitation of Rotons in Helium II by Cold Neutrons. *Physical Review*, **112**(1), 1958.

[19] W. F. Vinen. Mutual Friction in a Heat Current in Liquid Helium II I. Experiments on Steady Heat Currents. *Proceedings of the Royal Society of London. Series A. Mathematical and Physical Sciences*, **240**(1220), 1957.

[20] W. F. Vinen. Mutual Friction in a Heat Current in Liquid Helium II III. Theory of the Mutual Friction. *Proceedings of the Royal Society of London. Series A. Mathematical and Physical Sciences*, **242**(1231), 1957.

[21] V. P. Peshkov. Second Sound in Helium II. *Journal of Experimental and Theoretical Physics*, **11**(3), 1960.

[22] H. E. Hall and W. F. Vinen. The Rotation of Liquid Helium II II. The Theory of Mutual Friction in Uniformly Rotating Helium II. *Proceedings of the Royal Society of London. Series A. Mathematical and Physical Sciences*, **238**(1213), 1956.

[23] M. R. Smith and R. J. Donnelly. A Study of Homogeneous Turbulence in Superfluid Helium. In *High Reynolds Number Flows Using Liquid and Gaseous Helium*. Springer, 1991.

[24] W. Guo, J. D. Wright, S. B. Cahn, J. A. Nikkel, and D. N. McKinsey. Metastable Helium Molecules as Tracers in Superfluid ^{4}He. *Physical Review Letters*, **102**(23), 2009.

[25] W. Guo, M. la Mantia, D. P. Lathrop, and S. W. van Sciver. Visualization of Two-Fluid Flows of Superfluid Helium-4. *Proceedings of the National Academy of Sciences*, **111**(Supplement 1), 2014.

[26] L. Onsager. Statistical Hydrodynamics. *Il Nuovo Cimento*, **6**, 1949.

[27] R. P. Feynman. Application of Quantum Mechanics to Liquid Helium. In *Progress in Low Temperature Physics*, volume **1**. Elsevier, 1955.

[28] R. J. Donnelly. *Quantized Vortices in Helium II*. Cambridge University Press, 1991.

[29] S. N. Fisher, A. J. Hale, A. M. Guénault, and G. R. Pickett. Generation and Detection of Quantum Turbulence in Superfluid ^{3}He-B. *Physical Review Letters*, **86**(2), 2001.

[30] S. I. Davis, P. C. Hendry, and P. V. E. McClintock. Decay of Quantized Vorticity in Superfluid ^{4}He at mK Temperatures. *Physica B: Condensed Matter*, **280**(1-4), 2000.

[31] M. Blažková, M. Človečko, E. Gažo, L. Skrbek, and P. Skyba. Quantum Turbulence Generated and Detected by a Vibrating Quartz Fork. *Journal of Low Temperature Physics*, **148**(3-4), 2007.

[32] J. Jäger, B. Schuderer, and W. Schoepe. Turbulent and Laminar Drag of Superfluid Helium on an Oscillating Microsphere. *Physical Review Letters*, **74**(4), 1995.

[33] P. M. Walmsley, A. I. Golov, H. E. Hall, A. A. Levchenko, and W. F. Vinen. Dissipation of Quantum Turbulence in the Zero Temperature Limit. *Physical Review Letters*, **99**(26), 2007.

[34] R. K. Childers and J. T. Tough. Helium II Thermal Counterflow: Temperature- and Pressure-Difference Data and Analysis in Terms of the Vinen Theory. *Physical Review B*, **13**(3), 1976.

[35] K. P. Martin and J. T. Tough. Evolution of Superfluid Turbulence in Thermal Counterflow. *Physical Review B*, **27**(5), 1983.

[36] M. S. Paoletti, R. B. Fiorito, K. R. Sreenivasan, and D. P. Lathrop. Visualization of Superfluid Helium Flow. *Journal of the Physical Society of Japan*, **77**(11), 2008.

[37] D. N. McKinsey, W. H. Lippincott, J. A. Nikkel, and W. G. Rellergert. Trace Detection of Metastable Helium Molecules in Superfluid Helium by Laser-Induced Fluorescence. *Physical Review Letters*, **95**(11), 2005.

[38] W. G. Rellergert, S. B. Cahn, A. Garvan, J. C. Hanson, W. H. Lippincott, J. A. Nikkel, and D. N. McKinsey. Detection and Imaging of He_2 Molecules in Superfluid Helium. *Physical Review Letters*, **100**(2), 2008.

[39] S. N. Bose. Planck's Law and Light Quantum Hypothesis. *Zeitschrift für Physik*, **26**, 1924.

[40] A. Einstein. Quantum Theory of the Monatomic Ideal Gas. *Sitzungsberichte der Preussischen Akademie der Wissenschaften, Physikalisch-mathematische Klasse*, 1924.

[41] E. M. Lifshitz and L. P. Pitaevskii. *Statistical Physics: Theory of the Condensed State*, volume **9**. Elsevier, 2013.

[42] C. J. Pethick and H. Smith. *Bose-Einstein Condensation in Dilute Gases*. Cambridge University Press, 2008.

[43] J. Bardeen, L. N. Cooper, and J. R. Schrieffer. Theory of Superconductivity. *Physical Review*, **108**(5), 1957.

[44] C. A. Regal, M. Greiner, and D. S. Jin. Observation of Resonance Condensation of Fermionic Atom Pairs. *Physical Review Letters*, **92**(4), 2004.

[45] M. W. Zwierlein, C. A. Stan, C. H. Schunck, S. M. F. Raupach, A. J. Kerman, and W. Ketterle. Condensation of Pairs of Fermionic Atoms Near a Feshbach Resonance. *Physical Review Letters*, **92**(12), 2004.

[46] D. D. Osheroff, R. C. Richardson, and D. M. Lee. Evidence for a New Phase of Solid He^3. *Physical Review Letters*, **28**(14), 1972.

[47] D. D. Osheroff, W. J. Gully, R. C. Richardson, and D. M. Lee. New Magnetic Phenomena in Liquid He^3 Below 3 mK. *Physical Review Letters*, **29**(14), 1972.

[48] M. H. Anderson, J. R. Ensher, M. R. Matthews, C. E. Wieman, and E. A. Cornell. Observation of Bose-Einstein Condensation in a Dilute Atomic Vapor. *Science*, **269**(5221), 1995.

[49] T. W. Hänsch and A. L. Schawlow. Cooling of Gases by Laser Radiation. *Optics Communications*, **13**(1), 1975.

[50] W. Petrich, M. H. Anderson, J. R. Ensher, and E. A. Cornell. Stable, Tightly Confining Magnetic Trap for Evaporative Cooling of Neutral Atoms. *Physical Review Letters*, **74**(17), 1995.

[51] K. B. Davis, M-O. Mewes, M. A. Joffe, M. R. Andrews, and W. Ketterle. Evaporative Cooling of Sodium Atoms. *Physical Review Letters*, **74**(26), 1995.

[52] K. B. Davis, M.-O. Mewes, M. R. Andrews, N. J. van Druten, D. S. Durfee, D. M. Kurn, and W. Ketterle. Bose-Einstein Condensation in a Gas of Sodium Atoms. *Physical Review Letters*, **75**(22), 1995.

[53] C. C. Bradley, C. A. Sackett, J. J. Tollett, and R. G. Hulet. Evidence of Bose-Einstein Condensation in an Atomic Gas with Attractive Interactions. *Physical Review Letters*, **75**(9), 1995.

[54] G. Modugno, G. Ferrari, G. Roati, R. J. Brecha, A. Simoni, and M. Inguscio. Bose-Einstein Condensation of Potassium Atoms by Sympathetic Cooling. *Science*, **294**(5545), 2001.

[55] T. Weber, J. Herbig, M. Mark, H.-C. Nägerl, and R. Grimm. Bose-Einstein Condensation of Cesium. *Science*, **299**(5604), 2003.

[56] D. G. Fried, L. Killian, T. C.and Willmann, D. Landhuis, S. C. Moss, D. Kleppner, and T. J. Greytak. Bose-Einstein Condensation of Atomic Hydrogen. *Physical Review Letters*, **81**(18), 1998.

[57] F. P. dos Santos, J. Léonard, J. Wang, C. J. Barrelet, F. Perales, E. Rasel, C. S. Unnikrishnan, M. Leduc, and C. Cohen-Tannoudji. Bose-Einstein Condensation of Metastable Helium. *Physical Review Letters*, **86**(16), 2001.

[58] S. Kraft, F. Vogt, O. Appel, F. Riehle, and U. Sterr. Bose-Einstein Condensation of Alkaline Earth Atoms: ^{40}Ca. *Physical Review Letters*, **103**(13), 2009.

[59] A. Griesmaier, J. Werner, S. Hensler, J. Stuhler, and T. Pfau. Bose-Einstein Condensation of Chromium. *Physical Review Letters*, **94**(16), 2005.

[60] S. Stellmer, M. K. Tey, B. Huang, R. Grimm, and F. Schreck. Bose-Einstein Condensation of Strontium. *Physical Review Letters*, **103**(20), 2009.

[61] Y. N. M. de Escobar, P. G. Mickelson, M. Yan, B. J. DeSalvo, S. B. Nagel, and T. C. Killian. Bose-Einstein Condensation of ^{84}Sr. *Physical Review Letters*, **103**(20), 2009.

[62] M. Lu, N. Q. Burdick, S. H. Youn, and B. L. Lev. Strongly Dipolar Bose-Einstein Condensate of Dysprosium. *Physical Review Letters*, **107**(19), 2011.

[63] K. Aikawa, A. Frisch, M. Mark, S. Baier, A. Rietzler, R. Grimm, and F. Ferlaino. Bose-Einstein Condensation of Erbium. *Physical Review Letters*, **108**(21), 2012.

[64] Y. Takasu, K. Maki, K. Komori, T. Takano, K. Honda, M. Kumakura, T. Yabuzaki, and Y. Takahashi. Spin-Singlet Bose-Einstein Condensation of Two-Electron Atoms. *Physical Review Letters*, **91**(4), 2003.

[65] S. P. Mathew and S. N. Kaul. Bose-Einstein Condensation of Magnons in Polycrystalline Gadolinium with Nano-Size Grains. *Journal of Physics: Condensed Matter*, **23**(26), 2011.

[66] J. Kasprzak, M. Richard, S. Kundermann, A. Baas, P. Jeambrun, J. M. J. Keeling, F. M. Marchetti, M. H. Szymańska, R. Andre, J. L. Staehli, V. Savona, P. B. Littlewood, B. Deveaud, and Dang L. S. Bose-Einstein Condensation of Exciton Polaritons. *Nature*, **443**(7110), 2006.

[67] Y. Kawaguchi and M. Ueda. Spinor Bose-Einstein Condensates. *Physics Reports*, **520**(5), 2012.

[68] G. Modugno, M. Modugno, F. Riboli, G. Roati, and M. Inguscio. Two Atomic Species Superfluid. *Physical Review Letters*, **89**(19), 2002.

[69] G. Thalhammer, G. Barontini, L. De Sarlo, J. Catani, F. Minardi, and M. Inguscio. Double Species Bose-Einstein Condensate with Tunable Interspecies Interactions. *Physical Review Letters*, **100**(21), 2008.

[70] D. J. McCarron, H. W. Cho, D. L. Jenkin, M. P. Köppinger, and S. L. Cornish. Dual-Species Bose-Einstein Condensate of ^{87}Rb and ^{133}Cs. *Physical Review A*, **84**(1), 2011.

[71] N. Bogoliubov. On the Theory of Superfluidity. *Journal of Physics*, **11**(1), 1947.

[72] R. Onofrio, C. Raman, J. M. Vogels, J. R. Abo-Shaeer, A. P. Chikkatur, and W. Ketterle. Observation of Superfluid Flow in a Bose-Einstein Condensed Gas. *Physical Review Letters*, **85**(11), 2000.

[73] J. Weiner. *Cold and Ultracold Collisions in Quantum Microscopic and Mesoscopic Systems*. Cambridge University Press, 2003.

[74] J. Stenger, S. Inouye, M. R. Andrews, H.-J. Miesner, D. M. Stamper-Kurn, and W. Ketterle. Strongly Enhanced Inelastic Collisions in a Bose-Einstein Condensate near Feshbach Resonances. *Physical Review Letters*, **82**(12), 1999.

[75] T. W. Neely, E. C. Samson, A. S. Bradley, M. J. Davis, and B. P. Anderson. Observation of Vortex Dipoles in an Oblate Bose-Einstein Condensate. *Physical Review Letters*, **104**(16), 2010.

[76] S. Stellmer, C. Becker, P. Soltan-Panahi, E.-M. Richter, S. Dörscher, M. Baumert, J. Kronjäger, K. Bongs, and K. Sengstock. Collisions of Dark Solitons in Elongated Bose-Einstein Condensates. *Physical Review Letters*, **101**(12), 2008.

[77] T. P. Meyrath, F. Schreck, J. L. Hanssen, C.-S. Chuu, and M. G. Raizen. Bose-Einstein Condensate in a Box. *Physical Review A*, **71**(4), 2005.

[78] C. Ryu, M. F. Andersen, P. Clade, V. Natarajan, K. Helmerson, and W. D. Phillips. Observation of Persistent Flow of a Bose-Einstein Condensate in a Toroidal Trap. *Physical Review Letters*, **99**(26), 2007.

[79] A. L. Gaunt, T. F. Schmidutz, I. Gotlibovych, R.t P. Smith, and Z. Hadzibabic. Bose-Einstein Condensation of Atoms in a Uniform Potential. *Physical Review Letters*, **110**(20), 2013.

[80] L. Chomaz, L. Corman, T. Bienaimé, R. Desbuquois, C. Weitenberg, S. Nascimbène, J. Beugnon, and J. Dalibard. Emergence of Coherence via Transverse Condensation in a Uniform Quasi-Two-Dimensional Bose Gas. *Nature Communications*, **6**:6162, 2015.

[81] A. Ramanathan, K. C. Wright, S. R. Muniz, M. Zelan, W. T. Hill III, C. J. Lobb, K. Helmerson, W. D. Phillips, and G. K. Campbell. Superflow in a Toroidal Bose-Einstein Condensate: An Atom Circuit with a Tunable Weak Link. *Physical Review Letters*, **106**(13), 2011.

[82] L. J. LeBlanc, A. B. Bardon, J. McKeever, M. H. T. Extavour, D. Jervis, J. H. Thywissen, F. Piazza, and A. Smerzi. Dynamics of a Tunable Superfluid Junction. *Physical Review Letters*, **106**(2), 2011.

[83] K. W. Madison, F. Chevy, W. Wohlleben, and J. Dalibard. Vortex Formation in a Stirred Bose-Einstein Condensate. *Physical Review Letters*, **84**(5), 2000.

[84] C. Raman, J. R. Abo-Shaeer, J. M. Vogels, K. Xu, and W. Ketterle. Vortex Nucleation in a Stirred Bose-Einstein Condensate. *Physical Review Letters*, **87**(21), 2001.

[85] D. V. Freilich, D. M. Bianchi, A. M. Kaufman, T. K. Langin, and D. S. Hall. Real-Time Dynamics of Single Vortex Lines and Vortex Dipoles in a Bose-Einstein Condensate. *Science*, **329**(5996), 2010.

[86] P. B. Blakie and R. J. Ballagh. Spatially Selective Bragg Scattering: A Signature for Vortices in Bose-Einstein Condensates. *Physical Review Letters*, **86**(18), 2001.

[87] S. R. Muniz, D. S. Naik, and C. Raman. Bragg Spectroscopy of Vortex Lattices in Bose-Einstein Condensates. *Physical Review A*, **73**(4), 2006.

[88] Y. L'vov, S. Nazarenko, and R. West. Wave Turbulence in Bose-Einstein Condensates. *Physica D: Nonlinear Phenomena*, **184**(1-4), 2003.

[89] S. Nazarenko and M. Onorato. Wave Turbulence and Vortices in Bose-Einstein Condensation. *Physica D: Nonlinear Phenomena*, **219**(1), 2006.

[90] L. D. Carr, C. W. Clark, and W. P. Reinhardt. Stationary Solutions of the One-Dimensional Nonlinear Schrödinger Equation. I. Case of Repulsive Nonlinearity. *Physical Review A*, **62**(6), 2000.

[91] L. D. Carr, C. W. Clark, and W. P. Reinhardt. Stationary Solutions of the One-Dimensional Nonlinear Schrödinger Equation. II. Case of Attractive Nonlinearity. *Physical Review A*, **62**(6), 2000.

[92] B. P. Anderson, P. C. Haljan, C. A. Regal, D. L. Feder, L. A. Collins, C. W. Clark, and E. A. Cornell. Watching Dark Solitons Decay into Vortex Rings in a Bose-Einstein Condensate. *Physical Review Letters*, **86**(14), 2001.

[93] T. W. B. Kibble. Topology of Cosmic Domains and Strings. *Journal of Physics A: Mathematical and General*, **9**(8), 1976.

[94] W. H. Zurek. Cosmological Experiments in Superfluid Helium? *Nature*, **317**(6037), 1985.

[95] C. N. Weiler, T. W. Neely, D. R. Scherer, A. S. Bradley, M. J. Davis, and B. P. Anderson. Spontaneous Vortices in the Formation of Bose-Einstein Condensates. *Nature*, **455**(7215), 2008.

[96] A. L. Fetter and A. A. Svidzinsky. Vortices in a Trapped Dilute Bose-Einstein Condensate. *Journal of Physics: Condensed Matter*, **13**(12), 2001.

[97] J. R. Abo-Shaeer, C. Raman, J. M. Vogels, and W. Ketterle. Observation of Vortex Lattices in Bose-Einstein Condensates. *Science*, **292**(5516), 2001.

[98] E. J. Yarmchuk, M. J. V. Gordon, and R. E. Packard. Observation of Stationary Vortex Arrays in Rotating Superfluid Helium. *Physical Review Letters*, **43**(3), 1979.

[99] M. R. Matthews, B. P. Anderson, P. C. Haljan, D. S. Hall, C. E. Wieman, and E. A. Cornell. Vortices in a Bose-Einstein Condensate. *Physical Review Letters*, **83**(13), 1999.

[100] Ł. Dobrek, M. Gajda, M. Lewenstein, K. Sengstock, G. Birkl, and W. Ertmer. Optical Generation of Vortices in Trapped Bose-Einstein Condensates. *Physical Review A*, 60(5), 1999.

[101] N. G. Berloff and C. F. Barenghi. Vortex Nucleation by Collapsing Bubbles in Bose-Einstein Condensates. *Physical Review Letters*, **93**(9), 2004.

[102] B. Jackson, J. F. McCann, and C. S. Adams. Dissipation and Vortex Creation in Bose-Einstein Condensed Gases. *Physical Review A*, **61**(5), 2000.

[103] W. J. Kwon, G. Moon, S. W. Seo, and Y. Shin. Critical Velocity for Vortex Shedding in a Bose-Einstein Condensate. *Physical Review A*, **91**(5), 2015.

[104] G. W. Stagg, A. J. Allen, C. F. Barenghi, and N. G. Parker. Classical-Like Wakes Past Elliptical Obstacles in Atomic Bose-Einstein Condensates. *Journal of Physics: Conference Series*, **594**(1), 2015.

[105] P. D. Stein and H. N. Sabbah. Turbulent Blood Flow in the Ascending Aorta of Humans with Normal and Diseased Aortic Valves. *Circulation Research*, **39**(1), 1976.

[106] H. Lienhart and S. Becker. Flow and Turbulence Structure in the Wake of a Simplified Car Model. *SAE Transactions*, **112**(6), 2003.

[107] E. Guilmineau. Computational Study of Flow Around a Simplified Car Body. *Journal of Wind Engineering and Industrial Aerodynamics*, **96**(6-7), 2008.

[108] C. M. Rhie and W. L. Chow. Numerical Study of the Turbulent Flow Past an Airfoil with Trailing Edge Separation. *American Institute of Aeronautics and Astronautics Journal*, **21**(11), 1983.

[109] L. P. Chamorro and F. Porté-Agel. A Wind-Tunnel Investigation of Wind-Turbine Wakes: Boundary-Layer Turbulence Effects. *Boundary-Layer Meteorology*, **132**(1), 2009.

[110] A. E. Gargett. Ocean Turbulence. *Annual Review of Fluid Mechanics*, **21**(1), 1989.

[111] J. C. Wyngaard. Atmospheric Turbulence. *Annual Review of Fluid Mechanics*, **24**(1), 1992.

[112] J. M. Cordes, J. M. Weisberg, and V. Boriakoff. Small-Scale Electron Density Turbulence in the Interstellar Medium. *The Astrophysical Journal*, **288**:221–247, 1985.

[113] A. Brandenburg and Å. Nordlund. Astrophysical Turbulence Modeling. *Reports on Progress in Physics*, **74**(4), 2011.

[114] C. D. Argyropoulos and N. C. Markatos. Recent Advances on the Numerical Modelling of Turbulent Flows. *Applied Mathematical Modelling*, **39**(2), 2015.

[115] T. Ishihara, T. Gotoh, and Y. Kaneda. Study of High-Reynolds Number Isotropic Turbulence by Direct Numerical Simulation. *Annual Review of Fluid Mechanics*, **41**, 2009.

[116] T. Gotoh and T. Watanabe. Power and Nonpower Laws of Passive Scalar Moments Convected by Isotropic Turbulence. *Physical Review Letters*, **115**(11), 2015.

[117] T. Ishihara, K. Morishita, M. Yokokawa, A. Uno, and Y. Kaneda. Energy Spectrum in High-Resolution Direct Numerical Simulations of Turbulence. *Physical Review Fluids*, **1**(8), 2016.

[118] J. McMillan. *Turbulence Measurements in a High Reynolds Number Tidal Channel*. PhD thesis, Dalhousie University, 2017.

[119] The National Aeronautics and Space Administration. Perpetual Ocean. `https://www.nasa.gov/topics/earth/features/perpetual-ocean.html`. Accessed: 2019/08/29.

[120] K. Moffatt. Vortex Dynamics: The Legacy of Helmholtz and Kelvin. In *IUTAM Symposium on Hamiltonian Dynamics, Vortex Structures, Turbulence*. Springer, 2008.

[121] L. F. Richardson. *Weather Prediction by Numerical Process*. Cambridge University Press, 1922.

[122] A. S. Monin and A. M. Yaglom. *Statistical Fluid Mechanics, Volume II: Mechanics of Turbulence*. MIT Press, 1975.

[123] A. N. Kolmogorov. The Local Structure of Turbulence in Incompressible Viscous Fluid for Very Large Reynolds Numbers. *Soviet Physics Uspekhi*, **10**(6), 1968.

[124] F. Argoul, A. Arneodo, G. Grasseau, Y. Gagne, E. J. Hopfinger, and U. Frisch. Wavelet Analysis of Turbulence Reveals the Multifractal Nature of the Richardson Cascade. *Nature*, **338**(6210), 1989.

[125] K. R. Sreenivasan. On the Universality of the Kolmogorov Constant. *Physics of Fluids*, **7**(11), 1995.

[126] W.-C. Müller and D. Biskamp. Scaling Properties of Three-Dimensional Magnetohydrodynamic Turbulence. *Physical Review Letters*, **84**(3), 2000.

[127] O. Alexandrova, V. Carbone, P. Veltri, and L. Sorriso-Valvo. Small-Scale Energy Cascade of the Solar Wind Turbulence. *The Astrophysical Journal*, **674**(2), 2008.

[128] A. N. Kolmogorov. The Local Structure of Turbulence in Incompressible Viscous Fluid for Very Large Reynolds Numbers. *Proceedings of the USSR Academy of Sciences*, **30**, 1941.

[129] A. N. Kolmogorov. On Degeneration (Decay) of Isotropic Turbulence in an Incompressible Viscous Liquid. In *Proceedings of the USSR Academy of Sciences*, volume **31**, 1941.

[130] U. Frisch. *Turbulence: The Legacy of A. N. Kolmogorov*. Cambridge University Press, 1995.

[131] L. D. Landau and E. M. Lifshitz. *Fluid Mechanics*, volume **11**. Pergamon, 1959.

[132] F. Anselmet, Y. Gagne, E. J. Hopfinger, and R. A. Antonia. High-Order Velocity Structure Functions in Turbulent Shear Flows. *Journal of Fluid Mechanics*, **140**, 1984.

[133] A. Vincent and M. Meneguzzi. The Spatial Structure and Statistical Properties of Homogeneous Turbulence. *Journal of Fluid Mechanics*, **225**, 1991.

[134] A. Pouquet. Intermittent Turbulence in a Global Ocean Model. *Physics*, **11**, 2018.

[135] Z.-S. She and E. Leveque. Universal Scaling Laws in Fully Developed Turbulence. *Physical Review Letters*, **72**(3), 1994.

[136] T. Iztok, E. Stalio, D. Angeli, and O. Jure. Direct Numerical Simulations for Liquid Metal Applications. In *Thermal Hydraulics Aspects of Liquid Metal Cooled Nuclear Reactors*. Elsevier, 2018.

[137] H.-T. Liu. Energetics of Grid Turbulence in a Stably Stratified Fluid. *Journal of Fluid Mechanics*, **296**, 1995.

[138] J. J. Riley, R. W. Metcalfe, and M. A. Weissman. Direct Numerical Simulations of Homogeneous Turbulence in Density-Stratified Fluids. In *AIP Conference Proceedings*, volume **76**. AIP, 1981.

[139] O. U. V. Fuentes. Kelvin's Discovery of Taylor Columns. *European Journal of Mechanics-B/Fluids*, **28**(3), 2009.

[140] H Tennekes and J. L. Lumley. *A First Course in Turbulence*. MIT press, 1972.

[141] N. Ouellette. Turbulence in Two Dimensions. *Physics Today*, **65**(5), 2012.

[142] R. Fjørtoft. On the Changes in the Spectral Distribution of Kinetic Energy for Twodimensional, Nondivergent Flow. *Tellus*, **5**(3), 1953.

[143] U. Frisch and P.-L. Sulem. Numerical Simulation of the Inverse Cascade in Two-Dimensional Turbulence. *Physics of Fluids*, **27**(8), 1984.

[144] J. Paret and P. Tabeling. Experimental Observation of the Two-Dimensional Inverse Energy Cascade. *Physical Review Letters*, **79**(21), 1997.

[145] G. Boffetta and S. Musacchio. Evidence for the Double Cascade Scenario in Two-Dimensional Turbulence. *Physical Review E*, **82**(1), 2010.

[146] R. H. Kraichnan and D. Montgomery. Two-Dimensional Turbulence. *Reports on Progress in Physics*, **43**(5), 1980.

[147] Y. Jun and X. L. Wu. Large-Scale Intermittency in Two-Dimensional Driven Turbulence. *Physical Review E*, **72**(3), 2005.

[148] R. T. Cerbus and W. I. Goldburg. Intermittency in 2D Soap Film Turbulence. *Physics of Fluids*, **25**(10), 2013.

[149] W. F. Vinen. Mutual Friction in a Heat Current in Liquid Helium II. II. Experiments on Transient Effects. *Proceedings of the Royal Society of London. Series A. Mathematical and Physical Sciences*, **240**(1220), 1957.

[150] W. F. Vinen. Mutual Friction in a Heat Current in Liquid Helium. II. IV. Critical Heat Currents in Wide Channels. *Proceedings of the Royal Society of London. Series A. Mathematical and Physical Sciences*, **243**(1234), 1958.

[151] C. Nore, M. Abid, and M. E. Brachet. Kolmogorov Turbulence in Low-Temperature Superflows. *Physical Review Letters*, **78**(20), 1997.

[152] J. Maurer and P. Tabeling. Local Investigation of Superfluid Turbulence. *Europhysics Letters*, **43**(1), 1998.

[153] T. Araki, M. Tsubota, and S. K. Nemirovskii. Energy Spectrum of Superfluid Turbulence with no Normal-Fluid Component. *Physical Review Letters*, **89**(14), 2002.

[154] W. F. Vinen and J. J. Niemela. Quantum Turbulence. *Journal of Low Temperature Physics*, **128**(5-6), 2002.

[155] L. P. Kondaurova, V. A. Andryuschenko, and S. K. Nemirovskii. Numerical Simulations of Superfluid Turbulence Under Periodic Conditions. *Journal of Low Temperature Physics*, **150**(3-4), 2008.

[156] J. Salort, C. Baudet, B. Castaing, B. Chabaud, F. Daviaud, T. Didelot, P. Diribarne, B. Dubrulle, Y.s Gagne, F. Gauthier, A. Girard, B. Hébrai, P. Thibault, and P.-E. Roche. Turbulent Velocity Spectra in Superfluid Flows. *Physics of Fluids*, **22**(12), 2010.

[157] L. Kondaurova and S. K. Nemirovskii. Numerical Study of Decay of Vortex Tangles in Superfluid Helium at Zero Temperature. *Physical Review B*, **86**(13), 2012.

[158] C. F. Barenghi, L. Skrbek, and K. R. Sreenivasan. Introduction to Quantum Turbulence. *Proceedings of the National Academy of Sciences*, **111**(Supplement 1), 2014.

[159] P. M. Walmsley and A. I. Golov. Coexistence of Quantum and Classical Flows in Quantum Turbulence in the $T = 0$ limit. *Physical Review Letters*, **118**(13), 2017.

[160] P. M. Walmsley and A. I. Golov. Quantum and Quasiclassical Types of Superfluid Turbulence. *Physical Review Letters*, **100**(24), 2008.

[161] A. W. Baggaley, C. F. Barenghi, A. Shukurov, and Y. A. Sergeev. Coherent Vortex Structures in Quantum Turbulence. *Europhysics Letters*, **98**(2), 2012.

[162] A. W. Baggaley, J. Laurie, and C. F. Barenghi. Vortex-Density Fluctuations, Energy Spectra, and Vortical Regions in Superfluid Turbulence. *Physical Review Letters*, **109**(20), 2012.

[163] W. F. Vinen. Decay of Superfluid Turbulence at a Very Low Temperature: The Radiation of Sound from a Kelvin Wave on a Quantized Vortex. *Physical Review B*, **64**(13), 2001.

[164] E. Kozik and B. Svistunov. Vortex-Phonon Interaction. *Physical Review B*, **72**(17), 2005.

[165] R. Hänninen. Dissipation Enhancement from a Single Vortex Reconnection in Superfluid Helium. *Physical Review B*, **88**(5), 2013.

[166] E. Fonda, D. P. Meichle, N. T. Ouellette, S. Hormoz, and D. P. Lathrop. Direct Observation of Kelvin Waves Excited by Quantized Vortex Reconnection. *Proceedings of the National Academy of Sciences*, **111**(Supplement 1), 2014.

[167] D. Kivotides, J. C. Vassilicos, D. C. Samuels, and C. F. Barenghi. Kelvin Waves Cascade in Superfluid Turbulence. *Physical Review Letters*, **86**(14), 2001.

[168] W. F. Vinen, M. Tsubota, and A. Mitani. Kelvin-Wave Cascade on a Vortex in Superfluid ^{4}He at a Very Low Temperature. *Physical Review Letters*, **91**(13), 2003.

[169] E. Kozik and B. Svistunov. Kelvin-Wave Cascade and Decay of Superfluid Turbulence. *Physical Review Letters*, **92**(3), 2004.

[170] E. Kozik and B. Svistunov. Kolmogorov and Kelvin-Wave Cascades of Superfluid Turbulence at $T = 0$: What Lies Between. *Physical Review B*, 77(6):060502, 2008.

[171] J. Yepez, G. Vahala, L. Vahala, and M. Soe. Superfluid Turbulence from Quantum Kelvin Wave to Classical Kolmogorov Cascades. *Physical Review Letters*, **103**(8), 2009.

[172] J. Laurie and A. W. Baggaley. A Note on the Propagation of Quantized Vortex Rings Through a Quantum Turbulence Tangle: Energy Transport or Energy Dissipation? *Journal of Low Temperature Physics*, **180**(1-2), 2015.

[173] C. F. Barenghi, Y. A. Sergeev, and A. W. Baggaley. Regimes of Turbulence Without an Energy Cascade. *Scientific Reports*, **6**:35701, 2016.

[174] A. W. Baggaley, C. F. Barenghi, and Y. A. Sergeev. Quasiclassical and Ultraquantum Decay of Superfluid Turbulence. *Physical Review B*, **85**(6), 2012.

[175] M. S. Paoletti, M. E. Fisher, K. R. Sreenivasan, and D. P. Lathrop. Velocity Statistics Distinguish Quantum Turbulence from Classical Turbulence. *Physical Review Letters*, **101**(15), 2008.

[176] A. W. Baggaley and C. F. Barenghi. Quantum Turbulent Velocity Statistics and Quasiclassical Limit. *Physical Review E*, **84**(6), 2011.

[177] M. la Mantia and L. Skrbek. Quantum, or Classical Turbulence? *Europhysics Letters*, **105**(4), 2014.

[178] C. F. Barenghi, V. S. L'vov, and P.-E. Roche. Experimental, Numerical, and Analytical Velocity Spectra in Turbulent Quantum Fluid. *Proceedings of the National Academy of Sciences*, **111**(Supplement 1), 2014.

[179] L. Boué, V. L'vov, A. Pomyalov, and I. Procaccia. Enhancement of Intermittency in Superfluid Turbulence. *Physical Review Letters*, **110**(1), 2013.

[180] E. Rusaouen, B. Chabaud, J. Salort, and P.-E. Roche. Intermittency of Quantum Turbulence with Superfluid Fractions from 0% to 96%. *Physics of Fluids*, **29**(10), 2017.

[181] E. Varga, J. Gao, W. Guo, and L. Skrbek. Intermittency Enhancement in Quantum Turbulence in Superfluid ^{4}He. *Physical Review Fluids*, **3**(9), 2018.

[182] T. P. Simula. Crow Instability in Trapped Bose-Einstein Condensates. *Physical Review A*, **84**(2), 2011.

[183] G. W. Stagg, N. G. Parker, and C. F. Barenghi. Quantum Analogues of Classical Wakes in Bose-Einstein Condensates. *Journal of Physics B: Atomic, Molecular and Optical Physics*, **47**(9), 2014.

[184] A. W. Baggaley and N. G. Parker. Kelvin-Helmholtz Instability in a Single-Component Atomic Superfluid. *Physical Review A*, **97**(5), 2018.

[185] C. F. Barenghi. Is the Reynolds Number Infinite in Superfluid Turbulence? *Physica D: Nonlinear Phenomena*, **237**(14-17), 2008.

[186] M. Tsubota, T. Araki, and S. K. Nemirovskii. Dynamics of Vortex Tangle Without Mutual Friction in Superfluid ^{4}He. *Physical Review B*, **62**(17), 2000.

[187] S. R. Stalp, J. J. Niemela, W. F. Vinen, and R. J. Donnelly. Dissipation of Grid Turbulence in Helium II. *Physics of Fluids*, **14**(4), 2002.

[188] J. J. Niemela, K. R. Sreenivasan, and R. J. Donnelly. Grid Generated Turbulence in Helium II. *Journal of Low Temperature Physics*, **138**(3-4), 2005.

[189] D. Jou and M. Sciacca. Quantum Reynolds Number for Superfluid Counterflow Turbulence. *Bollettino di Matematica Pura e Applicata*, **6**:95–103, 2013.

[190] S. Babuin, E. Varga, L. Skrbek, E. Lévêque, and P.-E. Roche. Effective Viscosity in Quantum Turbulence: A Steady-State Approach. *Europhysics Letters*, **106**(2), 2014.

[191] S. Babuin, E. Varga, and L. Skrbek. The Decay of Forced Turbulent Coflow of He II Past a Grid. *Journal of Low Temperature Physics*, **175**(1-2), 2014.

[192] J. Gao, W. Guo, and W. F. Vinen. Determination of the Effective Kinematic Viscosity for the Decay of Quasiclassical Turbulence in Superfluid ^{4}He. *Physical Review B*, **94**(9), 2016.

[193] A. M. Guénault, A. Guthrie, R. P. Haley, S. Kafanov, Y. A. Pashkin, G. R. Pickett, M. Poole, R. Schanen, V. Tsepelin, D. E. Zmeev, E. Collin, O. Maillet, and R. Gazizulin. Probing Superfluid ^{4}He with High-Frequency Nanomechanical Resonators down to Millikelvin Temperatures. *Physical Review B*, **100**(2), 2019.

[194] M. Tsubota, T. Araki, and W. F. Vinen. Diffusion of an Inhomogeneous Vortex Tangle. *Physica B: Condensed Matter*, **329**:224–225, 2003.

[195] C. Bäuerle, Y. M. Bunkov, S. N. Fisher, H. Godfrin, and G. R. Pickett. Laboratory Simulation of Cosmic String Formation in the Early Universe Using Superfluid ^{3}He. *Nature*, **382**(6589), 1996.

[196] R. J. Donnelly and C. F. Barenghi. The Observed Properties of Liquid Helium at the Saturated Vapor Pressure. *Journal of Physical and Chemical Reference Data*, **27**(6), 1998.

[197] B. Rousset, C. Baudet, M. Bon Mardion, M. Bourgoin, A. Braslau, F. Daviaud, P. Diribarne, B. Dubrulle, Y. Gagne, B. Gallet, M. Gibert, A. Girard, T. Lehner, I. Moukharski, and F. Sy. Cryogenic Turbulence Test Facilities at CEA/SBT. In *IOP Conference Series: Materials Science and Engineering*, volume **101**. IOP Publishing, 2015.

[198] C. Nore, M. Abid, and M. E. Brachet. Decaying Kolmogorov Turbulence in a Model of Superflow. *Physics of Fluids*, **9**(9), 1997.

[199] M. Kobayashi and M. Tsubota. Kolmogorov Spectrum of Superfluid Turbulence: Numerical Analysis of the Gross-Pitaevskii Equation with a Small-Scale Dissipation. *Physical Review Letters*, **94**(6), 2005.

[200] D. E. Zmeev, P. M. Walmsley, A. I. Golov, P. V. E. McClintock, S. N. Fisher, and W. F. Vinen. Dissipation of Quasiclassical Turbulence in Superfluid ^{4}He. *Physical Review Letters*, **115**(15), 2015.

[201] P. M. Walmsley and A. I. Golov. Rotating Quantum Turbulence in Superfluid ^{4}He in the $T = 0$ Limit. *Physical Review B*, **86**(6), 2012.

[202] P. M. Walmsley, D. E. Zmeev, F. Pakpour, and A. I. Golov. Dynamics of Quantum Turbulence of Different Spectra. *Proceedings of the National Academy of Sciences*, **111**(Supplement 1), 2014.

[203] D. I. Bradley, R. P. Haley, S. Kafanov, M. T. Noble, G. R. Pickett, V. Tsepelin, J. Vonka, and T. Wilcox. Probing Liquid ^{4}He with Quartz Tuning Forks Using a Novel Multifrequency Lock-in Technique. *Journal of Low Temperature Physics*, **184**(5-6), 2016.

[204] M. J. Jackson, O. Kolosov, D. Schmoranzer, L. Skrbek, V. Tsepelin, and A. J. Woods. Measurements of Vortex Line Density Generated by a Quartz Tuning Fork in Superfluid ^{4}He. *Journal of Low Temperature Physics*, **183**(3-4), 2016.

[205] A. Guthrie, R. P. Haley, A. Jennings, S. Kafanov, O. Kolosov, M. Mucientes, M. T. Noble, Y. A. Pashkin, G. R. Pickett, V. Tsepelin, D. E. Zmeev, and V. Efimov. Multimode Probing of Superfluid ^{4}He by Tuning Forks. *Applied Physics Letters*, **115**(11), 2019.

[206] D. I. Bradley, S. N. Fisher, A. M. Guénault, R. P. Haley, C. J. Matthews, G. R. Pickett, V. Tsepelin, and K. Zaki. The Generation of Quantum Turbulence in ^{3}He-B by a Vibrating Grid at Low Temperatures. In *AIP Conference Proceedings*, volume **850**. AIP, 2006.

[207] D. I. Bradley, S. N. Fisher, A. Ganshin, A. M. Guénault, R. P. Haley, M. J. Jackson, G. R. Pickett, and V. Tsepelin. The Onset of Vortex Production by a Vibrating Wire in Superfluid ^{3}He-B. *Journal of Low Temperature Physics*, **171**(5-6), 2013.

[208] V. B. Eltsov, R. de Graaf, P. J. Heikkinen, J. J. Hosio, R. Hänninen, and M. Krusius. Vortex Formation and Annihilation in Rotating Superfluid ^{3}He-B at Low Temperatures. *Journal of Low Temperature Physics*, **161**(5-6), 2010.

[209] J. T. Mäkinen and V. B. Eltsov. Mutual Friction in Superfluid ^{3}He-B in the Low-Temperature Regime. *Physical Review B*, **97**(1), 2018.

[210] J. T. Mäkinen, V. B. Eltsov, Heikkinen P.J., Hosio J., Krusius M., V. S. L'vov, P. M. Walmsley, and V. V. Zavjalov. Wave Turbulence of a Rotating Array of Quantized Vortices in the $\rightarrow$ 0 Temperature Limit. In 15*th European Turbulence Conference*, 2015.

[211] W. Guo, S. B. Cahn, J. A. Nikkel, W. F. Vinen, and D. N. McKinsey. Visualization Study of Counterflow in Superfluid ^{4}He Using Metastable Helium Molecules. *Physical Review Letters*, **105**(4), 2010.

[212] A. Marakov, J. Gao, W. Guo, S. W. van Sciver, G. G. Ihas, D. N. McKinsey, and W. F. Vinen. Visualization of the Normal-Fluid Turbulence in Counterflowing Superfluid ^{4}He. *Physical Review B*, **91**(9), 2015.

[213] B. Mastracci and W. Guo. Exploration of Thermal Counterflow in He II Using Particle Tracking Velocimetry. *Physical Review Fluids*, **3**(6), 2018.

[214] S. Bao, W. Guo, V. S. L'vov, and A. Pomyalov. Statistics of Turbulence and Intermittency Enhancement in Superfluid ^{4}He Counterflow. *Physical Review B*, **98**(17), 2018.

[215] J. Gao, W. Guo, S. Yui, M. Tsubota, and W. F. Vinen. Dissipation in Quantum Turbulence in Superfluid ^{4}He above 1 K. *Physical Review B*, **97**(18), 2018.

[216] L. Skrbek, A. V. Gordeev, and F. Soukup. Decay of Counterflow He II Turbulence in a Finite Channel: Possibility of Missing Links Between Classical and Quantum Turbulence. *Physical Review E*, **67**(4), 2003.

[217] E. Varga, S. Babuin, and L. Skrbek. Second-Sound Studies of Coflow and Counterflow of Superfluid ^{4}He in Channels. *Physics of Fluids*, **27**(6), 2015.

[218] E. Varga, S. Babuin, V. S. L'vov, A. Pomyalov, and L. Skrbek. Transition to Quantum Turbulence and Streamwise Inhomogeneity of Vortex Tangle in Thermal Counterflow. *Journal of Low Temperature Physics*, **187**(5-6), 2017.

[219] S. Babuin, M. Stammeier, E. Varga, M. Rotter, and L. Skrbek. Quantum Turbulence of Bellows-Driven ^{4}He Superflow: Steady State. *Physical Review B*, **86**(13), 2012.

[220] D. Charalambous, L. Skrbek, P. C. Hendry, P. V. E. McClintock, and W. F. Vinen. Experimental Investigation of the Dynamics of a Vibrating Grid in Superfluid ^{4}He Over a Range of Temperatures and Pressures. *Physical Review E*, **74**(3), 2006.

[221] M. Blažková, D. Schmoranzer, L. Skrbek, and W. F. Vinen. Generation of Turbulence by Vibrating Forks and Other Structures in Superfluid ^{4}He. *Physical Review B*, **79**(5), 2009.

[222] D. Durì, C. Baudet, J.-P. Moro, P.-E. Roche, and P. Diribarne. Hot-Wire Anemometry for Superfluid Turbulent Coflows. *Review of Scientific Instruments*, **86**(2), 2015.

[223] P. Diribarne, P. Thibault, and P.-E. Roche. Nano-Shaped Hot-Wire for Ultra-High Resolution Anemometry in Cryogenic Helium. *Review of Scientific Instruments*, 2019.

[224] J. Salort, A. Monfardini, and P.-E. Roche. Cantilever Anemometer Based on a Superconducting Micro-Resonator: Application to Superfluid Turbulence. *Review of Scientific Instruments*, **83**(12), 2012.

[225] J. Salort, É. Rusaouën, L. Robert, R. du Puits, A. Loesch, O. Pirotte, P.-E. Roche, B. Castaing, and F. Chillà. A Local Sensor for Joint Temperature and Velocity Measurements in Turbulent Flows. *Review of Scientific Instruments*, **89**(1), 2018.

[226] W. B. Hanson and J. R. Pellam. Second Sound Attenuation in Liquid Helium II. *Physical Review*, **95**(2), 1954.

[227] D. S. Holmes and S. W. van Sciver. Attenuation of Second Sound in Bulk Flowing He II. *Journal of Low Temperature Physics*, **87**(1-2), 1992.

[228] S. N. Fisher, M. J. Jackson, Y. A. Sergeev, and V. Tsepelin. Andreev Reflection, a Tool to Investigate Vortex Dynamics and Quantum Turbulence in ^{3}He-B. *Proceedings of the National Academy of Sciences*, **111**(Supplement 1), 2014.

[229] A. W. Baggaley, V. Tsepelin, C. F. Barenghi, S. N. Fisher, G. R. Pickett, Y. A. Sergeev, and N. Suramlishvili. Visualizing Pure Quantum Turbulence in Superfluid ^{3}He: Andreev Reflection and its Spectral Properties. *Physical Review Letters*, **115**(1), 2015.

[230] R. Blaauwgeers, M. Blazkova, M. Človečko, V. B. Eltsov, R. de Graaf, J. Hosio, M. Krusius, D. Schmoranzer, W. Schoepe, L. Skrbek, P. Skyba, R. E. Solntsev, and D. E. Zmeev. Quartz Tuning Fork: Thermometer, Pressure- and Viscometer for Helium Liquids. *Journal of Low Temperature Physics*, **146**(5-6), 2007.

[231] M. Blažková, M. Človečko, V. B. Eltsov, E. Gažo, R. de Graaf, J. J. Hosio, M. Krusius, D. Schmoranzer, W. Schoepe, L. Skrbek, P. Skyba, R. E. Solntsev, and W. F. Vinen. Vibrating Quartz Fork - a Tool for Cryogenic Helium Research. *Journal of low temperature physics*, **150**(3-4), 2008.

[232] E. M. Pentti, J. T. Tuoriniemi, A. J. Salmela, and A. P. Sebedash. Quartz Tuning Fork in Helium. *Journal of Low Temperature Physics*, **150**(3-4), 2008.

[233] E. Rickinson, N. G. Parker, A. W. Baggaley, and C. F. Barenghi. Diffusion of Quantum Vortices. *Physical Review A*, **98**(2), 2018.

[234] E. Rickinson, N. G. Parker, A. W. Baggaley, and C. F. Barenghi. Inviscid Diffusion of Vorticity in Low-Temperature Superfluid Helium. *Physical Review B*, **99**(22), 2019.

[235] G. W. Stagg. 2D-GP. `https://github.com/extigy/2D-GP/`. Accessed: 2019/09/06.

[236] G. W. Stagg. *A Numerical Study of Vortices and Turbulence in Quantum Fluids*. PhD thesis, Newcastle University, 2016.

[237] A. W. Baggaley. QVORT. `https://github.com/abag/qvort`. Accessed: 2019/09/06.

[238] H. Helmholtz. Über Integrale der Hydrodynamischen Gleichungen, welche den Wirbelbewegungen Entsprechen. *Crelle*, **55**:25–55, 1858.

[239] H. Aref. Point Vortex Dynamics: A Classical Mathematics Playground. *Journal of Mathematical Physics*, **48**(6), 2007.

[240] D. S. Djukic and B. D. Vujanovic. Noether's Theory in Classical Nonconservative Mechanics. *Acta Mechanica*, **23**(1-2), 1975.

[241] A. Y. Toukmaji and J. A. Board Jr. Ewald Summation Techniques in Perspective: A Survey. *Computer Physics Communications*, **95**(2-3), 1996.

[242] P. K. Newton. *The N-Vortex Problem: Analytical Techniques*. Springer, 2001.

[243] H. Aref. Motion of Three Vortices. *The Physics of Fluids*, **22**(3), 1979.

[244] H. Aref and N. Pomphrey. Integrable and Chaotic Motions of Four Vortices I. The Case of Identical Vortices. *Proceedings of the Royal Society of London. A. Mathematical and Physical Sciences*, **380**(1779), 1982.

[245] B. Eckhardt and H. Aref. Integrable and Chaotic Motions of Four Vortices II. Collision Dynamics of Vortex Pairs. *Philosophical Transactions of the Royal Society of London. Series A, Mathematical and Physical Sciences*, **326**(1593), 1988.

[246] J. Koiller and S. P. Carvalho. Non-Integrability of the 4-Vortex System: Analytical Proof. *Communications in Mathematical Physics*, **120**(4), 1989.

[247] J. B. Kadtke and L. J. Campbell. Method for Finding Stationary States of Point Vortices. *Physical Review A*, **36**(9), 1987.

[248] T. J. Greytak, D. Kleppner, D. G. Fried, T. C. Killian, L. Willmann, D. Landhuis, and S. C. Moss. Bose-Einstein Condensation in Atomic Hydrogen. *Physica B: Condensed Matter*, **280**(1-4), 2000.

[249] N. P. Proukakis and B. Jackson. Finite-Temperature Models of Bose-Einstein Condensation. *Journal of Physics B: Atomic, Molecular and Optical Physics*, **41**(20), 2008.

[250] E. Madelung. Quantum Theory in Hydrodynamic Form. *Zeitschrift für Physik A Hadrons and Nuclei*, **40**, 1926.

[251] D. Pines and P. Nozières. *The Theory of Quantum Liquids: Superfluid Bose Liquids*. Addison-Wesley, 1990.

[252] D. G. Yakovlev, K. P. Levenfish, and Y. A. Shibanov. Cooling of Neutron Stars and Superfluidity in their Cores. *Physics-Uspekhi*, **42**(8), 1999.

[253] P. Courteille, R. S. Freeland, D. J. Heinzen, F. A. van Abeelen, and B. J. Verhaar. Observation of a Feshbach Resonance in Cold Atom Scattering. *Physical Review Letters*, **81**(1), 1998.

[254] Y. Kawaguchi and T. Ohmi. Splitting Instability of a Multiply Charged Vortex in a Bose-Einstein Condensate. *Physical Review A*, **70**(4), 2004.

[255] Y. Shin, M. Saba, M. Vengalattore, T. A. Pasquini, C. Sanner, A. E. Leanhardt, M. Prentiss, D. E. Pritchard, and W. Ketterle. Dynamical Instability of a Doubly Quantized Vortex in a Bose-Einstein Condensate. *Physical Review Letters*, **93**(16), 2004.

[256] G. P. Agrawal. Nonlinear Fiber Optics. In *Nonlinear Science at the Dawn of the 21st Century*. Springer, 2000.

[257] A. B. Shabat and V. E. Zakharov. Exact Theory of Two-Dimensional Self-Focusing and One-Dimensional Self-Modulation of Waves in Nonlinear Media. *Journal of Experimental and Theoretical Physics*, **34**(1), 1972.

[258] V. E. Zakharov and A. B. Shabat. Interaction Between Solitons in a Stable Medium. *Journal of Experimental and Theoretical Physics*, **37**(5), 1973.

[259] N. Dror and B. A. Malomed. Stability of Solitons in Time-Modulated Two-Dimensional Lattices. *Nonlinear Dynamics*, **91**(3), 2018.

[260] D. E. Galli, L. Reatto, and M. Rossi. Quantum Monte Carlo Study of a Vortex in Superfluid ^{4}He and Search for a Vortex State in the Solid. *Physical Review B*, **89**(22), 2014.

[261] J. Koplik and H. Levine. Vortex Reconnection in Superfluid Helium. *Physical Review Letters*, **71**(9), 1993.

[262] K. W. Schwarz. Generation of Superfluid Turbulence Deduced from Simple Dynamical Rules. *Physical Review Letters*, **49**(4), 1982.

[263] A. Cidrim, F. E. A. dos Santos, L. Galantucci, V. S. Bagnato, and C. F. Barenghi. Controlled Polarization of Two-Dimensional Quantum Turbulence in Atomic Bose-Einstein Condensates. *Physical Review A*, **93**(3), 2016.

[264] A. J. Groszek, T. P. Simula, D. M. Paganin, and K. Helmerson. Onsager Vortex Formation in Bose-Einstein Condensates in Two-Dimensional Power-Law Traps. *Physical Review A*, **93**(4), 2016.

[265] C. A. Jones and P. H. Roberts. Motions in a Bose Condensate. IV. Axisymmetric Solitary Waves. *Journal of Physics A: Mathematical and General*, **15**(8), 1982.

[266] B. Jackson, N. P. Proukakis, C. F. Barenghi, and E. Zaremba. Finite-Temperature Vortex Dynamics in Bose-Einstein Condensates. *Physical Review A*, **79**(5), 2009.

[267] S. Gautam, A. Roy, and S. Mukerjee. Finite-Temperature Dynamics of Vortices in Bose-Einstein Condensates. *Physical Review A*, **89**(1), 2014.

[268] I. M. Navarro, M. Guilleumas, R. Mayol, and A. M. Mateo. Bound States of Dark Solitons and Vortices in Trapped Multidimensional Bose-Einstein Condensates. *Physical Review A*, **98**(4), 2018.

[269] B. P. Anderson and P. Meystre. Nonlinear Atom Optics. *Contemporary Physics*, **44**(6), 2003.

[270] A. Görlitz, J. M. Vogels, A. E. Leanhardt, C. Raman, T. L. Gustavson, J. R. Abo-Shaeer, A. P. Chikkatur, S. Gupta, S. Inouye, T. Rosenband, and W. Ketterle. Realization of Bose-Einstein Condensates in Lower Dimensions. *Physical Review Letters*, **87**(13), 2001.

[271] K. E. Wilson, E. C. Samson, Z. L. Newman, T. W. Neely, and B. P. Anderson. Experimental Methods for Generating Two-Dimensional Quantum Turbulence in Bose-Einstein Condensates. In *Annual Review of Cold Atoms and Molecules: Volume 1*. World Scientific, 2013.

[272] D. S. Petrov, M. Holzmann, and G. V. Shlyapnikov. Bose-Einstein Condensation in Quasi-2D Trapped Gases. *Physical Review Letters*, **84**(12), 2000.

[273] J. M. Kosterlitz and D. J. Thouless. Ordering, Metastability and Phase Transitions in Two-Dimensional Systems. *Journal of Physics C: Solid State Physics*, **6**(7), 1973.

[274] Y. Kagan, B. V. Svistunov, and G. V. Shlyapnikov. Influence on Inelastic Processes of the Phase Transition in a Weakly Collisional Two-Dimensional Bose Gas. *Journal of Experimental and Theoretical Physics*, **66**(2).

[275] L. D. Carr, M. A. Leung, and W. P. Reinhardt. Dynamics of the Bose-Einstein Condensate: Quasi-One-Dimension and Beyond. *Journal of Physics B: Atomic, Molecular and Optical Physics*, **33**(19), 2000.

[276] J. J. P. van Es, P. Wicke, A. H. van Amerongen, C. Rétif, S. Whitlock, and N. J. van Druten. Box Traps on an Atom Chip for One-Dimensional Quantum Gases. *Journal of Physics B: Atomic, Molecular and Optical Physics*, **43**(15), 2010.

[277] F. Pampaloni and J. Enderlein. Gaussian, Hermite-Gaussian, and Laguerre-Gaussian Beams: A Primer. *arXiv preprint physics/0410021*, 2004.

[278] J. N. Reddy. *An Introduction to the Finite Element Method*. McGraw-Hill Education, 1993.

[279] J. C. Butcher. *The Numerical Analysis of Ordinary Differential Equations: Runge-Kutta and General Linear Methods*. Wiley-Interscience, 1987.

[280] W. H. Press, S. A. Teukolsky, W. T Vetterling, and B. P. Flannery. *Numerical Recipes 3rd Edition: The Art of Scientific Computing*. Cambridge University Press, 2007.

[281] J. R. Dormand and P. J. Prince. A Family of Embedded Runge-Kutta Formulae. *Journal of Computational and Applied Mathematics*, **6**(1), 1980.

[282] E. W. Weisstein. Simpson's Rule. `http://mathworld.wolfram.com/SimpsonsRule.html`. Accessed: 2019/08/29.

[283] J. B. Weiss and J. C. McWilliams. Nonergodicity of Point Vortices. *Physics of Fluids A: Fluid Dynamics*, **3**(5), 1991.

[284] A. Griffin, S. Nazarenko, V. Shukla, and M.-E. Brachet. The Vortex-Particle Magnus Effect. *arXiv preprint arXiv:1909.11010*, 2019.

[285] M. L. Chiofalo, S. Succi, and M. P. Tosi. Ground State of Trapped Interacting Bose-Einstein Condensates by an Explicit Imaginary-Time Algorithm. *Physical Review E*, **62**(5), 2000.

[286] W. Bao and W. Tang. Ground-State Solution of Bose-Einstein Condensate by Directly Minimizing the Energy Functional. *Journal of Computational Physics*, **187**(1), 2003.

[287] M. Edwards and K. Burnett. Numerical Solution of the Nonlinear Schrödinger Equation for Small Samples of Trapped Neutral Atoms. *Physical Review A*, **51**(2), 1995.

[288] J. Thijssen. *Computational Physics*. Cambridge University Press, 2007.

[289] M. Tsubota, K. Kasamatsu, and M. Ueda. Vortex Lattice Formation in a Rotating Bose-Einstein Condensate. *Physical Review A*, **65**(2), 2002.

[290] E. M. Lifshitz and L. P. Pitaevskii. *Physical Kinetics: Volume 10*. Pergamon, 1981.

[291] S. Choi, S. A. Morgan, and K. Burnett. Phenomenological Damping in Trapped Atomic Bose-Einstein Condensates. *Physical Review A*, **57**(5), 1998.

[292] P. B. Blakie, A. S. Bradley, M. J. Davis, R. J. Ballagh, and C. W. Gardiner. Dynamics and Statistical Mechanics of Ultra-Cold Bose Gases Using C-Field Techniques. *Advances in Physics*, **57**(5), 2008.

[293] K. Kasamatsu, M. Tsubota, and M. Ueda. Nonlinear Dynamics of Vortex Lattice Formation in a Rotating Bose-Einstein Condensate. *Physical Review A*, **67**(3), 2003.

[294] A. J. Allen, N. G. Parker, N. P. Proukakis, and C. F. Barenghi. Isotropic Vortex Tangles in Trapped Atomic Bose-Einstein Condensates via Laser Stirring. *Physical Review A*, **89**(2), 2014.

[295] J. Denschlag, J. E. Simsarian, D. L. Feder, C. W. Clark, L. A. Collins, J. Cubizolles, L. Deng, E. W. Hagley, K. Helmerson, W. P. Reinhardt, S. L. Rolston, B. I. Schneider, and W. D. Phillips. Generating Solitons by Phase Engineering of a Bose-Einstein Condensate. *Science*, **287**(5450), 2000.

[296] N. G. Berloff. Padé Approximations of Solitary Wave Solutions of the Gross-Pitaevskii Equation. *Journal of Physics A: Mathematical and General*, **37**(5), 2004.

[297] J. R. Abo-Shaeer, C. Raman, and W. Ketterle. Formation and Decay of Vortex Lattices in Bose-Einstein Condensates at Finite Temperatures. *Physical Review Letters*, **88**(7), 2002.

[298] W. Li, M. Haque, and S. Komineas. Vortex Dipole in a Trapped Two-Dimensional Bose-Einstein Condensate. *Physical Review A*, **77**(5), 2008.

[299] C. Rorai, J. Skipper, R. M Kerr, and K. R. Sreenivasan. Approach and Separation of Quantised Vortices with Balanced Cores. *Journal of Fluid Mechanics*, **808**, 2016.

[300] A. Villois, G. Krstulovic, D. Proment, and H. Salman. A Vortex Filament Tracking Method for the Gross-Pitaevskii Model of a Superfluid. *Journal of Physics A: Mathematical and Theoretical*, **49**(41), 2016.

[301] J. Munkres. Algorithms for the Assignment and Transportation Problems. *Journal of the Society for Industrial and Applied Mathematics*, **5**(1), 1957.

[302] C. F. Barenghi and D. C. Samuels. Evaporation of a Packet of Quantized Vorticity. *Physical Review Letters*, **89**(15), 2002.

[303] T. P. Billam, M. T. Reeves, B. P. Anderson, and A. S. Bradley. Onsager-Kraichnan Condensation in Decaying Two-Dimensional Quantum Turbulence. *Physical Review Letters*, **112**(14), 2014.

[304] N. Meyer, H. Proud, M. Perea-Ortiz, C. O'Neale, M. Baumert, M. Holynski, J. Kronjäger, G. Barontini, and K. Bongs. Observation of Two-Dimensional Localized Jones-Roberts Solitons in Bose-Einstein Condensates. *Physical Review Letters*, **119**(15), 2017.

[305] G. E. Uhlenbeck and L. S. Ornstein. On the Theory of the Brownian Motion. *Physical Review*, **36**(5), 1930.

[306] X. Yu, T. P. Billam, J. Nian, M. T. Reeves, and A. S. Bradley. Theory of the Vortex-Clustering Transition in a Confined Two-Dimensional Quantum Fluid. *Physical Review A*, **94**(2), 2016.

[307] T. Simula, M. J. Davis, and K. Helmerson. Emergence of Order from Turbulence in an Isolated Planar Superfluid. *Physical Review Letters*, **113**(16), 2014.

[308] D. E. Zmeev, F. Pakpour, P. M. Walmsley, A. I. Golov, W. Guo, D. N. McKinsey, G. G. Ihas, P. V. E. McClintock, S. N. Fisher, and W. F. Vinen. Excimers He_2^* as Tracers of Quantum Turbulence in ^{4}He in the $T = 0$ Limit. *Physical Review Letters*, **110**(17), 2013.

[309] P.-E. Roche, P. Diribarne, T. Didelot, O. Français, L. Rousseau, and H. Willaime. Vortex Density Spectrum of Quantum Turbulence. *Europhysics Letters*, **77**(6), 2007.

[310] I. L. Bekarevich and I. M. Khalatnikov. Phenomenological Derivation of the Equations of Vortex Motion in He II. *Journal of Experimental and Theoretical Physics*, **13**(3), 1961.

[311] P.-E. Roche, C. F. Barenghi, and E. Lévêque. Quantum Turbulence at Finite Temperature: The Two-Fluids Cascade. *Europhysics Letters*, **87**(5), 2009.

[312] F. Dalfovo. Structure of Vortices in Helium at Zero Temperature. *Physical Review B*, **46**(9), 1992.

[313] K. W. Schwarz. Three-Dimensional Vortex Dynamics in Superfluid ^{4}He: Line-Line and Line-Boundary Interactions. *Physical Review B*, **31**(9), 1985.

[314] S. Zuccher, M. Caliari, A. W. Baggaley, and C. F. Barenghi. Quantum Vortex Reconnections. *Physics of Fluids*, **24**(12), 2012.

[315] K. W. Schwarz. Three-Dimensional Vortex Dynamics in Superfluid ^{4}He: Homogeneous Superfluid Turbulence. *Physical Review B*, **38**(4), 1988.

[316] B. V. Svistunov. Superfluid Turbulence in the Low-Temperature Limit. *Physical Review B*, **52**(5), 1995.

[317] D. R. Poole, H. Scoffield, C. F. Barenghi, and D. C. Samuels. Geometry and Topology of Superfluid Turbulence. *Journal of Low Temperature Physics*, **132**(1-2), 2003.

[318] A. W. Baggaley. The Sensitivity of the Vortex Filament Method to Different Reconnection Models. *Journal of Low Temperature Physics*, **168**(1-2), 2012.

[319] L. Galantucci, A. W. Baggaley, N. G. Parker, and C. F. Barenghi. Crossover from Interaction to Driven Regimes in Quantum Vortex Reconnections. *Proceedings of the National Academy of Sciences*, **116**(25), 2019.

[320] C. F. Barenghi, R. J. Donnelly, and W. F. Vinen. Friction on Quantized Vortices in Helium II. A Review. *Journal of Low Temperature Physics*, **52**(3-4), 1983.

[321] C. E. Swanson, W. T. Wagner, R. J. Donnelly, and C. F. Barenghi. Calculation of Frequency- and Velocity-Dependent Mutual Friction Parameters in Helium II. *Journal of Low Temperature Physics*, **66**(5-6), 1987.

[322] P. H. Roberts and R. J. Donnelly. Dynamics of Vortex Rings. *Physics Letters A*, **31**(3), 1970.

[323] V. Ambegaokar, B. I. Halperin, D. R. Nelson, and E. D. Siggia. Dissipation in Two-Dimensional Superfluids. *Physical Review Letters*, **40**(12), 1978.

[324] V.y Ambegaokar, B. I. Halperin, D. R. Nelson, and E. D. Siggia. Dynamics of Superfluid Films. *Physical Review B*, —bf 21(5), 1980.

[325] C. J. Gorter and J. H. Mellink. On the Irreversible Processes in Liquid Helium II. *Physica*, **15**(3-4), 1949.

[326] A. V. Gordeev, T. V. Chagovets, F. Soukup, and L. Skrbek. Decaying Counterflow Turbulence in He II. *Journal of Low Temperature Physics*, 138(3-4), 2005.

[327] C. F. Barenghi, A. V. Gordeev, and L. Skrbek. Depolarization of Decaying Counterflow Turbulence in He II. *Physical Review E*, **74**(2), 2006.

[328] H. Adachi, S. Fujiyama, and M. Tsubota. Steady-State Counterflow Quantum Turbulence: Simulation of Vortex Filaments Using the Full Biot-Savart Law. *Physical Review B*, **81**(10), 2010.

[329] K. W. Schwarz. Turbulence in Superfluid Helium: Steady Homogeneous Counterflow. *Physical Review B*, **18**(1), 1978.

[330] W. I. Glaberson and R. J. Donnelly. Growth of Pinned Quantized Vortex Lines in Helium II. *Physical Review*, **141**(1), 1966.

[331] J. A. Geurst. Hydrodynamics of Quantum Turbulence in He II: Vinen's Equation Derived from Energy and Impulse of Vortex Tangle. *Physica B: Condensed Matter*, **154**(3), 1989.

[332] J. T. Tough. Superfluid Turbulence. In *Progress in Low Temperature Physics*, volume **8**. Elsevier, 1982.

[333] A. W. Baggaley and C. F. Barenghi. Tree Method for Quantum Vortex Dynamics. *Journal of Low Temperature Physics*, **166**(1-2), 2012.

[334] R. Hänninen and A. W. Baggaley. Vortex Filament Method as a Tool for Computational Visualization of Quantum Turbulence. *Proceedings of the National Academy of Sciences*, **111**(Supplement 1), 2014.

[335] G. Boffetta, A. Celani, D. Dezzani, J. Laurie, and S. Nazarenko. Modeling Kelvin Wave Cascades in Superfluid Helium. *Journal of Low Temperature Physics*, **156**(3-6), 2009.

[336] J. Barnes and P. Hut. A Hierarchical O($NlogN$) Force-Calculation Algorithm. *Nature*, **324**(6096), 1986.

[337] E. Bertschinger. Simulations of Structure Formation in the Universe. *Annual Review of Astronomy and Astrophysics*, **36**(1), 1998.

[338] J. K. Salmon. *Parallel Hierarchical N-Body Methods*. PhD thesis, California Institute of Technology, 1991.

[339] E. Kozik and B. Svistunov. Scale-Separation Scheme for Simulating Superfluid Turbulence: Kelvin-Wave Cascade. *Physical Review Letters*, **94**(2), 2005.

[340] D. Kivotides. Relaxation of Superfluid Vortex Bundles via Energy Transfer to the Normal Fluid. *Physical Review B*, **76**(5), 2007.

[341] D. R. Durran. The Third-Order Adams-Bashforth Method: An Attractive Alternative to Leapfrog Time Differencing. *Monthly Weather Review*, **119**(3), 1991.

[342] L. Kondaurova and S. K. Nemirovskii. Full Biot-Savart Numerical Simulation of Vortices in He II. *Journal of Low Temperature Physics*, **138**(3-4), 2005.

[343] M. Leadbeater, T. Winiecki, D. C. Samuels, C. F. Barenghi, and C. S. Adams. Sound Emission due to Superfluid Vortex Reconnections. *Physical Review Letters*, **86**(8), 2001.

[344] W. F. Vinen. Classical Character of Turbulence in a Quantum Liquid. *Physical Review B*, **61**(2), 2000.

[345] C. F. Barenghi, R. Hänninen, and M. Tsubota. Anomalous Translational Velocity of Vortex Ring with Finite-Amplitude Kelvin Waves. *Physical Review E*, **74**(4), 2006.

[346] D. R. Ladner and J. T. Tough. Temperature and Velocity Dependence of Superfluid Turbulence. *Physical Review B*, **20**(7), 1979.

[347] R. A. Ashton, L. B. Opatowsky, and J. T. Tough. Turbulence in Pure Superfluid Flow. *Physical Review Letters*, **46**(10), 1981.

[348] D. Jou, M. S. Mongiovi, M. Sciacca, and C. F. Barenghi. Vortex Length, Vortex Energy and Fractal Dimension of Superfluid Turbulence at Very Low Temperature. *Journal of Physics A: Mathematical and Theoretical*, **43**(20), 2010.

[349] M. S. Mongiovì, M. Sciacca, and D. Jou. Fractal Dimension of Superfluid Turbulence: a Random-Walk Toy Model. *Communications in Applied and Industrial Mathematics*, **5**, 2014.

[350] T. V. Chagovets and L. Skrbek. On Flow of He II in Channels with Ends Blocked by Superleaks. *Journal of Low Temperature Physics*, **153**(5-6), 2008.

[351] Y. Kaneda, T. Ishihara, M. Yokokawa, K. Itakura, and A. Uno. Energy Dissipation Rate and Energy Spectrum in High Resolution Direct Numerical Simulations of Turbulence in a Periodic Box. *Physics of Fluids*, **15**(2), 2003.

[352] T. D. Drivas. *Anomalous Dissipation, Spontaneous Stochasticity & Onsager's Conjecture*. PhD thesis, Johns Hopkins University, 2017.

[353] A. P. Finne, T. Araki, R. Blaauwgeers, V. B. Eltsov, N. B. Kopnin, M. Krusius, L. Skrbek, M. Tsubota, and G. E. Volovik. An Intrinsic Velocity-Independent Criterion for Superfluid Turbulence. *Nature*, **424**(6952), 2003.

[354] K. W. Schwarz and C. W. Smith. Pulsed-Ion Study of Ultrasonically Generated Turbulence in Superfluid ^{4}He. *Physics Letters A*, **82**(5), 1981.

[355] R. Hänninen and W. Schoepe. Universal Critical Velocity for the Onset of Turbulence of Oscillatory Superfluid Flow. *Journal of Low Temperature Physics*, **153**(5-6), 2008.

[356] D. Schmoranzer, M. J. Jackson, V. Tsepelin, M. Poole, A. J. Woods, M. Človečko, and L. Skrbek. Multiple Critical Velocities in Oscillatory Flow of Superfluid ^{4}He due to Quartz Tuning Forks. *Physical Review B*, **94**(21), 2016.

[357] M. J. Jackson, D. I. Bradley, A. M. Guénault, R. P. Haley, G. R. Pickett, and V. Tsepelin. Observation of Quantum Turbulence in Superfluid ^{3}He-B Using Reflection and Transmission of Ballistic Thermal Excitations. *Physical Review B*, **95**(9), 2017.

[358] P. M. Walmsley, A. I. Golov, H. E. Hall, W. F. Vinen, and A. A. Levchenko. Decay of Turbulence Generated by Spin-Down to Rest in Superfluid ^{4}He. *Journal of Low Temperature Physics*, **153**(5-6), 2008.

[359] S. K. Nemirovskii. Diffusion of Inhomogeneous Vortex Tangle and Decay of Superfluid Turbulence. *Physical Review B*, **81**(6), 2010.

[360] S. Boatto and D. Crowdy. Point-Vortex Dynamics. In *Encyclopedia of Mathematical Physics*. Elsevier, 2006.

[361] C. Marchioro and M. Pulvirenti. Vortices and Localization in Euler Flows. *Communications in Mathematical Physics*, **154**(1), 1993.

[362] M. Fecko. A Generalization of Vortex Lines. *Journal of Geometry and Physics*, **124**:64–73, 2018.

[363] A. L. Fetter and J. D. Walecka. *Quantum Theory of Many-Particle Systems*. McGraw-Hill, 1971.

[364] C. J. Isham. *Lectures on Quantum Theory, Mathematical and Structural Foundations*. London: Imperial College Press, 1995.

[365] M. Olshanii. Atomic Scattering in the Presence of an External Confinement and a Gas of Impenetrable Bosons. *Physical Review Letters*, **81**(5), 1998.

[366] A. L. Fetter. Nonuniform States of an Imperfect Bose Gas. *Annals of Physics*, **70**(1), 1972.

[367] E. P. Gross. Hydrodynamics of a Superfluid Condensate. *Journal of Mathematical Physics*, **4**(2), 1963.

[368] L. P. Pitaevskii. Vortex Lines in an Imperfect Bose Gas. *Journal of Experimental and Theoretical Physics*, **13**(2), 1961.

[369] P. G. Saffman. The Velocity of Viscous Vortex Rings. *Studies in Applied Mathematics*, **49**(4), 1970.

[370] A. Leonard. Vortex Methods for Flow Simulation. *Journal of Computational Physics*, **37**(3), 1980.

[371] H. Lamb. Hydrodynamics 6th edition. 1993.

[372] R. J. Arms and F. R. Hama. Localized-Induction Concept on a Curved Vortex and Motion of an Elliptic Vortex Ring. *The Physics of Fluids*, **8**(4), 1965.

[373] L. Gamet, F. Ducros, F. Nicoud, and T. Poinsot. Compact Finite Difference Schemes on Non-Uniform Meshes. Application to Direct Numerical Simulations of Compressible Flows. *International Journal for Numerical Methods in Fluids*, **29**(2), 1999.

[374] P. J. Prince and J. R. Dormand. High Order Embedded Runge-Kutta Formulae. *Journal of Computational and Applied Mathematics*, **7**(1), 1981.